Dissertation
submitted to the
Combined Faculties of the Natural Sciences and Mathematics
of the Ruperto-Carola-University of Heidelberg. Germany
for the degree of
Doctor of Natural Sciences

CERN-THESIS-2018-014
07/02/2018

put forward by
Alexander Deisting (M.Sc. Physics)
born in Hachenburg, Westerwald, Germany
Oral examination: February 7$^{\text{th}}$, 2018

Measurements of ion mobility and GEM discharge studies for the upgrade of the ALICE time projection chamber

Referees: Prof. Dr. Silvia Masciocchi
Prof. Dr. Norbert Herrmann

Measurements of ion mobility and GEM discharge studies for the upgrade of the ALICE time projection chamber

ALICE is one of the four experiments at the Large Hadron Collider (LHC). The quark-gluon plasma, which is predominantly produced in lead-lead collisions at LHC, is of particular interest for ALICE. After the long shut-down 2 (2019-2021) the LHC will provide lead-lead collisions at an increased interaction rate of 50 kHz. In order to examine every event at this interaction rate the ALICE Time Projection Chamber (TPC) needs to be upgraded. The TPC's ReadOut Chambers (ROCs) are currently multi-wire proportional chambers. To prevent space charge build-up of slow ions, drifting from the ROCs into the TPC, a gating grid is used. The corresponding closure time imposes a dead time on the TPC read out, which prohibits data taking at a readout rate higher than 3 kHz. New ROCs have therefore been designed, relying on stacks of Gas Electron Multiplier (GEM) foils for the gas amplification, allowing for continuous readout.
With the new ROCs, a certain fraction of ions will be drifting at all time into the TPC. Knowing the exact ion mobility in the counting gas is thus required in order to determine which amount of ion-back drift is tolerable. In this work we study the ion mobility in Ne-CO_2-N_2 (90-10-5), which is the gas mixture for the upgraded TPC, as well in several other argon- and neon-based mixtures.
During stability studies for the new ROCs the phenomenon of secondary discharges has been observed. We thus also study discharges in GEM stacks and provide a detailed investigation of secondary discharges.

Ionenmobilitätsmessungen und GEM Entladungsstudien für die Umrüstung der ALICE Zeitprojektionskammer:

ALICE wurde entwickelt um das Quark-Gluon-Plasma zu untersuchen. Dieser Zustand von Materie wird z.B. in Blei-Blei Kollisionen am Large Hadron Collider (LHC), produziert. Ab dem Jahre 2021 wird der LHC Bleikerne mit einer Rate von 50 kHz zur Kollision bringen. Um alle Kollisionen bei dieser Rate aufzuzeichnen zu können, muss der ALICE Detektor verbessert werden.
Die ALICE Zeitprojektionskammer wird mit Vieldraht Proportional Kammern ausgelesen. Diese Kammern verfügen über eine Drahtebene mit variablem Potential, die je nach Potential für geladenen Teilchen transparent oder intransparent ist. Somit können Ionen, die während der Elektronenverstärkung entstehen, daran gehindert werden in das Detektionsvolumen der Zeitprojektionskammer zu driften. Würden diese Ionen das Detektionsvolumen erreichen, entsteht eine Raumladung, die es nicht erlaubt Teilchenspuren mit der nötigen Präzision zu rekonstruieren. Die Zeit, in der die Vieldraht Proportional Kammern für Ladungsträger geschlossen sind, erlaubt im Falle der ALICE Zeitprojektionskammer eine Ausleserate von höchstens 3 kHz. Aus diesem Grund wurden neue Auslesekammern entwickelt die Gas Electron Multiplier (GEM) Folien zur Elektronenverstärkung benutzten und somit eine kontinuierliche Datennahme erlauben.
Wir haben die Mobilität von Ionen in Ne-CO_2-N_2 (90-10-5), dem Zählgas der Zeitprojektionskammer, gemessen. Mit dieser Mobilität kann berechnet werden, welcher Prozentsatz der in den Auslesekammern produzierten Ionen in die Zeitprojektionskammer driften kann, bevor die Raumladung zu groß wird. Weiterhin haben wir Gasentladungen in GEM Folien und zwischen GEMs in GEM Stapeln untersucht. Dabei war die Beobachtung von Sekundären Entladungen von besonderem Interesse, die mit einer gewissen Häufigkeit auf eine Entladung in einer GEM folgen.

Contents

1. Introduction

In experiments where two particle beams collide with each other or where a single particle beam impinges upon a fixed target, detectors are needed to detect the presence of a charged particle, measure its trajectory and momentum, and determine its species. Experimental conditions, such as the collision rate and expected particle densities impose additional requirements on the possible detectors, extending the list of design constraints.

1.1. The Time Projection Chamber

In 1974 David R. Nygren introduced a novel concept for charged particle detection [1]. He proposed a gaseous detector, which allows to record a 3D image of the particles trajectories in the gas volume. His concept was based on a gas volume to which a parallel electric and magnetic field are applied. Particles propagating in this detector ionise gas atoms or molecules along their trajectories and the liberated electrons drift in the electric field towards ReadOut Chambers (ROCs) at the end of the detector, where they are amplified and their signal is read out. The specific energy loss of the particle in the gas allows to identify the species of the particle, if its momentum is known. A momentum measurement is as well possible with this detector, because the incident particles are deflected in the applied magnetic field. The *Time Projection Chamber* (TPC), as this detector was baptised, hence, offers in one detector tracking of an incident particle in three dimensions and a momentum measurement together with the possibility to perform Particle IDentification (PID). Because the entire gas volume of the detector serves as an active medium for the particle detection, events with high particle densities can be recorded.

In prototypes test, Nygren's concept was proved to be successful [2] and led to the construction of the PEP-4 TPC [3] at the SLAC facility, US. Since PEP-4, TPCs have been operated at lepton colliders and in experiments inspecting hadron-hadron collisions [4–7]. While the wish-list of particle physicists for the capabilities of their detectors remained roughly the same until now, experimental conditions and therefore the additional requirements on detectors did change. The TPC concept has been continuously improved in order to adapt to these changing requirements and to ensure stable operation and high quality data taking [8]. Nowadays, the TPC of A Large Ion Collider Experiment (ALICE) [9–12] is, with a gas volume of almost $90\,\mathrm{m}^2$, the largest of its kind. It is operated at challenging conditions imposed by the *Large Hadron Collider* (LHC) [13], located at the *European Centre for Nuclear Research* (CERN) next to Geneva, Switzerland.

1.2. Readout chambers for Time Projection Chambers

Many details of the TPC construction and operations have been improved in the course of the development of new TPCs. Here we want to focus on the improvement of the ROCs, which are critical for the performance of a TPC as a whole. So far all large TPCs have been or are equipped with *Multi-Wire Proportional Chambers* (MWPCs) [14], which have been developed in 1968 by G. Charpak *et al.*, who has received the Nobel Price for his invention in 1992. In a MWPC different potentials are applied to a set of wire planes, resulting in a high electric field. Electrons from the TPC volume are accelerated in this electric field until they have enough energy to ionise further gas atoms. The resulting electrons are accelerated as well, resulting in electron avalanches. In this way the original electrons from the TPC volume are amplified and can be read out by dedicated readout electronics. During the electron amplification ions are produced as well. These ions gain the same energy from the electric field like the electrons do. However, because of their positive charge and high mass they drift with a smaller velocity in the opposite direction than the electrons. A good

fraction of these slow ions can drift into the TPCs volume and accumulates there. The resulting space charge distorts the electric field in the detector and therefore the drift paths of the electrons in the gas volume are distorted. A *gating grid* has been added to the MWPCs [15, 16] in order to stop the ion back drift. Depending on the voltage supplied to this grid, it either collects electrons from the TPC volume as well as ions from the readout chambers or it is transparent to both. In a TPC with gated readout, a trigger opens the gating grid for a time which usually corresponds to the maximal electron drift time through the full TPC. Afterwards the grid is closed for the time needed to collect all the ions produced during the gas amplification. This introduces a dead time for the MWPC as well as the TPC. The ALICE TPC uses currently MWPCs in a gated readout mode, with a maximum readout rate of about 3 kHz. This rate is determined by the maximal drift time of electrons ($\sim 100\,\mu s$) and the closure time of gating grid (200 µs).

1.3. ALICE at CERN's Larger Hadron Collider

ALICE has been designed to study phenomena governed by the strong interaction. It is in particular dedicated to examine the properties of the Quark-Gluon Plasma (QGP) [17], which is predominantly produced in nucleus-nucleus collisions. The ALICE detector therefore needs the ability to record events with very high particle multiplicities, as expected for lead-lead collisions at LHC, and also to record particles with momenta as low as a few 100 MeV/c [10]. Both of these features make ALICE unique among the four LHC large-sclae experiments (ALICE, ATLAS [18], CMS [19] and LHCb [20]), and are the reason why ALICE employs a TPC as the experiment's key detectors for particle tracking and PID. During LHC Run 1 (2009-2013) and Run 2 (2015-2018), ALICE and its TPC have been successfully taking data at increasing interaction rate. While taking data at higher luminosity during Run 2, one observes higher space-point distortions along the recorded tracks than expected. The origin of the space charge creating these distortions was studied and at the same time a dedicated procedure was developed in order to correct the distorted particle tracks [21].

After the Long Shut-down 2 (2019-2021), the LHC will provide a collision rate of 50 kHz in lead-lead collisions. Several components of the ALICE detector will be modified, replaced or added [22] so as to improve the amount and quality of data recorded for the physics program of the ALICE collaboration. Different detectors, the readout electronics of a variety of detectors as well as the data acquisition systems will be upgraded. After the upgrade ALICE will be able to examine all events at 50 kHz.

1.4. The ALICE Time Projection Chamber upgrade

At an interaction rate of 50 kHz it is not feasible to use MWPCs with a gating grid. The ALICE TPC Upgrade project therefore developed new ROCs and front-end electronics [23, 24]. The design goals can be stated as follows. First, the new ROCs must be able to record data continuously. Second, the excellent tracking and PID capabilities as well as momentum resolution of the current TPC need to be preserved. In order to achieve these two goals at the same time, the amount of ions escaping from the ROCs into the drift volume must be kept small. These ions otherwise build up space charge in the drift volume, which distorts measurements of the particles' tracks. A third performance goal has therefore been defined. The amount of ions in the drift volume, including primary ionisations, can be at most 1 % of all the ions produced during the electron multiplication in the ROCs. To this end new readout chambers have been developed, which use stacks of four Gas Electron Multipliers (GEMs) [25] as electron multiplication stage. On top of that, a space charge distortion correction will be applied, which is in part currently employed with the existing TPC.

The requirements on a TPC running under LHC Run 3 conditions are ambitious. Regarding the evolution of the TPC concept, the continuous, ungated readout mode is the next step for gaseous TPCs. The ALICE TPC Upgrade therefore pushes forward the development of novel and existing techniques, which can be useful for future projects, including but not restricted to, a TPC at a future linear collider [26].

1.5. Ion mobility measurements and discharge studies

The knowledge of ion mobility and ion drift velocity is necessary in order to estimate for how long ions drift through a gaseous detector. The amount of tolerable Ion Back Flow (IBF) from the ROCs into the drift volume depends on the actual mobility of ions drifting in the counting gas. Therefore, the ion mobility of the gas mixture used in the upgraded TPC largely impacts our third performance goal, namely that an IBF of less than 1 % is necessary in order to keep the field distortions in the TPC at a tolerable level. In case the mobility is lower as assumed during the definition of this goal, the limit for the IBF needs to be reduced. Although there are many measurements of ion mobility in pure gases, only few exist for gas mixtures. We extend these measurements and present a method which can be used by other groups to measure the ion mobility in their desired gas mixture (Chapter 5). Our measurements are done with a detector using a stack of three $10 \times 10\,\mathrm{cm}^2$ GEMs. With a special analysis procedure of the signals recorded with the detector, the drift time of ions and in turn the mobility can be measured. We find the mobility in the baseline gas mixture of the upgraded ALICE TPC Ne-CO_2-N_2 (90-10-5) to be $(2.92 \pm 0.04)\,\mathrm{cm}^2\,\mathrm{V}^{-1}\,\mathrm{s}^{-1}$ and therefore about 30 % lower than it was assumed in [23].

We also perform discharge studies motivated by the occurrence of *secondary discharges*. This special type of discharge occurs with a certain probability after an initial discharge in a GEM. Discharges threaten to damage a GEM permanently. Any mechanism creating additional discharges after an initial one therefore need to be understood and mitigated as much as possible. In order to examine the GEM stack behaviour during (secondary) discharges, our set-up is operated in a regime where the probability for initial discharges is relatively high. We study the exact probabilities at which initial (Chapter 6) and secondary discharges (Chapter 7) occur, as well as the time evolution of the potentials at different electrodes of our detector, during the course of (secondary) discharges. Such potential measurements allow to identify the location of a discharge in the GEM stack. Furthermore, they reveal weather large potential differences build up after a discharge, creating the conditions for further discharges, and allow understanding between which electrodes such potential differences build up. Our measurements of the potentials at the different electrodes reveal that secondary discharges are discharges of the gap below the discharging GEM. A way of mitigating them is to decouple the GEMs better from the respective power supply as it is achieved by introducing decoupling resistors.

This work has been preformed within the ALICE TPC Upgrade project, although both main topics of this work, namely ion mobility measurements and discharge studies, address general questions of great interest related to gaseous detectors using GEMs in a high-rate environment.

1.6. Detailed outline of this work

To embed our studies in the context of the research done by the ALICE collaboration, we recap the strong interaction and introduce ways to examine the QGP in Chapter 2 (Sec. 2.1 and Sec. 2.2, respectively). We then discuss experimental signatures of the QGP (Sec. 2.2.3) and the corresponding requirements on detectors. After we introduce the ALICE detector (Sec. 2.3) and explain how it matches these requirements. The motivation of the ALICE collaboration to upgrade its detectors for LHC Run 3 is outlined in Section 2.3.3. The following Chapter 3 summarises the physics principles on which gaseous detectors are based. We focus on the mechanisms related to ion drift (Sec. 3.1) and discharge phenomena (Sec. 3.3). Furthermore we introduce techniques employed in gaseous detectors for electron amplification, such as wire chambers and GEMs (Sec. 3.4 and following). Based on these foundations, we introduce in Chapter 4 the general concept a TPC (Sec. 4.1) and the ALICE TPC (Sec. 4.2) in particular. We discuss the details of the ALICE TPC Upgrade in Section 4.3.

In Chapter 5 we present our measurements of ion mobility. We develop a method relying on the measurement of the signal induced by ions drifting through a gap of few cm. The time of the ions' arrival at the end of the gap is extracted from the derivative of the recorded signal (Sec. 5.3). This procedure is tested thoroughly with simulated data (Sec. 5.4) and

we compare the measured mobilities to published data to validate our method and results. The counting gas in our detector has ambient pressure and room temperature. Results are therefore also relevant for other groups operating their detectors under similar conditions. We measure ion mobilities of the respective drifting ions in argon- and neon-based gas mixtures with carbon dioxide as quencher (Sec. 5.5.2). In addition we use our set-up to measure the ion mobility of the gas mixture used in the current and future ALICE TPC, namely Ne-CO_2-N_2 (90-10-5) with a water content of about 100 ppm (Sec. 5.5.3). Our findings show an ion mobility that is lower than previously expected and that therefore imposes to strictly respect the limit of an IBF lower than 1 %. We also examine water contents ranging from $\sim$ 100 ppm to more than 1000 ppm (Sec. 5.5.4), in order to provide additional data for the study and simulations of the space-point distortions in the current TPC.

Our discharge studies in Chapter 6 and Chapter 7 have been performed to understand the phenomenon of *secondary discharges*, which is extensively described in Chapter 7. This kind of discharges happen with a certain probability after initial discharges in a GEM. We therefore use a highly ionising source and High Voltage (HV) settings, which make discharges likely if ionisation is present. The large number of recorded discharges allows us to study secondary discharges in detail. This number allows in addition to make quantitative statements on the behaviour of a GEM system when an initial discharge occurs. In Chapter 6 we focus on these initial discharges and on the corresponding potential changes. The experimental set-up for discharge studies and tools to examine the potentials are introduced in Section 6.2. The radiation source is discussed in Section 6.3.3. We confirm that observed discharges are in line with the expectations drawn from the underlying process responsible for the discharges (Sec. 6.4). Furthermore, we draw conclusions from the observed discharge probabilities for the operation of GEM stacks. Afterwards we discuss how the potentials applied to a GEM stack change in the moment of the discharge (Sec. 6.5). The potential analysis also allows investigating the phenomenon of *discharge propagation* from one GEM to another (Sec. 6.5.3). This phenomenon depends on the HV settings and should be mitigated in order to maintain the number of discharges as low as possible. In addition, we emulate the way HV will be supplied to the GEM stacks in the future ALICE TPC by constructing a mock-up of segmented GEMs and using a cascaded power supply (Sec. 6.6), as is planned for the final detector. Analysing the potential changes during a discharge in this system helps understanding the dead-time of ALICE TPC GEM stacks after discharges and reveals possible regions with high potential differences, after a discharge occurred.

The set-up and methods tested with discharges (Chapter 6) are then used to examine secondary discharges (Chapter 7). Our work has been initiated by the study in [27], therefore we first reproduce the measurements therein. We measure the probability of occurrence of secondary discharges and the average time between initial and secondary discharge as a function of the electric field between a GEM and the readout plane (Sec. 7.2). We find for example that secondary discharges occur only after an initial discharge in a GEM and only if the electric field in the gap between GEM and readout plane is larger than a certain value. These results agree with the ones in [27]. Furthermore we show with potential measurements that a secondary discharge is a discharge of the gap between GEM and anode plane. Next we extend these studies to the gaps between adjacent GEMs (Sec. 7.3) and find the same qualitative features like we observed in the gap between a GEM and the readout plane. We present measurements of secondary discharges in Ne-CO_2-N_2 (90-10-5) in Section 7.4. A possible way to make the occurrence of secondary discharges less likely in commonly used electric fields is discussed in Section 7.5. Introducing decoupling resistors in the high voltage path to the bottom electrode of a GEM foil leads to an increase of the electric field value where secondary discharges occur. In Section 7.6 we report on studies of secondary discharges where the GEMs are either biased with a cascaded PS or a voltage divider. These two high voltage systems are foreseen for the operation of the ALICE TPC GEM stacks after the upgrade. General consequences of secondary discharges on the operation of GEM stacks are discussed (Sec. 7.7). We propose a hypothetical mechanism responsible for secondary discharges (Sec. 7.8), however, the origin of secondary discharges still remains unknown and subject for further studies.

In Chapter 8 we present two research and development topics that aim at testing the

stability of the upgraded ALICE TPC's GEM stacks. Using the largest GEMs produced for the ALICE TPC Upgrade, we investigate the sagging of the foils due to electrostatic forces occurring when HV is applied (Sec. 8.1). We investigate which kind of spacers in the gap below a GEM ensures a planar foil without sagging. Furthermore, we study whether having a spacer in direct contact with the foil results in more discharges in the region, where this contact is made. Doing so, we use discharge probability measurements and the analysis of videos of discharging GEMs.

Our work has contributed to answer two important questions for the upgrade of the ALICE TPC. We measured the ion mobility in Ne-CO_2-N_2 (90-10-5) and provided information on how to improve the stability of the new ROCs against discharges. We can not do a projection in time to 3.5 years form now, however, we look forward to the moment our studies will not be only applied to the operation of ROCs but to the operation of the entire, upgraded ALICE TPC.

2. A Large Ion Collider Experiment

A Large Ion Collider Experiment (ALICE) [10] is the one dedicated heavy-ion experiment at the *Large Hadron Collider* (LHC) at CERN, Geneva. In collisions of heavy-ions at sufficient energy, lead ions at the LHC, a medium of high energy density and temperature is created. This medium exists only temporarily and undergoes a phase transition towards a hadron gas or nuclear matter as it cools down. The creation of this medium, its properties as well as the phase transition are governed by the strong interaction of the *Standard Model* (SM) of particle physics. In Section 2.1 we recap some features of the strong interaction, which are of importance for the afore mentioned phase changes of nuclear matter. After (Sec. 2.2) we discuss, how this phase transition may occurs and which experimental observables can be used to examine it. Based on these considerations we discuss the ALICE detector and how it is designed to measure these observables.

2.1. The strong interaction in the standard model of particle physics

The standard model of particle physics comprises the electromagnetic, the weak and the strong interaction, as well as the known elementary particles. It has passed extensive experimental test and was even able to predict the existence of new particles. A recent experimental confirmation of the SM is the discovery of the Higgs boson at the LHC [28, 29]. However, the SM is not a full theory of all fundamental interactions. Despite the fact that the SM describes successfully all ordinary matter, it e.g. lacks a description of dark matter and it fails to incorporate gravity.

The strong interaction is described by a quantum field theory with symmetry group SU(3), which goes by the name of *Quantum Chromodynamics* (QCD). Analogue to the electric charge of particles taking part in electromagnetic interactions, particles interacting by the strong interaction are characterised by a colour charge. Each quark carries one of three possible colours or anti-colours and the gluons, which mediate the strong interaction, carry one colour and an anti colour at the same time. The possible interaction vertices in terms of Feynman graphs are a quark anti-quark gluon vertex, a three gluon vertex and a four gluon vertex.

2.1.1. Asymptotic freedom and confinement

Fundamental parameters of QCD are the (bare) quark masses and the strong coupling constant (α_S). These parameters can not be experimentally observed, however, α_S enters the calculation of experimental observables, which are obtained using perturbation theory techniques. In perturbative methods the calculation of a quantity of interest (e.g. a cross-section) requires series expansions in α_S to converge. Therefore, perturbative methods are applicable if the strong coupling constant takes a value smaller than one. A peculiarity of α_S is, however, that the coupling strength decreases with increasing momentum transfers or decreasing space-time distance and vice versa (Fig. 2.1). The renormalisation of the strong coupling constant to a scale μ_R allows to assign a value to $\alpha_S(\mu_R^2)$ based on measurements of different processes (Fig. 2.1). At a momentum transfer (Q^2) equal to the chosen value of the renormalisation scale $Q^2 \sim \mu_R^2$ the quantity $\alpha_S(\mu_R^2)$ gives a measure for the interaction strength of the strong interaction. As shown in Figure 2.1, the interaction strength is relative small at high μ_R (Q in the figure). At this energies quarks appear as free, which is known as *asymptotic freedom*. Furthermore the small value of α_S allows to use perturbative methods to calculate processes at this energy range.

Figure 2.1 illustrates as well that the interaction strength increases for small momentum

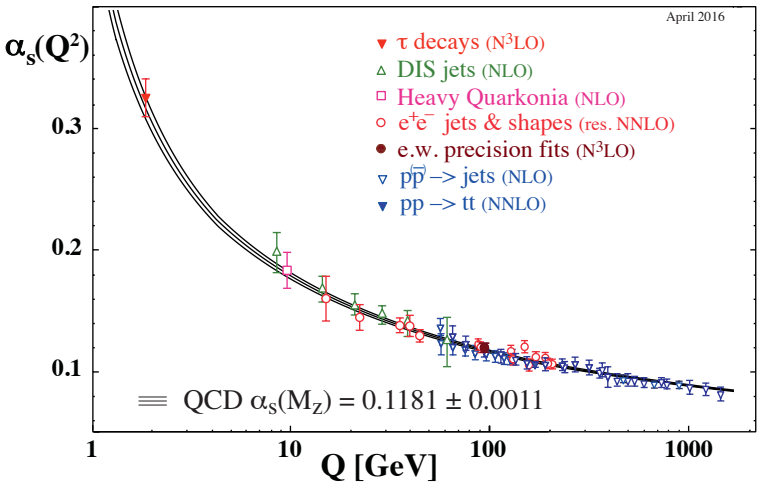

Figure 2.1: The strong coupling constant $\alpha_S(Q^2)$ as function of the normalisation scale Q. In the text we use $\alpha(\mu_R^2)$ and μ_R, respectively. The values for $\alpha_S(Q^2)$ are extracted from the measurements indicated in the legend. In brackets the degree of QCD perturbation theory used to extract $\alpha_S(Q^2)$ from the measurements is indicated. NLO corresponds to next-to leading order, NNLO corresponds to next-to-next-to leading order and so on. The figure has been adopted from [30].

transfer or large space-time distance between two interacting particles. This phenomenon is known as *infrared slavery* or *confinement* and is believed to be the reason why quarks and gluons are never observed as free particles, but only in bound states which are colour-neutral.

2.1.2. The phase diagram of strongly interacting matter

Confinement of quarks and gluons into colour neutral particles is no longer present in matter at high temperature and/or density. This is an immediate consequence of the low α_S at high momentum transfer or small space-time separation between interacting particles. Therefore a state of *QCD matter*[a] is expected, in which quarks are able to move freely and quarks and gluons are the relevant degrees of freedom, instead of colour-neutral states of the two. For a period of about 10 µs after the big bang, the early universe is believed to have been in such a state. This state of deconfined matter is called *Quark-Gluon Plasma* (QGP). The chiral symmetry is restored if matter is present at the temperature and/or pressure which is necessary to form the QGP. If chiral symmetry is broken, quarks polarise the vacuum around them and thus create a gluon cloud which gives the quarks an effective mass [31]. Masses of hadrons are caused by the effective mass of their quark constituents. In the QGP, where chiral symmetry is restored, the quarks have only their bare masses, without the mass generated by the spontaneous breaking of chiral symmetry. Especially the masses of hadrons containing only the light quarks (up, down, and strange) are almost exclusively generated by the spontaneous chiral symmetry breaking, and hence these quarks appear as quasi massless after the restoration of chiral symmetry.

A QGP is one of the phases of QCD matter. The phase diagram in Figure 2.2 shows different phases of such matter as function of the temperature T and the quark chemical potential μ_q, which is a measure for the net quark density.[b] An order parameter is necessary to quantify the phase change of matter with varying T and/or μ_B. In one example given in [32], the quark-anti-quark condensate $\langle q\bar{q}\rangle$ is used as order parameter. This condensate value describes the vacuum expectation value of a certain ground state of a bound quark and anti-quark. If chiral symmetry is broken, such states have a non vanishing vacuum

[a] With the term QCD matter we refer to all matter, which is made up of particles carrying colour charge.
[b] The baryochemical potential μ_B is as well frequently used in this context. It is a measure for the baryon number density.

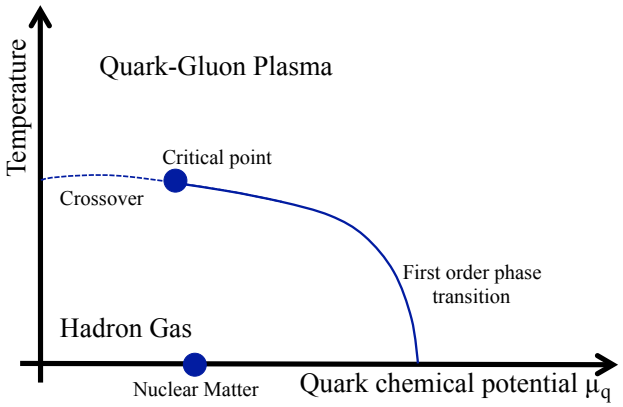

Figure 2.2: Sketch of the phase diagram of strongly interacting matter. The *Quark-Gluon Plasma* phase and the *Hadron gas* phase of matter are indicated. See the text for the discussion of the respective phase transitions. The figure has been created using the discussions and informations in [31, 32].

expectation value and can therefore be seen as particles. If we consider the phase transition of matter at initially small μ_q and $T \sim 0$ for increasing T, the order parameter $\langle q\bar{q}\rangle$ is observed to change smoothly until $\langle q\bar{q}\rangle = 0$ in the QGP phase. This smooth transition gives rise to the expectation, that the phase transition from a hadron gas to the QGP is a second order (or *crossover*) phase transition. However, the phase transition of matter at T with increasing quark chemical μ_q potential is characterised by an abrupt change in the quark anti-quark condensate. The discontinuity in $\langle q\bar{q}\rangle$ thus fulfils the characteristics of a first order phase transition. A *critical point* on the phase boundary between the QGP phase and the hadron gas phase is expected at the point, where the kind of phase transition changes from first to second order.

2.2. Examining the quark-gluon plasma

The study of different QCD matter phases and the transitions between these phases offers insights into the process of confinement and deconfinement and thus insights into the creation of all nuclear matter we observe today. Furthermore, the (approximate) restoration of the chiral symmetry during the phase transition from the hadron gas to the QGP phase is interesting beyond the aspects of QCD, because phase transitions with a spontaneous symmetry breaking are common in the standard model. The fact that this particular QCD phase transition and the chiral symmetry breaking can be achieved in laboratory experiments, makes it a very attractive topic to study. These studies are advanced with calculations as well as in experiments with heavy-ion collisions.

2.2.1. Lattice QCD

However, calculations of phase transitions from confined matter to deconfined matter can not (yet) be done in the framework of perturbative QCD, because of the reasons mentioned in Section 2.1.1. An alternative method to calculate such phenomena is *lattice QCD*. In this approach path integrals describing the theory are numerically solved on a discrete space-time lattice [33]. In this way many QCD phenomena like the phase transitions of QCD

matter can be calculated, which are not accessible by perturbative QCD. E.g. for $\mu_q = 0$ the temperature at which the second order phase transition of a hadron gas to the QGP takes place has been calculated to be (154 ± 9) MeV [34]. To check if there is a critical point, lattice calculations have been extended to $\mu_q > 0$. In [35] the authors obtain results, which agree on the one hand with the previously quoted temperature at the crossover from [34] and, on the other hand, their results support the existence of a critical point.

2.2.2. The Quark-Gluon plasma in the laboratory

The time interval during which our universe may have been in the QGP state is not accessible to astrophysical observations. Therefore the QGP, or other states of matter with high temperature and/or energy density, need to be created in the laboratory to study them experimentally.

At many accelerators and colliders, nucleus-nucleus collisions have been examined on the quest for the QGP, after head-on collisions of (ultra) relativistic (heavy) ions have been first proposed as a possible way to probe different phases of matter [36]. Depending on the collision energy and the ions used for such collisions, different regions in the phase diagram can be probed. See e.g. [37] for a review on experimental results obtained at various accelerators, colliding (heavy) ions. At CERN's *Super Proton Synchrotron* (SPS) first evidence for the existence of a QGP has been found [38], while at the *Relativistic Heavy-Ion Collider* (RHIC), *Brookhaven National Laboratory* (BNL), US, the QGP was finally discovered [39–42]. In contrast to what has been widely expected, the QGP was found to be a strongly interacting state of matter. For this reason it is sometimes referred to as sQGP.

Current experiments

Nowadays, RHIC is still in operation and a dedicated collider for heavy-ion collisions, colliding gold atoms at centre of mass energies ($\sqrt{s_{NN}}$) of up to 200 GeV per nucleon pair. Furthermore, ALICE takes data at the LHC and is there the only experiment with the main focus on heavy-ion collisions. However, the other three large experiments (ATLAS, CMS, LHCb) have as well a heavy-ion program. Although the LHC collides protons most of the time, there are dedicated periods during which lead-lead collisions in the energy range $2.76\,\text{TeV} \leq \sqrt{s_{NN}} \leq 5.02\,\text{TeV}$ took and take place. Proton-proton collisions at the same centre of mass energy per nucleon pair as used during heavy-ion collisions, are as well part of the LHC program and are needed as reference data (Sec. 2.2.3). Furthermore, proton-lead collisions have been performed to provide reference data for the studies of heavy-ion collisions.

At the collision energies of RHIC and LHC the phase diagram is probed at high temperature and small or vanishing μ_B, respectively. The latter is the case, because the strongly interacting quark matter, the so called medium, is dominated by the quark anti-quark pairs produced early during the collisions and not by the valence quarks of the originally colliding nuclei. In order to study other regions of the phase diagramm new facilities are planned. The heavy-ion program at the future *Facility for Antiproton and Ion Research*, now under construction at the *Gesellschaft für Schwerionenforschung*, will probe the phase diagram at lower T, but higher density μ_B [43, 44].

Creation and evolution of the quark-gluon plasma in heavy-ion collision

Figure 2.3 illustrates the evolution of the quark-gluon plasma using a simulation of two lead nuclei colliding at LHC energies. The two ultra relativistic nuclei collide (Fig. 2.3, (1)) and pass through each other within 1×10^{-2} fm/c. A large amount of energy is deposited in the collision region, generating quark and anti-quark pairs as well as colour neutral particles, which we neglect here. Then a strongly interacting medium is formed on a time scale of 0.1 - 1 fm/c. During this time a thermal equilibrium is established by collisions between the quarks and anti-quarks, which can move freely over the full volume of the QGP (Fig. 2.3, (2)). At LHC energies this volume can be as big as several hundreds to thousands of fm^3. The strongly interacting medium has a life time of about 10 - 20 fm/c during which

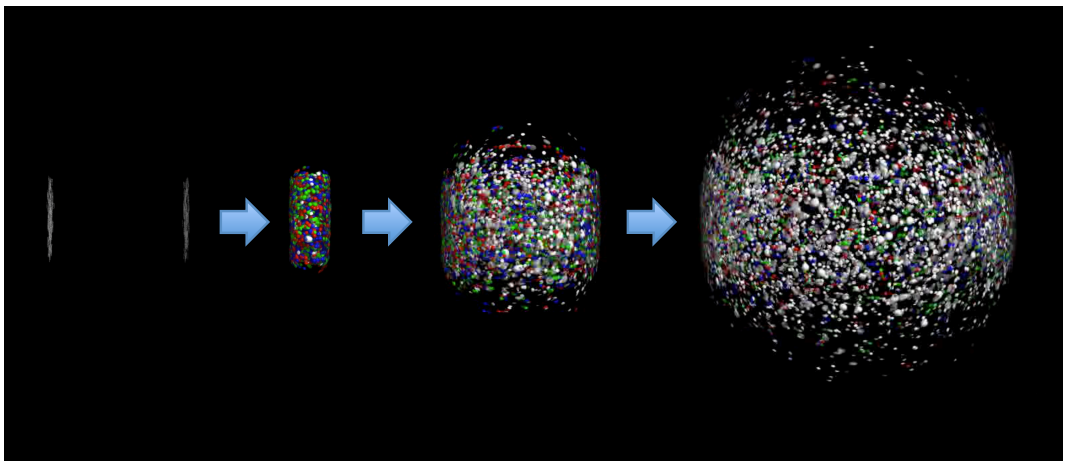

Figure 2.3: Simulation of four stages in a lead-lead collision at LHC energies. 1) In the very left part of the figure, two lead nuclei approaching each other are shown. They are Lorentz contracted and appear as flat discs. Their white colour indicates that they solely consist out of hadrons. 2) The middle left of the figure shows the two nuclei passing through each other, thereby creating the QGP. The colours indicate, that now quarks and gluons are the relevant degrees of freedom. 3) Afterwards, the QGP expands (middle right part of the figure) and during this expansion it cools down. Quarks and gluons start to be confined into colour neutral hadrons. 4) In the very right part of the figure, the expansion continuous. Almost all particles are now colour neutral. All figures are adopted from a simulation of H. Weber, UrQMD, Frankfurt.

it expands and cools down. Eventually the quarks get confined into colour neutral states, which is known as the *chemical freeze-out* (Fig. 2.3, (3)). This happens either before or at the time of hadron formation (*hadronisation*). After the hadronisation these hadrons still collide with each other and therefore the matter can still be in thermal equilibrium. During the ongoing cooling process inelastic collisions stop at some time and hence the exact composition of particles emerging from the collision region is eventually fixed. As the distance between the hadrons increases (Fig. 2.3, (4)), elastic collisions become less frequent until no more such collisions occur (*kinetic freeze-out*). From this time onwards hadrons move freely away from the region, where the medium was present.

2.2.3. Experimental observables to probe QCD matter

As outlined in Section 2.1, it is only possible to observe colour-neutral particles. Therefore, experimental observables are necessarily based on the detection of such particles, but they have to provide insights into the stages of the evolution of a medium, where particles carrying colour are the relevant degrees of freedom. The review in [37] contains an overview of a variety of experimental observables in heavy-ion collisions and gives as well the corresponding results from several experiments at different accelerators. Here we present a few observables to explain on the one hand, how the evolution of (strongly interacting) QCD matter can be measured in experiments. On the other hand, we want to use properties of the selected observables to illustrate in a later section (Sec. 2.3.1) the requirements on an experiment, which examines heavy-ion collisions.

One parameter to quantify the difference between the same observable measured in nucleus-nucleus (AA) and in proton-proton (pp) collisions is the *nuclear modification factor* R_{AA}.

$$R_{\mathrm{AA}} = \frac{1}{\langle N_{\mathrm{Coll}} \rangle} \frac{\mathrm{d}N_{\mathrm{AA}}/\mathrm{d}p_{\mathrm{T}}}{\mathrm{d}N_{\mathrm{pp}}/\mathrm{d}p_{\mathrm{T}}} \tag{2.1}$$

The number $\langle N_{\mathrm{Coll}} \rangle$ corresponds to the average number of binary nucleon-nucleon collisions, which occur if two nuclei collide. $\mathrm{d}N_{\mathrm{AA}}/\mathrm{d}p_{\mathrm{T}}$ and $\mathrm{d}N_{\mathrm{pp}}/\mathrm{d}p_{\mathrm{T}}$ yield the same quantity

measured in AA and pp collisions as function of the transverse momentum p_{T}.[c] In case a process behaves in the same way in a single proton-proton collision as well as in $\langle N_{\mathrm{Coll}} \rangle$ nucleon-nucleon collisions occurring during one AA collision, $R_{\mathrm{AA}} = 1$ is obtained. However, observing $R_{\mathrm{AA}} \neq 1$ indicates that the observable measured by $\mathrm{d}N_i/\mathrm{d}p_{\mathrm{T}}$, $i \in (\mathrm{AA}, \mathrm{pp})$ behaves differently for the two collision systems and this difference may be attributed to a change in the state of matter during AA collisions. In order to calculate the nuclear modification factor an experiment has to record nucleon-nucleon as well as proton-proton collisions at comparable conditions. Therefore the centre-of-mass energy per nucleon pair in both collision systems should be the same. To complete the picture, pA collisions are recorded as well. These are needed to disentangle so called *cold nuclear matter* effects from effects, which are exclusively observed in e.g. heavy-ion collisions and thus pA collisions can help to pin down the QGP less ambiguously.

The different experimental observables, which are measured in the different collision systems, are grouped into bulk observables and single-particle observables. The bulk observables are based on all the (final) particles emerging from the collision region, while single-particle observables focus only on one particle species. Some of these observables are listed in the following.

Centrality

The *centrality* of the collision is one of the bulk observables. In a similar manner as the impact parameter, the centrality measures the overlap of the two colliding nuclei in the plane to which the velocity vectors of the nuclei are orthogonal. For 0 % centrality the nuclei collide head on. The centrality is determined using the number of particles (particle multiplicity) produced in a heavy-ion collision. A model is fitted to multiplicity versus event distributions and the events are then sorted into centrality classes depending on their multiplicity. Furthermore, the centrality can be used to deduce the fraction of nucleons of the two nuclei, which actually take part in a collision and thus contains geometrical information about the collision region. Also $\langle N_{\mathrm{Coll}} \rangle$ in equation (2.1) is determined from the centrality.

Flow

Different collision geometries with nucleons, which do not take part in the collision but pass the collision region close by, give rise to different pressure gradients in the collision region. When the strongly interacting medium cools down and expands these gradients are reduced. The distribution of the final particles in space and their momenta carry information about the matter at the moment of the kinetic freeze-out. In order to extract this information, correlations of the momenta of different particles are examined and the resulting experimental observable is the *flow*. Flow measurements, in combination with theoretical models, can be used to constrain the thermodynamic properties of strongly interacting matter at the time of the kinetic freeze-out, as for example the freeze-out temperature. In general, flow is a bulk observable, however there are also flow studies on the basis of single-particle species.

Hadron yields

Yields of individual hadron species are by definition single-particle observables. The (relative) abundances of the different hadrons allow to gain information about the production mechanism of hadrons and they contain information about the temperature at the chemical freeze-out. The temperature at which the chemical freeze-out takes place can be calculated from a fit of a model to the measured hadron yields. One model is the *thermal model* [45, 46], which describes the particle production with a statistical model of a hadron resonance gas. If this model is fitted to hadron yields recorded by the ALICE experiment at a centrality of 0 - 10 % a chemical freeze-out temperature of (156 ± 2) MeV is found [47]. This number is in agreement with the previously mentioned results from lattice QCD, for zero net quark (or baryon) density, which is the case for heavy-ion collisions at LHC.

[c] The transverse momentum is the component of the momentum, which is perpendicular to the beam axis. However, the measured parameter can be as well a function of something else than $\mathrm{p_T}$ or be a function of the transverse momentum and another variable at the same time.

Photons and dileptons

Photons can be used as a probe for different stages of heavy-ion collisions, because they do not take part in the strong interaction. This enables them to escape the strongly interacting QGP unaffected. During the initial collision of the two nuclei *prompt direct photons* are produced, while *direct photons* are thermal photons emitted during all phases of the QCD matter's evolution. Direct photons therefore carry information on the temperature evolution of the (strongly) interacting medium. The challenge remains to separate (prompt) direct photons from the ones, which are the result of hadron decays after the chemical freeze-out. In a single-particle analysis of photons, the photon yields are fitted to models taking all photon sources into account. Doing so, the temperature of the QGP produced in lead-lead collisions at LHC ($\sqrt{s_{\mathrm{NN}}} = 2.76\,\mathrm{TeV}$) could be estimated to be on the order of a few 100 MeV [48].

In a similar way dileptons (lepton anti-lepton pairs), can be used to probe different stages of the medium created in heavy-ion collisions. The challenges are similar, because dileptons can be as well produced by decaying hadrons after the chemical freeze-out.

Heavy quarks

Even at the highest temperature of the QGP expected during lead-lead collisions at LHC only light quarks (up, down, strange) can be produced thermally. All heavier quarks have to be produced as quark anti-quark state in the initial hard scattering of the nucleons before (strongly interacting) QCD matter is formed. After their production, these quarks take part in the full evolution of the QGP until they hadronise. The measured hadrons with heavy quark content can then be used as tool to test properties of the medium formed in heavy-ion collisions.

To this end charmonium states $\langle c\bar{c}\rangle$, consisting out of a charm quark and charm anti-quark, are an important experimental observable. Originally it has been predicted that the J/ψ production should be suppressed, because the creation of $\langle c\bar{c}\rangle$ states in a deconfined medium is hindered by colour screening effects [49]. Later, J/ψ suppression has been observed at RHIC [50]. However, these results can as well be explained by the statistical hadronisation model [51]. The statistical hadronisation model predicts an decrease of the J/ψ suppression in heavy-ion collisions at LHC as compared to RHIC [17], which has indeed been observed by the ALICE collaboration [52].

2.3. The ALICE detector

The experimental observables in Section 2.2.3 lead to a set of requirements on a detector, which is used to study heavy-ion collisions at a collider experiment. In advance we introduce coordinates used in the context of such experiments. Usually the origin of the coordinate system is placed in the point, where the particle beams collide, the interaction point. The *longitudinal* (respectively *transversal*) direction is the direction in parallel (perpendicular) to the beam axis. In the transversal plane the coordinates are r, the distance to the beam axis, and the polar angle ϕ running from 0 to $2\,\pi$. The azimuthal angle θ (0 - π) is measured in the longitudinal plane between a point of interest and the beam-axis. Instead of θ, the *pseudo rapidity* η is often used [53].

$$\eta = -\ln\left(\tan\frac{\theta}{2}\right) = \frac{1}{2}\ln\left(\frac{\mathrm{p}+\mathrm{p_L}}{\mathrm{p}-\mathrm{p_L}}\right) \tag{2.2}$$

Where p is the absolute value of the three momentum $\mathbf{p}$ and $\mathrm{p_L}$ is the part of $\mathbf{p}$ parallel to the beam axis. For ultra relativistic particles where the particle's energy (ε) is much larger than the particle mass, $\varepsilon \sim \mathrm{p}$ holds. In this case the pseudo rapidity is equal to the *rapidity*, which is defined as

$$y = \frac{1}{2}\ln\left(\frac{\varepsilon+\mathrm{p_L}}{\varepsilon-\mathrm{p_L}}\right) \quad . \tag{2.3}$$

Regions with high absolute values of the pseudo rapidity ($|\eta| \gtrsim 2$) are referred to as *forward rapidity* or *backward rapidity* and are close to beam axis. On the contrary, regions with $\eta \sim 0$ are at *mid rapidity*.

2.3.1. Design requirements

The particle multiplicity needs to be measured, because this quantity enters the calculation of several parameters as the centrality or $\langle N_{\mathrm{Coll}} \rangle$. Accordingly we need detectors, which can determine the number of particles originating from the interaction point. The direction of the outgoing particles depends on the exact collision geometry, therefore a detector measuring multiplicities should cover $2\,\pi$ in ϕ and a range in $|\eta|$ from zero to an as high as possible value. The latter is challenging for collider experiments, because the beam-pipe needs to be fed through the experiment. Particles emitted at very forward rapidity are likely to escape detection in detectors, which are located in less than several meters (longitudinal) distance to the interaction point.

In addition to the bare number of particles, the respective particle trajectory and momentum are of great interest for many observables in heavy-ion collisions. In a magnetic field the trajectory of a charged particle is bent according to the Lorentz force. If a magnetic field B is applied parallel to the beam axis, the transverse momentum can be determined by the relation

$$\mathrm{p_T[GeV]} \sim 0.3 \cdot q[e] \cdot \mathrm{B[T]} \cdot r_{\mathrm{p}}[\mathrm{m}] \quad , \tag{2.4}$$

where r_{p} is the radius of the particles curvature and the unit e is the electron charge. Neutral particles (neutral hadrons, photons) are obviously not deflected in the magnetic field and they are as well not detected in typical tracking detectors. They are detected in calorimeters where they are (ideally) stopped and their energy deposit is recorded. Accurate measurements of the photon energy are for example a requirement to probe the thermal evolution of strongly interacting matter with direct photons.

In addition to tracking of charged particles, Particle IDentification (PID) is required in order to perform any single-particle analysis. Proper identification of the hadrons and/or their decay products is important to study the colour content of the medium created during a heavy-ion collision.

Particle tracking, determining a particles' momentum and energy as well as certain PID capabilities are important for any collider experiment. However, there are some peculiarities for dedicated heavy-ion experiments. First, the number of particles produced in a single heavy-ion collision can be as high as several 1000 per η interval. All the corresponding tacks have to be recorded simultaneously, hence the particle tracking in such an environment needs to be robust. Furthermore, the momentum spread between different particles can span several orders of magnitude. This momentum range arises e.g. between the momenta of particles produced during the hard scattering of two colliding nuclei and the momenta of particles produced during the hadronisation of a strongly interacting medium. The magnetic field can not be too large in order to examine low momentum particles. Otherwise the particle spirals in the magnetic field at a low r_{q} (Eq. (2.4)) and therefore never reaches detectors in the experiment, which are located at r higher than $2r_{\mathrm{q}}$. Furthermore the material budget of subsequent detectors has to be low for the first detectors, as seen from the interaction point. Otherwise particles may be stopped before they are fully characterised.

2.3.2. Detectors of ALICE

The ALICE detector has been designed according to the specifications for a heavy-ion experiment. See [10, 54] and the references therein. It is interesting to note that RHIC was not yet running during the design phase of ALICE. Therefore the design requirements of the ALICE detector had to be based on extrapolations from the heavy-ion experiments at SPS. Therefore, a detector design with a very broad set of features was adopted and the design was kept flexible enough to allow the addition of new detectors.

Figure 2.4 shows a schematic view of the ALICE detector as it is used to take data during LHC Run 2. The experiment consists out of two parts. First, the *central barrel*, which is

located inside the L3 solenoid [55]. The solenoid is a room temperature magnet, which can provide an magnetic field of up to 0.5 T. The second part is a muon spectrometer, which is located at backward rapidity $-4.0 < \eta < -2.5$. It is equipped with a dipole magnate providing a magnetic field of 0.6 T at the centre of the magnet's coils.

In the following we introduce the detectors most frequently used during data taking in proton-proton and lead-lead collisions.

Inner tracking system

The Inner Tracking System consists of six layers of silicon detectors surrounding the beam pipe close to the interaction point ($4\,\text{cm} < r < 43\,\text{cm}$, $|\eta| < 0.9$). The closest two ITS layers to the beam pipe have a pseudo rapidity range of $|\eta| < 1.4$. As seen from the interaction point there are first two layers of silicon pixel detectors, then two layers of silicon drift detectors and finally two layers of silicon strip detectors. The ITS determines the interaction vertex with a resolution better than 100 µm and it is also used to determine secondary vertices from the decay of long lived mesons containing charm and bottom quarks. The silicon strip detectors allow the ITS to provide not only tracking information, but as well PID for particles with a momentum down to $200\,\text{MeV}\,c^{-1}$.

The combined material budget of the full ITS with support structures is about 7.2 % of the radiation length, which ensures that as few particles as possible are stopped there.

Multiplicity detectors

The following three detectors are used for multiplicity measurements. They cover 2π in ϕ and extend over different η.

V0: The V0 detectors (V0A: $2.8 < \eta < 5.1$, V0C: $-1.7 < \eta < -3.7$) are two arrays of scintillator counters. They count particles and are therefore used to measure the event multiplicity and centrality. Furthermore they allow to measure the luminosity provided by the LHC. The detector can be used as minimum bias trigger as well as trigger for events with a certain centrality or multiplicity.

T0: T0 consists of two arrays of *Cherenkov* counters (T0A $4.61 < \eta < 4.92$, T0C $-3.28 < \eta < -2.97$). The detector determines the time of the collision (t_0) with 50 ps resolution and the position of the interaction vertex within ± 1 cm, thus it can be used to detect if an event is created by a collision at the interaction point or if the collision is due to beam gas interactions taking place somewhere else. T0 provides as well redundant information on the particle count in addition to V0.

FMD: The *Forward Multiplicty Detector* (FMD) is made up of three rings of silicon sensors, which are highly segmented in r direction. Two rings are located at forward rapidity ($3.62 < \eta < 5.03$ and $1.7 < \eta < 3.68$) and one ring at backwards rapidity ($-3.4 < \eta < -1.7$). Charged particle multiplicity is measured with the FMD in the specified regions, reaching down to high η regions, which are not covered by the ITS.

Time projection chamber

The ALICE *Time Projection Chamber* is discussed in detail in Chapter 4, therefore we do not elaborate many details here. The TPC is a gaseous detector filled with Ne-CO_2-N_2 (90-10-5) or Ar-CO_2 (88-12) and is read out by *Multi Wire Proportional Chambers* (MWPC) (Sec. 3.4). It is the main tracking detector for charged particles in the central barrel and is as well used for PID. It covers 2π in ϕ, extends over $0.848 < r < 2.466$ and over a rapidity range of $|\eta| < 0.9$ (respectively $|\eta| < 1.5$) for particle trajectories covering the full radial length (respectively one third of the radial length) inside the TPC.

The TPC is a rather slow detector, because of the maximum electron drift time in the TPC ($\lesssim 100\,\mu\text{s}$) and the dead-time after each event. However, its PID capabilities and the

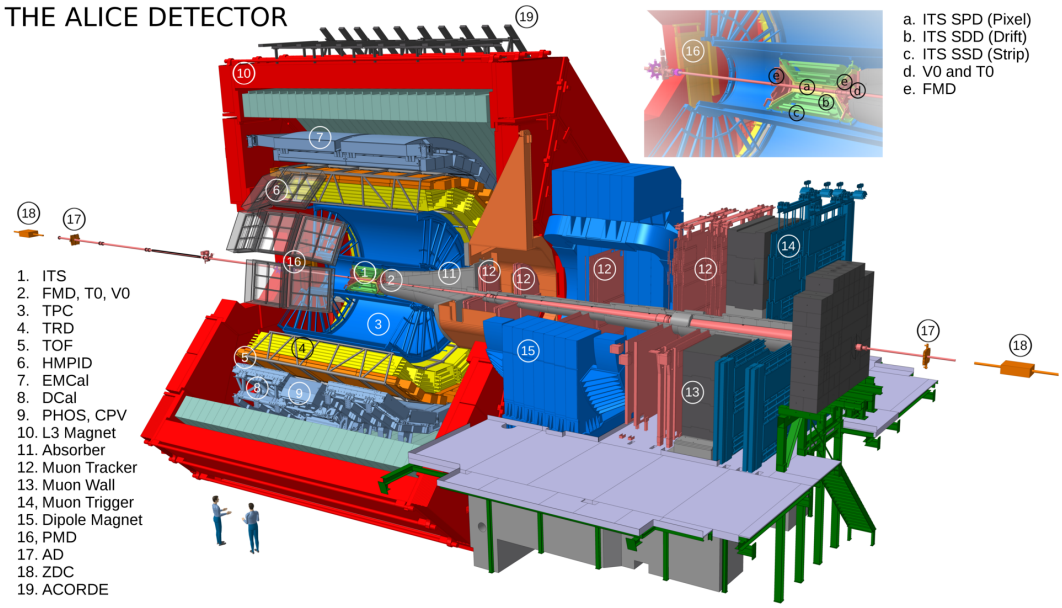

Figure 2.4: Layout of ALICE. The detectors shown correspond to the configuration of ALICE, which has been used during LHC Run 2.

robust tracking in high multiplicity events balance the disadvantage of the slow readout. In central lead-lead collisions the TPC is read out with a rate of a few 100 Hz, while during normal data taking the rate is about 1.5 kHz.

Transition radiation detector

The *Transition Radiation Detector* (TRD) is a gaseous detector, covering 2π in ϕ and $|\eta| < 0.84$ in pseudo rapidity. The TRD has in total 540 readout modules which are grouped into 18 super modules, in a way that there are always six modules stacked in r. Each module has a 48 mm radiator and a 30 mm drift region, filled with Xe-CO_2 (85-15). The modules are read out with MWPCs. All charged particles leave ionisations along their trajectory in the gas, however, such particles with a Lorentz factor ($1/\sqrt{1-(v/c)^2}$, with the speed of light c and the particle velocity v) higher than 1000, emit transition radiation in the radiator. The corresponding photons convert in the gas into additional ionisation electrons. The presence of these additional ionisations allows to discriminate electrons from pions, therefore the TRD is able to provide PID for electrons with momentum larger than 1 GeV c^{-1}. Furthermore the TRD is used for tracking and can be used as trigger detector for events with charged particles (hadrons or electrons) at high transverse momentum. Together with the ITS, the TRD is used for the space-point distortion correction of the TPC [21], which relies on reconstructed particle trajectories passing through all three detectors at the same time.

Time-of-flight detector

The *Time-Of-Flight* detector (TOF) ($0 < \phi < 2\pi$, $|\eta| < 0.9$) uses *Multi-gap Resistive-Plate Chambers* (MRPCs) [56] filled with $C_2H_2F_4$-iC_4H_{10}-SF_6 (90-5-5). Together with the t_0 time from the T0 detector it is used to determine the time-of-flight with a time resolution of about 50 ps. Based on time-of-flight measurements, the detector provides PID for pions and kaons (respectively protons) with an momentum lower than 2.5 GeV c^{-1} (respectively 4 GeV c^{-1}) and is for example used for pion-kaon and kaon-proton separation. It is furthermore used for PID of nuclei as alpha particles or deuterons.

Calorimeters

The ALICE detector has three calorimeters, the *ElectroMagnetic Calorimeter* (EMCal) ($0.22\pi < \phi < 0.52\pi$, $|\eta| < 0.7$), the *PHOton Spectrometer* (PHOS) ($0.61\pi < \phi < 0.89\pi$, $|\eta| < 0.12$) and the (hadronic) *Zero Degree Calorimeter* (ZDC) at very forward and backward rapidity.

EMCal: The EMCal is sampling calorimeter composed of stacks with alternating lead (1.44 mm, 76 layers) and polystyrene based scintillator (1.76 cm, 77 layers) layers. As an electromagnetic calorimeter it is used to determine the energy of electrons with high transverse momentum and for photon detection. It serves furthermore as trigger detector for electromagnetic probes.

Furthermore it is used to examine jet physics, in particular *jet quenching*. In the detector a jet appears as a shower of high energy particles, which is contained in a relatively small solid angle. When a high-energetic-coloured particle decays into colour-neutral particles, the latter are detected as a yet inside the detector. If such a particle moves through the strongly interacting medium, produced in heavy-ion collisions, it is slowed down. This phenomenon is called jet quenching.

PHOS: PHOS is a highly segmented electromagnetic calorimeter built from lead-tungstate crystals, which is designed for photon detection. On its side facing the interaction point, the Charged-Particle Veto (CPV) detector is mounted, which relies on Ar-CO_2 (80-20) filled MWPCs. Together, PHOS provides PID of photons and discriminates against charged hadrons, neutrons and anti-neutrons.

ZDC: The ZDCs are located at forward and backward rapidity at a distance of 116 m to the interaction point. They are composed of separate neutron (ZN) and proton (ZP) detectors. The ZNs (respectively ZPs) are sampling calorimeters with alternating layers of quartz fibres and brass (respectively a tungsten alloy). Each ZN is located between the two beam pipes, while the ZPs are mounted on the side of the beam pipe, to which positive particles are deflected. There are as well two electromagnetic calorimeters (ZEM) at forward rapidity at 7 m distance from the interaction point. These two sampling calorimeters are located on both sides of the beam pipe and they are built with alternating lead and quartz fibre layers.[d]

The ZPs and ZNs detect spectator nucleons. During a nucleus-nucleus collision, only the nucleons in the overlap region of the two nuclei collide. The remaining nucleons are the so called spectator nucleons and after the collision they continue to move with a high $|\eta|$ along the beam pipe. For very central and very peripheral nucleus-nucleus collisions the number of spectators measured in the ZPs and ZNs can be similar. To remove this ambiguity, the ZEMs information of particles at a different value of forward rapidity is used.

Muon spectrometer

The Muon spectrometer detects (di-)muons from the decay of mesons with heavy quark content. The source of such (di)-muons can either be the decay of direct produced J/ψ or they result from the decay of other mesons with heavy quark content. In the first (respectively latter) case the corresponding muons have a high (respectively a low) transverse momentum.

The spectrometer consists of several parts. In the central barrel the front absorber is located, which is made from carbon and concrete. Behind the absorber the *Muon tracker* is mounted, which is a series of 10 tracking planes which are located inside the L3 solenoid, inside the dipole magnet as well as outside the dipole magnet at backward rapidity. The detectors are gaseous detectors filled with Ar-$C_2H_2F_4$-iC_4H_{10}-SF_6 (50.5-41.3-7.2-1). There is a 1.2 m thick Iron wall after the tracking stations, then four planes with trigger chambers

[d] At the LHC the two proton or lead beams are circulated in a beam pipe each. The two beam pipes merge into one at four different areas in order to collide the two beams in each experiment's (ALICE, ATLAS, CMS, LHCb) interaction point.

follow. These trigger detectors are resistive plate chambers and they can provide a trigger on muons with high or low transverse momentum, where the momentum threshold can range from about 0.5 GeV c^{-1} to 2 GeV c^{-1}.

2.3.3. The ALICE detector upgrade

In LHC Run 3, the LHC will deliver lead-lead collisions at an interaction rate of 50 kHz. Therefore, the ALICE collaboration will upgrade some of the afore mentioned detectors at the end of LHC Run 2. The exact plans and the motivation of all the detector upgrades as well as the upgrade of the data acquisition system are written down in [22–24, 57–60] and the references therein.

The goal of the ALICE upgrades is essentially to exploit the increased interaction rate for a deeper study of the strongly-interacting state of matter produced in lead-lead collisions. Therefore ALICE will focus on rare probes such as, but not only, heavy-flavour particles, their coupling to the medium and their hadronisation during LHC Run 3 and Run 4. In order to achieve this goal, the ALICE detector needs the ability to examine all events the LHC will provide at 50 kHz. In addition, ALICE wants to maintain its excellent PID capabilities and the ability to study particles with low momentum down to $\sim 100\,\mathrm{MeV}\,c^{-1}$. The ALICE TPC is one of the detectors, which will be upgraded to achieve this goal [23, 24]. In Section 4.3 we discuss this upgrade in detail, however, the goal for the upgraded TPC is to take data continuously and to preserve otherwise the performance of the current TPC.

3. Working principle of gaseous detectors

In this section we briefly introduce some of the working principles of gaseous detectors. The movement of charge carriers in gases is covered in Section 3.1. Especially, we discuss the ion drift in preparation for the measurements in Chapter 5. After, we introduce different ionisation mechanisms (Sec. 3.2). Doing so, we on the one hand explain how the energy loss in the gas can be used for particle identification. This is a key feature applied in Time Projection Chambers (TPC). On the other hand, the different ionisation processes are the first step to explain gas discharges (Sec. 3.3). We approach this topic by first discussing gas amplification in general and then different breakdown phenomena. These foundations are needed for out discharge measurements in Chapters 6 and 7. In the last Section 3.4 and Section 3.5 two gas amplification systems of relevance for the ALICE TPC upgrade are presented. The multi-wire proportional chamber and the gas electron multiplier.

3.1. Movement of charge carriers in gases

We consider two types of movement for charge carries in gases. First there is the random motion of a charge carrier due to collisions with gas atoms or molecules, which is called diffusion and treated in Section 3.1.2. Second, in presence of an electric or magnetic field electrons (respectively ions) gain energy from this field and move in a direction determined by these fields. This is the drift of a charge carrier (Sec. 3.1.1).

3.1.1. Drift of charge carriers

A charger carrier with charge q and mass m in an electric field $\mathbf{E}$ and a magnetic field $\mathbf{B}$ is accelerated by the Lorentz force according to $m \cdot \ddot{\mathbf{x}} = q \cdot (\mathbf{E} + \dot{\mathbf{x}} \times \mathbf{B})$.[a] However, in the gas the charge carrier will collide with the gas molecules during this acceleration. Following the Langevin formalism [61, 62] these collisions are added as a resistive force $\mathbf{A} = -\dot{\mathbf{x}}m/\tau$, proportional to the velocity, to the Lorentz force. The time τ in $\mathbf{A}$ is the mean time between two collisions of the drifting particle. The corresponding equation of motion for a charged particle hence reads:

$$\begin{aligned} m \cdot \ddot{\mathbf{x}} &= q \cdot (\mathbf{E} + \dot{\mathbf{x}} \times \mathbf{B}) - \frac{\dot{\mathbf{x}}m}{\tau} \\ \ddot{\mathbf{x}} &= \frac{q}{m} \cdot \mathbf{E} - \frac{\dot{\mathbf{x}}}{\tau} \quad . \end{aligned} \tag{3.1}$$

In the second line we set $\mathbf{B} = 0$, which is the case for all the measurements done for this work. The energy lost during the scattering of the charge carriers with the gas atoms or molecules and the acceleration will balance themselves at large $t \gg \tau$ and a steady state ($\ddot{\mathbf{x}} = 0$) is reached. The drift velocity $\mathbf{v}_\mathrm{d}$, which is parallel to the electric field, reads then

$$\mathbf{v}_\mathrm{d} = \dot{\mathbf{x}} = \frac{\tau \cdot q}{m} \cdot \mathbf{E} = K \cdot \mathbf{E} \quad . \tag{3.2}$$

The factor K is referred to as mobility and its actual value depends on the scattering processes responsible for the friction term in Equation (3.1). The average time between collisions can be parametrised as

$$\tau = \frac{1}{N\sigma\mathbf{v}} \quad , \tag{3.3}$$

[a] We use bold letters, e.g. $\mathbf{a}$, for vectors and for the absolute value of $\mathbf{a}$ we write a. Vector components are indicated by indices. The time derivative of $\mathrm{d}\mathbf{a}/\mathrm{d}t$ is written as $\dot{\mathbf{a}}$. This notation is as well used for multiple derivatives with respect to the time (e.g. $\ddot{\mathbf{a}}$) and time derivatives of scalars (e.g. $\dot{a}$).

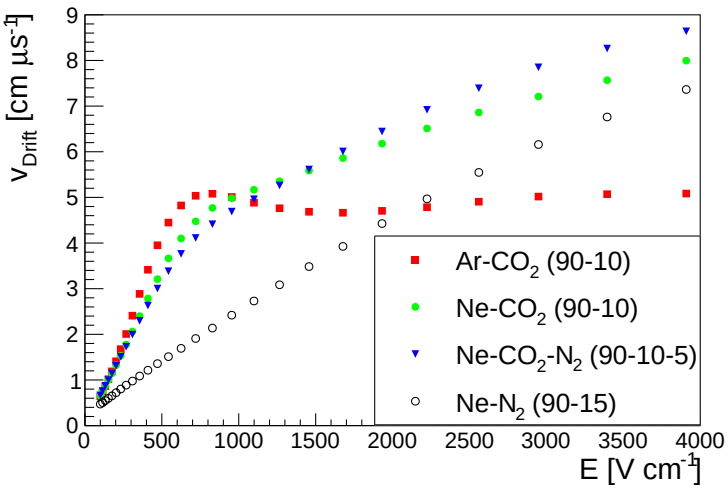

Figure 3.1: Magboltz [64] simulation of the electron drift velocity as a function of the electric field. A gas pressure of 1000 mbar and a temperature of 22 °C are used to obtain the displayed points.

where N is the number density of the gas atoms, σ is the collision cross-section and $\mathbf{v}$ is the instantaneous velocity after a collisions, which can differ significantly from $\mathbf{v}_\mathrm{d}$ for times on the order of τ.

The quantities derived so far are valid for the drift of electrons as well as ions. Examining the scattering process of an ion or an electron with a gas atom or molecule reveals the difference between the respective formula of the drift velocity.

Drift velocity of electrons

As an electron hits a gas molecule, its velocity $\dot{\mathbf{x}}$ is fully randomised after each collision and, provided the collision is elastic, only a small fraction of the electron's energy is lost. In the time between collisions, electrons are accelerated in direction of $\mathbf{E}$ and the component of their velocity parallel to the electric field ($\dot{\mathbf{x}}_\mathrm{E}$) increases. There is an equilibrium between the average energy gained in-between two consecutive collisions and the average energy loss in a collision, which can be expressed as

$$\frac{\mathrm{x}}{\dot{\mathrm{x}}_\mathbf{E}\tau}\lambda\varepsilon_\mathrm{E} = e\mathrm{Ex} \quad , \tag{3.4}$$

following [63]. Here λ is the average fractional energy loss per collisions, e is the electrons charge and ε_E is the (equilibrium) energy gained from the electric field. The full energy of the electron contains as well the thermal energy: $\varepsilon = \varepsilon_\mathrm{E} + \frac{3}{2}kT$ with the Boltzmann constant k. In case of gaseous detectors $\varepsilon_\mathrm{E} \gg \frac{3}{2}kT$, therefore the thermal movement can be neglected and thus $\varepsilon = m\dot{\mathbf{x}}^2/2$. Equations (3.2), (3.3) and (3.4) can be combined to find the drift velocity of electrons ($\mathbf{v}_\mathrm{d,e}$) as well as the instantaneous velocity ($\mathbf{v} = \dot{\mathbf{x}}$):

$$\mathbf{v}^2 = \frac{2}{\lambda}\mathbf{v}_\mathrm{d,e}^2 \quad , \tag{3.5}$$

$$\mathbf{v}_\mathrm{d,e}^2 = \frac{e\mathrm{E}}{m_\mathrm{e}N\sigma}\sqrt{\frac{\lambda}{2}} \quad . \tag{3.6}$$

A comparison of Equation (3.6) to Equation (3.2) yields that the electron-mobility K_e depends on the average fractional energy loss between collisions and on the collision cross-section. Both quantities in turn depend on the electrons energy ε. Therefore the electron drift velocity can have a very non-linear dependence on the electric field. This is illustrated

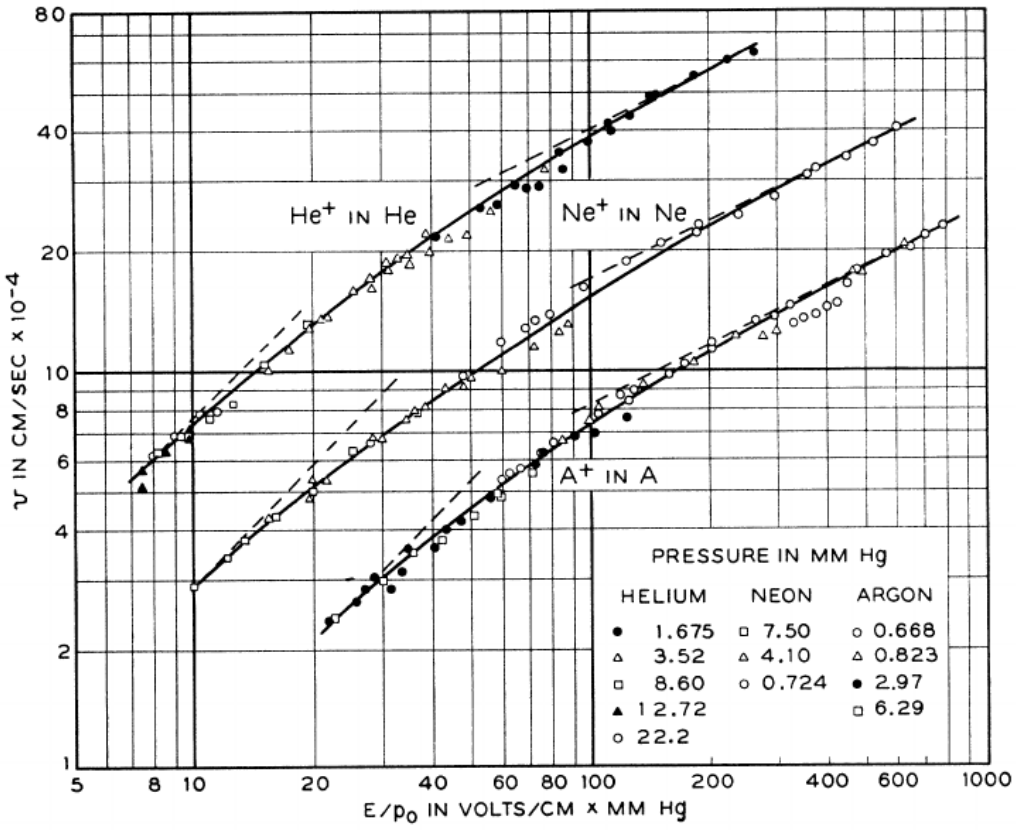

Figure 3.2: Measurements of the ion drift velocity for different inert gases (Helium, Neon and Argon) as function of the reduced drift field (E/p_0) are shown. For each data point the pressure is given in the box on the lower left. The two trends of $K \sim$ const and $K \sim 1/\sqrt{E}$ are indicated with lines in the low E and high E region, respectively. The plot is adopted from [67].

by the *Magboltz* [64] simulations displayed in Figure 3.1.[b] An example of the dependence of σ on ε is the *Ramsauer minimum* [66], which is observed in the effective momentum transfer cross-section. This minimum is observed in Argon and other gas mixtures and leads to the peak of the electron drift velocity, observed in the Ar-CO_2 (90-10) data points in Figure 3.1. Equation (3.6) and the comparison of the different gas mixtures in Figure 3.1 make it very clear that K_e (and therefore v and v_d) depend strongly on the actual gas mixture used, because $\sigma(\varepsilon)$ and $\lambda(\varepsilon)$ behave different for different gases.

Drift velocity of ions

Ions gain the same amount of kinetic energy from the electric field as electrons, but their acceleration is smaller, because of their higher mass, and therefore they reach a lower maximal velocity between collisions. Furthermore the scattering of ions with the gas atoms or molecules differs from the electrons' scattering. Ions lose a higher fraction of their energy in elastic collisions and their velocity is not randomised as much as an electron's velocity is. Even immediately after the collision, the velocity has always a non zero component in direction of the electric field.

Taking this component into account, results in a change of the velocity in Equation (3.2)

[b] Magboltz is a software, which can be used to simulated electron transport in gas mixtures. The desired gas mixture and the gas conditions are passed to the software, as well as the electric and magnetic field range of interest. Magboltz then solves the Boltzmann transport equations for electrons in the specified mixture under the given conditions. The simulation results agree well with measurements as e.g. shown in [65].

as shown in [63]: The mass m of the drifting charge carrier is replaced by the reduced mass $m^* = m^{-1} + M^{-1}$. There M is the mass of the gas atom or molecule, the charge carrier collides with. While inserting τ into the modified velocity equation and separately considering the case of low and high electric fields it can be shown [63] that

$$\text{low E}: \quad \mathrm{v_{d,Ion}} = \sqrt{\frac{1}{3kT} \cdot \frac{1}{m^*}} \cdot \frac{q\mathrm{E}}{N\sigma_{\mathrm{Ion}}} \tag{3.7}$$

$$\text{high E}: \quad \mathrm{v_{d,Ion}} = \sqrt{\frac{1}{M}\left(1 + \frac{m}{M}\right)} \cdot \sqrt{\frac{q\mathrm{E}}{N\sigma_{\mathrm{Ion}}}} \quad . \tag{3.8}$$

An electric field is considered as low, if the ion's random velocity after a collision is thermal [68]. The collision cross-section is written as σ_{Ion}, to highlight that it is different from the cross-section in Equation (3.6). In contrast to this cross-section for collisions of electrons with gas atoms or molecules, σ_{ion} is rather constant, because the ions' collisions are elastic for the typical fields present in a gaseous detector.

Comparing the ion drift velocity in Equations (3.7) and (3.8) to the more generic formula $\mathrm{v_d} = K \cdot \mathrm{E}$ (Eq. (3.2)), shows that the ion mobility K is constant for low E and has a $1/\sqrt{E}$ dependence for high drift fields.[c] In Figure 3.2 measurements of the drift velocity of noble gas ions in the respective noble gas are shown. The change of the drift velocity as well as the change of the mobility as function of the electric field is clearly visible in the figure. The low E and the high E region can be identified as well.

The ions' drift velocity in gas mixtures

The mobility of gas mixtures is of great interest, because gaseous detectors are typically operated with a mixture of different gases. To calculate such mobilities the collisions of ions with the different gas atoms or molecules in the gas mixture need to be considered. It can be shown that the velocity of a ion in a gas mixture is still described by an equation of the type $\mathbf{v}_{\mathrm{d,Ion}} = K_{\mathrm{Mix}} \cdot \mathbf{E}$, where K_{Mix} is the ion mobility of the gas mixture. In an early study of ion mobilities [69] it has been realised that

$$\frac{1}{K_{\mathrm{Mix}}} = \sum_i \frac{f_i}{K_i} \quad . \tag{3.9}$$

Here, f_i is the fraction to which the gas mixture is composed of the gas i. K_i is the mobility of the drifting ion in the pure gas i, but with the same number density N as the gas mixture has. Equation (3.9) is known as *Blanc's law* and has been originally formulated for a mixture of two gases. For high electric fields, at which the random movement of the ions is larger than the thermal movement, Blanc's law has to be modified. This is demonstrated in [68].

There are many measurements of the mobility of ions in their parent gases [70–73], similar to the ones shown in Figure 3.2. However Equation (3.9) does not allow to calculate the ion mobility from these measurements, because the ion species drifting in a gas mixture is not necessarily the same ion, which drifts in the pure gases. Therefore additional measurements of the mobility in the actual gas mixtures are needed (Ch. 5).

A comment on the reduced electric field

The electron and ion velocity depend on the electric field over the number density E/N (Equations (3.6), (3.7) and (3.8)), the so called reduced electric field. The energy of electrons in an electric field ε_{e} does as well.[d] It follows that all quantities based on the electron energy (e.g. the gain of a gas amplification stage) are functions of E/N. While quoting e.g. measurements of such quantities it is not enough to give only the electric field E. The

[c] Both, the mobility in general and the ion mobility, are denoted with K, while the electron-mobility is highlighted with a lower case e as K_e.

[d] For electrons, the cross-section σ and the average fractional energy loss λ depend themselves on the electrons energy. However, they are as well functions of E/N as illustrated in the first chapter of [63]. Where are no methods of calculating these from first principle, hence they are usually measured from drift velocity measurements.

number density N, which depends on the gas conditions, needs to be quoted as well. In case N is not well known, the fact that N is proportional to p/T can be exploited, where p is the ambient gas pressure and T the ambient temperature of the gas. Hence providing a measured quantity as function of $\mathrm{E}/(p/T)$ allows a comparison to measurements done at different gas conditions.

3.1.2. Diffusion

Without electric and magnetic fields, the electrons' and ions' movement through a gas (mixture) is only thermal movement. Charge carriers collide with gas atoms or molecules and exchange energy with them. Eventually they lose their initial energy in to these collisions and their energy distribution approaches the *Maxwell-Boltzmann* distribution. In this case the average electron energy is $\varepsilon_{\mathrm{therm}} = \frac{3}{2}kT$.

The direction of the thermal movement is uniformly distributed through the whole solid angle. Considering a point-like cloud of N_{q} charges at $t = 0$, this cloud will spread with increasing t. Starting from a point like distribution, the resulting distribution of charges at a distance x after a drift time t is

$$\frac{\mathrm{d}N_{\mathrm{q}}}{N_{\mathrm{q}}} = \frac{1}{\sqrt{4\pi Dt}} \exp\left(-\frac{\mathbf{x}(t)^2}{4Dt}\right) \mathrm{d}\mathbf{x} \quad . \tag{3.10}$$

The factor D is the *Diffusion coefficient*, which is a characteristic property of a gas (mixture). Following [63] it can be related to the mobility K by the relation

$$\frac{D}{K} = \frac{Tk}{q} \quad . \tag{3.11}$$

This relation is called *Einstein relation* or *Nernst-Townsend relation* in the literature [63, 68]. It is valid for electrons and ions in the case of no or vanishing electric field.

Diffusion in presence of an electrical field or magnetic field

In order to relate the diffusion of a charge cloud to the distance (d) these charges drift in an electric field, the time t in Equation (3.10) is substituted by $t = d/\mathrm{v}_d$. Using as well Equation (3.2) the width of the charge cloud reads

$$\sigma^2_{\mathrm{Trans}} = 2Dt = \frac{2Dd}{KE}$$

In this context the subscript *Trans* refers to the *transversal* width, which is perpendicular to the electric field direction. The *longitudinal* diffusion in parallel to the electric field, is smaller than the transversal one. This is known as *Electric Anisotropy* [63].

In a magnetic field the diffusion transversal to $\mathbf{B}$ is reduced [63].

$$D(\mathrm{B} \neq 0) = \frac{D(\mathrm{B} = 0)}{1 + \omega^2\tau^2} \tag{3.12}$$

The factor τ corresponds again to the mean time between subsequent collisions of the drifting particle with gas atoms or molecules, while ω is the cyclotron frequency $\omega = (q/m)\mathrm{B}$. The diffusion along the magnetic field direction is not altered.

The transversal diffusion in a gaseous detector (e.g. a Time Projection Chamber (TPC)) can be decreased if the detector is operated in a magnetic field in parallel to the electric field, thus allowing for a higher position resolution. The fact that this way of decreasing the diffusion is already considered in the first proposal for a TPC [1], illustrates how attractive it is. All this makes $\omega\tau$ an important parameter to consider while choosing a gas mixture for a gaseous detector.

The diffusion constant

In order to express (3.10) as function of the drift distance of the charge cloud in an electric field (d) the *diffusion constant*

$$\widetilde{D} = \sqrt{2Dt/d} = \sqrt{2D/\mathrm{v}_d} \tag{3.13}$$

is defined. Therefore, the transversal width of the charge cloud reads $\sigma_{\mathrm{Trans}} = \widetilde{D}\sqrt{d}$. The term diffusion constant is misleading, because it is a function of T, q and K (Eq. (3.11)) and in addition $\widetilde{D}$ depends on the electric field, because of its velocity dependence (Eq. 3.2).

The diffusion constant as function of the electric field can be simulated for certain gas mixtures and gas conditions using Magboltz [64]. The knowledge of this quantity allows to calculate the expected diffusion width, because the drift distance in a detector is usually known. To give an example: The transversal diffusion constant of Ar-CO_2 (90-10) (respectively Ne-CO_2-N_2 (90-10-5)) at atmospheric pressure and 22 °C is $\sim 365\,\mu\mathrm{m\,cm^{-1/2}}$ (respectively $\sim 305\,\mu\mathrm{m\,cm^{-1/2}}$) if an electric field of $1100\,\mathrm{V\,cm^{-1}}$ and no magnetic field is applied. Therefore the width of an electron cloud drifting 2 mm in either Ar-CO_2 (90-10) or Ne-CO_2-N_2 (90-10-5) at this gas conditions is 163 µm or 136 µm, respectively.

3.2. Energy loss of particles traversing gases

Charged particles lose a fraction of their energy as they collide with gas atoms or molecules, as mentioned during the discussion of the drift of charged particles. These collisions can as well be inelastic and lead to either the excitation or ionisation of the gas atom or molecule. If the initial energy of a particle traversing a gaseous detector is high enough, its energy loss in the gas is mainly due to this two effects. Particles with even higher initial energy, lose energy as well by the radiation of photons (*Bremsstrahlung*).

3.2.1. Ionisations and excitations

In a gaseous detector there is the distinction between *primary* and *secondary* ionisation. The primary ionisation are due to the direct interaction of a particle traversing a gaseous detector with the gas. Such a particle ejects one to three electrons from the gas atoms it interacts with. These electrons in turn ionise further gas atoms or molecules and these secondary ionisation are the larger contribution to the total amount of electrons produced in the detection volume.

An particle a can, provided it has a large enough energy, ionise a target atom.

$$a + B \Rightarrow a + B^+ + e^-$$

It is furthermore possible that a charged particle a, colliding with an atom or molecule B, transfers a part of its energy to the target and excites it.

$$a + B \Rightarrow a + B^* \Rightarrow A + B + \gamma$$

Eventually the excited gas atom or molecule de-excites to its ground state and emits a photon (γ). In a gas a fraction of these photons can have a high enough energy to eject an electron (e^-) from a gas atom.

$$\gamma + B \Rightarrow B + e^-$$

Auger-Meitner effect

After an ionisation, the corresponding vacancy in a shell is filled with an electron from an outer shell. A γ is emitted in this case. However, the energy of the shall transition can as well be transferred to an other electron with lower binding energy, which is then emitted

from the atom.

$$B^{+*} \Rightarrow B^{++} + e^-$$

This effect is named after Lise Meitner and Pierre Auger [74, 75] and it is as well known as *Auger effect* although Auger discovered the effect after, but independent of, Meitner.

Penning effect

There is an additional ionising mechanism in some gas mixtures composed of two noble gases or a noble and a molecular gas. If a gas atom is excited by an incident particle, it can reach a metastable state with a long live time compared to the mean time between collisions of two atoms in the gas mixture. If an excited atom of the inert gas (B^*) collides with an atom or molecule of the other component of the gas mixture (inert gas or molecular gas, C), the energy transferred during the collision can lead to the ionisation of C.

$$B^* + C \Rightarrow B + C^+ + e^-$$

This phenomenon is known as *Penning effect*, after its discoverer Frans Michel Penning [76]. Gases, as well as gas mixtures, in which this phenomenon is observed are called *Penning gases*. In a Penning gas the average ionisation energy is effectively reduced and therefore more free electrons, as expected for a gas (mixture) without Penning gas, are created.

The energy deposit of a high-energy particle passing through a gaseous detector is only a little affected by this additional possibility for gas ionisations. However, the electron amplification (Sec. 3.3) is noticeably higher in Penning gases.

Charge transfer among different ions

After the ionisation has happened, an ion B^+ can neutralise itself in a collision with another gas atom or molecule.

$$B^+ + C \Rightarrow B + C^+$$

Of course, this is only possible if the ionisation potential of the atom or molecule C is lower than the one of B. Eventually only ions of the gas component with the lowest ionisation potential remain in a gas mixtures with several components. For example in Ar-CO_2 (respectively Ne-CO_2) the Ar^+ (respectively Ne^+) transfer their charge to the CO_2 molecules on the time scale of a few ns [77]. In addition to charge transfer reactions *cluster ions* can form. Such ions consists out of a core ion and one or several neutral atoms and or molecules. In [77] the authors show calculations for Ar-CO_2 and Ne-CO_2 mixtures and they find that $CO_2^+(CO_2)_n$ ($n = 0$ - 4) and $CO^+(CO_2)_n$ ($n = 2$ - 3) likely to form. Previously, such clusters have already been observed and found to be stable for several ms [78]. Additional impurities in the gas as H_2O give again raise to different clusters, making the topic of ion transport in a gas more complex.

3.2.2. Electron Attachment

Electron attachment is process removing free electrons from the counting gas. An atom A with an almost full outer electron shell can capture an electron, thus forming a negative ion A^-:

$$e^- + A \Rightarrow A^- + \gamma$$

This process is possible for electronegative atoms. The electron is bound to the atom, which emits a photon after the electron capture. Therefore such negative ions are stable. Gases can be characterised by the binding energy of the additional electron, while forming a negative ion. For inert gases this energy is negative – these gases have negative electron affinity. An example for a gas with positive electron affinity is Oxygen.

The removal of electrons from the primary and secondary ionisations of a particle traversing a gaseous detector, spoils the energy resolution quite significantly. Furthermore, the addition of gases with positive electron affinity reduce the gas multiplication factor (gas gain), which is introduced in Section 3.3.1. This is why contaminations of the counting gas with electronegative gases like O_2 have to be avoided.

3.2.3. Parametrisation of the energy loss

In case the incident particle has an energy higher than the highest atomic binding energies, the atomic electrons can be treated as free electrons. Therefore the corresponding scattering cross-section simplifies to the Rutherford cross-section, as shown in [63]. The maximal energy transfer to the electron in such a collision can be orders of magnitude higher as the most probable energy transfer. Electrons, receiving such high energies, are called δ-electrons or knock-on electrons. They can travel considerable distances in a gaseous detector and ionise further gas atoms or molecules along their trajectory. The probability distribution of the total energy loss of a particle traversing a medium of finite width is as well characterised by a long tail to high energies, due to these knock-on electrons.

Average ionisation energy

The average energy necessary to produce an electron-ion pair can be described as

$$W = \frac{\langle N_{\text{Pairs}} \rangle}{L \langle \mathrm{d}\varepsilon / \mathrm{d}x \rangle} \quad . \tag{3.14}$$

Where $\langle N_{\text{Pairs}} \rangle$ is the average number of electron-ion pairs produced, L is the length of a particles trajectory and $\langle \mathrm{d}\varepsilon / \mathrm{d}x \rangle$ is the average energy loss per track length for this particular particle. The average energy W normally includes all the ionisation processes discussed in this section, as well as the electron attachment.

W depends on the gas composition and as well on the kind of particle traversing the detector. For example Ar-CO_2 (90-10) has a W value of 28.8 eV, while the baseline gas mixture for the ALICE TPC, Ne-CO_2-N_2 (90-10-5), has a W of 37.7 eV [23].

If a particle deposes a known amount of energy ($\varepsilon_{\text{Known}}$) in the gas, this parameter can be used to estimate the number of electron-ion pairs produced

$$N_{\text{Pairs}} = \frac{\varepsilon_{\text{Known}}}{W} \quad .$$

Examples for particles with a well known energy deposit in the gas are photons (respectively alpha particles), which are absorbed (respectively stopped completely) in a sufficiently large gas volume.

The Bethe-Bloch equation

The *Bethe-Bloch equation* [79, 80] describes the average energy loss $\mathrm{d}\varepsilon$ per length $\mathrm{d}x$ as a function of the particles momentum. It is valid for heavy charged particles with a mass M being $M \gg m_e$, and describes the average energy loss due to ionisations and excitations inside a absorber material. A maximal energy transfer is introduced in the derivation of the equation (ε_{Max}), therefore e.g. the energy loss due to knock-on electrons is not taken into account. We give the Bethe-Bloch equation in the notation used in [30]:

$$-\frac{\mathrm{d}\varepsilon}{\mathrm{d}x} = 4\pi N_{\text{A}} r_e^2 m_e c^2 z^2 \frac{Z}{A} \frac{\rho}{\beta^2} z^2 \left[\frac{1}{2} \ln \frac{2 m_e c^2 \gamma^2 \beta^2 \varepsilon_{\text{Max}}}{I^2} - \beta^2 - \frac{\delta(\beta\gamma)}{2} \right] \tag{3.15}$$

The factors β (respectively γ) is the ratio of the velocity over the speed of light (respectively the Lorentz factor $1/\sqrt{1-\beta^2}$). The other parameters are:

- N_A: Avogadro number
- r_e: Classical electron radius $r_e = \frac{1}{4\pi\epsilon_0} \frac{e^2}{m_e c^2}$
- z: Charge of the incident particle q in units of the electron charge e, therefore $z = q/e$

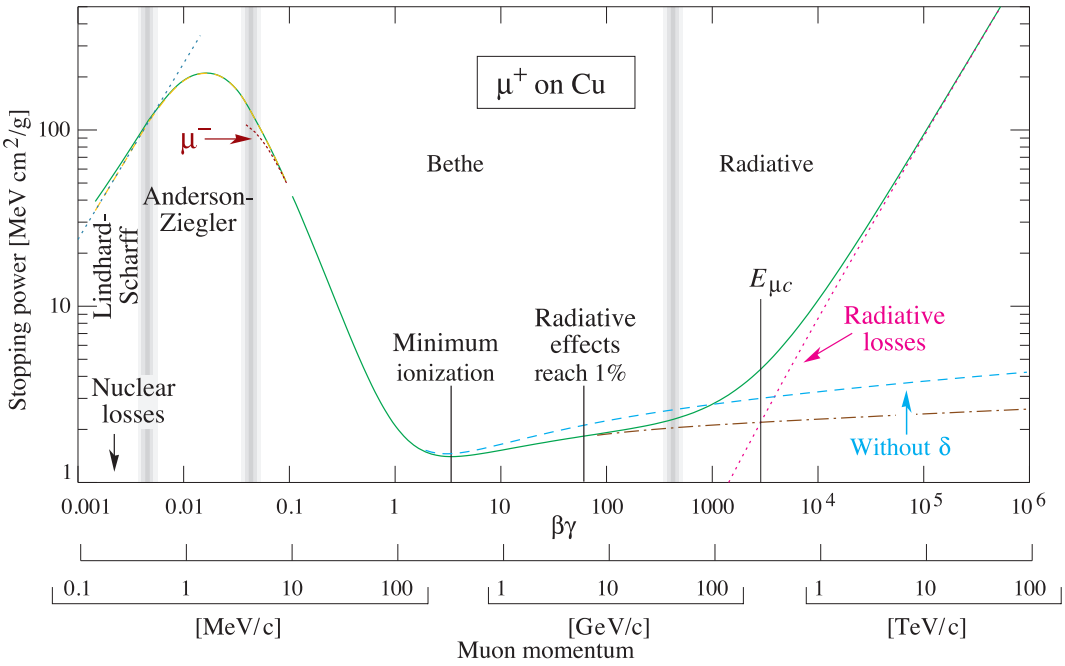

Figure 3.3: *Stopping power*, which is proportional to the Average energy loss per track length ($\langle -\mathrm{d}\varepsilon/\mathrm{d}x\rangle$) for μ^+ in copper. There are the two main momentum ranges highlighted: On the one hand the *Bethe* range, where the energy loss can be described by the *Bethe-Bloch formula* (Eq. 3.15) and on the other hand the *Radiative* range, where the energy loss due to the radiation of γ is dominant [81].

ρ: Density of the target medium

Z, A: Atomic number and atomic mass number of the target

I: Characteristic ionisation constant of the target material ($I = Z13.5\,\mathrm{eV}$ for $Z \leq 14$ and $I = Z10\,\mathrm{eV}$ for $Z > 14$)

δ: Correction term for the screening of the incident particle by the charge density of the atomic electrons

The correction term δ wasn't originally a part of the equation and it has been added latter [82]. Modified versions of Equation 3.15 exist, which describe the $\langle -\mathrm{d}\varepsilon/\mathrm{d}x\rangle$ for electrons in an absorber material. Over the momentum range highlighted in Figure 3.3 as *Bethe*, the energy loss is described by the Bethe-Bloch equation. First, the $1/\beta^2$ term is dominant, therefore $\langle -\mathrm{d}\varepsilon/\mathrm{d}x\rangle$ decreases. Eventually, there is a minimum of ionisation per track length ($\beta\gamma \approx 4$) and all relativistic particles with a momentum in this minimum of their energy loss are refereed to as *Minimum Ionising Particles* (MIPs). After the MIP region, the energy loss increases again with $\sim \ln \beta^2\gamma^2$, because the contributions from radiation losses get more and more dominant.

Another concept is highlighted in the figure: As the muon's energy increases, at some point the critical energy ($E_{\mu\mathrm{C}}$ in the figure), is reached. At this energy, the energy loss due to radiation of photons (*Bremsstrahlung*) equals the energy loss due to ionisations and excitations and for higher energies the stopping power increases fast. The *Bethe-Bloch equation* does not account for such losses, therefore, it is not valid in this energy range. In the figure the influence of the density correction term δ is illustrated as well, which increases with increasing particle momentum.

3.2.4. The energy loss as tool for particle identification

The species of a particle can be identified by a simultaneous measurement of the particle's momentum and most probable energy loss per unit length in a medium ($\langle \mathrm{d}\varepsilon/\mathrm{d}x\rangle_{\mathrm{MPLoss}}$). For the latter, several measurements of the energy loss are needed and the most probable energy

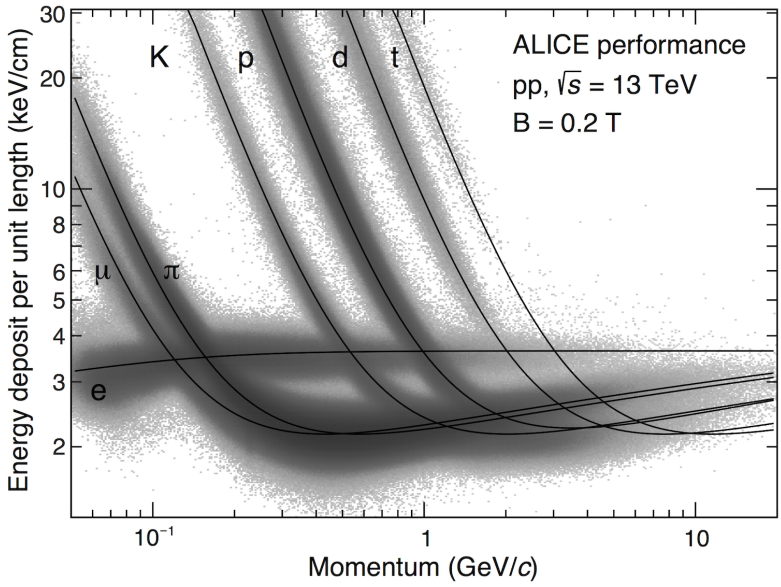

Figure 3.4: Energy deposit per track length versus momentum measured in the ALICE TPC [84]. The similarity to the Bethe-Bloch curve in Figure 3.3 is obvious.

loss can be determined from the resulting energy loss distribution. Such a distribution can be obtained if the ionisation produced along a particles track is measured and sampled over small intervals $\mathrm{d}x$ along this track. As mentioned during the discussion of the knock-on electrons, the probability distribution of the particles energy transfer to electrons has a tail to very high energies. Therefore, the distribution of the particles energy deposit per track sample has a similar tail, which shifts the average energy loss ($\langle \mathrm{d}\varepsilon/\mathrm{d}x \rangle_{\mathrm{Average}}$) to higher values. The most probable energy loss, however, is stable against such fluctuations and is hence a better measure for a particles energy loss. In practice the average of the 50-70 % smallest values of the energy loss distribution is used in experiment [83], example given $\langle \mathrm{d}\varepsilon/\mathrm{d}x \rangle_{\mathrm{MPLoss}} \sim \langle \mathrm{d}\varepsilon/\mathrm{d}x \rangle_{\mathrm{Average}}^{0\,\%-70\,\%}$.

Together with the particle's momentum, which is usually obtained from the measured deflection of the particle's trajectory in a magnetic field, the most probable energy loss per distance allows to identify the particle species. Each point in Figure 3.4 corresponds to a particle track, measured with the ALICE TPC [12]. The curves drawn onto the plot are parametrisations of the energy loss for the respective particle species as function of the momentum. The similarity to the curve in the *Bethe* region in Figure 3.3 is obvious, although the curve's parametrisation in Figure 3.4 does not correspond exactly to Equation (3.15) for the here discussed practical reasons.

3.3. From gas amplification to discharges

After ionisations have taken place in the active volume of a gaseous detector the electrons drift towards the anode plane and the ions towards the cathode. Usually the electrons are read out at the anode plane. These electrons need to be amplified, because common readout electronics are not sensitive to single electrons. Therefore the electrons from the drift volume are accelerated in a electric field until their energy is high enough to allow them the ionisation of further gas molecules. Eventually electron avalanches are produced, since the newly liberated electrons are accelerated as well in the field. The change $\mathrm{d}N_e$ in the number N_e of electrons, moving a distance $\mathrm{d}x$, can be described by the following formula:

$$\mathrm{d}N_e = N_e \alpha \mathrm{d}x \tag{3.16}$$

The parameter α is the the first *Townsend coefficient* [85]. All the ionisation process, which are discussed in Section 3.2.1 contribute to the first Townsend coefficient and need to be

taken into account. There is no fundamental expression for α, since it depends on the excitation- and ionisation cross-sections of the electrons having sufficient energy to excite or ionise gas atoms and molecules. Because these cross-sections depend on the electron energy and in turn on the reduced electric field, the first Townsend coefficient depends as well on these quantities. Based on the known values of such cross-sections, software packages like Magboltz [64] are able to calculate the first Townsend coefficient for a given gas-mixture and electric field. There are as well empirical formulas describing $\alpha(\mathrm{E}/N)$ for certain gases over a given E/N range.

3.3.1. Electron multiplication factor: The gas gain

Solving Equation (3.16) allows to find the factor by which N_0 electrons are multiplied on the path between x_0 and x_1

$$G = \frac{N_e}{N_0} = \exp\left(\int_{x_0}^{x_1} \alpha\left(\frac{\mathrm{E}(x)}{N}\right)\mathrm{d}x\right) \quad . \tag{3.17}$$

The quantity G is the gas gain and N – without an index – is still the number density of the gas atoms or molecules. This equation is valid for a constant electric filed, which is high enough to actually achieve gas amplification. The integration variable in Equation (3.17) needs to be substituted by the electric field, in order to calculate the gas gain when the electric field changes along the particles path.

$$G = \frac{N_e}{N_0} = \exp\left(\int_{\mathrm{E}_{\mathrm{min}}}^{\mathrm{E}(x_1)} \alpha\left(\frac{\mathrm{E}}{N}\right)\frac{1}{\mathrm{dE}/\mathrm{d}x}\mathrm{dE}\right) \tag{3.18}$$

The lower limit of the integral is the smallest electric field at which gas amplification still happens, which is given by $\alpha(\mathrm{E}_{\mathrm{Min}}/N) > 1$. Due to this exponential nature the gas gain G is sensitive to any change of the applied electric field or the gas conditions. From Equations (3.17), (3.18) and Figure 3.5 it is as well obvious that G is especially prone to changes in E/N if the electric field is only a little larger than $\mathrm{E}_{\mathrm{min}}$. For cases with known G, it is easily possible to deduce the original number of primary and secondary electrons from the number of electrons after the amplification. This allows to calculate the energy loss of a particle in the detector from the multiplied electrons and therefore the amplified signal can be used for particle identification (Sec. 3.2.4).

3.3.2. The first Townsend coefficient for different gas mixtures

In Figure 3.5 simulations of α for four gas mixtures at a fixed temperature and pressure are displayed. It is immediately visible that there are substantial differences between the four gas mixtures, even between the three gas mixtures consisting mainly out of Neon. Adding even a small amount of another gas to a gas (mixture) changes the total cross-section (σ) of the electrons' collisions with the gas atoms or molecules in the resulting mixture as well as it changes the fractional energy loss per collision (λ). In turn all the gas mixture's properties, which depend on σ and λ, change with the gas composition. Such properties are for example the electron drift velocity (Eq. (3.5) and (3.6)), the diffusion constant (Eq. (3.11) and (3.13)) and the first Townsend coefficient.

Figure 3.6 shows cross-sections for different interactions of electrons with gas atoms or molecules as a function of the electron energy (ε_e). The differences are well visible among the different gas mixtures – only for high energies ($\varepsilon_e > 100\,\mathrm{eV}$) the respective total cross-sections start to approach each other and for all gases the ionisation cross-section becomes dominant. The different cross-sections of Carbon dioxide (Figure 3.6b) are quite high over all ε_e smaller than 100 eV and the ionisation cross-section starts only to play a role for $10\,\mathrm{eV} < \varepsilon_e < 100\,\mathrm{eV}$. For lower energies a collision of an electron with a CO_2 molecule will either be an elastic collision or the molecule absorbs a part of the electrons energy into a vibrational state. Photons are as well able to excite vibrational or rotational states and they will therefore be removed from the gas. The rotational and vibrational states do not de-excite in the sense that an electron or photon is emitted. Therefore the energy used

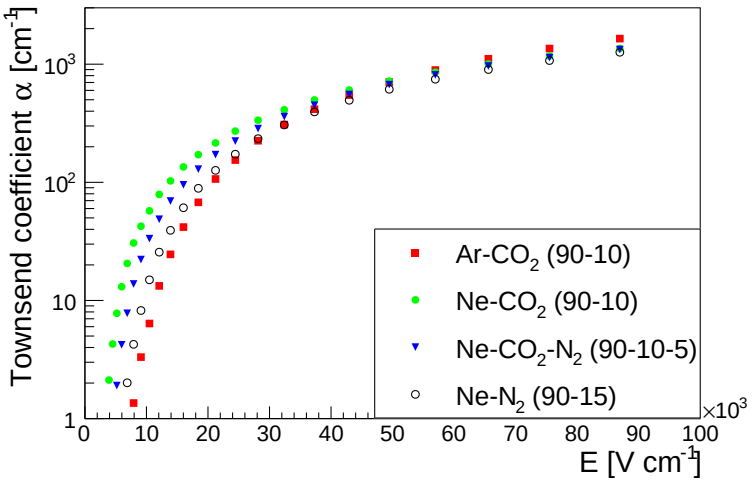

Figure 3.5: Magboltz [64] simulation of the first Townsend coefficient. A gas pressure of 1000 mbar and a temperature of 22 °C were used to obtain the displayed points.

to excite such a state in the first place is lost for the production of primary or secondary electrons as well as for the gas amplification, which affects the Townsend coefficient.

Connecting the cross sections for the gases in Figure 3.6 and the first Townsend coefficients in Figure 3.5 is not trivial. The relevant energy range in the plots in Figure 3.6 are the energies larger than $\sim$ 10 eV, because then it becomes probable that an electron ionises a gas atom or molecule. For $\varepsilon_e \gtrsim 10$ eV to a few 10 eV various excitation and ionisation cross-sections are relevant, which influence the instantaneous velocity between subsequent electron gas molecule collisions and therefore the energy an electron can gain from the electric field, before it collides again with a gas atom or molecule. With increasing electric field the initially large spread of the first Townsend coefficient among the four shown gas mixtures gets smaller. At high electron energies ($\varepsilon_e > 100$ eV), the total cross-section of interactions between electrons and gas atoms or molecules is dominated by the ionisation cross-section. Because the ionisation cross-sections do not differ as much between different gas mixtures, as e.g. the cross-sections for different excitations do (see e.g. Fig. 3.6), the Townsend coefficients for different gas mixtures are more similar at high electric field. The fact the the ionisation cross-section of Argon (Fig. 3.6d) is larger then the one of Neon (Fig. 3.6a) at high ε_e, explains why the first Townsend coefficient for the Ar-CO_2 (90-10) grows larger for high electric fields than compared to the Neon based mixtures.

3.3.3. Breakdown or gas discharges

Breakdown of a non-conducting material refers to the process, where a voltage is applied to this material and increased until the material becomes conductive. The breakdown of a gas filled gap between a cathode and an anode can either mean that there is a self sustained current through the gap or that there is a short circuit from cathode to anode through the gas. In order to distinguish this two cases we will refer to the short circuit cases as *full breakdown* or a *full discharge* of the gap. The voltage difference between cathode and anode needed in order to achieve breakdown is referred to as breakdown voltage ($U_{\text{Breakdown}}$).

3.3.4. Townsend theory of breakdown

Figure 3.7a is a sketch showing an detail of a gas filled detector with a radial geometry, such as a *Geiger-Müller Counter* [87]. At (1) in the figure a particle passing through the detector and is amplified, the avalanche evolves in direction of the anode. The gas amplification corresponds to the discussion in the previous Sections 3.3.1 and 3.3.2. A comparable number of photons (N_γ) and electrons (N_e) is produced during the amplification of one primary electron ($N_0 = 1$) and a fraction of these photons has high enough energy to ionise a gas

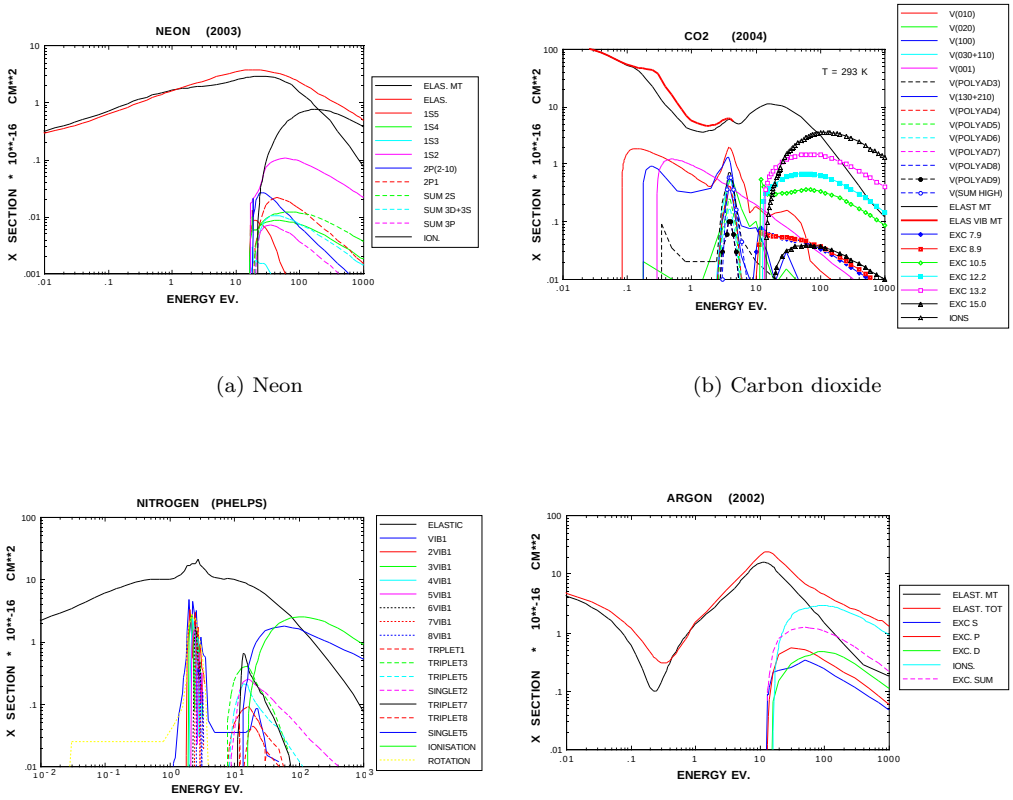

(a) Neon

(b) Carbon dioxide

(c) Nitrogen

(d) Argon

Figure 3.6: Different cross-sections for excitation, excitation of vibrational and rotational states and ionisation of a gas atom or molecule by an electron as function of the electron energy ε_e. These cross-sections have been extracted from [86] and are used by Magboltz [64].

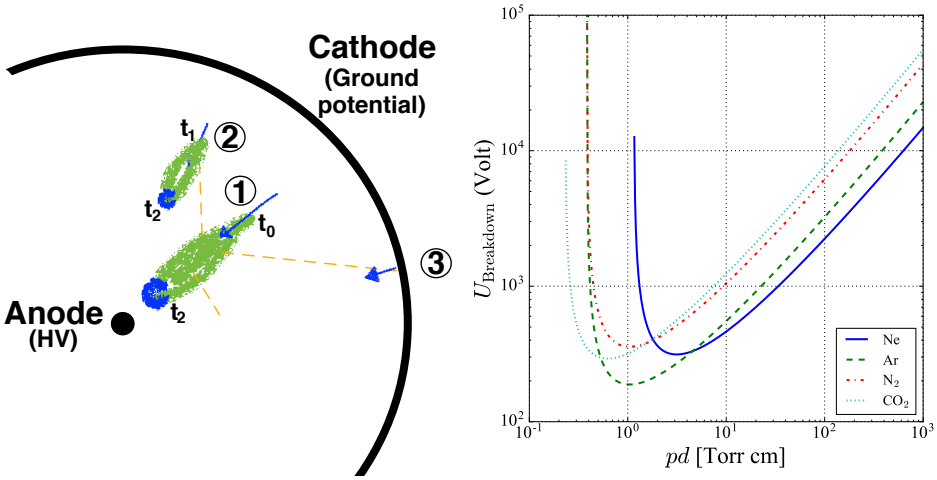

(a) (b)

Figure 3.7: (a) Example for different stages of a discharge governed by the Townsend breakdown. (1) A primary ionisation (marked by an arrow) is amplified towards the anode, which is at High Voltage (HV). In the time interval between t_0 and t_2 the avalanche evolves over green shaded area. The avalanche head is marked blue. (2) At a time t_1 a photon is emitted by a gas atom in the main avalanche and ionises a gas atom outside of the avalanche. This electron is amplified as well. (3) Another photon ejected by an de-exciting atom in the main avalanche hits the cathode and liberates an electron there. (b) Paschen curves for the four gases widely used in gas mixtures throughout this work. The parametrisation as well as the parameters for these curves can be found in [85] and they are valid for a range of $100\,\mathrm{V\,cm^{-1}\,Torr^{-1}} \lesssim \mathrm{E}/p \lesssim 600\,\mathrm{V\,cm^{-1}\,Torr^{-1}}$ (respectively $500\,\mathrm{V\,cm^{-1}\,Torr^{-1}} < \mathrm{E}/p < 1000\,\mathrm{V\,cm^{-1}\,Torr^{-1}}$) for all gases except Carbon dioxide (respectively CO_2).

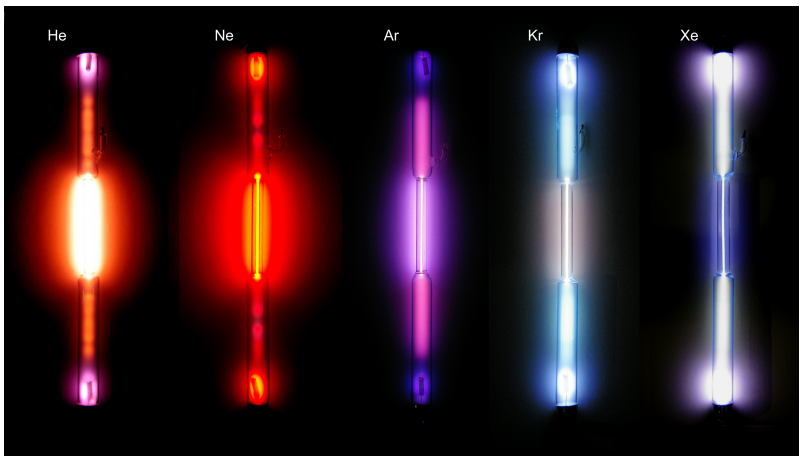

Figure 3.8: Glow discharge of different inert gases in discharge tubes. The respective tube is about $\sim 20\,\text{cm}$ long, contains gas at a pressure of about 10 mbar. An alternating voltage (35 kHz) of 1.8 kV with a current limit of 18 mA is applied to the tube. Picture by courtesy of Heinrich Pniok License FAL (*Free Art License 1.1*) [88].

atom or molecule. The primary electron of such an ionisation is then as well accelerated towards the anode and a new avalanche starts, which is denoted by (2) in the figure. If P_{Close} is the probability for a photon to ionise an gas atom closer to the cathode, then the starting point of the previous avalanche, we can formulate the following breakdown condition:

$$P_{\text{Close}} \cdot N_\gamma > 1$$

Using the gas gain G and the fact that N_γ is proportional to N_e in an avalanche [63], the breakdown condition reads:

$$u \cdot G \cdot P_{\text{Close}} \cdot > 1 \tag{3.19}$$

with $u = N_\gamma / N_e$. If we consider only constant electric fields we can use Equation 3.17 to write

$$\alpha \cdot (x_1 - x_0) > \ln \frac{1}{u \cdot P_{\text{Close}}} \quad ,$$

where the distance $(x_1 - x_0)$ can be chosen to be the distance between cathode and anode. This breakdown condition neglects additional sources of electrons, such as electrons which are either liberated by photons imping on the cathode due to the photoelectric effect ((3) in Figure 3.7a) or by ions impinging on the cathode. However, Equation (3.19) shows that breakdown depends on the electron amplification factor and therefore on the first Townsend coefficient. If all process liberating electrons from the cathode are taken into account the following breakdown condition is obtained [85]

$$\alpha \cdot d \geq \ln\left(\frac{1}{\gamma} + 1\right) \quad . \tag{3.20}$$

The factor d corresponds to the gap width between anode and cathode and γ is the *second Townsend coefficient*. This factor takes into account the additional sources of electrons like the afore mentioned emission of electrons from the cathode as well as ionisations by photons. The breakdown voltage $U_{\text{Breakdown}}$ can be expressed as a function of pd (so called *Paschen curves*), the gap width multiplied by the pressure, using empirically found parametrisations of α [85]. Figure 3.7b shows Paschen curves for Neon, Argon, Nitrogen and Carbon dioxide. Paschen found the relation between $U_{\text{Breakdown}}$ and pd [89] in measurements, while the corresponding theory of breakdown in gases was developed by Townsend (e.g [90]).

Townsend's breakdown model works well for larger gaps of several cm length and low

gas pressure fulfilling $pd < 200\,\text{Torr cm} \sim 266\,\text{mbar cm}$. Such gas conditions are typically present in gas discharge lamps. Figure 3.8 shows pictures of the glow discharge for the five lightest inert gases.[e] Such lamps are operated at voltage $U \gtrsim U_{\text{Breakdown}}$ and a current limit, which allows a self sustained glow discharge.

3.3.5. Quench gases

Gaseous detectors can be grouped into two sets. There are such gaseous detectors which operate at a very high gain, where the signal after the gas amplification is not proportional to the charge initial deposited in the detector (e.g. Geiger-Müller Counter [87], Streamer Chamber [91]). For these detectors breakdown, or the onset of breakdown, is actually desirable. On the other hand there are such detectors, which operate at lower gains where the signal after gas amplification is proportional to the primary and secondary electrons in the detector. For example, the readout chambers of a TPC are operated usually in this regime.[f]

A stable and therefore discharge free operation of such chambers is desired. To this end the voltage settings in readout chambers are chosen such that the resulting electric fields are low enough to neither fulfil the breakdown condition in Equation (3.19) nor in Equation (3.20). Furthermore a molecular gas is added to the gas mixture. Photons are then effectively absorbed into rotational and vibrational states of the gas molecules and therefore hindered to travel large distances in the gas mixture, thus reducing P_{Close} (Eq. 3.19) and γ (second Townsend coefficient, Eq. 3.20). This process is referred to as *quenching*. Therefore the additional, molecular component of a gas mixture is usually referred to as *quench gas* or *quencher*.

3.3.6. Streamer mechanism

It has been observed that an avalanche can only grow until a critical number $N_{\text{Crit}} \sim 10^7$ of electrons are produced [92]. This is upper limit is known as the *Raether limit*. The gap between anode and cathode is found to discharge, as soon as N_{Crit} electron-ion pairs in the avalanche are reached. This observation, the time scale on which such a (full) discharge develops as well as the fact that emission of electrons from the cathode does not play a role, can not be explained by the Townsend theory of discharges. Therefore, the *Streamer mechanism* has been developed.

A *streamer* is a weakly ionised, thin channel which can form from the primary avalanche if the electric field is strong enough. Furthermore the streamer can grow in direction of either the cathode or the anode or it grows in both directions at the same time.

In the following we explain a model of the streamer mechanism presented in [85]. Doing so we assume gas amplification between a cathode and an anode with a constant electric field E_0.[g] During the production of an electron avalanche in the gas, the ions remain static as compared to the speed of the electrons. Therefore a space charge composed by the ions remains, as the electrons have already moved to the anode. If this space charge is as big as N_{Crit} ions, it is assumed that the electric field of this space charge E_{Q} is comparable to E_0 and high enough to enhance gas amplification in the vicinity of space charge. This is a necessary condition for the streamer ignition and as this condition is fulfilled the streamer initiates the breakdown of the gas filled gap between cathode and anode.

Cathode directed streamer

The sketch in Figure 3.9a illustrates the streamer growth as well as the electric field configuration in a gap with a cathode-directed streamer. The streamer first follows the original

[e] We consider only the case of breakdown in electric fields supplied by constant voltages. The discharge tubes shown are operated with an alternating voltage. We refer to [85] for the case of discharges in gaps with oscillating potential.

[f] Two commonly used techniques employed for the gas amplification in a readout chamber, the multi wire proportional chamber and the gas electron multiplier, are introduced in Sections 3.4 and 3.5.

[g] In Section 6.3.1 the possibility of streamer development in the hole of a gas electron multiplier foil will be examined, in the context of discharge development in such foils (Sec. 6.3). However, we decided to do this only later and closer to the corresponding discharge measurements (Sec. 6.4).

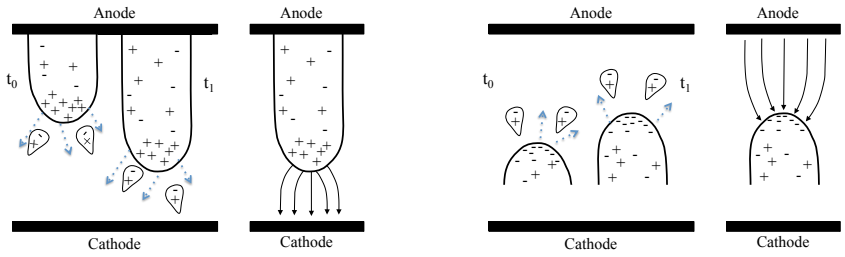

(a) Cathode-directed streamer (b) Anode-directed streamer

Figure 3.9: The time development of a streamer (left hand side of both sketches) as well as the electric field lines (right hand side of both sketches) of the indicated two streamer types are shown. While the cathode-directed streamer (a) follows the avalanche backwards, the anode-directed streamer (b) evolves with the avalanche. As soon as the anode-directed streamer made contact with the anode, it starts to develop like the cathode-directed streamer in direction of the cathode. Dashed line represent photons. See the text for more explanations.

avalanche backwards. Thereby it feeds on secondary avalanches, which evolve in its direction because the electrons are attracted by the charged streamer head. The seed electrons for this avalanches are provided by three sources: 1) De-exiting atoms along the path of previous avalanches, 2) primary electrons arriving later than the bulk of the charges, which has just been amplified, 3) ionisations due to photons produced in the vicinity of the streamer head. Electrons are accelerated towards the streamer head, thus producing more electrons and ionised gas atoms or molecules. Then, the electrons are absorbed by the streamer, while the ions contribute first to the charged streamer head. Eventually the ions become part of the weekly ionised plasma of the streamer, because they are static as compared to the streamer's velocity. Streamers evolve fast, their velocity can be up to an order of magnitude faster than the electron drift velocity. In case the anode end of the streamer made contact with the anode, the weekly conducting plasma of the streamer conducts the anode potential. Therefore the streamer behaves like a tip connected to the anode and growing towards the cathode. The closer the streamer approaches the cathode, the higher the electric field and the more the streamer growth is accelerated.

Anode-directed streamer

In case the N_{Crit} charges are produced at a distance to the anode and the streamer condition is fulfilled, the streamer starts to grow in both directions. The growth in the cathode direction works as described before. The streamer moves with the electrons of the actual avalanche in direction of the anode. The steamers head on the anode side is negatively charged, due to these electrons. Photons are emitted as well in the vicinity of the streamer head, which ionise gas atoms in advance of the electrons. The streamer connects then to the additional avalanches created by the ionisation electrons due to the photons. However, photons do not seem critical for the streamer growth in direction of the anode. The electric field between the negative charged streamer head and the anode increases as the streamer approaches the anode. Therefore the streamer growth is accelerated, similar to what was discussed for cathode-directed streamers.

3.3.7. Sparks

Eventually a streamer connects both, cathode and anode and then this streamer breakdown can initiate a *spark* between the two electrodes. To our knowledge there is not yet a widely accepted theory for the early stages of the spark formation. What can be said is, that a

spark evolves fast between cathode and anode and exists usually only for a short duration. The spark can evolve in homogeneous as well as arbitrary electric fields, it is visible by eye and it is accompanied by a sound. Consider for example a *lightning*, which is a spark in air across very long gaps.

In [85] sparks are described to evolve through the streamer channel starting from the cathode, with a speed faster than the electron drift velocity. The weekly conducting plasma of the streamer is highly ionised during this process and the former streamer channel becomes highly conductive, achieving the full breakdown of the gap. Joule heating increases the gas temperature in the centre of the spark channel up to 20 000 K. Therefore, the heated gas expands and creates a cylindrical shock wave along the full spark channel, which can be heard. As long as the spark is present, its diameter grows. Because the spark creates a short circuit between cathode and anode, the potential difference across the gap usually drops and the spark is quenched. However, if the power supply to the electrodes can sustain a high current through the spark channel, the spark can evolve into a permanent arc discharge.

Discharges in Micro Pattern Gaseous Detectors (MPGD) are usually accompanied by a spark. The heat of the spark as well as the shock-wave can pose a serious thread to the delicate structures of most MPGDs.[h] Therefore studies of discharges in such detectors are a current topic of research (See for a review [93] and Chapters 6 and 7 and the references quoted within.) Our discharge studies in Chapter 6 and 7 are as motivated by studying discharges in gas electron multipliers, which are a particular type of MPGD structure, introduced in Section 3.5.

3.4. Multi wire proportional chambers

One device to amplify primary and secondary ionisation and which allows to read out the corresponding signals is the Multi Wire Proportional Chamber (MWPC) [14]. The MWPC has been invented in 1968 by G. Charpak *et al.* (Nobel Price in 1992). In a MWPC a plane of wires is mounted between two electrodes. Each wire is supplied with the same potential and is at the same time connected to electronics, allowing to read out the induced signal or the charge on each wire. As explained in Figure 3.10a, a particle crossing the gas volume of the MWPC will liberate electrons. These drift towards the wires and are eventually amplified in the electric field, which increases towards the wires (Fig. 3.10b). The induced signals have a fast component due to the electrons accelerating towards the anode wires and performing gas amplification there. They also have a slow component due to the drift of the ions from the location, where they are created, to the next cathode. Signals are induced on the anode wires as well as on the surrounding electrodes. The energy deposit in the detector as well as the position of the particle in one dimension can be determined using the signals at the different wires. However, the signal at the two plane electrodes, which are both cathodes, contains as well the information on the energy deposit in the detector.

If one of these two cathodes is segmented into strips, two spatial coordinates can be obtained by combining the information from the signals at the strips and at the wires. In case an electrode is segmented into pads instead of strips, two spatial coordinates can be obtained only from the pad readout.

3.4.1. MWPCs as readout chambers of gaseous detectors

If a MWPC is used as ReadOut Chamber (ROC) of an larger detector, as e.g. a TPC, one cathode is replaced by a cathode wire plane. This wire plane it then the boundary between the ROC and the gas volume of the detector. The potential difference between the potential at the cathode wires and the potentials as electrodes in the detector (e.g. the drift cathode) defines the electric field, which guides primary and secondary electrons into the MWPC. Different wire plane layouts have been deployed in various detectors, see [63] for a review of representative drift chambers and time projection chambers. Here we use the wire configuration of the Inner Readout Chambers of the ALICE TPC (Fig. 3.11a) as example.

[h] We discuss the possible damage of gas electron multipliers caused by sparks in Section 6.3.2.

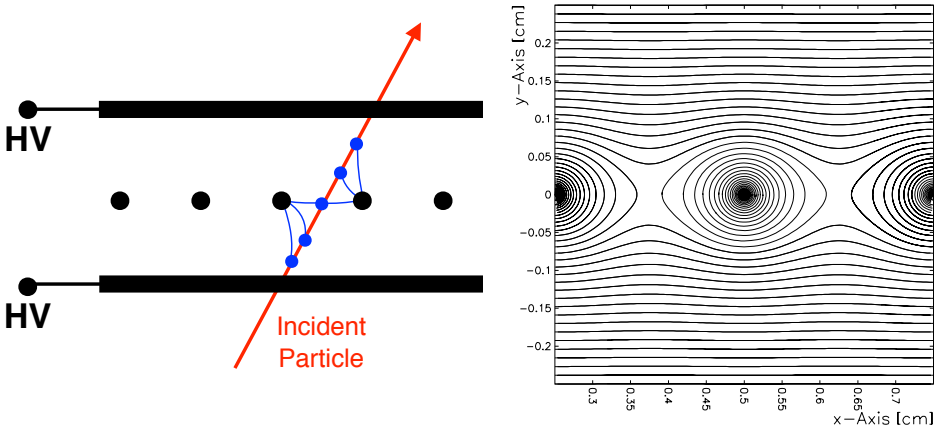

(a) (b)

Figure 3.10: (a) Cross section of a Multi Wire Proportional Chamber (MWPC), not to scale. A plane of wires is located between two electrodes. All wires are equipped with readout electronics and they are supplied with a less positive potential than the two electrodes, however, this is not shown in the sketch. Figure (b) shows a Garfield [94] simulation of the equipotential lines of a MWPC as sketched in (a). The regions of high line density correspond to the increasing electric field towards the wires. A particle traversing the gas in such MWPC ionises some gas atoms. The resulting primary and secondary ionisation are accelerated in direction to the wires. Depending on the voltage settings, the electric field close to the wires is high enough to achieve gas amplification and the according induced signal is read out.

3.4.2. Ion gates

The ALICE TPC multi wire proportional chambers

The layout of the wires planes in the ALICE TPC [9, 12] is typical for the readout chambers of TPCs. On top of a pad plane the anode wire grid is mounted, followed by the cathode wire grid. The cathode wires are staggered with respect to the position of the anode wires and they have a diameter of 75 µm and are hence thicker than the anode wires (diameter of 20 µm). The cathode wires and the pad plane are at ground potential, while the anode wires are supplied with a positive potential. Furthermore only the induced signal at the pads is read out in the ALICE TPC ROCs.[i]

A third grid of gating wires follows after the cathode grid. This grid has been introduced to block the ions from entering into the detector's (drift) volume [15, 16]. Without a gating grid, the ions from the gas amplification region accumulate in the drift volume and they build up a space charge, distorting the electric field inside the detector. As a result the reconstructed particle trajectories are distorted and all performance parameters relying on the particles trajectories are seriously deteriorated. For this reason a *gating grid* has been already introduced in the readout chambers of the first TPC at PEP [96] and is used so far in all TPCs running at high rate and employing MWPCs.

[i] In some MWPCs an array of alternating sense and field wires is used instead of an anode wire plane. The sense wires are read out and a positive potential is applied to them, while the field wires are at a different potential. E.g. the ROCs of the ALEPH TPC [4, 95] used such a configuration with sense wire and pad readout.

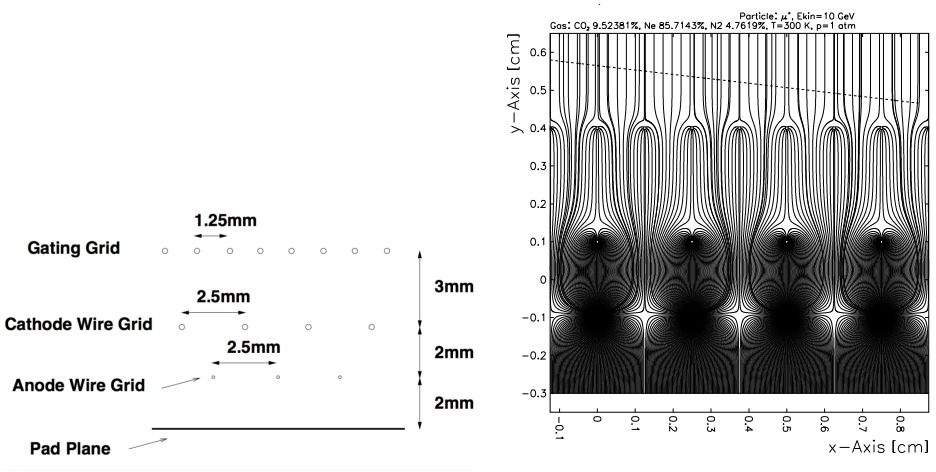

(a) (b)

Figure 3.11: (a) Layout of the wire-planes of an Inner ReadOut Chamber (IROC) of the ALICE TPC [9]. The second type of ROC in the ALICE TPC, the outer readout chambers, follow a similar layout, but with a 3 mm spacing between pad plane and anode wires and anode wires and gating grid wires. (b) Garfield [94] simulation of a muon (dotted line) passing through the drift space above a wire configuration as sketched in (a). The electrons drift towards the anode wires and are amplified there and eventually collected by the wires. The resulting ions drift to the pad plane, the cathode wires, the gating grid wires or into the drift volume.

No gating grid or open gating grid

A gating grid can be operated in two voltage configuration. Either the potential on all its wires is matched to the drift field in the detector. This means for the ALICE TPC drift field of $400\,\mathrm{V\,cm^{-1}}$, that the gating grid wires are set to a potential U_{Gate} which is $0.3\,\mathrm{mm} \times 400\,\mathrm{V\,cm^{-1}} = 120\,\mathrm{V}$ smaller than the cathode wire potential. At these settings the grid wires do not affect the drift of charge carriers, except if these charge carriers move into the vicinity of the wires. Figure 3.11b shows the electron and ion drift lines in a MWPCs with the layout given in Figure 3.11a, while the gating grid is in the open configuration. In the figure it is not very well visible that the primary and secondary electrons drift into the MWPC and are amplified, because the ion drift lines dominate the figure. Most ion drift lines originate close to the anode wires and end either on the pad plane or on the cathode wires. A smaller fraction of the ions ends up on the gating grid wires, while a similar fraction of drift lines extends into the drift volume.

Closed gating grid

The gating grid is closed in order to collect all the remaining ions, which are not collected by the cathode wires or the pad plane. To this end a different voltage configuration is applied to the gating grid wires. This results in a change of the field lines from the ROCs to the detector volume and vice versa. If the gating grid is closed, all field lines from and to the MWPC end on a gating grid wire. Because of their higher mass ions have a smaller mobility and hence smaller diffusion (Eq. (3.11)) and follow the field lines, therefore, they get collected with high efficiency by the gating grid wires. Also electrons from the detector volume are hindered by the gating grid to enter the ROC as long as the grid is closed. In our example of the ALICE TPC ROC the closure of the gating grid is achieved by applying alternating voltages $U_{\mathrm{Gate}} - \Delta U$ and $U_{\mathrm{Gate}} + \Delta U$ to every second wire of the grid.

The gating grid is usually kept closed in the gated operation of a MWPC, except it is triggered to open. Then it stays open for as long as an electron needs to travel across the

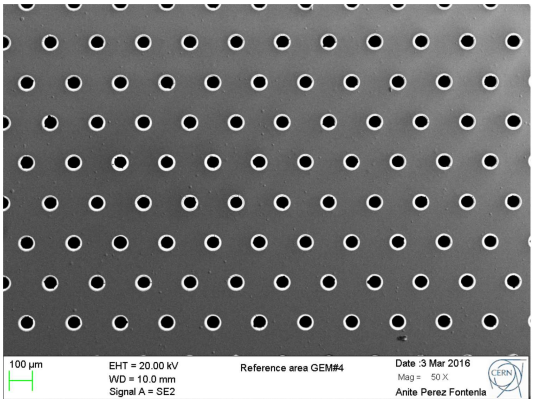

Figure 3.12: Scanning electron microscope picture of a standard GEM foil. The picture was done by Anité Perez Fontenla (CERN/EN/MME-MM) and provided to the author by C. Garabatos (GSI – Helmholtzzentrum für Schwerionenforschung GmbH, Germany), M. Jung (Johann-Wolfgang-Goethe Universität, Germany) and R. Negrão De Oliveira (Universidade de São Paulo, Brazil).

full drift length in the detector. This ensures that all primary and secondary electrons in the gas volume are collected. Afterwards the gating grid is closed for as long as needed to collect all the ions produced during the gas amplification. For the ALICE TPC this corresponds to a $t_O \lesssim 100\,\mu s$ opening time of the gating grid and about 200 µs (t_C) closure time. As for all detectors employing such a technique, the maximum readout read is therefore limited to $(t_O + t_C)^{-1}$. However, the gating efficiency is very high, e.g. the gating efficiency of the ALICE TPC has been found to be $\sim 0.7 \times 10^{-4}$ [12].

3.5. Gas electron multipliers

There many different systems to achieve gas amplification applied in different gaseous detectors, other then MWPCs. For this work the Gas Electron Multiplier (GEM), which was invented in 1996 by F. Sauli [25], is the most relevant. Therefore we will only introduce this technology and not discuss the others. For information on other types of gas amplification stages see e.g. the chapter on gaseous detectors in [53], the last chapters in [63] or e.g. the micro pattern gaseous detectors chapter of [97].

The GEM is a polyimide foil with a copper cladding on both sides and a regular hole pattern. GEM foils have a polyimide layer of 50 µm width and their copper layers are 5 µm wide. The foil's hole pattern is a hexagonal one as illustrated in the scanning electron microscope picture in Figure 3.12. For a standard GEM foil the hole pitch is 140 µm.

3.5.1. GEM production

The GEM holes are created with an etching process using different chemicals for the copper and polyimide. First a mask, defining the hole pattern, is transferred to the raw material by means of photolithographic techniques. Then the copper is etched according to this mask, while the holes in the copper serve as mask for the polyimide etching in a later step. Double-mask GEMs are produced by adding a mask to both sides of the future GEM. This requires an alignment precision of $\sim 10\,\mu m$ among the two masks and the raw material and allows to produce GEMs of a size up to $40 \times 40\,cm^2$. To overcome this limitation, the single-mask technique was developed [98], allowing to produce GEMs as big as a square-meter as e.g. needed for the future ALICE TPC readout chambers. As the name suggests, only one mask is used to define the hole pattern to etch the first copper layer. While this layer is etched, the other one is protected. After the polyimide etching the second copper layer is etched, using the holes in the polyimide as mask and protecting the first copper layer.

The different production techniques result in a different GEM hole geometry. Double-mask foils have hourglass-shaped holes (as sketched in Fig. 3.13a). The diameter at the

centre is about 50 µm and extends to 70 µm at the outer boundary of the GEM hole. The holes of single-mask GEMs, however, are slightly conical. See [98, 99] for examples of hole cross-sections created by the different techniques.

3.5.2. Working principle of a GEM foil

Electron amplification in a GEM hole

A electric field builds up in the GEM holes if there is a voltage difference (ΔU_{GEM}) between the two copper layers of a GEM. Figure 3.13b shows a simulation of the electric field in a GEM hole with the geometry of a double-mask GEM.[j] For a ΔU_{GEM} of a few 100 V this field is already of several 10 kV cm^{-1}, which is sufficient for gas amplification in common gas mixtures as discussed in Section 3.3 (e.g. Fig. 3.5). If an electron enters the GEM hole it is accelerated in the electric field there and eventually amplified. A simulation of gas amplification is displayed in Figure 3.13a. Two electrons enter the GEM hole from the drift region above the GEM, where a drift field of 250 V cm^{-1} is applied. The field in the GEM hole is provided by a ΔU_{GEM} of about 350 V. In this field both electrons are accelerated and undergo gas amplification. The green dots in the figure mark places where excitations take place, while dark dots mark ionisations. These latter dots are hence the starting points of ion drift lines. This simulation illustrates that most of the ionisations are produced in the region around the lower end of the hole as a result of the exponential nature of the gas amplification (e.g. Eq. (3.18)). In this simulation the electric field below the GEM is 3.75 kV cm^{-1}. However in the vicinity of a GEM hole, the field inside the holes enhances the field below the GEM. This effect is illustrated in the simulation of the electric field, displayed in Figure 3.13b.

Extraction and collection efficiency of electrons

The simulation in Figure 3.13a shows that some electrons end up on the lower copper layer of the GEM. These electrons electrons reduce the effective gas amplification, as well as electrons do which end up on the top side of the foil and do not enter a GEM hole in the first place. These are not amplified at all. The effective gain

$$G_{\mathrm{Eff}} = C_{\mathrm{e}} \cdot G \cdot X_{\mathrm{e}} \tag{3.21}$$

is used to take the efficiency to collect (C_{e}) (respectively extract (X_{e})) electrons into (respectively from) the GEM holes and the actual gain G into account. It has been shown with numerical simulations and measurements that C_{e} and X_{e} are functions of the ratio between the electric field in the respective region above (C_{e}) or below (X_{e}) the GEM and the electric field in the GEM hole [102]. A more recent approach based on calculations of the electric flux, yields analytic expressions for this dependence [103], which is able to explain more features in the measured data than the model in [102].

3.5.3. Ion back flow

The ions produced during the electron amplification drift into the GEM hole, as the dark ion drift lines in Figure 3.13a show. They follow closely the field lines (Sec. 3.1.1) and are hence either guided to the top copper layer of the GEM foil or into the region above the GEM, as displayed in Figure 3.13a. Since ions produced during the gas amplification are distributed over the full diameter of the hole, their probability of getting extracted from the GEM is related to the fraction of field lines, which do not end on the top copper layer. Ions collected into a GEM hole, however, are guided by the field lines into the centre region of this hole. Hence these collected ions have a higher extraction efficiency compared to ions produced during the electron multiplication. This difference was parametrised and quantified in [102] as well.

[j] The simulation was performed with Ansys [100]. This software provides tools for the numerical simulation of (among others) electrostatic problems.

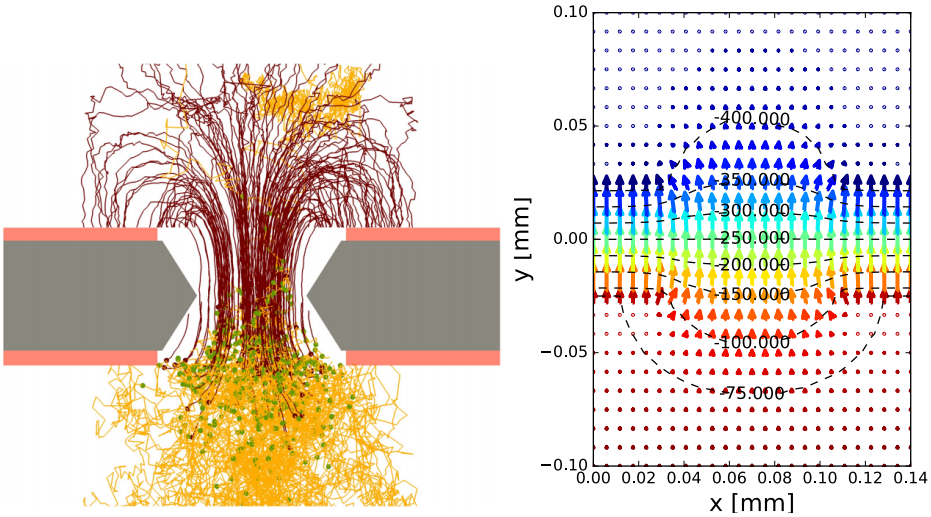

(a) (b)

Figure 3.13: (a) Garfield [94] simulation of the gas amplification of two electrons in a GEM as explained in Sec. 3.5.2. The figure is adopted from [101]. All the paths displayed are projections to the cross-section plane. (b) ANSYS [100] simulation of the electric field in a GEM hole. The GEM has the geometry of a standard GEM as described in the text and e.g. displayed in Figure (a). $\Delta U_{\mathrm{GEM}} = 350\,\mathrm{V}$ is applied across the two copper layers. The dashed lines are potential lines and the arrows are field vectors. Their colour code corresponds to the potential present and their size corresponds to the potential gradient. In both figures the field below (respectively above) the foil is $3.75\,\mathrm{kV\,cm^{-1}}$ (respectively $250\,\mathrm{V\,cm^{-1}}$).

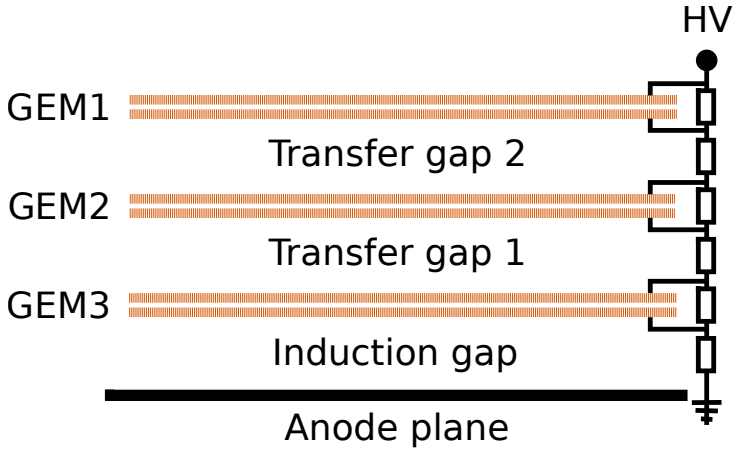

Figure 3.14: An example of a triple GEM stack: Three GEMs are mounted on top of an anode plane. The High Voltage (HV) for the GEM electrodes is provided through a voltage divider. The resistors in the divider chain have to be chosen according to the desired potentials for each GEM electrode.

There are different means of defining the Ion Back Flow (IBF). For the ALICE TPC Upgrade and the definition

$$\mathrm{IBF} = \frac{1+\epsilon}{G_{\mathrm{Eff}}} \tag{3.22}$$

is used [23]. ϵ is the number of ions drifting from the gas amplification stage into the gas volume above an amplification stage per amplified primary electron. This definition equals the ratio of the cathode current and the anode current $I_{\mathrm{Cathode}}/I_{\mathrm{Anode}}$, and can be directly related to measurements.

3.5.4. Stacking GEMs

Usually a gas amplification stage in a ROC consist out of a cascade of several GEMs, as sketched in Figure 3.14, instead of just a single GEM. The electron multiplication is shared between all GEM foils in the stack. Thus a high net gain can be reached, but only a moderate gain in each individual foil is needed.

Discharge probability

A lower gain per foil decreases the discharge probability for discharges between the top and bottom electrode of the GEM through a GEM hole [104]. In addition, the lower foil gain and the diffusion of the electrons in the gaps between GEMs reduce the charge in the GEM holes, which lowers as well the probability for breakdown. Section 6.3 focuses on the discharge development in GEM holes.

Other performance parameters

The performance of a GEM stack depends on the gain in- and electron collection and extraction from each GEM foil and thus on the combination of the ΔU_{GEM} of the different GEMs and the fields between the different foils. Tuning these parameters as well as choosing the appropriate gas, allows to match the performance of the stack to the desired requirements. Hence a GEM stack can be matched to a wide range of applications in gaseous detectors as discussed e.g. in [99]. Some of the performance parameters as the energy resolution and the IBF of GEM stacks are discussed in Section 4.3.3.

3.5.5. Powering a GEM stack

In a GEM stack all the GEM sides need to be supplied with its own potential. This can be done using different systems, which define the flexibility with which the voltages can be changed wile operating a GEM stack in a ROC.

Voltage divider

In Figure 3.14 the electrodes of the three GEMs are connected to a *voltage divider*, sometimes referred to as *resistor chain*. One voltage is supplied to the divider and the voltage drop across each of the resistors defines the potential difference across the sides of the respective GEM or across the two GEM electrodes defining a gap. Usually protection resistors are added in the HV path from the voltage divider to the respective GEM electrode, but these are not shown in the figure. Powering a GEM stack with a resistor chain offers the advantage that only one channel of a power supply is needed to power the full stack and all the potentials at the different electrodes change simultaneously as the voltage at this channel is adjusted. On the other hand it is not possible to adjust the voltage difference applied between the two sides of just one GEM or to change only the field in one gap.

Multi channel power supplies

Another possibility is to bias each GEM electrode directly from an individual channel of an multi channel power supply. This gives maximum flexibility in choosing and changing the voltages at each electrode in the stack, but additional caution while setting the voltages is required. In contrast to the operation of a GEM stack with a voltage divider, the voltages defining the different ΔU_{GEM} and ΔU_{Gap} do not necessarily change simultaneously as the voltages are ramped up to the desired value. If a ΔU_{GEM} or ΔU_{Gap} exceeds $U_{\mathrm{Breakdown}}$ for the corresponding gap width of either 50 µm or d_{Gap}, respectively, discharges may occur which damage the GEM. In Section 6.6.1 we discuss different power supplies using the experience we gained during measurements with a GEM stack.

4. Towards a time projection chamber with continuous readout

In this chapter we explain first the working principle of a *Time Projection Chamber* (TPC) (Sec. 4.1), as it has been proposed in [1] and is still applied nowadays. The TPC layout has been continuously improved since its original proposal. Therefore, we discuss details of the layout of modern TPCs and important parameters for the TPC operation. Doing so we use the ALICE TPC [12] as example (Sec. 4.2). We do not discuss the topic of readout electronics, because it is too complex to cover it in a short section but dedicating a long section to this topic is out of the scope of this work. See [12, 105] for further information on the readout electronics of the ALICE TPC. In Section 4.3 we discuss the upcoming upgrade of the ALICE time projection chamber.

4.1. Working principle of a time projection chambers

A TPC consists of a gas volume with an electric field, as sketched in Figure 4.1. When a charged particle with sufficiently high momentum moves through the TPC, it ionises gas atoms and/or molecules along its path as explained in Section 3.2.1. The electric field (drift field, $\mathrm{E_D}$) guides the electrons towards ReadOut Chambers (ROCs), while the ions drift towards the (drift) cathode. The ionisation electrons along the trajectory of the incidents particle will eventually arrive at the ROCs, where they are amplified and read out. The x and y (respectively, r and ϕ) coordinates of the particle's trajectory through the TPC are obtained from the locations where the electrons arrive. The third coordinate (z) of the points along the particle's trajectory can be calculated as $z = (t_\mathrm{e} - t_0) \cdot \mathrm{v_d}$, using the electrons' time-of-arrival at the readout chambers (t_e), the time t_0 and the electron drift velocity $\mathrm{v_d}$. The time t_0 is the time when incident particles pass through the TPC, which can be e.g. provided by an external trigger.

The magnetic field deflects charged particles and it therefore allows to determine the momenta of particles crossing the TPC by a curvature measurement of the respective trajectories. Furthermore, the transversal diffusion is significantly reduced (Sec. 3.1.2, e.g. Eq. (3.12)) if a magnetic field is applied in parallel to the drift direction.

A high density of track points along a particles trajectory is obtained, because all the counting gas inside the TPC is the active medium. Therefore, tracks can be reconstructed with high precision, although the resolution of each single track point is not as good. In case of the ALICE TPC a track resolution of 200 µm is achieved, while the single point resolution is about 1 mm in $r\phi$ and z (see the beginning of Section 2.3 for the coordinate system). In addition, the absence of a sampled active volume of discrete layers allows tracking of particles at high particle multiplicities. A disadvantages of a TPC is the slow readout time, because a time of $z_\mathrm{Full}/\mathrm{v_d}$, where z_Full is the maximal drift length, is needed to read out a complete event. A fast trigger on event properties is thus not feasible.

In order for a TPC to work well, the gas conditions need to be under control and the electric field needs to be uniform over the full volume of the TPC. In Section 4.2 these points are addressed using the ALICE TPC as example.

4.1.1. Time projection chambers with a liquid detection medium

TPCs with gas as active medium are valued, among other things, for their low material budget, which allows to track particles with low momenta down to a few $100\,\mathrm{MeV}\,c^{-1}$. Since this work concentrates on the ALICE TPC (upgrade), we focus only on TPCs filled with a gaseous detection medium, neglecting TPCs using a gas in its liquid state as well as TPCs

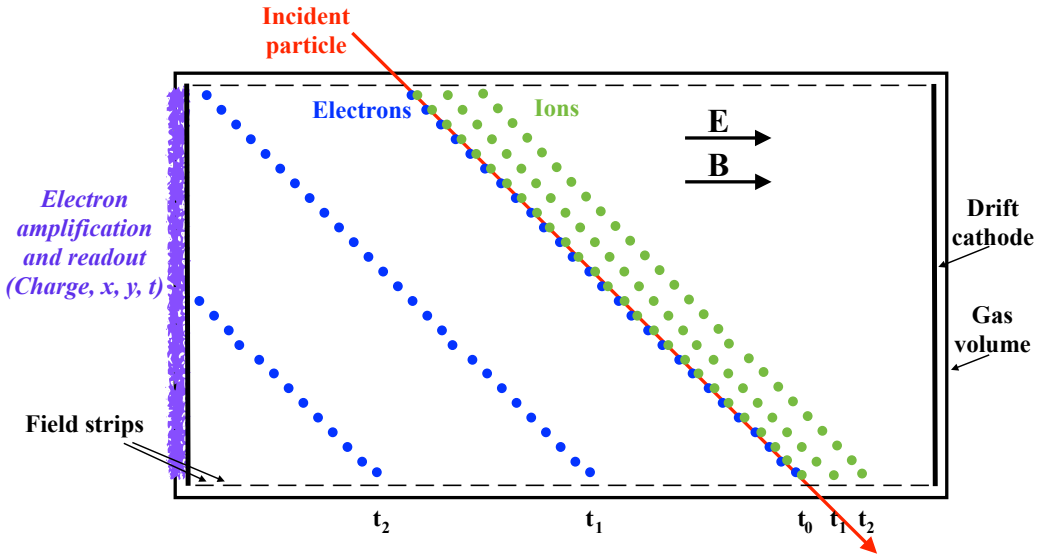

Figure 4.1: Working principle of a Time Projection Chamber (TPC): At the time t_0 an incident particle ionises gas atoms and/or molecules along its trajectory in the gas volume. The corresponding electron-ion pairs drift in opposite direction in the electric field applied to the gas volume. The positions of the drifting charges are displayed at the times t_0, t_1 and t_2 ($t_0 < t_1 < t_2$). At the later time, a part of electrons has already reached the readout plane, where the electrons are amplified and their signal as well as their position on the readout plane is read out. Also, the time of arrival of the electrons is recorded, which allows to reconstruct the coordinate in drift direction, if the time t_0 and the electron drift velocity are known. The electric field in the TPC, the drift field, is provided by the voltage difference between drift cathode and readout plane as well as by field strips (Sec. 4.2.1, Fig. 4.4a) along the walls of the gas volume.

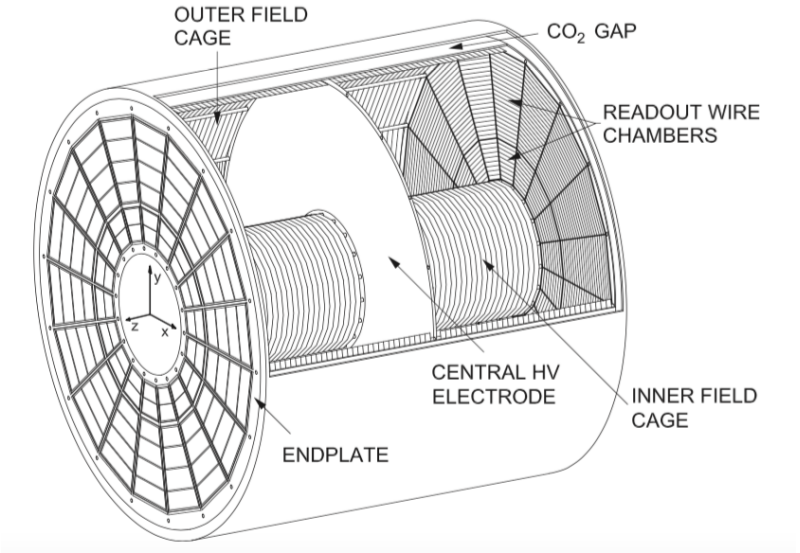

Figure 4.2: A schematic view of the ALICE TPC. The readout chambers are indicated by their trapezoidal shape. Readout chambers close to the outer (respectively, inner) field cage are the so called Outer ReadOut Chambers (OROCs) (respectively, Inner ReadOut Chambers (IROCs)). The figure is adopted from [23].

with a liquid and a gaseous phase (dual phase TPC). See [106] for the original proposal of liquid argon TPCs and [107] for a recent example of such a detector. An example for a dual phase TPC is described in [108]. Such TPCs work by the same principles as described before, however, there a large differences in the realisation between TPCs using a gas and such using a gas in its liquid state. Liquid gas (and dual phase) TPCs are used as dense absorbers for weekly interacting particles like neutrinos and at the same time they allow for tracking of particles produced in an interaction of a weekly interacting particle with the gas atoms.

4.2. The ALICE time projection chamber

The ALICE TPC [12] layout is shown in Figure 4.2. In order to leave space for the beam pipe as well as the *Inner Tracking System* (ITS) (Sec. 2.3.2, Fig. 2.4), the gas volume is shaped like a hollow cylinder. The TPC is 5 m long, has an outer radius of almost 2.5 m and an inner radius of 85 cm and therefore an active volume of almost 90 m^3. On both endplates of the TPC 18 *Inner ReadOut Chambers* (IROCs) (respectively, *Outer ReadOut Chambers* (OROCs)) are mounted at the inner (respectively, outer) part of the TPC. In the figure, IROCs and OROCs are visible by their trapezoidal shape. One TPC sector is composed of an IROC and the adjacent OROC, which cover together the TPC's length in r. The ROCs are currently *Multi-Wire Proportional Chambers* (MWPCs), following the layout which has already been introduced in Section 3.4 (Fig. 3.11). The central drift cathode divides the TPC into two halves with a drift length of 2.5 m each. As drift gas Ar-CO_2 (88-12), Ne-CO_2 (90-10) as well as Ne-CO_2-N_2 (90-10-5) have been used. The exact gas composition is tuned according to the ambient pressure in order to have an electron drift time of $\sim$ 95 µs at $E_D = 400\,V\,cm^{-1}$. Also the gas gain in the readout chambers and the chamber stability is considered for the fine adjustment of the mixture.

The exact knowledge of the drift velocity is critical for the reconstruction of the z coordinate in any TPC. Therefore the gas conditions (temperature T, pressure p) have to be stable and contamination of the mixture have to be avoided. A temperature gradient along the electrons' drift path from the incident particle's trajectory to the ROCs will result in a varying drift velocity, which impacts the reconstruction of the z coordinate. E.g. for the ALICE TPC the temperature uniformity over the full volume of the TPC has to be better

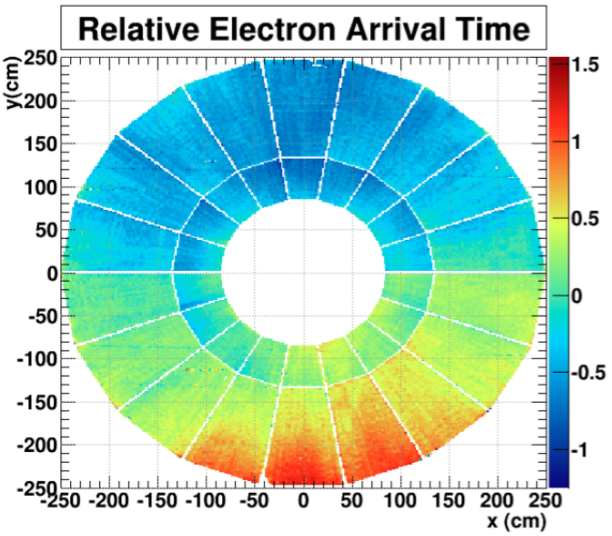

Figure 4.3: The plot shows the relative arrival time of electrons, which drifted the full drift distance of 2.5 m inside the ALICE TPC. The relative arrival time is encoded in the colour according to the axis on the right, the unit on this time axis is 100 ns. The gradient in the arrival time from top to bottom of the TPC is caused by a pressure gradient due to gravity. The plot is adopted from [8].

than 0.1 K, because otherwise the change of the z coordinate is larger than the anticipated resolution. Therefore, a system of thermal shields is used to obtain the desired temperature stability. Furthermore the drift velocity is regularly monitored with calibration laser tracks. An ultra violet laser is guided into the ALICE TPC and split in order to produce tracks at defined positions inside the drift volume. Similar laser systems have already been used by different TPCs [5, 6, 95, 109] and are planed for future TPCs [26]. Furthermore, stray light from the laser tracks hits the drift cathode and ejects photoelectrons from there, which drift the full drift distance and are eventually recorded at the ROCs. Figure 4.3 shows one such calibration measurement. A gradient in the arrival time of the electrons due to the gas pressure in the TPC is visible. In the lower part of the TPC the gas density is higher and thus the electron drift velocity lower (see Sec. 3.1.1, (3.6)). Note that the pressure is uniform along z and therefore this spread in the arrival time on the order 0.2 % can be accounted for during the reconstruction of the z coordinate. The laser is shot regularly during data taking and therefore provides regular monitoring of the drift velocity.

The exact gas conditions affect as well the gain (Sec. 3.3.1, e.g. Eq. (3.18)) of the gas amplification stage in the ROCs. For the MWPCs of the ALICE TPC the gain changes by 1 % for a temperature change of 1 K [8]. However, using signals with a known energy deposit in the gas (e.g. laser tracks, tracks of minimum ionising particles) it is possible to monitor gain fluctuations and correct for them.

4.2.1. Field cage

In addition to uniform gas conditions, an homogeneous electric field is desired over the whole full active of a TPC. To this end a field cage is used, which consists of equally spaced field strips surrounding the drift volume. In the cross section view of a TPC in Figure 4.1, these field strips are indicated by the horizontal bars at the top and bottom of the figure. Each field strip i is supplied with a dedicated potential ($U_{\mathrm{S}i}$) corresponding to the drift field at the strip's position. In case of the ith strip at a distance $z_{\mathrm{S}i}$ from the drift cathode, this potential equals $U_{\mathrm{S}i} = U_{\mathrm{Cathode}} + |\mathrm{E_D}| \cdot z_{\mathrm{S}i} = U_{\mathrm{Cathode}} + |\mathrm{E_D}| \cdot d_{\mathrm{S}} \cdot i$, where d_{S} is the distance between the centre of two subsequent strips. In order to supply the different $U_{\mathrm{S}i}$, a voltage divider chain as shown in Figure 4.4a is a suitable choice. All the resistors in the divider have usually the same resistance. The divider is supplied with the cathode potential at the cathode side

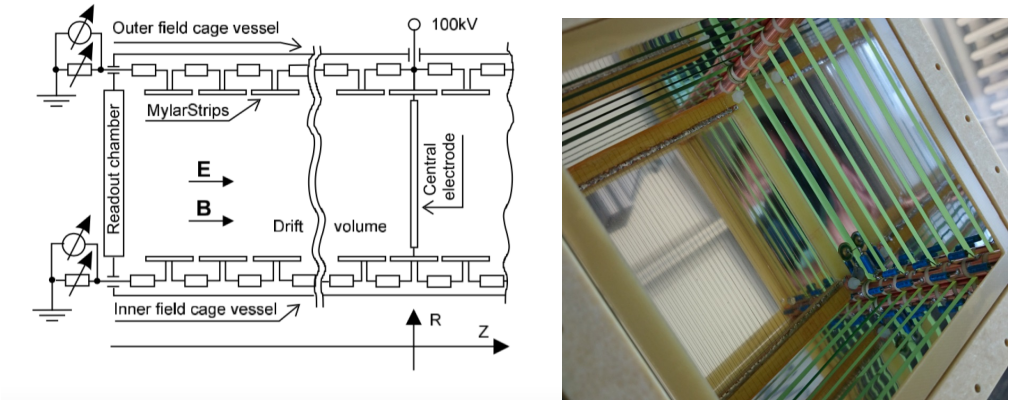

(a) (b)

Figure 4.4: (a) Schematic of the voltage divider supplying the field strips of the ALICE TPC field cage with their respective potential. Because the ALICE TPC layout is a hollow cylinder (Fig. 4.2), two voltage dividers are needed in order to supply the field strips at the inner and outer wall of the TPC. The figure is adopted from [9]. (b) Field cage of a small prototype detector. Eight suspended field strips can be seen as well as the drift cathode (behind a grid). In the lower right a the voltage divider with seven resistors is visible.

and connected through a last resistor to ground. The resistance of this last resistor is chosen such, that the potential on the last strip properly matches other constraints, e.g. the last strip's distance to the ROCs. The electric field is slightly distorted in the vicinity of the field strips, because the strips have a finite width in z but everywhere along this width the same potential U_{Si}. However, these distortions decrease fast with increasing distance from the strip. E.g. for the ALICE TPC ($E_D = 400\,V\,cm^{-1}$, $d_S = 1.5\,cm$) it was found that these distortions are less then $0.5 \cdot 10^{-4}$ of the nominal field, when a (radial) distance of 2 cm from the strip is reached [9].

In the NA49 TPCs [5] field cages were employed in which the individual field strips are suspend on a number of rods and are not glued to the detector wall. In this way the space charge build up on the insulating material between two adjacent strips can be minimised. Figure 4.4b shows a small detector as example for a field cage with suspended strips. Two rods are visible, which hold the field strips, as well as the voltage divider.

The ALICE TPC field cage

The field cage of the ALICE TPC adopts the NA49 design with field strips suspended on rods. There is an outer and an inner field cage (Fig. 4.2 and 4.4a) located close to the respective inner and outer wall of the gas volume. Both, the inner and outer field cage have 18 rods on which the suspended strips are mounted. The rods are positioned at the sector boundaries, as slightly visible in Figure 4.2, and several services are housed inside these rods: The voltage divider to supply the field strips with their corresponding potential, the high voltage line to the drift cathode, the laser system and the gas supply to and from the TPC are distributed among several rods on the inner and outer field cage.

The drift field of $400\,V\,cm^{-1}$ requires a cathode voltage of 100 kV. In order to properly insulate this potential from ground and the surrounding world, there is one additional gas volume filled with CO_2 each, on the inner and outer radius of the TPC. In these volumes aluminium rings are glued to the walls, which are connected with a voltage divider chain. This construction is needed in order to avoid the build up of large space charges on the outer walls of the field cage. More information on the filed cage can be found in [9, 12].

The material budget of the whole ALICE TPC, including the field cage, the additional CO_2 volumes and the counting gas is only 4.1 % of the radiation length at the $\eta \sim 0$ region.

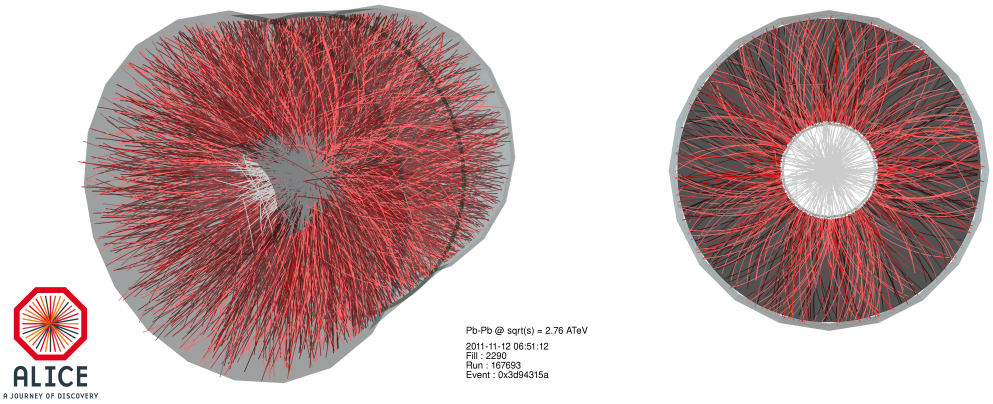

Figure 4.5: A lead-lead collision at $\sqrt{s} = 2.76\,\mathrm{ATeV}$, where the A corresponds to the number of nucleons in the lead nuclei. This event was recorded by the ALICE TPC during the LHC lead-lead run in 2012.

4.2.2. Space charge

The accumulation of space charge from slow ions in the drift volume can lead to seizable distortions of the electric field and in turn to distortions of the measured particle trajectories. These ions are produced by two sources. First, there are the ions resulting from primary ionisations in a TPC's drift volume. In case of TPCs operated at collider experiments the gas volume is illuminated in a uniform manner in ϕ by particles passing through the TPC. Therefore the corresponding distortions are symmetric in ϕ and distort only the measurements of track points in the r coordinate [21, 23, 101, 110]. To give an example from the ALICE TPC: In case of the highest interaction rates in proton-proton and lead-lead collisions at the *Large Hadron Collider* (LHC), these distortions have been found to be about 1 mm for ionisation electrons, which have to drift over the full drift length of the TPC [21].

The second source of ions are the ROCs. Ions, which drift from the gas amplification region into the drift volume, contribute strongly to the space charge in the drift volume. Their contribution to the space charge in the detector is not uniform, because of e.g. dead regions in the readout plane or differences in gain among different ROCs. Therefore, these ions give rise to track point distortions in r and ϕ. To avoid such space charge, an ion gate is usually employed in readout MWPCs of TPCs as discussed in Section 3.4.2. Reference [21] describes the observed track-point distortions observed in the ALICE TPC, together with a dedicated calibration procedure in order to correct for these distortions.

4.2.3. Performance of the ALICE time projection chamber

As mentioned frequently throughout this work, TPCs are well suited to perform particle tracking in a high multiplicity environment. In Figure 4.5 a lead-lead collision as recorded by the ALICE TPC is shown, which illustrates this very well.

The ALICE TPC achieves a $\mathrm{d}\varepsilon/\mathrm{d}x$ resolution (see Sec. 3.2.4, Fig. 3.4) of about 5.2 % in proton-proton collisions and slightly worse $\mathrm{d}\varepsilon/\mathrm{d}x$ resolution of $\sim 6.5\,\%$ in the most central lead-lead collisions [111]. The TPC is capable of tracking pions (respectively, protons) with a momentum larger than $200\,\mathrm{MeV}\,c^{-1}$ ($400\,\mathrm{MeV}\,c^{-1}$). For lower momenta, proper tracking is hindered by (multi-)scattering of the particles in the detector material. The transverse momentum resolution of the TPC is about 6 % for particles with a momentum about $10\,\mathrm{GeV}\,c^{-1}$. For particles with a momentum of $1\,\mathrm{GeV}\,c^{-1}$ the resolution is better than 1 % [12, 111]. If the ITS and the TPC are combined for tracking and momentum measurements, a momentum resolution better than 2 % can be reached for the high momentum particles [111].

4.3. Upgrade of the ALICE time projection chamber for LHC Run 3

ALICE will take data at an interaction rate of up to 50 kHz in lead-lead collisions during LHC Run 3, starting in 2021. The ALICE detector needs the ability to examine all events at this interaction rate, in order to obtain sufficient statistics for the analysis of rare processes, like the decay of mesons with heavy quark content ([22], Sec. 2.3.3). However, the gated readout of the ALICE TPC MWPCs has an upper limit on the readout rate of ~ 3 kHz, as discussed in Section 3.4.2. This limit results from the combined times $(t_O + t_C)^{-1}$, where t_O is the time the gating grid is open in order to collect all drifting electrons from the TPC (100 µs) and t_C is the gating grid closure time of about 200 µs. The ALICE TPC needs to be upgraded in order to overcome this limitation.

4.3.1. Upgrade goals and definitions

The goal of the ALICE TPC upgrade has been the development of new ROCs, which can be read out continuously, while at the same time preserving the performance of the MWPCs currently employed in the TPC [22, 23].

Gas Electron Multiplier (GEM) foils ([25], Sec. 3.5) have promising features with respect to their operation in a ROC, which is read out continuously. For example, a certain fraction of the ions, produced during the gas amplification in the holes of a GEM, is usually collected by the upper copper layer of the same GEM foil (Sec. 3.5.2, Fig. 3.13). This is a feature of the field geometry in the GEM holes. Using GEM stacks, a better ion back drift suppression can be reached.

In advance of the ALICE TPC upgrade, the *GEM TPC collaboration* collaboration made first experiences with a large TPC using GEMs as gas amplification stage. They tested in 2011 a TPC with a triple GEM stack in the FOPI spectrometer at the *Gesellschaft für Schwerionenfroschung*, Darmstadt, Germany [112, 113]. Based on this experience the development of a continuous readout for the ALICE TPC has been pushed forward by the GEM TPC collaboration and the ALICE TPC upgrade project [114], where eventually the GEM TPC collaboration joined the ALICE collaboration. (For a recent paper on the *FOPI TPC* see [115].) An extensive research and development program with small prototypes and prototypes of full IROCs was done until the design of the future ALICE TPC ROCs has been finalised. In [23, 24] the different steps of this program are described. In this section we present some of the corresponding main findings and the final design for the ALICE TPC ROCs.

4.3.2. Energy resolution and ion back flow

Energy resolution

To guide the research programme the performance goals for the full TPC had to be defined in quantities, which are easily accessible in measurements with small prototypes. Therefore, the requirements on the future TPC's energy resolution have been defined in terms of a local energy resolution $\sigma_\varepsilon/\varepsilon < 12\,\%$ at the photopeak of ^{55}Fe X-rays, which peaks at an energy of 5.89 keV [116]. The parameter σ_ε (respectively, ε) corresponds to the width (respectively, centre) of a Gaußian distribution, which is fitted to the photopeak, once it has been measured.

Ion back flow

It has been estimated with simulations that the performance of the current TPC in terms of position and momentum resolution can be maintained with an *Ion Back Flow* (IBF) of less than 1 % [23]. The IBF is a measure for the amount of ions accumulating in the drift volume and includes the ions from the gas amplification stage moving into the drift volume

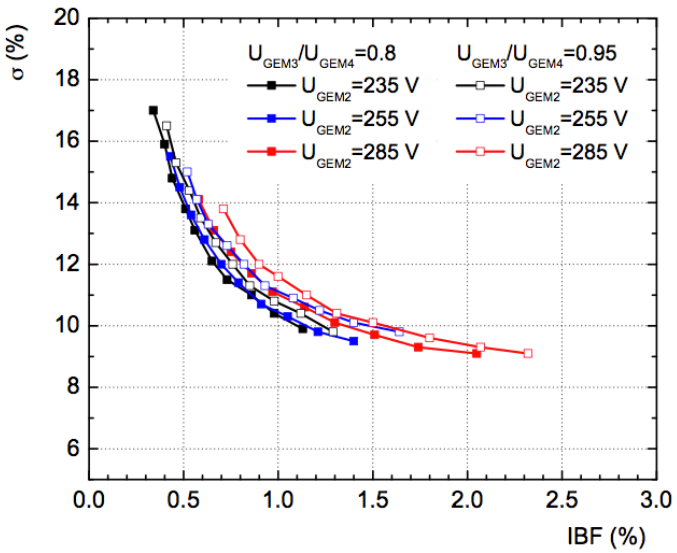

Figure 4.6: All the points in this figure have been obtained with quadruple GEM stacks of $10\,\mathrm{cm} \times 10\,\mathrm{cm}^2$ GEMs and 2 mm distance between the respective GEMs (between GEM4 and the readout plane). Standard GEMs (hole pitch 140 µm) have been used at position one and four in the respective stack, while the GEMs at position two and three have been large pitch foils (hole pitch 280 µm). For the measurements, the voltage difference between the two sides of GEM3 and GEM4 (ΔU_{GEM3} and ΔU_{GEM4}) have been varied. At the same time, ΔU_{GEM1} has been adjusted in the range $225\,\mathrm{V} \leq \Delta U_{\mathrm{GEM1}} \leq 315\,\mathrm{V}$ in order to keep the gain of the full stack at 2000. The electric fields between GEMs have been as follows: $\mathrm{E_{T1}} = \mathrm{E_{Ind}} = 4\,\mathrm{kV\,cm^{-1}}$, $\mathrm{E_{T2}} = 2\,\mathrm{kV\,cm^{-1}}$, $\mathrm{E_{T3}} = 0.1\,\mathrm{kV\,cm^{-1}}$. The $\mathrm{E_{T}}i$ represent the transfer fields between adjacent GEMs and $\mathrm{E_{Ind}}$ the induction field between GEM4 and the pad plane. All measurements have been done in Ne-CO_2-N_2 (90-10-5). Figure adopted from [23].

(N_{Back}), as well as the primary ionisations (N_{Prim}) produced directly in the drift volume.

$$\mathrm{IBF} = \frac{N_{\mathrm{Back}} + N_{\mathrm{Prim}}}{G \cdot N_{\mathrm{Prim}}} = \frac{1+\epsilon}{G} < 1\,\%$$

G is the (effective) gain of a gas amplification stage and ϵ is the number of back drifting ions per primary electron. The second part of the equation corresponds to the previously shown definition (Sec. 3.5.3, Eq. (3.22)). For the ALICE TPC a gain G of 2000 is desired, therefore ϵ has to be smaller than 20. The IBF can be measured for a certain gain by a simultaneous measurement of the current at the cathode and anode of a detector. The ratio of both currents gives the IBF.

Optimising the ion back flow and the energy resolution

The IBF and the energy resolution have been studied simultaneously for different HV settings, using small detectors containing stacks of $10 \times 10\,\mathrm{cm}^2$ GEMs. It has been realised that a fourth GEM needs to be added to the common triple GEM stacks in order to reach an IBF below 1 %, while having at the same time the desired gain and energy resolution.

Optimising the IBF and the energy resolution are an competing effect, as Figure 4.6 illustrates. The increase in IBF with improving energy resolution can be understood to a large extend by the influence of the GEM facing the drift volume (GEM1) on the gas amplification of the full stack. Form GEM1 onwards some electrons are lost, because they are either not extracted from the holes of GEM1 or not collected into the holes of GEM2. If the gain in GEM1 is low, these loses have a larger effect – relative to the total number of electrons –

than at high GEM1 gain. The fluctuations of the amplified signals of a certain number of primary charges increase with decreasing GEM1 gain. On the other hand, all ions extracted from GEM1 enter immediately the drift volume, therefore the IBF increases with increasing GEM1 gain.

Settings of a GEM stack optimised for a low IBF thus usually have a rather low GEM1 gain and most of the gas amplification happens in GEM3 and/or GEM4. In case of the HV settings of the future ALICE TPC (Table 4.1) GEM4 has the highest gain. The transfer field above this GEM (E_{T3}) is low, in order to have a very low ion extraction efficiency from the holes of GEM4. The remaining ions are then blocked by the other GEMs. In order to improve this ion blocking, GEMs with different hole pitch have been tested as to increase the misalignment between the GEM holes among the GEMs in a stack. The hexagonal hole pattern of a GEM foil has rotation symmetry of 60 °. Rotating each GEM mask by 90 ° with respect to the adjacent GEMs in the stack allows to reach an uniform misalignment of the GEM holes between subsequent foils.

4.3.3. Layout of the GEM-based readout chambers

Eventually, stacks with two Standard (S) GEMs (hole pitch 140 µm) and two Large Pitch (LP) GEMs in the order S-LP-LP-S has been found to fulfil the previously stated requirements if the voltage settings in Table 4.1 are applied to the GEM stack. The mask of every second GEM is rotated by 90 ° with respect to the other GEMs and the inter GEM distances, as well as the distance of GEM4 to the pad plane, are all 2 mm. Figure 4.7 shows an exploded view of an 3D model of an OROC. To facilitate the production and the handling of the GEM foils, the OROCs will be covered by three GEM stacks as shown in the figure. The IROCs, on the other hand, will be only covered by one stack. Figure 4.8 gives an impression of the size of the readout plane of the ALICE TPC. The figure shows an IROC GEM foil, as well as one GEM foil from each OROC GEM stack in a row.

ΔU_{GEM1}	ΔU_{GEM2}	ΔU_{GEM3}	ΔU_{GEM4}	E_{T1}	E_{T2}	E_{T3}	E_{Ind}
270 V	230 V	288 V	359 V	$4\frac{kV}{cm}$	$4\frac{kV}{cm}$	$0.1\frac{kV}{cm}$	$4\frac{kV}{cm}$

Table 4.1.: The baseline high voltage setting, foreseen for the future ALICE TPC with Ne-CO_2-N_2 (90-10-5) as counting gas. The drift field of the future TPC will be 400 V cm^{-1}. An exploded view of a corresponding ALICE TPC readout chamber is shown in Figure 4.7. This table reflects the settings at the time of the Production readiness review [117].

Discharge and $d\varepsilon/dx$ studies an IROC prototype

A prototype of an IROC has been constructed with the layout described here and was tested with the HV settings in Table 4.1 at a beam-time with electron and pion beams. During this test the $d\varepsilon/dx$ resolution of this IROC was measured and found to be compatible with the resolution of the current MWPCs of the ALICE TPC [24, 118].

The same chamber has been tested in hadron showers to measure the discharge probability of the quadruple GEM system with the HV settings in Table 4.1. In previous discharge measurements with small prototypes only upper limits on the discharge probability could be obtained, because the rates of the radiation sources used for these discharge studies were to low to see discharges in a reasonable measurement time [24]. At CERN's *Super Proton Synchrotron* the IROC prototype is placed in the cone of hadron showers produced by a pion beam impinging on an iron target. During this beam-time a discharge probability of $(6 \pm 4) \times 10^{-12}$ discharges per incoming hadron is measured [24, 119]. For comparison: During one month of 50 kHz lead-lead collisions 5×10^{13} particles will cross the readout area of the full ALICE TPC [24]. This number includes already a factor two to account for background radiation. Hence, on average 7×10^{11} particles will cross one of the 144[a] GEM

[a] There will be 2×18 IROCs with one GEM stack each and the same number of OROCs, but with three GEM stacks each.

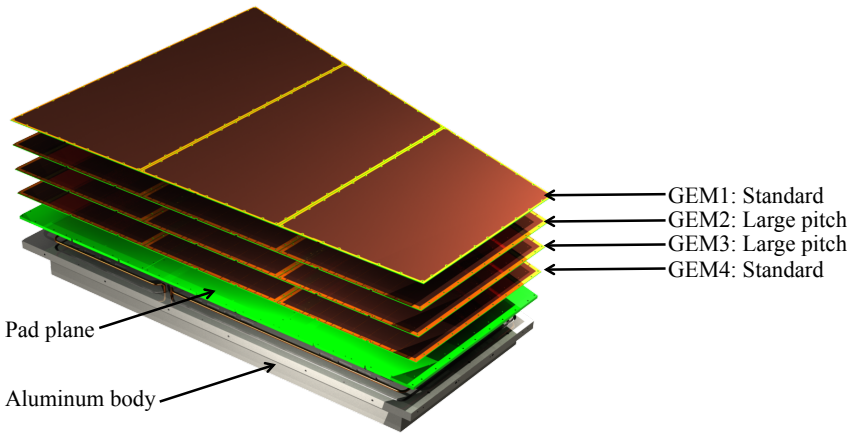

Figure 4.7: An Outer ReadOut Chamber (OROC) as foreseen for the upgraded ALICE TPC. All chambers will employ GEM stacks with four GEM foil and the foil types indicated in the figure. The hole mask of every second GEM is rotated by 90 ° with respect to the previous foil in order to maximise the GEM hole misalignment. The Inner ReadOut Chambers (IROCs) are constructed in a similar way as the OROCs, but employ only one GEM stack.

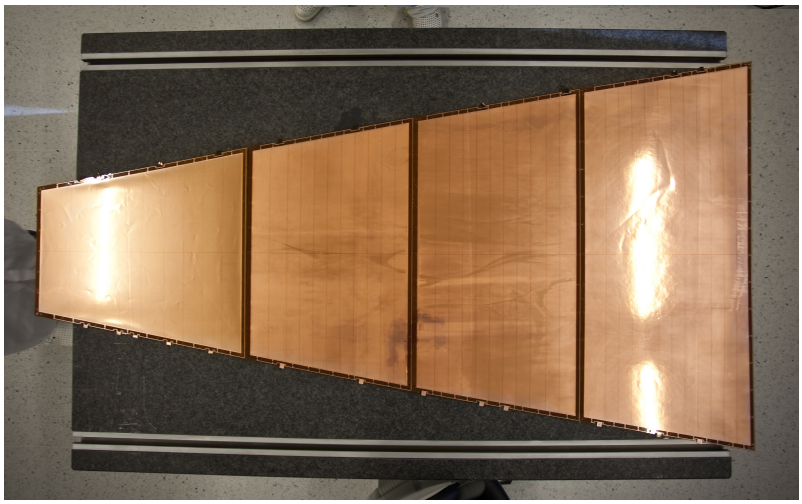

Figure 4.8: One GEM of each GEM type of the future ALICE TPC. From left to right there is an IROC GEM and the three OROC (ORCO1, OROC2, OROC3) GEMs. A sector of the future TPC seen from the top will look approximately like this. Picture provided by P. Gasik (Technische Universität München, Germany).

stacks during the considered time. Therefore, between 2 and 10 discharges are expected per GEM stack during one month of lead-lead data taking. During proton-proton collisions the particle multiplicities in the TPC are significantly lower and therefore a much lower number of discharges is expected during such periods. However, the exact number should be carefully evaluated considering the interaction rate in proton-proton collisions.

4.3.4. Further discharge studies

In order to further test the discharge probability for ALICE TPC ROCs equipped with GEMs, several full size chambers are right now tested in the L3 magnet of the ALICE detector (Sec. 2.3.2, Fig. 2.4) at forward rapidity in about 10 m distance to the interaction point. These measurements will reveal if there are systematic differences in the discharge probability among different GEM stacks. In addition to these measurements, tests with small prototypes are done like our measurements in Chapter 6 and Chapter 7. These are complementary to stability measurements (measurements of the discharge probability), because they are not done in order to measure the discharge probability for certain HV settings, but their goal is to understand the impact of a discharge on a GEM (stack) and the subsequent recovery from a discharge.

4.3.5. Ion mobility of the baseline gas mixture

The baseline gas mixture of the upgraded ALICE TPC is Ne-CO_2-N_2 (90-10-5). This mixture has been chosen because of its performance in the current TPC and because the ion mobility in this mixture is higher than e.g. in Ar-CO_2 (88-12). However, the mobility of the ions drifting in Ne-CO_2-N_2 (90-10-5) is in [23] assumed to correspond to the mobility of Ne^+ ions drifting in pure neon. This was the assumption made, as the gas mixture for the ALICE TPC has been initially chosen [120]. The requirement IBF $< 1\,\%$ has as well been defined assuming the mobility of Ne^+ in neon. In order to check the actual mobility in the Ne-CO_2-N_2 (90-10-5) our measurements in Chapter 5 have been performed.

5. Ion mobility measurements

5.1. Introduction

In the theory part (Sec. 3.1.1, Eq. (3.2)) the mobility (K) is introduced as the factor relating the drift velocity of charge carriers such as ions to the drift field: $\mathrm{v_{Drift}} = K \cdot \mathrm{E}$. In this section we present our measurements of the ion mobility for different gas mixtures as well as for different water content in Ar-CO_2 (90-10) and Ne-CO_2 (90-10). All studies presented in this chapter are measurements of K at atmospheric pressure and electric field strengths which are typically used in the drift region of gaseous detectors, i.e $200\,\mathrm{V\,cm^{-1}}$ to $1000\,\mathrm{V\,cm^{-1}}$.

Many measurements exist where the mobility for ions in their parent gases, e.g. Ne^+ in neon, is measured (e.g. [70–73]). However, the mobility of an ion species depends on the gas mixture it drifts in. Because the ion drift is not (yet) well implemented in common simulation frameworks such as Garfield [94], input from measurements as done in this work are needed in order to determine the ion-mobility in a gas mixture.

This study is motivated by the needs of the ALICE Time Projection Chambers (TPC) Upgrade [23]. In gaseous detectors operated at high interaction rates and particle multiplicities (slow) ions accumulate in the drift volume of the detector. These ions produce a large space charge which distorts the drift-field [21, 23, 101, 110]. The exact knowledge of K is thus necessary in order to estimate and simulate this space charge. Based on such simulations the impact of the Ion Back Flow (IBF) (Sec. 3.5.3, Eq. (3.22) or Sec. 4.3.2) on the performance of a TPC can be evaluated and in turn the maximal affordable IBF can be defined. In [23] the corresponding simulations for the ALICE TPC are described. The ion mobility in Ne-CO_2-N_2 (90-10-5), which is the foreseen gas mixture for the upgraded TPC, has been assumed to correspond to the Ne^+ mobility in Ne [23, 120]. We have performed the studies described in this chapter as to measure the actual mobility in Ne-CO_2-N_2 (90-10-5). Another example for the need of a precise knowledge of the ion mobility, are studies of the track point distortions created by space charge in the running ALICE TPC [21]. The goal of this study has been to find the source of the space charge by a combination of dedicated measurement runs and simulations and to correct for it.

To measure the ion drift velocity a dedicated set-up is constructed. It is described in Section 5.2, while the principle idea of the measurements follows in Section 5.3. The measured signals are treated with a special procedure, described in Section 5.4. In the same section we discuss also the uncertainties of the measurement, which are related to the signal analysis and to other sources. Our results are given in Section 5.5. The ion mobility found for different Ar-CO_2 and Ne-CO_2 gas mixtures are presented as a function of the drift field $\mathrm{E_{Drift}}$ (Sec. 5.5.1) and as function of the quencher content in the gas mixture (Sec. 5.5.2). Furthermore the effect of admixtures of N_2 to Ne-CO_2 (90-10) is examined (Sec. 5.5.3) and the effect of water on the ion mobility is studied using Ar-CO_2 (90-10) and Ne-CO_2 (90-10) (Sec. 5.5.4). We summarise our findings in Section 5.6.

5.2. Experimental set-up

We use a detector with a stack of three $10 \times 10\,\mathrm{cm^2}$ GEMs as gas amplification stage. The transfer gaps and the induction gap have all a width of 2 mm. A schematic of the set-up is shown in Figure 5.1. On top of the GEM stack a wire-grid (wire spacing: 2 mm, wire diameter 100 µm) is mounted at a distance of $d_{\mathrm{Drift}} = (21.35 \pm 0.12)\,\mathrm{mm}$. After the grid follows a mesh serving as drift cathode, while the gap between grid and mesh is $d_{\mathrm{Acc}} =$

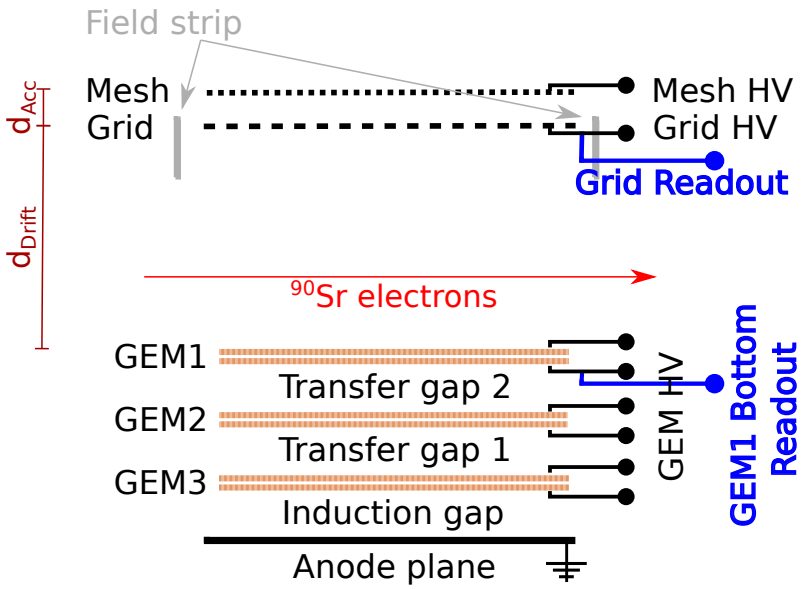

Figure 5.1: Set-up for the measurement of ion mobility. Both electrodes of each GEM as well as the grid and the mesh are powered by an independent channel power supply with two channels. The field strip close to the grid and the mesh is as well supplied with HV. Signals from the GEM1 bottom electrode and the grid are read out through a capacitor, to decouple the high voltage, and are then passed on to a preamplifier and to an oscilloscope. With the oscilloscope the signals are stored directly for later processing or several signals are first averaged and then the average is stored. Radiation enters the detector in the drift region and in parallel to all electrodes. See the text for further explanations and Figure 5.2. for a photo of the set-up.

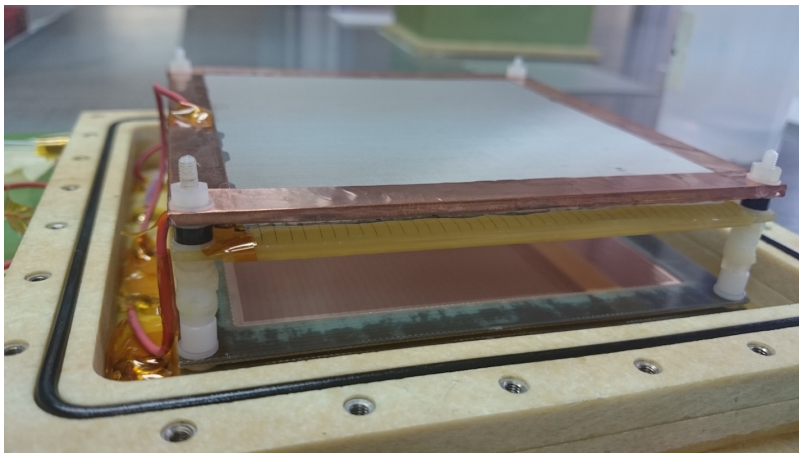

Figure 5.2: A part of the detector used for the ion mobility measurements, corresponding to the sketch in Figure 5.1. On top the mesh, serving as drift cathode, is visible. Below the mesh a wire grid is mounted. Its reflection can be seen in the GEM1, which is the only GEM of the GEM stack visible. Not shown is the detector, housing several field strips.

(6.4 ± 0.2) mm wide.[a] This region is referred as *acceleration gap* and the region between the grid and the GEM1 top electrode is referred as *drift gap*. A ^{90}Sr source, emitting electrons, creates tracks in the drift gap in parallel to the electrodes in the set-up. A photo of the set-up is shown in Figure 5.2.

Gas supply

The gas system allows to mix up to three different gases to create the gas mixture supplied to the detector. Because it is an open gas system, the pressure in the detector follows the atmospheric pressure. Therefore the atmospheric pressure (as well as the temperature in the laboratory) is monitored and recorded to later correct the measured mobilities (Sec. 5.5, Eq. 5.5). Furthermore a water sensor is placed shortly after the detector in the gas exhaust line, to monitor the water content of the counting gas. In several measurements the oxygen content is monitored as well.

Signal read out

Signals are read out from the GEM1 bottom electrode as well as the grid. For the latter case, the signals are decoupled from the High Voltage (HV) line using a $C_{\mathrm{Dec}} = 20\,\mathrm{nF}$ capacitor and afterwards the signals are fed into an ORTEC 142IH [121] preamplifier. Different values for the decoupling capacitor have been tested, but lower capacitances are not well suitable to decouple the signal from the grid, because of the detector's internal capacitance. An ORTEC 142IH preamplifier is as well used to decouple and process signals from the HV line supplying the GEM1 bottom electrode. To prevent signal-loss the decoupling circuit with the preamplifer (respectively the preamplifier) is mounted as close as possible to the grid (respectively GEM1). The signals can have a length of a few ms, as will be discussed in Section 5.3. With test signals from a pulse generator it is confirmed that the preamplifier can process signals of this length without deterioration. In addition the readout circuit is designed such that the signals are read out with as little additional shaping by the electronics as possible.

Electronic noise

Each GEM is powered with one individual CAEN N471 [122] double channel Power Supply (PS). In addition the wire grid and the mesh are biased from a module of the same type, while the field strip is supplied from a CAEN N470 [123] independent channel PS. This allows us the free choice of the voltage on each electrode. However, we realise that these PS modules induce noise in several frequency ranges at all electrodes of the set-up as they supply high voltage. To reduce this noise, each GEM electrode is powered through a $15\,\mathrm{M\Omega}$ resistor, with an additional 2.2 nF capacitor to ground. Additional low-pass filters are added in the supply of grid, mesh and field strip. Furthermore, the whole set-up, including the preamplifiers, is mounted inside a copper box, which serves as Faraday cage. Nevertheless, we still observe electronic noise. This is however at a level which allows us to perform our measurements.

Because the remaining noise is highly regular, further measures to improve the signal quality can be done on the basis of the stored signals (Sec. 5.4). In addition, we average over more than 1000 individual signals. This procedure reduces as well the noise appearing with a regular frequency.

5.3. Principle of measurement

Figure 5.3 illustrates the principle of measurement with a minimal sketch of the set-up and an example of the recorded signals. Electrons from the tracks in the drift gap are amplified

[a] For one series of measurements $d_{\mathrm{Acc}} = (6.4 \pm 0.2)\,\mathrm{mm}$ and $d_{\mathrm{Drift}} = (25.31 \pm 0.09)\,\mathrm{mm}$ is used. The errors on the distances are based on measurements of the spacers, which define the distances between electrodes. A possible bending of e.g. the grid wires or the GEM1 foil is not taken into account. However, the sagging distance of the GEM foil as well as of the grid wires is not expected to be larger than the distance errors, because of the small surface of the GEM and the short wire length.

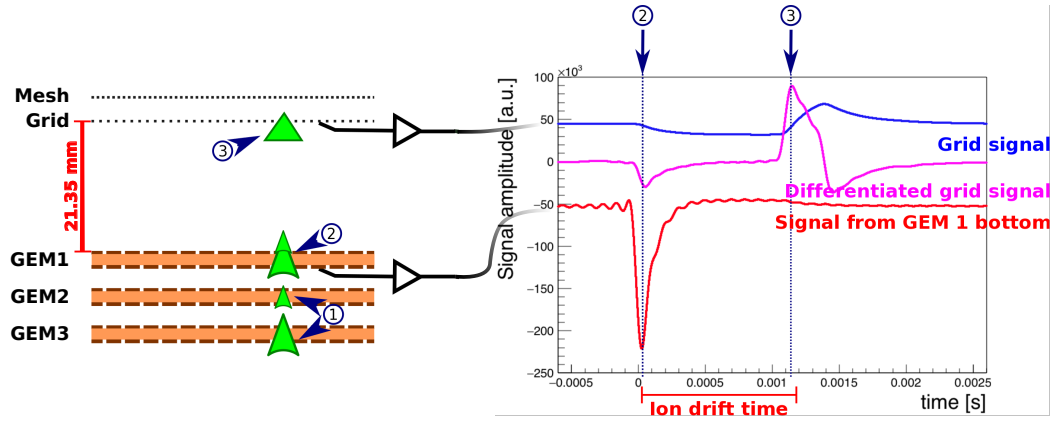

Figure 5.3: Left half: A minimal sketch of the detector set-up. (See Fig. 5.1 for the full schematic.) Right half: Typical signals recorded at the wire-grid and GEM1 respectively. The different stages of the measurement process are indicated by numbers: 1) Production of ions (indicated by green triangles) during the electron amplification in the GEM stack. 2) These ions drift through the GEMs and induce a signal on the bottom side of GEM1 as they move towards it. 3) As the ions move towards the wire-grid they induce a signal there. While they pass through the grid this signal changes polarity, yielding an inflection point. Information extracted from these signals is used to determine the ion drift velocity.

in the GEM stack. These tracks are created with a ^{90}Sr source, emitting electrons which move through the detector in parallel to the anode, GEM and wire planes. During this process ions are produced in GEM3 and GEM2 and these ions induce a signal on GEM1, as they leave the GEM stack. This signal is used to extract the start-time (t_{GEM}, Nb. 2 in the figure) of the ion drift. Afterwards the ions drift in a uniform electric field towards a wire-grid. Behind the grid a similar field as in the drift gap is set, using the appropriate voltage difference between grid and mesh. Throughout the full time of the ions movement in the drift and the acceleration gap, a signal is induced on the grid. The time at which the ions pass the grid (t_{Grid}, Nb. 3 in the figure) is extracted from this signal. We use the time difference $\Delta t = t_{\mathrm{Grid}} - t_{\mathrm{GEM}}$ and the known length of the drift gap to calculate the ions velocity $\mathrm{v}_{\mathrm{Drift}}$

$$\mathrm{v}_{\mathrm{Drift}} = \frac{d_{\mathrm{Drift}}}{\Delta t} \quad .$$

In a next step the ion mobility is calculated from this velocity and the voltage difference across the drift gap $\Delta U_{\mathrm{Drift}} = U_{\mathrm{GEM1\ Top}} - U_{\mathrm{Grid}}$

$$\begin{aligned} K &= \frac{\mathrm{v}_{\mathrm{Drift}}}{\mathrm{E}_{\mathrm{Drift}}} = \frac{\mathrm{v}_{\mathrm{Drift}} \cdot d_{\mathrm{Drift}}}{\Delta U_{\mathrm{Drift}}} \\ &= \frac{(d_{\mathrm{Drift}})^2}{\Delta t \cdot \Delta U_{\mathrm{Drift}}} \quad . \end{aligned} \tag{5.1}$$

In the next two sections we will comment on finding the stop-time (Sec. 5.3.1) and the exact start-time (Sec. 5.3.2) in the signals induced at the wire-grid and the bottom electrode of GEM1, respectively.

5.3.1. Finding the arrival-time of the ions' drift

At the time the ions pass through the grid, the polarity of the induced signal changes. In the right half of Figure 5.3 this is visible in the *Grid signal*, modulo an offset on the vertical axis. The signal amplitude changes from positive to negative for positive charged particles [124]. The signal amplitude changes in the plot from negative to positive, because

the preamplifiers invert the actual signals. A distinct feature in the signal is needed, to measure the ion mobility as precisely as possible. It turns out that the zero crossing of the signals does not mark the time at which the ions cross the grid. However, the inflection point does if the electric field in the drift and acceleration gap are the same. The *Differentiated grid signal* in Figure 5.3 has a distinct peak, which allows to quantify the inflection point without problem. In this section we want to motivate the choice of this point with Garfield [94] simulations.

Garfield

Garfield is a software to simulate the movement of charge carriers in electric fields. To this end the software can calculate electric field maps for a given input detector geometry consisting e.g. out of planes and wires. It is as well possible to provide Garfield with a field map from a different program. Interfacing Magboltz [64], Garfield is able to calculate the electron transport in almost any chosen gas mixture and the interface to Heed [125] enables the program to calculate the ionisation of gas molecules by fast moving electrons. Ions are not well parametrised in Garfield, it is for example necessary to pass the ion mobility of a gas mixture to the program. This shows once more the necessity of measurements of the mobility as shown later on.

Simulation set-up

The drift and acceleration gap of the set-up in Figure 5.3 (or Fig. 5.1) are approximated with Garfield in order to simulate the signal on the wire-grid. A Cartesian coordinate system is used for the simulations. All the electrodes (anode plane, wire-grid and cathode) are parallel to x-y-planes and the shortest distance between different electrodes is in z direction. We define $z = 0$ at the anode plane and the positive z direction points from the anode plane towards the grid and the cathode. At $z = 2.5\,\mathrm{cm}$ a wire-grid is placed. The wires of the grid are spaced with a distance of 2 mm in x direction. As for the real wire-grid the wire diameter is 100 µm. A cathode perpendicular to the z coordinate follows 5 mm after the wire-grid. The anode and cathode have an infinite length in the x and y direction, while each wire extends infinitely in y direction and in x direction there is an infinite number of wires without interruption. This layout of the simulation allows to reduce the calculation to a 2D problem in the x and z plane.

A gas file is generated using Magboltz for an Ar-CO_2 (82-18) gas mixture. The ion mobility is set to $1.77\,\mathrm{cm^2\,V^{-1}\,s^{-1}}$, which roughly corresponds to the mobility expected for this gas mixture at a temperature of 300 K and pressure of 1013 mbar, as used in the simulation.

Simulation of drifting ions and their signals

An electric field $\mathrm{E_{Drift}}$ (respectively $\mathrm{E_{Acc}}$) is applied in the gap between anode and grid (respectively grid and cathode) in the simulation. The field lines point in positive z direction, however, in the vicinity of the wires obviously the direction of electric field differs. Figure 5.4 shows a simulation of the signal on the wire-grid, which is produced by 3000 ions drifting first through the drift gap and than through the acceleration gap. For this simulation the ions are distributed in a Gaußian distribution with $\sigma_z = 375\,\mu\mathrm{m}$ and its mean at $z = 0.5\,\mathrm{mm}$. Therefore, the ions have to drift on average 2 cm to reach the grid. In x direction the distribution is not Gaußian and ranges over 1 cm with a Full Width Half Maximum (FWHM) of 4.71 mm.

For all the four signals in Figure 5.4a the electric field in the drift gap is the same ($\mathrm{E_D} = 1000\,\mathrm{V\,cm^{-1}}$), while a different values of $\mathrm{E_{Acc}}$ is used. From the mobility we pass to the simulation $K = 1.77\,\mathrm{cm^2\,V^{-1}\,s^{-1}}$ and the drift distance to the grid $d^{\mathrm{Ions}}_{\mathrm{Drift}} = 2.0\,\mathrm{cm}$ the expected time of arrival at the grid is obtained (Eq. 5.1)

$$t^{\mathrm{Expected}}_{\mathrm{Grid}} = \frac{d^{\mathrm{Ions}}_{\mathrm{Drift}}}{\mathrm{E_D} \cdot K} = \frac{2\,\mathrm{cm}}{1000\,\mathrm{V\,cm^{-1}} \cdot 1.77\,\mathrm{cm^2\,V^{-1}\,s^{-1}}} = 1129.94\,\mu\mathrm{s} \quad . \tag{5.2}$$

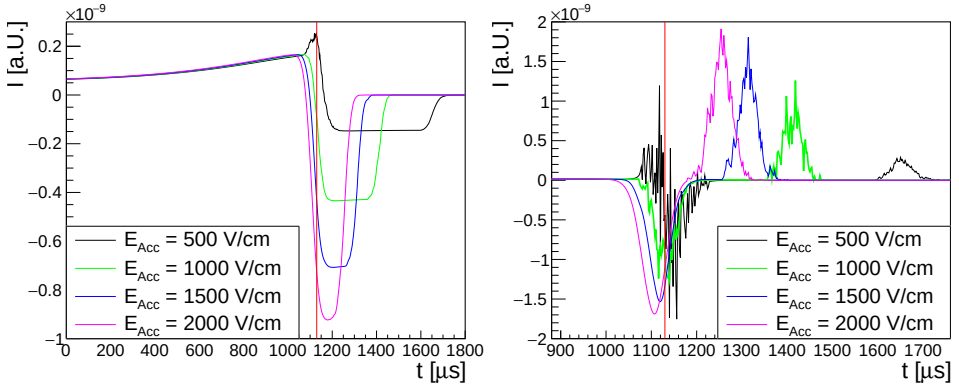

(a) (b)

Figure 5.4: (a) Garfield [94] simulations of the induced ion signal on a wire-grid. The ions drift for 2 cm in an electric field $E_{Drift} = 1\,kV\,cm^{-1}$ into the direction of the grid. The grid is followed by a cathode in a distance of 0.5 cm. The electric field in the gap between the grid and the cathode is E_{Acc}. (b) The derivative of the signals shown in (a). The vertical red line marks the time at which the ions are expected to arrive at the grid. For more details see the text.

This time is marked with a vertical line in both plots in Figure 5.4.

All four signals in Figure 5.4a are very similar for the first $\sim 1000\,\mu s$. Later, the signals change polarity, as the ions pass the grid and eventually the signals are zero, because the ions reach the cathode. The most negative value of the individual signals increases with increasing E_{Acc} and the ions arrive as well faster at the cathode, as expected because of velocity's dependence on the field strength. Furthermore it is visible that the signals have their zero crossing earlier, the higher E_{Acc} is, but none of these zero crossings coincides with the $t_{Grid}^{Expected}$ line. This shows that the zero crossing is not a suitable measure of the time at which ions pass through the grid. The peak in the signal simulated with $E_{Acc} = 500\,V\,cm$, is due to ions ending up on the grid wires. These accelerate in the vicinity of the wires until they are collected by a wire. For higher E_{Acc} this effect is strongly reduced, because no field lines end up any more on the wires of the grid.

The inflection point as measure of t_{Grid}

Calculating the derivative of the signal yields a peak at the inflection points. Figure 5.4b shows a part of each signals' derivative, corresponding to the time range during which the ions reach the grid, pass it and move through the gap between grid and cathode. There is an inflection point during the signals' polarity change. For the $E_{Acc} = E_{Drift} = 1000\,V\,cm^{-1}$ signal, this inflection point occurs at $t_{Grid}^{Expected}$. Therefore the inflection point in the ion signal on the wire-grid is suitable to determine the time t_{Grid} at which ions reach the grid, if the electric field in the gaps before and after the grid is the same.

The peaks in the derivative of the $E_{Acc} = 500\,V\,cm^{-1}$ and $1000\,V\,cm^{-1}$ signal have some spikes, which are not present in case of the other two derivatives. These spikes are created by the irregularities in the corresponding signals, which arise because of the ion collection on the grid wires and the distortion of the ions movement in the vicinity of the grid. In the simulation these spikes are mitigated for more regular induced signals. E.g. if the number of ions in the simulation is increased, these spikes are smoothed out. For the actual measurement we learn from this that a high amount of initial ions is not only needed to create a higher signal amplitude, but helps as well to have a cleaner signal as the ions pass the grid.

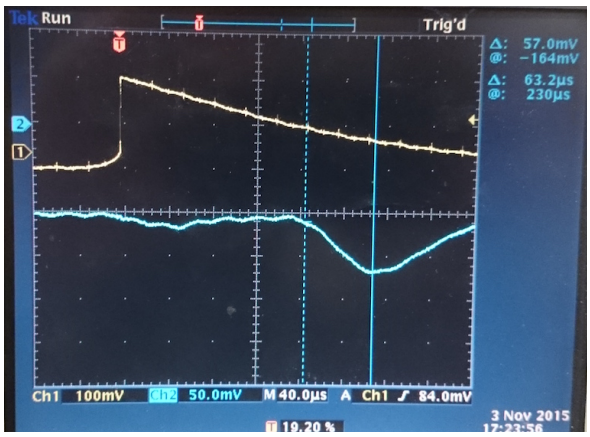

Figure 5.5: Oscilloscope picture of signals originating from the readout plane signal (yellow) and from the GEM1 bottom electrode (blue). This particular picture shows the average of 512 signals recorded at both channels, while each recording is triggered by the signal from the readout plane. There are two peaks in the GEM1 bottom signal, corresponding to ions produced during the gas amplification in GEM2 (left peak) and GEM3 (right peak), respectively.

Different initial distributions of the ions

Using a different initial ion distribution does not change the result that the inflection point is located at $t_{\text{Grid}}^{\text{Expected}}$, as long as the condition $\text{E}_{\text{Acc}} = \text{E}_{\text{Drift}}$ is fulfilled and the drift distance is measured from the spatial centre (in z) of the ion distribution to the grid.[b]

This is because the signal induced by each individual ion at the grid depends on its initial x coordinate and on the x coordinate at which it reaches the grid. If many ions are drifted, their grid signal is a convolution of the ion distributions' z profile with the sum of the different signals which are possible for ions with different coordinate in x.

5.3.2. Defining the start-time of the measurement

In case of the real set-up the $z = 0$ plane of the simulation coincides with the top side of GEM1. The time t_{GEM} therefore needs to equal the time, when half of the ions has passed this GEM and entered the drift gap and the other half is about to do so. This time is estimated based on the signal the ions induce on the GEM1 bottom electrode.

Ion signal on the GEM1 bottom electrode

Step 1) in Figure 5.3 depicts the ions produced during the gas amplification and at step 2) these ions move through GEM1 into the drift gap. The induced signal on GEM1 depends on the amount of ions produced in GEM2 and GEM3 and on the ions' drift through the GEMs and the transfer gaps. Signals from the anode plane (yellow curve) and GEM1 bottom (blue curve) are displayed in Figure 5.5. Electrons (respectively ions) moving towards the anode plane (respectively the GEM1 bottom electrode) induce a negative (respectively positive) charge [124].[c] During the measurement shown in Figure 5.5 the transfer fields in the GEM stack are set to $\sim 100\,\text{V}\,\text{cm}^{-1}$. The peaks in the GEM1 bottom signal correspond to the ions produced in GEM2 and in GEM3. This is confirmed by changing a voltage difference across one of the GEMs or gaps and observing the resulting change of the peak, produced by the ions from GEM3, or the change of both peaks. As the transfer fields are further increased, the peak separation decreases until the peaks eventually merge.

The qualitative arguments to describe the ion signal on the grid are valid for the ion signal

[b] In the section on data analysis (Sec. 5.4) we show the fraction $t_{\text{Grid}}/t_{\text{Grid}}^{\text{Expected}}$ for different K, calculated from simulated signals (Fig. 5.7b). For this test, the simulated signals are treated with the analysis procedure for real data. Therefore this plots are only shown, after this procedure is explained.

[c] Again, because the preamplifiers invert the input signal the opposite signal polarity as expected is observed.

on the GEM1 bottom electrode as well: The rising edge of the signal is due to the ions being accelerated towards GEM1, while the falling edge indicates that ions move either through the GEM holes or are collected by the bottom GEM electrode. Therefore, the time during which the maximal signal amplitude is observed, is the time at which about half of the ions have reached (or passed) the bottom side of GEM1.

Definition of the start-time

However, the goal is to find a measure where half of the ions have passed the GEM1 top electrode. Using the peak of the GEM1 bottom signal introduces an offset of the width of the GEM foil ($\sim 50\,\mu m$), which is about half of the error on d_{Drift}. All ions are subject to the electric field inside the GEM hole, which is high as compared to the drift field $\mathrm{E}_{\mathrm{Drift}}$. With ΔU_{GEM}= 250 V and $K = 1\,\mathrm{cm}^2\,\mathrm{V}^{-1}\,\mathrm{s}^{-1}$ we estimate the additional time, needed for the ions to pass GEM1 to be

$$\begin{aligned}\frac{50\,\mu m}{t} &= \frac{\Delta U_{\mathrm{GEM}}}{50\,\mu m} \cdot K \\ &= 50\,\mathrm{kV\,cm}^{-1} \cdot 1\,\mathrm{cm}^2\,\mathrm{V}^{-1}\,\mathrm{s}^{-1} \\ \Rightarrow t &= 0.1\,\mu s \quad .\end{aligned}$$

Note that this is a rather conservative estimate, given the choice of ΔU_{GEM} and K. Therefore the ions' drift time through the GEM will rather be shorter than longer. The effective drift field in the vicinity of the GEM foil is enhanced by the electric field in the GEM holes, leaking out into the the drift volume (Sec. 3.5.2, Fig. 3.13b). Therefore the ions move faster during the beginning of the drift period in the gap between GEM1 and grid. The magnitude of this effect is hard to estimate, however it affects the overall drift time measurement in the opposite way as the ion drift through the GEM1 holes. The latter (respectively previous) mentioned phenomenon increases (respectively decreases) the overall ion drift time.

Based on all these considerations the start-time of the ions' drift time measurement – t_{GEM} – is chosen to be the time of the highest amplitude in the GEM1 bottom signal. The HV-settings are tuned to have a FWHM of less than 100 µs of the peak indicating the ions movement into the drift gap. To this end, the voltages have to be (re)adjusted for each gas mixture. Example signals are in the right half of Figure 5.3 (*Signal from GEM1 bottom*) and in Figure 5.6d in the next section.

5.4. Signal analysis and measurement uncertainties

The measured signals are overlaid with a regular noise in the form of oscillations in the frequency range between about 40 kHz to about 200 kHz. The peak in the signal of the GEM1 bottom electrode is about a factor 10 larger than the peak-to-peak amplitude of these oscillations, while the amplitude of the ion signal on the grid is about as big as this noise. This is well visible in Figure 5.6, where a measurements of both signals are shown (e.g. Fig. 5.6a). Figure 5.6b shows a zoom of the signals, into the region used to determine t_{GEM}. The frequency of this noise can be seen in this view. Despite these oscillations it is possible to identify the time at which the signal at the GEM1 bottom electrode reaches its highest amplitude. However, the same noise overlaid on the grid signal makes it impossible to extract the inflection point, which indicates the ions are passing the grid. This is due to the fact the oscillating noise dominates the derivative of the signal.

5.4.1. Noise removal

In order to remove this noise two methods are applied at the same time. First, signals from several measurements are averaged as discussed in the following section. In a second step the signals are transformed to the frequency domain via a Fast Fourier Transform (FFT), cuts are applied and then the signals are transformed back. This procedure is discussed later on.

Averaging signals

During a single measurement the signal induced at the grid as well as the signal from the GEM1 bottom electrode are simultaneously recorded. The latter signal is used to trigger the measurement. About 100 of these single measurements are stored and afterwards the arithmetic mean of the amplitude is calculated for each time sample of all the measured grid (respectively GEM1 bottom electrode) signals. Each average amplitude has hence a corresponding time value from the time sample and like this the average signals are constructed from these average amplitude values.

This approach leads to rather big data files of several 100 MByte to GByte, because of the long recording length and the high sampling frequency chosen for the measurements. To save disc space, but to increase the number of signals in the respective average, the oscilloscope is used to calculate average signals and only these averages are stored. The average of 2000 individual measurements (as shown in Fig. 5.6a) is displayed in Figure 5.6c. Comparing the *GEM1 bottom signal* in Figure 5.6a and Figure 5.6c illustrates the reduction of the oscillations, while averaging over several measurements. The *Grid signal* has been scaled up by a factor 100 in the two plots in the lower row of Figure 5.6. The reduction of the periodic noise is visible as well, but the zoomed view in Figure 5.6d reveals, that there is still a remainder of the oscillations overlaid with the signal. This is an artefact of the trigger. A signal is recorded or included in the average if the signal from the GEM1 bottom electrode is more negative than the trigger threshold. It is therefore more likely that a signal exceeds the trigger threshold at the time of a falling amplitude of the oscillation. This leads to a trigger bias with respect to the period of these oscillations, which are in turn still visible in the average of many measurements.

Fast Fourier transform

The oscillations observed on top of a signal as visible in Figure 5.6b (respectively Figure 5.6d) can be removed after a frequency analysis of these signals (respectively of the average of several signals). The signals are Fourier transformed from the time into the frequency domain, a cut on the resulting frequency spectrum is applied and afterwards the remaining spectrum is transformed back into the time domain.

The signals we measure are discrete, therefore, the *discrete Fourier transform* is used. This algorithm transforms data, which is sampled in discrete time samples, from the time domain to the frequency domain. The resulting frequency spectrum is again a discrete one.[d] For this work we rely on the implementation of the Fast Fourier Transform (FFT) into the data analysis framework *Root* [127]. Root in turn interfaces to the *FFTW3* software [128] for calculating the FFT of signals.[e]

In practice, the algorithm treats the full signal as one period of a regular signal with infinite length. A difference in the amplitude value of the first and last sample of the input signal appears to the FFT as a non continuous region in the infinite length signal. In such cases edge effects appear in the first and last time samples of the back-transformed signal. Our measurements are not affected by such edge effects, because the measurement starts (respectively stops) long enough before (respectively after) the induced signal of the ions.

The used FFT algorithm is only based on the number of samples and not as well on the sampling frequency. Therefore the value used for the cut on the frequencies has to be adjusted as different measurements with varying number of samples or a different sampling frequency are analysed. If the highest allowed frequency is chosen to be slightly lower than 10 kHz satisfying results are obtained for the full process of first transforming the signals to the frequency domain, performing a cut on the frequency and transforming the frequency spectrum back to the time domain. In all plots of Figure 5.6 the FFT of the *Grid signal* is drawn as well. Especially the two zoomed plots (Fig. 5.6b and Fig. 5.6d) illustrate that the here described procedure allows to efficiently remove the oscillations on top of the signal.

[d] For more explanations see the book [126]. It focuses on processing of digital signals and covers the discrete Fourier transform and how it is used for the FFT in detail.

[e] For the analysis of the signals induced on the GEM1 bottom electrode and the wire-grid we use Root, version 6.04.02, with FFTW 3.3.4.

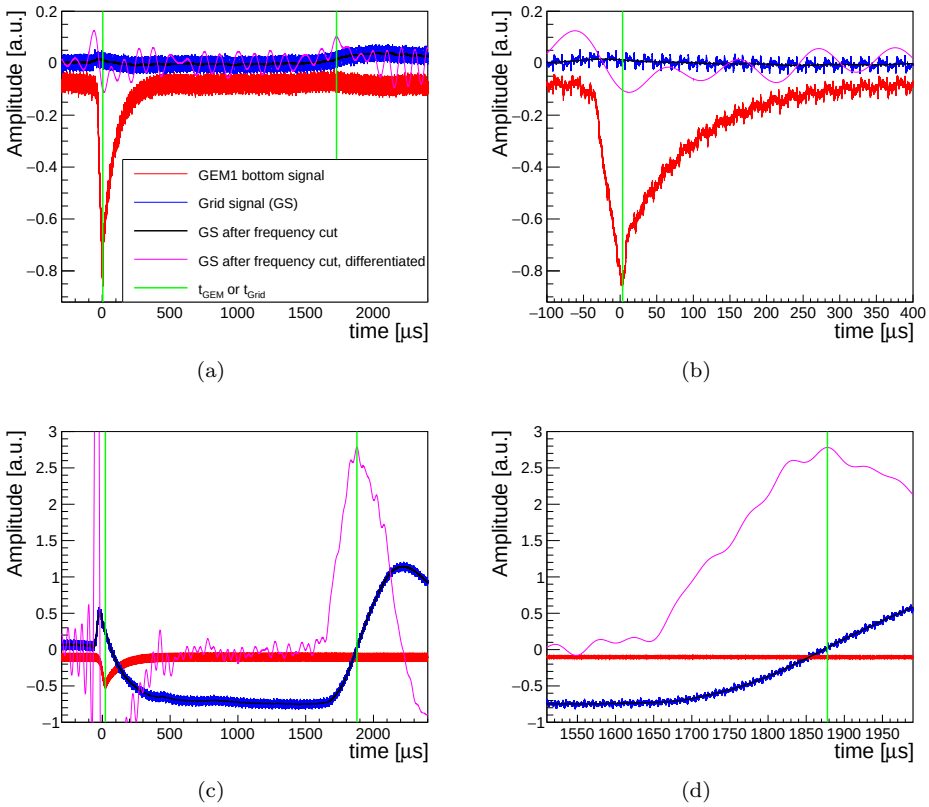

Figure 5.6: (a) A simultaneous measurement of the signal from the bottom side of GEM1 and the wire-grid and (c) the average of 2000 of such measurements. The legend in Figure (a) applies as well to the other three plots. Figure (b) (respectively (d)) shows a zoom of Figure (a) (respectively (c)) into the region used to determine t_{GEM} (respectively t_{Grid}). In the two figures in the lower row the *Grid signal* is scaled up by a factor 100 and is shifted at the vertical axis, to fit the scaled signal again into the plots. All the measurements are done in Ne-CO_2 (90-10), however, the single measurements are not part of the measurements included in the averages. Therefore the gas conditions vary: For Figure (a) (respectively (c)) an atmospheric pressure of 953 mbar (956 mbar), a temperature of 19 °C (21 °C) and a water content of 246 ppm (593 ppm) is present in the detector.

5.4.2. Measurement errors while determining the ions' drift time

Uncertainty of the start-time

As discussed in Section 5.3.2, t_{GEM} is determined as the time, at which the peak in the signal from the GEM1 bottom electrode reaches its most negative amplitude. No correction is applied to this signal beforehand. The (first) vertical line in the Figures 5.6a, 5.6b and 5.6c marks t_{GEM}. A minimum (respectively maximum) of the oscillations peaking close to (respectively at) the actual minimum in the signal induced at the bottom side of GEM1, will lead to a shift of the measured t_{GEM}. This shift can be at most half a period of the oscillations, therefore we take $\delta(t_{\mathrm{GEM}}) = 20\,\mu\mathrm{s}$ as conservative error estimate for the measurement of the ion-drift's start-time.

Uncertainty of the ion's arrival time at the wire-grid

To determine t_{Grid} the derivative of the grid signal after FFT, frequency cut and inverse FFT is calculated. The maximal amplitude in this derivative is identified and thus the inflection point. In the Figures 5.6a, 5.6c and 5.6d the position of this point and its time coordinate t_{Grid} is indicated by the (second) green line.[f]

All the plots in Figure 5.6 show oscillations in the differentiated signals. These are due to remaining oscillations in the *Grid signal* after the removal of the high frequencies. While these oscillations aren't visible by eye, they still affect the derived signal. Furthermore the edge effects in the beginning and the end of the signal affect as well the derivative. The location of the maxima in the derivative's oscillations influence the t_{Grid}, which is found. This can be seen in Figure 5.6a as well as in Figure 5.6d. In the following we analyse the error on the t_{Grid} measurement, which is created by this effect.

First step: Similar to the simulations shown in Figure 5.4, the induced signals on the grid is simulated with Garfield. With respect to the previous simulations changes are made, in order to achieve a better matching between simulated and measured signals: The width of the drift and acceleration gap is increased in the simulation to corresponds to the respective gap widths in the experimental set-up. Furthermore a mesh is used as final cathode after the grid and the initial ion distribution is smeared out as compared to the previous simulations. The way of this smearing is varied and as well different initial distributions are used, to check if the initial distribution has an effect on the arrival time of the ions at the grid. Signals are simulated for different values of the ion mobility K_{Sim}.

Second step: Then sinusoidal oscillations with a frequency of 50 kHz are laid over the simulated signals. In addition, each amplitude value is summed with a random value in the range of $\pm 10\,\%$ from the peak-to-peak amplitude of the sinus. An example is the *Signal* in Figure 5.7a.

Third step: These signals are feed into the data analysis procedure. Like the measured signals at the wire-grid, the simulated signals are transformed to the frequency space, the high frequencies are removed starting from a given threshold and afterwards the remaining signals is transformed back. To test dependence of the oscillations in the derived signal on the actual threshold used for the frequency cut, the cut threshold is varied between 4 kHz and 14 kHz in 2 kHz steps. Between 8 kHz and 10 kHz finer steps of 0.4 kHz are used, because this is the range for the typical cut threshold applied in the actual data analysis. For each of the simulated signals with different K_{Sim}, each cut threshold is applied.

Fourth step: The time coordinate of inflection point t_{Grid} is determined in the derivative of the signals after each frequency cut. We compare these times to the theoretical arrival time of the ions at the grid ($t_{\mathrm{Grid}}^{\mathrm{Expected}}$), which we calculate from K_{Sim}, the drift distance and

[f] A similar $\Delta t = t_{\mathrm{Grid}} - t_{\mathrm{GEM}}$ of 1724 µs and 1856 µs is found for the single measurement and the average of 2000 measurements, respectively. The agreement in about 8 % between the two values is remarkable, given the visible oscillations in the derivative of the grid signal after the frequency cut (Fig. 5.6a).

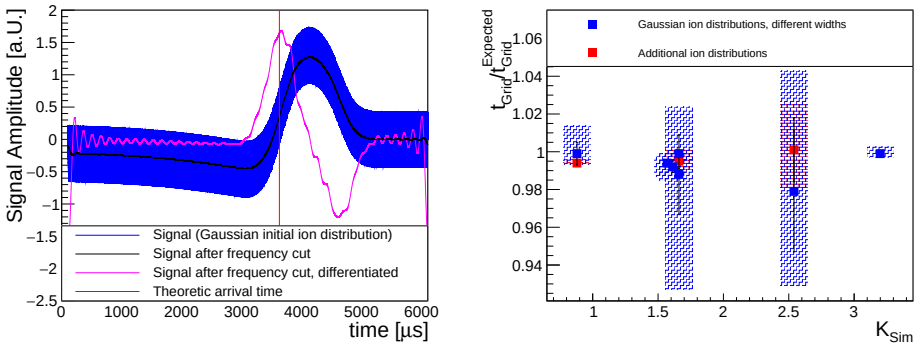

(a) (b)

Figure 5.7: With Garfield [94] the signal induced by ions, which pass a wire-grid, at this wire-grid are simulated. This signal is overlaid with a periodic noise, similar to the noise observed in the measurements. The same analysis procedure is applied to the thus modified simulation, as is used for signals induced at the grid in our detector. In Figure (a) the simulation with the overlaid noise as well as different analysis steps are displayed. For more details see the four steps in the surrounding text. Signal simulations, as shown in Figure (a), are done for varying initial ion distribution, K_{Sim} and threshold frequency of the frequency cut during the signal analysis procedure. The time at which the ions pass the wire-grid is extracted from these signals (t_{Grid}) and compared to the value expected from the input parameters of the simulation ($t_{\mathrm{Grid}}^{\mathrm{Expected}}$). Figure (b) shows the result as function of K_{Sim}. The vertical bands show the full range of different t_{Grid} extracted for different frequency threshold, while the average (respectively standard deviation) of the corresponding t_{Grid} values is marked by a square (respectively the error bars).

the drift field in the simulation (Eq. (5.2)). Figure 5.7a shows this comparison on base of one event. In this example the $t_{\text{Grid}}^{\text{Expected}}$, indicated as *Theoretical arrival time*, is slightly lower than the t_{Grid} found.

Results: While comparing the derivative of signals for different threshold of the frequency-cut we observe that the frequency (or frequencies) of the derivative's oscillations depends on the threshold value. This in turn changes the t_{Grid} extracted from the derivative. The vertical bands in Figure 5.7b corresponds to the range of all the t_{Grid} found for the different combinations of K_{Sim} and initial ion distribution. The three bands with a range in $t_{\text{Grid}}/t_{\text{Grid}}^{\text{Expected}}$ larger than 2 % correspond to the simulations with the largest z width of the initial ion distribution. Looking at the different average $t_{\text{Grid}}/t_{\text{Grid}}^{\text{Expected}}$ and their standard deviations, no dependence on K_{Sim} can be observed. In the experimental set-up the width of the initial ion distribution is controlled by the HV settings of the GEM stack, where we chose settings to keep the width low.

Based on this test we conclude that the relative error of our method to determine t_{Grid} is not larger than $\pm 2\,\%$. The error on t_{Grid} is hence $\delta(t_{\text{Grid}}) = 0.02 \cdot t_{\text{Grid}}$.

Full drift time error

The drift time is defined as $\Delta t = t_{\text{Grid}} - t_{\text{GEM}}$. Gaußian error propagation is used to calculate the error on the full drift time

$$\begin{aligned} \delta(\Delta t) &= \sqrt{\delta(t_{\text{Grid}})^2 + \delta(t_{\text{GEM}})^2} \\ &= \sqrt{(0.02 \cdot t_{\text{Grid}})^2 + (20\,\mu\text{s})^2} \quad . \end{aligned} \tag{5.3}$$

5.4.3. Other error sources

Equation (5.1) is the formula to calculate the ion mobility from the measured parameters. Its second row reads

$$K = \frac{(d_{\text{Drift}})^2}{\Delta t \cdot \Delta U_{\text{Drift}}} \quad .$$

In addition to the uncertainty of Δt, the uncertainty of the drift length and of the voltage difference across the drift gap need to be considered.

The uncertainty on each set voltage is $\delta(U_{\text{Set}}) = 2\,\text{V}$. Therefore the full uncertainty on the voltage difference across the drift gap is

$$\delta(\Delta U_{\text{Drift}}) = \sqrt{\delta(U_{\text{GEM1 Top}})^2 + \delta(U_{\text{Grid}})^2} = \sqrt{2} \cdot 2\,\text{V} \quad . \tag{5.4}$$

For several measurements without changing the voltage in-between, this uncertainty is fully correlated among these measurements. However, the mobility is always measured for different E_{Drift} and therefore different voltage settings.[g]

The error on the drift length is a special case, as it is the precision of the measurement of the drift gap's width. Because this gap stays constant between measurements, $\delta(d_{\text{Drift}})$ is a systematic uncertainty, which is fully correlated among all the measurements with the same d_{Drift}. The drift length is defined by spacers, defining the width between the grid-frame and the GEM1-frame, and by the frame widths themselves. All these could be precisely measured, resulting in an uncertainty of $\delta(d_{\text{Drift}}) = 0.12\,\text{mm}$ (respectively $\delta(d_{\text{Drift}}) = 0.09\,\text{mm}$) for the 21.35 mm (respectively 25.31 mm) drift gap.

We need to correct the mobility for the ambient pressure p_{Meas} and the temperature T_{Meas}, to give a result independent of the pressure and temperature present during the measurement (see Sec. 3.1.1). The related statistical errors are $\delta(p) = 1\,\text{mbar}$ and $\delta(T) = 0.5\,\text{K}$.

[g] We will comment more on the measurements of K as function of E_{Drift} in Section 5.5.1.

5.5. Results

For a given gas mixture, the induced signals at the GEM1 bottom electrode and at the wire grid are simultaneously recorded for various field settings. We average the signal from the grid as well as the signal from GEM1B over 2000 (or 3000) subsequent events for each field setting. The ions' drift time is extracted as explained in Section 5.4 and the ion mobility $K(\mathrm{E_{Drift}})$ is calculated (Eq. (5.1)), from this drift time. During each measurement the temperature (T_{Meas}) and atmospheric pressure (p_{Meas}) is recorded. These values are used to calculate the reduced mobility K_0. To this end we use a density correction to the gas density at 273.15 K and 1013 mbar as it is common in the literature (e.g. [68, 70]).

$$K_0 = K \times \frac{273.15\,\mathrm{K}}{T_{\mathrm{Meas}}} \times \frac{P_{\mathrm{Meas}}}{1013\,\mathrm{mbar}} \tag{5.5}$$

5.5.1. Mobility as function of the drift field

Figure 5.8 shows $1/K_0^{\mathrm{Mix}}(\mathrm{E_{Drift}})$ measurements for different Ar-CO_2 and Ne-CO_2 mixtures. The drift field varies in a range of several 100 V cm^{-1} for every mixture. Overall, the minimal and maximal drift field used are 200 V cm^{-1} and 1100 V cm^{-1}, respectively.

In this range of $\mathrm{E_{Drift}}$, the (reduced) ion mobility of each mixture can be described in its error-bars by a constant. A constant mobility corresponds to the expected behaviour for low electric fields, because otherwise the mobility should change with the electric field and approach a $K \sim 1/\sqrt{E}$ behaviour for a high drift field (Sec. 3.1.1, Equations (3.7) and (3.8)). The value of the electric field is considered as low, if the energy, gained by an ion from the field, is much smaller than the thermal energy. This is expressed by the relation

$$\left(\frac{m_1}{m_2} + \frac{m_2}{m1}\right) e\mathrm{E}l \ll kT \tag{5.6}$$

as mentioned in [68]. The masses m_1 and m_2 have to be chosen according to the masses of the ion and its collision partner and l is the mean free path between collisions. To estimate if this condition is fulfilled during our measurements we chose $l = 100$ nm and E = 1000 V.[h]

$$\begin{gathered}\left(\frac{m_1}{m_2} + \frac{m_2}{m1}\right) \cdot e \cdot 1000\,\mathrm{V\,cm^{-1}} \cdot 100\,\mathrm{nm} \ll 8.6173 \times 10^{-5}\,\mathrm{eV\,K} \cdot 273.15\,\mathrm{K} \\ \left(\frac{m_1}{m_2} + \frac{m_2}{m1}\right) \cdot 0.01 \ll 0.0235\end{gathered} \tag{5.7}$$

In [77] it is shown that the amount of Ar (respectively Ne) and CO_2 ions, which is produced during the gas amplification, corresponds to the fraction the two individual gases have in the gas mixture. However, as discussed in Section 3.2.1, the ions of the inert gas transfer their charge in a few a ns time to a CO_2 molecule. Furthermore, at our p and T it is likely that cluster ions from around the CO_2 ions [77, 78]. Considering the masses of argon atoms and carbon-dioxide molecules the factor with the masses in Equation (5.7) will be ~ 2 for any choice of m_1 and m_2. For the case of CO_2 molecules colliding with Ne the factor is ~ 2.6. Considering cluster ions would result in an even larger $(m_1 m_2^{-1} + m_2 m_1^{-1})$. Therefore, the inequality in Equation (5.6) is not fulfilled. At our gas conditions the energy the ions gain from the electric field is rather on the order of the thermal energy and not much smaller then kT.

As illustrated by the measurements displayed in Figure 3.2, there is a two orders of magnitude difference between the electric field range with constant mobility and such fields where $K_0(\mathrm{E}) \sim 1/\sqrt{\mathrm{E}}$. Extrapolating these measurements to the pressure at which our measurements are done, yields an electric field strength on the order of several 100 V cm^{-1} at which the transition from constant ion mobility to an E dependent mobility starts. Although we measure the drift of different ions, the energy the ions gain from the field are comparable

[h] At $p = 1013$ mbar and $T = 273.15$ K the mean free path between collisions is 39.5 nm, 63.2 nm and 125 nm for pure CO_2, Ar and Ne, respectively [129].

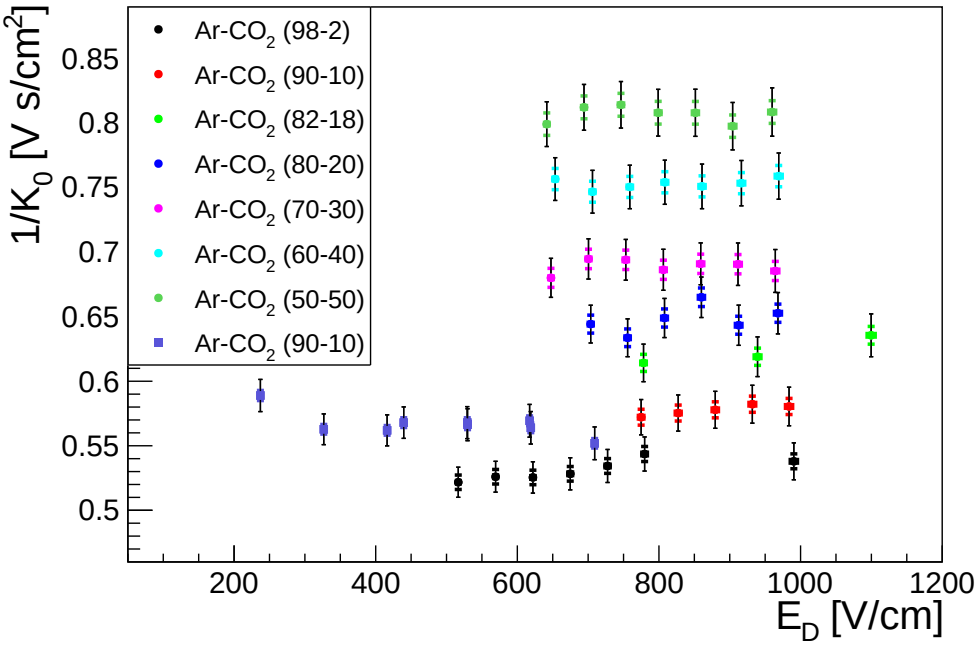

(a) Ar-CO_2 mixtures

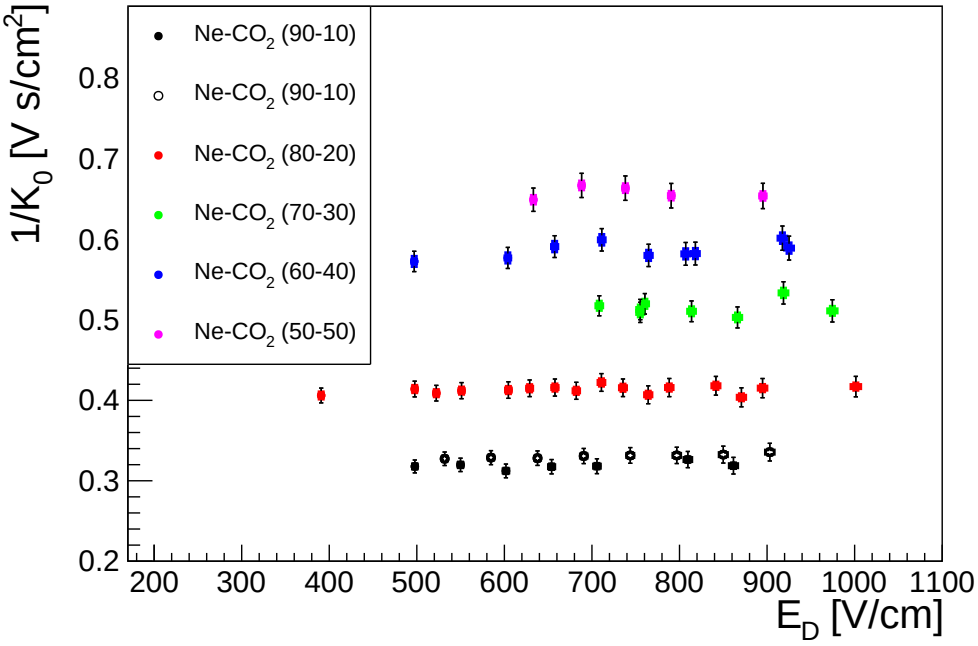

(b) Ne-CO_2 mixtures

Figure 5.8: For different Ar-CO_2 (respectively Ne-CO_2) mixtures the inverse reduced ion mobility is shown. All the points depicted as circles (respectively squares) are measured with a drift length of 21.35 mm (respectively 25.31 mm). The water content varies between different measurements, however all points are in the range given by 34 ppm $< H_2O <$ 98 ppm (respectively 120 ppm $< H_2O <$ 180 ppm) for the Ar-CO_2 (respectively Ne-CO_2) mixtures. There is one exception: The open Ne-CO_2 (90-10) points are recorded with a water content between 40 ppm and 60 ppm. In Section 5.5.4 the effect of water on the mobility will be discussed. The coloured error-bar represents the error due to the drift length uncertainty, while the black error bar represents the combined error of all other sources. As for K_0, E_{Drift} has been as well corrected to $E_{Drift} = E_{Drift\ applied} \cdot 1013\,mbar \cdot p_{Meas}^{-1} \cdot T_{Meas} \cdot (273.15\,K)^{-1}$

between our and their measurement. Therefore, the observed constant $K_0^{\mathrm{Mix}}(\mathrm{E_{Drift}})$ are sensible.

5.5.2. Blanc's law for the Ar-CO_2 and Ne-CO_2 mixtures

Because we found the reduced mobilities measured constant for different $\mathrm{E_{Drift}}$, we average individual measurements, using the weighted mean

$$K_0^{\mathrm{Mix}} = \frac{\sum_{\mathrm{E}} K_0^{\mathrm{Mix}}(\mathrm{E}) \cdot w(\mathrm{E})}{w(\mathrm{E})}$$
$$\text{with : } \; w(\mathrm{E}) = \frac{1}{\delta\left(K_0^{\mathrm{Mix}}(\mathrm{E})\right)^2} \quad .$$

The error of the mean mobility is calculated by the corresponding error of the weighted mean:

$$\delta\left(K_0^{\mathrm{Mix}}\right) = \frac{\sqrt{\sum_{\mathrm{E}} w(\mathrm{E})^2 \cdot \delta\left(K_0^{\mathrm{Mix}}(\mathrm{E})\right)^2}}{\sum_{\mathrm{E}} w(\mathrm{E})} = \frac{1}{\sqrt{\sum_{\mathrm{E}} \delta\left(K_0^{\mathrm{Mix}}(\mathrm{E})\right)^{-2}}}$$

The electric field E indicates that the different $K_0^{\mathrm{Mix}}(\mathrm{E})$ (respectively $\delta(K_0^{\mathrm{Mix}}(\mathrm{E}))$) are measured at different drift field and it serves at the same time as summation index in these equations. The $\delta(K_0^{\mathrm{Mix}}(\mathrm{E}))$ for each measured mobility is calculated from the individual uncertainties discussed in Sections 5.4.2 and 5.4.3. For all the statistical errors we use Gaußian error propagation. The drift length error is added in quadrature to the final $\delta\left(K_0^{\mathrm{Mix}}\right)$. Like this we obtain one $1/K_{0\ \mathrm{Mix}}$ and its uncertainty for each gas mixture, which is displayed in Figure 5.8. All points in Figure 5.9a (respectively 5.9b) correspond to a measurement series of an Ar-CO_2 (respectively Ne-CO_2) mixture in Figure 5.8a (respectively 5.8b). However, the Ne-CO_2 (90-10) points for low water content are not used in order to have less than 100 ppm difference in the water content among all points in each plot of Figure 5.9. See Section 5.5.4 for measurements of the water's influence on the ion mobility.

In the Ar-CO_2 and the Ne-CO_2 mixtures, only CO_2 ions or cluster ions based around CO_2 should drift, as calculated in [77]. Therefore we assume that in both gas mixtures only one ion species is drifting. This enables us to use Blanc's law [69] (Eq. (3.9), Sec. 3.1.1) to extract the mobility of these ions in pure argon (respectively neon) and pure carbon-dioxide. To this end we fit

$$\frac{1}{K_0^{\mathrm{Mix}}} = a + f_{\mathrm{CO_2}}\,(b - a) \tag{5.8}$$

to our measured $1/K_0$ in each plot of Figure 5.9. The parameter a and b correspond to $1/K_0^{\mathrm{Ar}}$ (respectively $1/K_0^{\mathrm{Ne}}$) and $K_0^{\mathrm{CO_2}}$, respectively, while $f_{\mathrm{CO_2}}$ is the CO_2 fraction in the mixture. In Table 5.1 the fit results are shown. The function in Equation (5.8) describes the data well. We find a χ^2/N_{DF} of 1.65 and 4.62 for the fit to the $1/K_0^{\mathrm{Mix}}$ points of the Ar-CO_2 and Ne-CO_2 mixtures, respectively.[i] For the argon- as well as the neon-based gas mixtures the $K_0^{\mathrm{CO_2}}$ values agree within their error bars. This confirms that in both mixtures the same (cluster) ion species drifts. Our gas mixtures have a water content on the order of 100 ppm, therefore it is likely that the migrating ions in these mixture are cluster ions $CO_2^+(CO_2)_n$ ($n \sim 5$), to which water ions attach themselves [77]. We choose running at this water content, because the gas mixture in the ALICE TPC has a water content of 100 ppm.

Comparison to literature

In order to check if our method to measure the mobility is sensible, we compare our results to existing measurements. The $1/K_0$ measurements with Ar-CO_2 (squares in Fig. 5.9a) agree

[i] N_{DF} stands for the number of the degrees of freedom of the fit.

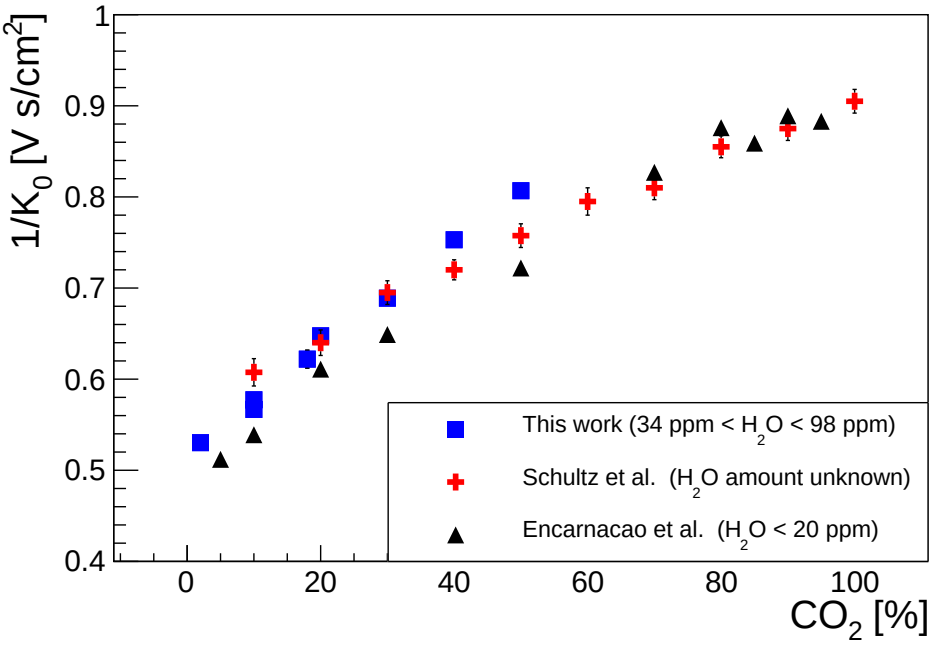

(a) Different CO_2 content in Ar-CO_2

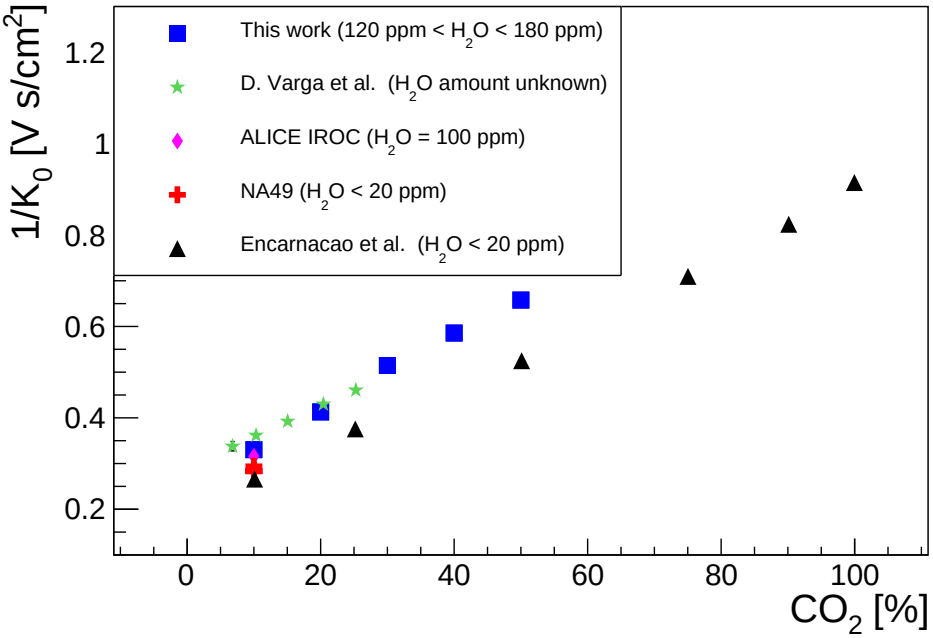

(b) Different CO_2 content in Ne-CO_2

Figure 5.9: Each $1/K_0$ point corresponds to the average over all the points measured for the respective gas mixture. All ion mobilities for the different Ar-CO_2 mixtures (a) (respectively Ne-CO_2 mixtures (b)) result from the corresponding measurements in Figure 5.8a (respectively 5.8b). For comparison, results from other groups are shown. The *Schultz et al.* points are extracted from [130], the *Encarnação et al.* points from [131] (Ar-CO_2) and [77] (Ne-CO_2). From the later paper the *NA41* and *ALICE IROC* points are extracted as well. The *D. Varga et al.* points have been previously shown in [132]. Both plots have been shown in [133].

	Ar	CO_2
K_0	$(1.94 \pm 0.01)\,\mathrm{cm^2\,V^{-1}\,s^{-1}}$	$(1.10 \pm 0.01)\,\mathrm{cm^2\,V^{-1}\,s^{-1}}$

	Ne	CO_2
K_0	$(4.06 \pm 0.07)\,\mathrm{cm^2\,V^{-1}\,s^{-1}}$	$(1.09 \pm 0.01)\,\mathrm{cm^2\,V^{-1}\,s^{-1}}$

Table 5.1.: A linear fit according to Equation (5.8) has been performed to our measurements shown in Figures 5.9a and 5.9b. The tabulated values are the results of this fits. According to Blanc's law [69] (Eq. (3.9), Sec. 3.1.1) the reduced ion mobilities here, are the mobilities in pure argon, neon and carbon-dioxide for the ion species drifting in the Ar-CO_2 and Ne-CO_2 mixtures used in the measurements.

well with the results of Schultz *et al.* [130] (crosses in the same figure) for a carbon-dioxide fraction of 20-30 %. Their measurements are done at a pressure and temperature comparable to our measurements. However, the slope differs, which describes $1/K_0$ as function of the CO_2 content. They find a $K_0^{CO_2}$ and a K_0^{Ar} which is 20 % higher and 10 % lower, respectively, as our results in Table 5.1. Because our two results of $K_0^{CO_2}$ are measured independently and agree well with each other, we think that the discrepancy is not due to a measurement error, but it may be due to the different amount of water in their and our set-up. As compared to the results from Encarnação *et al.* [131] (triangles in Fig. 5.9a), K_0 seems to be under-estimated. These measurements are taken at much lower water content and at a pressure between 8 mbar and 13 mbar. At this pressure the formation of cluster ions is expected to differ, therefore mobility measurements at our gas conditions and theirs are not expected to have the exact same result [134].

With Ne-CO_2 mixtures a similar difference between our results (squares in Fig. 5.9b) and the results of Encarnação *et al.* [77] (triangles in the same figure) is observed. This can be attributed as well to the different pressure in our and their measurements. Measurements by D. Varga *et al.* [132] (stars in Fig. 5.9b) agree well with our measurement at Ne-CO_2 (80-20). They measure at a similar pressure and temperature as compared to our measurements. The remaining difference may be due to a different water content of the gas. For Ne-CO_2 (90-10) there are two more measurements in the paper [77]: Two points from NA49 (crosses) and one point from an ALICE IROC (diamond). These points are based on an analysis of signals, which are induced by ions drifting through the wire planes of a readout chamber of the NA49 and ALICE TPC, respectively. With both readout chambers a higher ion mobility is found, as for our measurements with the Ne-CO_2 (90-10) mixture. Partially the water content will be responsible for this difference. However, the methods to measure the ion mobility differ significantly and there may be an so far not known error source in our or their measurements.

Conclusions

Overall, the comparison of our measurements to existing measurements shows that our method to determine the ion mobility works well. We measure ion mobilities at a regime of temperature, pressure and electric field at which TPCs are usually operated at. In case of the different Ar-CO_2 mixtures existing results are reproduced, while for the Ne-CO_2 mixtures we reproduce existing results and we provide ion mobilities for mixtures with higher CO_2 content, which have not been measured before.

5.5.3. Admixture of N_2 to Ne-CO_2 mixtures

The gas mixture which will be used for the upgraded ALICE TPC is Ne-CO_2-N_2 (90-10-5) [23]. This mixture has been used previously in the ALICE TPC and is used currently (2017) as well. Adding N_2 to Ne-CO_2 (90-10) improves the gain stability of the current TPC's wire chambers as compared to pure Ne-CO_2 (90-10) [11]. However, no systematic study of the ion mobility for this mixture existed so far. We perform such measurements and analyse them, as done for the other measurements presented in this section.

In Figure 5.10a we show several $1/K_0^{Mix}(E_{Drift})$ for different amounts of nitrogen and

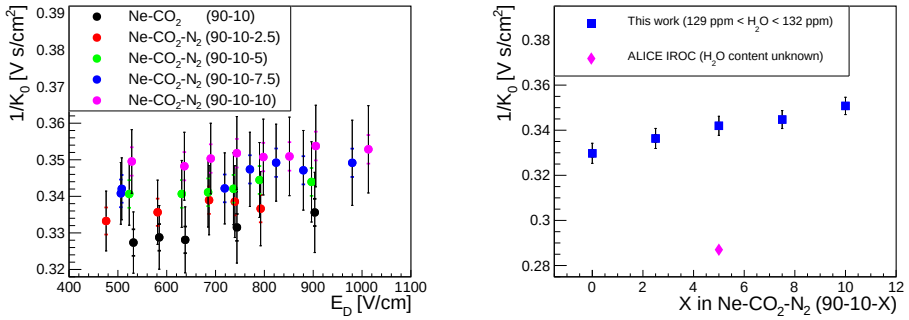

(a) (b)

Figure 5.10: Measurements of $1/K_0$ for different amount of N_2 admixtures to a Ne-CO_2 (90-10) gas mixture. Figure (a) shows one over the reduced mobility for different E_{Drift} for different Ne-CO_2-N_2 mixtures. As in the similar plots in Figure 5.8, the set E_{Drift} has been corrected to its value 1013 mbar and 273.15 K. Also, the same convention for the error bars as in that figure is used here. The points in Figure (b) correspond to the average of each of these measurement series. Furthermore one point from [77] (*ALICE IROC*) is shown, however, the water content is not indicated for this measurement. Most likely it is $H_2O < 20$ ppm.

values of the drift field between $400\,\mathrm{V\,cm^{-1}}$ and $1100\,\mathrm{V\,cm^{-1}}$. Adding nitrogen reduces the ion mobility slightly as checking e.g. the results for Ne-CO_2-N_2 (90-10-10) against measurements with Ne-CO_2 (90-10). However, this change is only a bit larger than our measurement precision.[j]

Nevertheless, we average the $1/K_0^{Mix}(E_{Drift})$ to obtain the reduced mobility for each gas mixture as explained in Section 5.5.2. In Figure 5.10b the resulting plot is shown. The trend of decreasing K_0^{Mix} with increasing N_2 content can be clearly seen. Nitrogen has a higher ionisation energy than neon or carbon-dioxide, as well as water or Oxygen [135]. Therefore it is likely that the same (cluster) ions drift, as in the Ne-CO_2 mixtures examined before. In [77] it is as well assumed that cluster ions, which form around CO_2^+, drift in a Ne-CO_2-N_2 (90-10-5) mixture.

While fitting Blanc's law as in Equation (5.8) to the data, a sensible result is only obtained if either the reduced mobility of the drifting ions in pure Ne or CO_2 is fixed to the value in Table 5.1. Therefore the fit function has only two free parameters. The fit result yields $K_0^{N_2} = (1.8 \pm 0.2)\,\mathrm{cm^2\,V^{-1}\,s^{-1}}$. The other free parameter – either K_0^{Ne} or $K_0^{CO_2}$ – is found to be about 8 % lower than the reduced mobility previously found and listed in Table 5.1. Therefore the $K_0^{N_2}$ and its uncertainty may deviate from the actual mobility, which the ions drifting in Ne-CO_2-N_2 mixtures would have in pure N_2.

Except for the *ALICE IROC* point in Figure 5.10b, which has been extracted from [77] there are no measurements of the ion mobility with Ne-CO_2-N_2 mixtures. The difference between their point and our point may be due to the different water content or due to the different experimental method used by us and them. As for the *ALICE IROC* point in Figure 5.9b, they obtain the ion mobility from the ion tail of signals induced during the gas amplification in a wire chamber. Therefore they need to extract the ion mobility from the ion drift over a short distance in a non-homogeneous electric field. In [136] ion mobility is measured for nitrogen based cluster ions in Ne-N_2 at a pressure between 8 mbar and 11 mbar and a water content smaller than 20 ppm. Their measured mobility in Ne-N_2 (90-15) is about a factor two higher than our K_0 measured in Ne-CO_2-N_2 (90-10-5).[k] The

[j] We measured as well Ne-CO_2-N_2 (90-10-15) and (90-10-29). However, these measurement are not included in Figure 5.10, because their water content differs significantly. Therefore no strong conclusion about the effect of nitrogen can be drawn from these measurements. See as well Section 5.5.4.

[k] The ion mobility they find for Ne-N_2 (95-5) is higher.

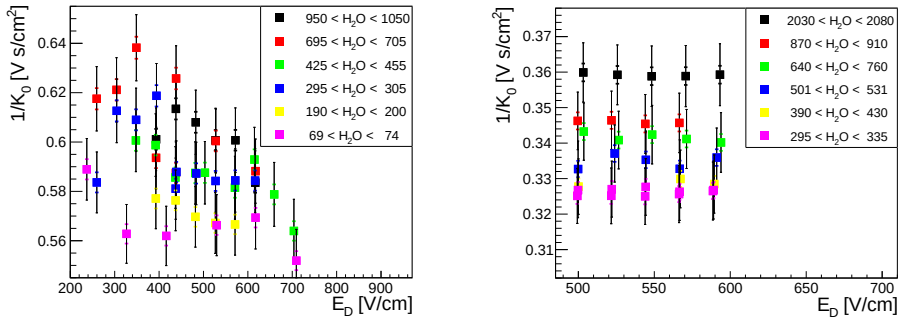

(a) Ar-CO_2 (90-10) (b) Ne-CO_2 (90-10)

Figure 5.11: The reduced ion mobility for varying water content in the gas. As for the other plots of the reduced ion mobility as function of the drift field (Fig. 5.8 and Fig. 5.10a), the set E_{Drift} is corrected to its value 1013 mbar and 273.15 K and the same convention for the error bars as in these similar figures applies here.

difference is due to the fact that a different (cluster) ion moves in the mixture without CO_2.[1] Indirectly, we can conclude from these measurements in [136], that despite the addition of N_2 to the Ne-CO_2 mixture, the drifting ions are still CO_2^+ ions, or corresponding cluster ions. Otherwise a more drastic change from Ne-CO_2 (90-10) to a Ne-CO_2-N_2 is expected and then a change of ion mobility with increasing nitrogen content.

Conclusions

Adding nitrogen to a Ne-CO_2 (90-10) gas mixture reduces the (reduced) ion mobility of the resulting mixture as compared to the mixture without N_2. The effect is however not big: Changing from 0 % nitrogen to 9 % nitrogen, results in a reduction of K_0^{Mix} of about 6 %. For the drifting ions in Ne-CO_2-N_2 (90-10-X) mixtures we find a preliminary value of $K_0^{N_2} = (1.8 \pm 0.2)\,\mathrm{cm^2\,V^{-1}\,s^{-1}}$, where $K_0^{N_2}$ is the reduced mobility of these ions in pure nitrogen.

The reduced ion mobility of the baseline gas mixture for the future ALICE TPC Ne-CO_2-N_2 (90-10-5) is $(2.92 \pm 0.04)\,\mathrm{cm^2\,V^{-1}\,s^{-1}}$, measured at a water content of (130 ± 1) ppm.

5.5.4. Traces of H_2O in Ne-CO_2 (90-10) and Ar-CO_2 (90-10)

One difference of our measurements to the measurements of other groups is the water content in the gas. Our goal has been to measure the ion mobility in the baseline gas mixture for the future ALICE TPC, therefore most of our measurements are done with a water content around 100 ppm, give or take a few 10 ppm. In order to study the effect of traces of H_2O on the (reduced) ion mobility, the water content in Ar-CO_2 (90-10) (respectively Ne-CO_2 (90-10)) has been increased from about 70 ppm to about 1000 ppm (respectively from $\sim$ 320 ppm to $\sim$ 2050 ppm). In Figure 5.12 the corresponding plots are displayed.

From the measurements done in Ar-CO_2 (90-10) (Fig. 5.11a) no conclusion about the effect of water admixtures can be made. It is visible that there is a change in $1/K_0^{\mathrm{Mix+H_2O}}(\mathrm{E})$ for different water content, but this change is on the order of the measurement precision. The points in the figure are a compilation of several measurements, partially with a large time between subsequent measurements. In case of the Ne-CO_2 (90-10) (Fig. 5.11b) measurements, all measurements are done directly after each other in order to minimise other changes in the gas conditions. Also in this case the change of the reduced mobility for different H_2O content is on the order of the measurement precision. However, in this case a clear decrease of $K_0^{\mathrm{Mix+H_2O}}(\mathrm{E})$ with increasing water content can be seen.

The weighted mean of each measurement series is again calculated and the correspond-

[1] We expect as well an effect of the different gas conditions in our and their measurements. This effect should be similar to the difference observed while checking our measurements in Ne-CO_2 mixtures against their results. (Both in Fig. 5.9b.)

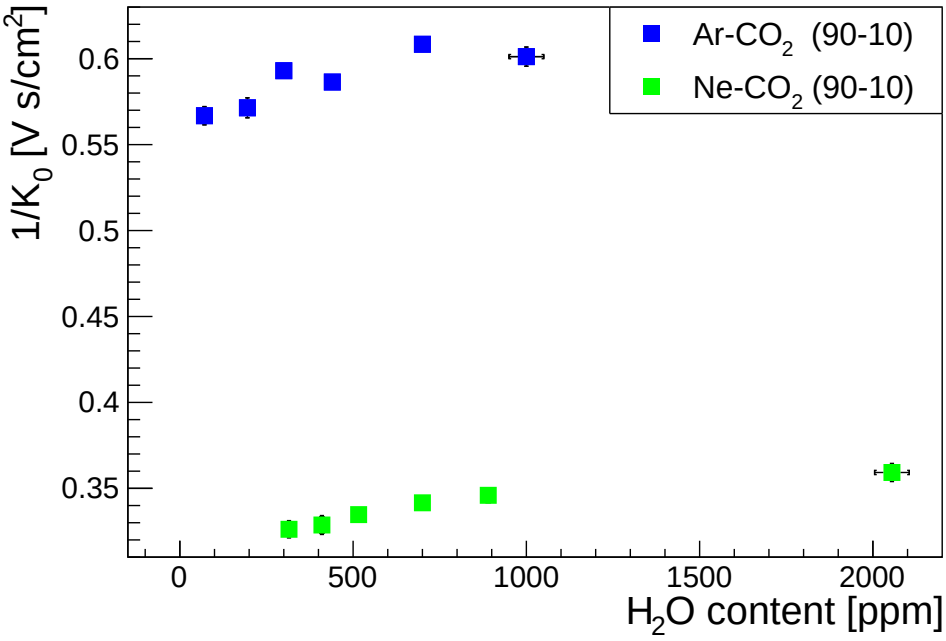

Figure 5.12: The weighted mean of the data series in Figure 5.11a (respectively Fig. 5.11b) showing the change in mobility for varying water content in Ar-CO_2 (90-10) (respectively Ne-CO_2 (90-10)). The horizontal error-bars do not represent an uncertainty, but indicate the range over which the water content is varied.

ing points are displayed in Figure 5.12. For the Ar-CO_2 (90-10) mixture a decrease of $K_0^{\mathrm{Mix+H_2O}}$ between 5.5 % to 7 % is found as the water content is increased from about 72 ppm to 1000 ppm. In case of Ne-CO_2 (90-10) a clearer trend can be identified: While increasing the water content in the mixture from 365 ppm to 900 ppm the (reduced) mobility decreases by 5.8 %. Only one measurement series with even higher water content (2200 ppm) has been done. It seems that the decrease of mobility with increasing water content is more prominent at lower water content.

The fact that we observe a clearer trend in the neon-based gas mixture might be as well to the fact that Ne-CO_2 mixtures are faster mixtures than Ar-CO_2 mixtures, with respect to the ion mobility. Therefore the impact of the H_2O molecules is more drastic in the Ne-CO_2 case. A follow up study could examine the low water content behaviour – e.g. the change from zero water content to a few ppm. This should help to understand the effect of the water on the mobility better. This we couldn't examine, because our detector is not tight enough to rule out completely that humidity from the air diffuses into the counting gas.

5.6. Summary

A set-up to measure the mobility of ions was commissioned successfully. The drift time of ions through the drift gap was measured using two simultaneous recorded signals. One signal recorded at the bottom side of GEM1 provided the start-time of the ion drift. In order to determine the time of arrival of the ions at a wire grid, defining the end of the drift volume, we developed a novel method. We recorded the induced signal over the full drift time of the ions and used an inflection point in this signal to extract the ions' arrival time at the grid. From these two time values the drift time and thus the mobility was calculated. This was done for different gas mixtures and for each gas mixture different drift fields were examined. The effect of water admixtures was examined as well.

Our measurements were done at drift fields on the order of several 100 V and at atmospheric pressure and room temperature. These settings are typical for TPCs. Furthermore, the water content of the gas mixtures during our measurements was around 100 ppm as it is

foreseen for the upgraded ALICE TPC. We found the ion mobility to be compatible with a constant for the examined range of E/p. The mobility of CO_2 ions (or cluster ions formed around CO_2^+) in Ar was found to be consistent with previous publications at similar gas conditions [130]. Compared to measurements done by Encarnação *et al.*, the measured K_0 of CO_2^+ in Ar [131] (respectively Ne) was up to 10 % (20 %) lower. However, the Encarnação *et al.* measurements were done at a very low pressure of about 10 mbar, at which the clustering reactions and hence the drifting ion is expected to differ as compared to our measurements. Other, existing measurements of Ne-CO_2 mixtures at ambient pressure agree better [77, 132] and were extended to higher carbon-dioxide content during our measurements.

From fits of Blanc's law to our Ar-CO_2 data we found the reduced mobility of the drifting (cluster) ion in pure argon to be $(1.94 \pm 0.01)\,\mathrm{cm^2\,V^{-1}\,s^{-1}}$ and in pure carbon-dioxide to be $(1.10 \pm 0.01)\,\mathrm{cm^2\,V^{-1}\,s^{-1}}$. For similar fits to the Ne-CO_2 data we found the reduced mobility of the drifting (cluster) ion to be $(4.06 \pm 0.07)\,\mathrm{cm^2\,V^{-1}\,s^{-1}}$ in pure neon and $(1.09 \pm 0.01)\,\mathrm{cm^2\,V^{-1}\,s^{-1}}$ in pure carbon-dioxide. The similarity of both mobilities in CO_2 suggest that the same ion drifts in the argon- as well as the neon-based gas mixture. As suggested in [77] it is likely that the ion species is either CO_2^+ or a cluster ion formed around CO_2^+. From a similar analysis of nitrogen admixtures to Ne-CO_2 (90-10) we found a preliminary value of $(1.8 \pm 0.2)\,\mathrm{cm^2\,V^{-1}\,s^{-1}}$ for the mobility of the drifting ion in pure nitrogen. Admixtures of N_2 reduced the mobility as compared to pure Ne-CO_2 (90-10) by $\sim 6\,\%$ for an increase of the nitrogen content in the mixture from 0 % to 9 %. For the baseline gas mixture of the future ALICE TPC, Ne-CO_2-N_2 (90-10-5), we found a reduced mobility of $(2.92 \pm 0.04)\,\mathrm{cm^2\,V^{-1}\,s^{-1}}$. This value was measured with a water content of (130 ± 1) ppm in the gas mixture. Therefore, the actual mobility in the ALICE TPC gas mixture is 30 % smaller compared to the ion-mobility of neon used in [23, 120].

Furthermore the change of the ion mobility induced by the water content in the gas was examined using Ar-CO_2 (90-10) and Ne-CO_2 (90-10) mixtures. In case of Ar-CO_2 (90-10) a decrease of the mobility about 6 % was found as the water content is increases from 72 ppm to 1000 ppm. However, these results are not conclusive, because of the high spread and uncertainties of the measured points as compared to the size of the water's effect on the mobility. While increasing the water content in the Ne-CO_2 (90-10) mixture from 365 ppm to 900 ppm the (reduced) mobility decreased by 5.8 %. The effect seemed to level slowly off for a further increase of the H_2O content. There are no previous results in the literature, we are aware of, in order to compare to these measurements. They agree with the general assumption that water lowers the ion mobility.

6. Discharge studies

No repairs of the ALICE TPC readout chambers are possible once the TPC is installed in its final position. Therefore it has to be ensured beforehand that the new GEM-based readout chambers survive the full lifetime of the upgraded TPC of about ten years. The ageing of the detector materials has to be taken into account [137]. Furthermore, the chambers have to be stable against discharges. In one month of lead-lead data taking at 50 kHz between 2 and 10 discharges are expected per GEM stack of the future ALICE TPC. This number is based on the result of a beam-test of an Inner Readout Chamber (IROC) discussed in Section 4.3.3 [24].

A discharge may create a permanent short between the two sides of a GEM foil and in the worst case scenario of several shorts in one foil, the whole GEM stack can be rendered non operational. The goal is therefore that the discharge probability per crossing particle is low and that the occurring discharges do not damage the detector.

The term *discharges studies* usually is used for *stability studies*. These aim at determining the probability of discharge occurrence in a detector operated at conditions (e.g. High Voltage (HV) settings) foreseen for the detector's operation at an experiment. The afore mentioned test with a prototype ALICE TPC IROC, determining the discharge probability of this chamber is a good example for this kind of study. The measurements in this chapter, however, are actual studies of the properties of discharges. Therefore, we have chosen the detector's settings to the end of producing a high amount of discharges. We examine the discharging detector and draw conclusions for the future ROCs of the ALICE TPC. The measurements shown in this chapter are focusing on initial discharges in GEM foils. Secondary discharges are discussed in Chapter 7. Most studies use Ar-CO_2 (90-10) as counting gas, some or done using the ALICE TPC baseline gas mixture Ne-CO_2-N_2 (90-10-5).

6.1. Chapter outline

In this chapter we describe the methods and tools used for the discharge studies as well as for the secondary discharge studies. In Section 6.2 we describe our experimental set-up using GEM foils in either a single-GEM or a double-GEM configuration. Furthermore, the high voltage probes are described. These allow to measure the change of potentials at different electrodes in the detector as discharges occur. Based on statements already made in Section 3.3.3, we discuss the discharge development in GEM foils in Section 6.3. Furthermore, our radiation source, which is used to trigger discharges, is introduced. In this context we show simulations, which allow us to disentangle effects of our set-up's geometry from the source's properties.

From Section 6.4 on, discharge studies are described and their results are discussed in the context of detector operation in general and the special case of the ALICE TPC ROCs. We start with the measurement of discharge probability (Sec. 6.4) at our voltage settings, tuned to produce many discharges. This is done in order to compare to the considerations of the discharge mechanism in the previous section. We also compare our results to the findings of other groups, measuring at different voltage settings. Furthermore we measure the difference in discharge probability between a large pitch and a standard pitch GEM foil. Studies of the evolution of GEM potentials during and after a discharge are reported in Section 6.5. Different resistors in the circuit supplying the GEM foils with HV as well as different power supplies (PSs) are used and the differences among them quantified. Afterwards we move on to an extension of our experimental set-up, which is a mock-up of a stack of two segmented GEMs. This mock-up as well as the corresponding studies with it are the content of Section 6.6. They are done with a cascaded PS as well as the circuit elements currently foreseen for

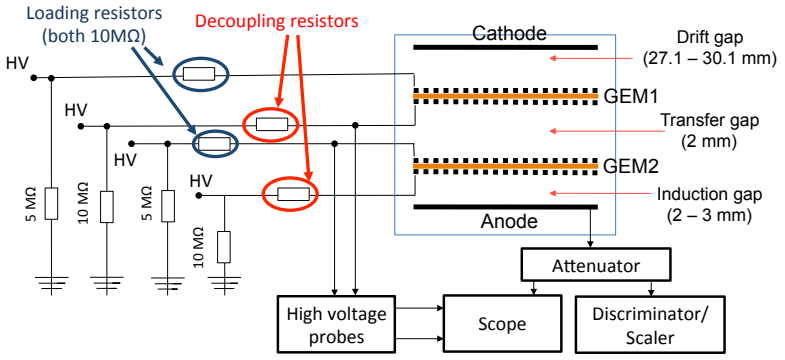

Figure 6.1: Sketch of the set-up used for the measurements in this chapter and the ones in Chapter 7: A stack of two GEMs (or one GEM) is mounted on top of an anode. On top of the GEM stack a mesh serves as drift cathode. Discharges are triggered in either of the GEMs by a combination of a highly ionising source and a sufficient voltage difference across the respective GEM. Then, discharges induce a signal on the anode plane, which are counted using NIM modules. In addition, the induced signals are recorded and stored with an oscilloscope. Two high voltage probes are used at different electrodes in the detector to monitor the potential changes during a discharge.

the upgraded ALICE TPC. On the one hand these studies allow to draw conclusions about the expected potential changes in a GEM stack of the TPC after the upgrade. On the other hand they apply as well to the usage of segmented GEMs in general.

All measurements in this chapter and Chapters 7 and 8 are triggered by the needs of the ALICE TPC Upgrade. However they are as well applicable to other experiments using GEMs or planning to do so. The challenge of building detectors with an either very low discharge probability or a certain robustness against occurring discharges is common among all these experiments.

6.2. Experimental set-up

The studies described in this section have been performed with a small detector equipped with $10 \times 10\,\mathrm{cm}^2$ gas electron multiplier foils as sketched in Figure 6.1. The GEM (stack) is enclosed by the detector volume, being flushed with either Ar-CO_2 (90-10) or Ne-CO_2-N_2 (90-10-5) at atmospheric pressure. A water sensor in the exhaust line allows to monitor the gas quality, since contaminations originating from the surrounding air (e.g. O_2) are known to follow a similar trend as water. A photo of the GEM stack without the box defining the gas volume is shown in Figure 6.2. To power all the GEM electrodes, three different systems are used: A CAEN 470 [123] power supply with four independent channels, a CAEN A1515 cascaded 16 channel PS [138], and a resistor chain. The power supplies are operated with a current limit several 100 µA higher than the expected currents and set to the *over current* mode. Therefore they do not trip in case of a discharge. A loading resistor (R_L) of usually 10 MΩ is present in the high voltage path to the top side of each GEM. The bottom sides of the foils are powered without any resistor or with a decoupling resistors (R_D). During measurements with the independent channel PS, a resistor to ground is added to each HV channel in order to sink excess currents in case of a discharge.

Discharges in one of the two GEMs induce a signal on the anode plane. This signal is attenuated[a] and then passed on to a discriminator. If it is higher than a set threshold ($\sim 150\,\mathrm{mV}$), it is counted by a scaler. A gate of several hundreds of µs is opened for each

[a] In most measurements, a 10 kΩ resistor in series with a 3 dB T-type attenuator was used.

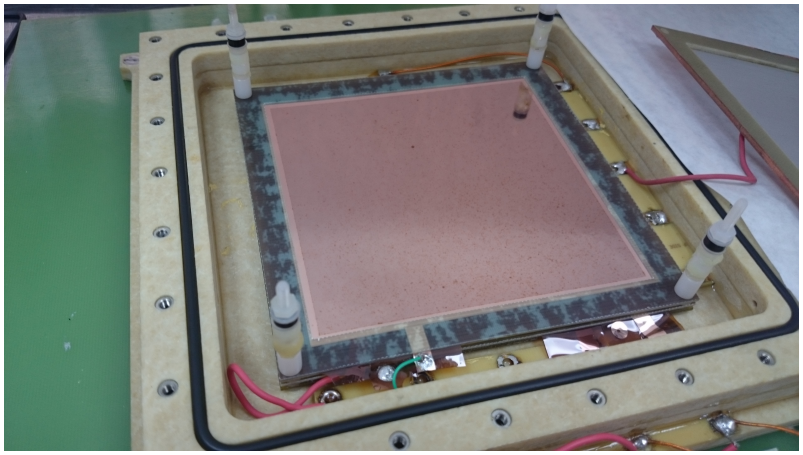

Figure 6.2: A part of the set-up shown in Figure 6.1 GEM1 is mounted on top of GEM2 and the anode plane. On the right side of the picture a part of the mesh is visible, which serves as cathode and is here dismounted. The four supports for the mesh are seen on top of each corner of the GEM stack. The box enclosing the GEM stack, anode plane and cathode is not shown. The dots on GEM1 are marks due to discharges.

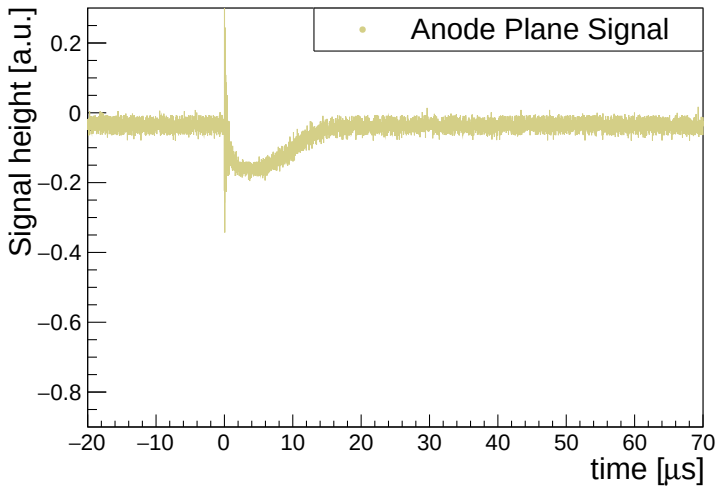

Figure 6.3: Anode plane signal measured during a discharge in GEM2 (double-GEM configuration) with the standard attenuation as described in the text. The signal was obtained during measurements with Ar-CO_2 (90-10) using no decoupling resistance and a loading resistor of 10 MΩ.

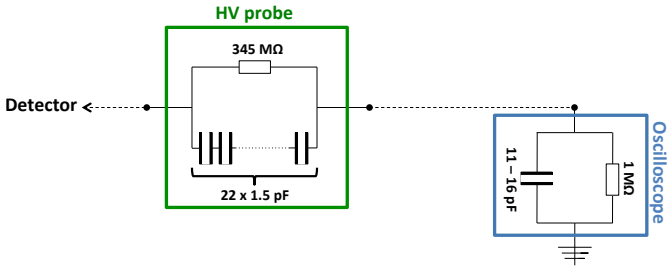

Figure 6.4: Circuit diagram of HV probe, showing the components used to construct the probe. Especially the internal capacitance of the two probes may differ, because of parasitic capacitances introduced during the soldering. The oscilloscope's internal capacitance differs between the two different used oscilloscopes.

discharge detected. During this time, no further signals are accepted. The gate's length of $> 100\,\mu s$ is longer than the decay time of such discharge signals, which is on the order of $50\,\mu s$ in case of the standard attenuation (Fig. 6.3), and far shorter than the recharging time of the GEM ($\sim 100\,ms$) given by the RC-constant of the supply circuit. The gate ensures that double counting of the same discharge is avoided. Finally this method does not introduce a dead-time to the discharge measurements.

6.2.1. High voltage probes

Two custom made high voltage probes are used to examine the potentials on the GEM electrodes during a discharge. Such a probe is directly plugged into the oscilloscope and forms a voltage divider with its internal resistance and the input resistance of the oscilloscope (Fig. 6.4). For each probe, a combination of resistors with a total resistance of $345.5\,M\Omega$ and $343.7\,M\Omega$ is chosen for probe 1 and probe 2, respectively. The voltage divider formed by a probe and the $1\,M\Omega$ input resistance of the oscilloscope allows to measure the highest potential of interest ($U_{\mathrm{GEM1,\ Top}} \sim 3\,kV$) in the dynamic range of the oscilloscope, which is about $\pm 10\,V$. As input capacitance of the oscilloscopes we use either 11 pF [139] (DSO9254A 2.5GHz, by Keysight, former Agilent) or 16 pF [140] (RTE1054, by Rohde&Schwarz) for an input resistance of $1\,M\Omega$. Unfortunately, the manufacturers of both oscilloscopes quote the input capacitance only as approximate value. To ensure proper signal transmission, we attempt to match the impedance of the probes to the input impedance of the oscilloscope. Therefore, a series connection of $22 \times 1.5\,pF$ capacitors is introduced in parallel to the internal resistance of both probes. In theory, the resulting probe capacitance is $C_{\mathrm{Probe}} = 0.0682\,pF$. However, parasitic capacitances in series with C_{Probe} are expected, because of the soldering connections between the single capacitors. Shunt capacitances to ground are expected as well. The theoretical RC constants of the probes and the used oscilloscopes are therefore $\sim 24\,\mu s$ and $11\,\mu s$ or $16\,\mu s$, respectively.

Parametrisation of the AC response

To check the quality of the impedance matching between probes and the oscilloscope, we perform a calibration using signals, which rise fast from zero to a given voltage U_{set}. The probes are connected to a power supply via a fast switching relay (FT2 D3423 [141]). In total, 20 different voltages (U_{set}) between $50\,V$ and $1000\,V$ are applied to the relay and, after switching the relay, to the probes. Two example signals are displayed in Figure 6.5a: At $t = 0$, the voltage rises in about $\sim 1\,\mu s$ to $500\,V$ and so do the signals measured by the probes. The signals appear as broad bands, because the relay (being powered by a $5\,V$ power supply) and the high voltage power supply introduce noise in the frequency region above several $10\,kHz$. Both signals feature an overshoot which decays until only U_{Set} remains. This excess on top of the expected rectangular signal can either be a feature of the signals or the calibration circuit or it is due to imperfect impedance matching between scope and probes. The faster and the higher the actual voltage change is, the higher is the excess. We

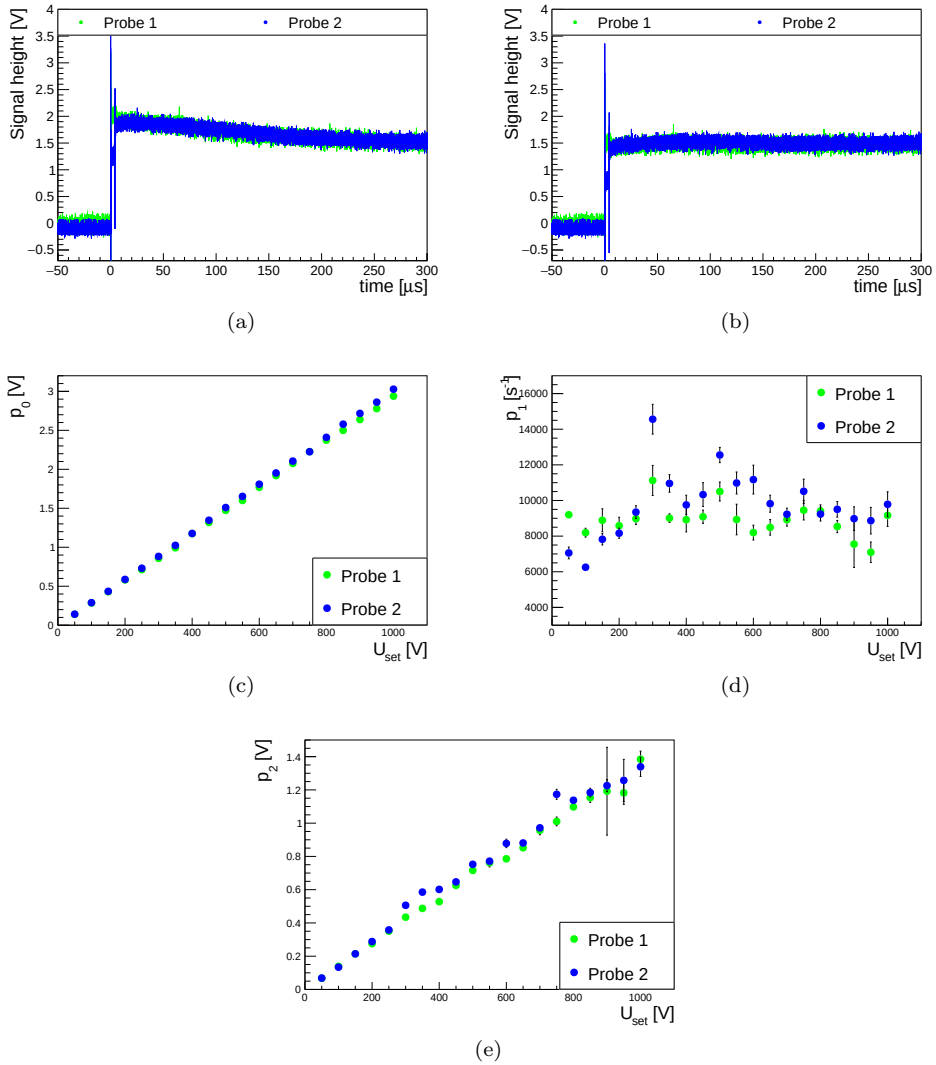

Figure 6.5: Illustration of the calibration of the high voltage probes: (a) The response of the two probes to a fast voltage rise of 500 V. Figure (b) shows the same signals, but with the applied calibration. Figures (c) to (e) show the parameters obtained during the probe calibration for each voltage step. For explanations see Section 6.2.1.

	Probe 1	Probe 2
$1/c_0$	$(340 \pm 1)\,\mathrm{V}^{-1}$	$(333 \pm 1)\,\mathrm{V}^{-1}$
$1/c_1$	$(112 \pm 11)\,\mu\mathrm{s}$	$(102 \pm 19)\,\mu\mathrm{s}$
$1/c_2$	$(731 \pm 5)\,\mathrm{V}^{-1}$	$(695 \pm 5)\,\mathrm{V}^{-1}$

Table 6.1.: Straight line fit results (c_0, c_2) as given in Equation (6.2) to the data displayed in Figures 6.5c and 6.5e. The parameter c_1 was obtained by fitting a constant to the data in Figure 6.5d.

parametrise this overshoot, using all the recorded calibration signals. In each recording the overshoot is fitted with the function

$$U_{\mathrm{fit}}(t) = p_0 + p_2 \cdot \exp\left(t \cdot p_1\right) \quad , \tag{6.1}$$

but only with p_1 and p_2 as free parameters. The parameter p_0 corresponds to U_{Set} and is fitted in advance by a constant in a region of the signal where the overshoot has already decayed (i.e. at high t). The time range of the fit in Equation (6.1) is chosen from $t = 40\,\mu\mathrm{s}$ until the end of the recorded signal, because at small t the signal deviates from the exponential parametrisation in Equation (6.1). This deviation is partially due to the relay itself. In some cases, it does not switch on the full voltage immediately but with an intermediate step occurring a few micro seconds after the initial one. The *Probe 2* data points in Figure 6.5a illustrate this case. After the full voltage is present, signals have first a plateau until eventually the actual decay starts. For each U_{Set} and HV probe, 20 calibration signals are recorded and fitted. These fit results are then averaged for each U_{Set}. The corresponding averaged values for both probes can be found in Figures 6.5c to 6.5e. As uncertainty, the full spread between the 20 values obtained for each p_i, $i = 0, 1, 2$ is given.

The amplitude of the overshoot (p_2) and the parameter accounting for the set-voltage (p_0) obviously depend on U_{Set}, as can be seen in Figures 6.5c and 6.5e. On the other hand, p_1 should correspond to the inverse of the probes' RC constants in case the overshoot is due to bad impedance matching. Therefore, the parameter should be independent of the applied voltage. Linear fits and a constant fit to the data following

$$\begin{aligned} p_i(U_{\mathrm{Set}}) &= U_{\mathrm{Set}} \cdot c_i \quad i = 0, 2 \quad , \\ p_1(U_{\mathrm{Set}}) &= c_1 \quad , \end{aligned} \tag{6.2}$$

respectively, yield the parameters given in Table 6.1. Except for p_1, the fitted parameters show a small spread and follow closely the respective linear or constant trends. For highest voltages used, the spread of the p_2 values increases. For $U_{\mathrm{Set}} > 500\,\mathrm{V}$ the decay seems to be steeper than an exponential decay. As a consequence the fit describes the data less well. This deviation from the expected exponential behaviour can be an indication that the observed signal shape (Fig. 6.5a) is not only due to a difference of the impedances of the probes and oscilloscope. The actual signal may feature already an overshoot.

Consistency checks

The value of $1/c_0$ is the conversion factor from the amplitude of set (DC) voltage to the measured voltage. Following the equation of a voltage divider

$$U_{\mathrm{Meas}} = U_{\mathrm{Set}} \cdot \frac{R_{\mathrm{Scope}}}{R_{\mathrm{Scope}} + R_{\mathrm{Probe}}}$$

it is expected

$$\frac{R_{\mathrm{Scope}}}{R_{\mathrm{Scope}} + R_{\mathrm{Probe}}} = \frac{1}{346} \quad .$$

This is indeed close to the values reproduced by the fit (Table 6.1).

The results for p_1 (Fig. 6.5d) show a high spread and they are compatible with the

expected constant trend as well as with a slight linear decrease of p_1 with increasing U_{Set}. Only the result of fitting a constant to the data is shown in Table 6.1, because the constant behaviour is motivated by $1/c_1$ corresponding to the RC constant of the probes. The c_1 values of both probes are compatible with each other. However, they are approximately five times larger than the RC constant calculated from the capacitors and resistors in each probe. Because p_1 is the most unstable parameter of the fit, as the spread in the values displayed in Figure 6.5d illustrates, the uncertainty on this parameter are quite large. The discrepancy between the two $1/c_0$ results and the expected RC constant may be due to the fact that the actual capacitance of the probes is not known. The soldering process of the probes introduces parasitic capacitances, altering the total capacitance. However, the overshoot can as well be a feature of the signal themselves, and not be due to a problem in the impedance matching. In this case, the decay time can differ significantly from the RC constant of the probes, explaining the larger values of $1/c_1$.

As last consistency check the test set-up is simulated with LTSpice [142]. Doing so, we use the values discussed in this section for the probe resistance, probe capacitance and the input resistance as well as input capacitance of the oscilloscope. The calibration signals are approximated by rectangular signals, being fed into the probes input labelled *Detector* in Figure 6.4. Furthermore we examine the effect of having different values for capacitors and resistors in our test circuit. Always one parameter is scanned, while the others are kept constant. The simulated signals are qualitatively in agreement with the signals recorded. However, the decay of the overshoot is faster than found in the measured calibration signals. If we change the impedance matching in the simulation, we can alter the amplitude (or c_2) of the overshoot. The time constant, however, can not be changed in this way as to reproduce c_1 listed in Table 6.1. The circuit diagram of the FT2 D3423 relay is not included in the simulation. This can be the reason for not reproducing the signals exactly, because additional (or missing) circuit elements impact the outcome of the simulations. It is also possible that the calibration signals themselves contribute to the observed excess.

Correcting discharge signals

In order to correct a measured signal for the overshoot, Equations (6.1) and (6.2) are combined to yield

$$\begin{aligned} U_{\mathrm{Corr}}(t) &= U_{\mathrm{Meas}}(t) - p_2(U_{\mathrm{Drop,\ assumed}}) \cdot \exp\left(-t \cdot p_1(U_{\mathrm{Corr}})\right) \\ &= U_{\mathrm{Meas}}(t) - c_2 \cdot U_{\mathrm{Drop,\ assumed}} \cdot \exp\left(-\frac{t}{c_1}\right) . \end{aligned} \tag{6.3}$$

An iterative procedure is used for the correction of signals with a voltage drop, because the correction depends on the actual drop, which is usually not known beforehand. During the first iteration the value $U_{\mathrm{Drop,\ assumed}}$ is found by subtracting the voltage present before the drop – the baseline – from $U_{\mathrm{Meas}}(t_{\mathrm{a}})$ at a given time t_{a} after the voltage drop. After the correction is applied, the new value of the voltage drop is calculated using $U_{\mathrm{Corr}}(t_{\mathrm{a}})$. If it is smaller (respectively larger) than $U_{\mathrm{Drop,\ assumed}}$ used for the correction, the value assumed for the actual voltage drop is decreased (respectively increased) for the next iteration. This is repeated until $U_{\mathrm{Drop,\ assumed}}$ matches the voltage drop calculated from U_{Corr} within 3 %.

Figure 6.5b shows the signals in Figure 6.5a after correction. It is well visible that the correction leads to a rectangular shape of the signals. After the correction both signals appear to increase slightly after the initial voltage step at $t \sim 0$ until $t \sim 25\,\mu\mathrm{s}$. This is most likely because too much of the signal is subtracted, since the data is not well described by Equation (6.1) during the first $\sim 10\,\mu\mathrm{s}$ after the initial voltage step.

Differences among the calibration and measurement circuit

The circuit elements of the calibration set-up and the biasing schema of a GEM stack differ. Furthermore, the bottom and top electrode of a GEM are on a potential. Therefore the voltage drops during a discharge in a GEM e.g. from the potential at the top GEM electrode towards the value of the potential present at the bottom electrode and not from the ground potential to a positive potential as in the calibration case. On the other hand,

a discharge in a GEM will produce a voltage drop smaller than 500 V. Therefore, the signal amplitudes are similar to the calibration signals used here and the direction of the voltage drop is usually towards more positive potentials. Discharges occur faster than the switching of the relay, hence the discharge-induced voltage drop, as well as the calibration voltage drop, are faster than the RC constant of the probes.

Applicability of the probes' calibration to discharge data

Because of these differences between the calibration set-up and the detector, the parametrisation of the RC response of the probes (Table 6.1) may not be suitable to correct measurements of potential changes during a discharge. Furthermore we can not exclude that the overshoot is part of the actual signal after the relay is switched. The discrepancy between the LTSpice simulations and the measured signals as well as the result for the parameter c_1 suggest this. However, the parameter describing the DC part of the signal ($1/c_0$) can be used in any case with the discharge data, since it is not affected by possible problems with the impedance matching, and because it is not affected by effects occurring during the relay switching.

Finally the probe parametrisation might not be applicable for the discharge measurements. An AC correction may be needed. In this case the observed overshoot would be due to the probes and the calibration would work also with different values of the parametrisation of the probes' AC response. Fig. 6.5 illustrates that an overshoot of signals can be parametrised with linear (constant) parameters with respect to the occurring voltage drop. This linearity is important to find a new parametrisation on the basis of real data. Nevertheless, the probes allow a qualitative analysis of potential evolution at any times.

6.2.2. Measurement procedure

This study focuses on the analysis of the behaviour of the detector during discharges. However, under standard conditions discharges are too rare to perform a detailed, quantitative study of the typical detector behaviour during discharges. Therefore, discharges are triggered voluntarily in (one of) the GEM(s) by a combination of a highly ionising (Rn) source and a high voltage across the respective foil. For example, with a single-GEM in Ar-CO_2 (90-10) the potential difference between the two sides of the GEM foil ΔU_{GEM} is set to a value higher than 400 V. At this voltage, the ionizations created by the α decay of ^{222}Rn in the gas lead to a discharge in the GEM foil with a high probability.

The number of discharges is measured over a given time. During a series of measurements a set of discharge signals is usually stored with the oscilloscope. If HV probes are connected, their signals are recorded as well. The probes draw a small current because they are connected to ground via the input resistance of the scope. In some configurations, mainly when measuring the potentials on the top side of the GEMs, this current leads to a voltage drop. In such cases, the applied voltages are adjusted to compensate for this effect. In addition it has been checked that the presence of the HV probes in the GEM system does not alter the discharging behaviour. Once a satisfactory amount of signals is has been recorded (usually more than 20), the settings are changed (e.g. the HV settings) and the next measurement is started.

6.3. Discharge development in a GEM foil

A discharge of a GEM foil corresponds to a (full) breakdown (Sec. 3.3.3) between the top and bottom side of the foil through (at least) one hole in the foil. This breakdown is characterised by a spark, which eventually builds up and shortens the two foil sides. A spark can be initiated by avalanche multiplication (Townsend discharge, Sec. 3.3.4) or a streamer (Sec. 3.3.6). Here, we only consider sparks initiated by the streamer mechanism for the explanation of the GEM-hole breakdown. The Townsend mechanism does not seem well applicable, because of the small width between the two foil sides.

During the gas amplification in the GEM holes electrons, photons, ions and excited atoms are created. The latter ones can de-excite and release photons, which in turn can ionize

further atoms and start secondary avalanches. Due to the exponential nature of the electron multiplication process, the majority of ions is created close to, but outside of the GEM hole (Fig. 3.13). After their last ionisation, electrons are no longer subject to the strong field in the GEM and move without amplification towards the next electrode. Ions can be considered as static when compared to the speed of the electrons. Therefore, they make up all the space charge in the GEM hole as the electrons have left.

6.3.1. A streamer in a GEM hole

To initiate a streamer, the sum $\mathrm{E}_0 + \mathrm{E}_\mathrm{Q}$ of the electric field created by the ions' space charge (E_Q) and the external electric field (E_0), has to be high enough to achieve gas amplification [85]. This is the so-called *streamer condition*. We now estimate the number of charge carriers needed to create such an electric field. This number is then used to discuss the necessary amount of primary electrons, which can create this space charge after the gas amplification. To estimate E_Q, a spherical space charge is assumed. As radius half the GEM hole diameter is chosen, namely $R_\mathrm{Q} = 20\,\mu\mathrm{m}$. In Ar-$CO_2$ (90-10), which is the gas mixture used for most of the studies presented hereafter, gas amplification starts at an electric field slightly lower than $10\,\mathrm{kV\,cm^{-1}}$ (at a pressure of 1 bar and at 22 °C, Fig 3.5). Using this electric field and $R_\mathrm{Q} = 20\,\mu\mathrm{m}$, yields:

$$\begin{aligned} \frac{10\,\mathrm{kV}}{\mathrm{cm}} = \mathrm{E}_\mathrm{Q} + \mathrm{E}_0 \quad \Rightarrow \quad \frac{10\,\mathrm{kV}}{\mathrm{cm}} &= \frac{eN_\mathrm{e}}{4\pi\epsilon_0\epsilon_\mathrm{r}R_\mathrm{Q}^2} + \mathrm{E}_0 \\ 1\frac{\mathrm{V}}{\mu\mathrm{m}} &= \frac{eN_\mathrm{e}}{4\pi\epsilon_0\epsilon_\mathrm{r} 20\cdot 20\,\mu\mathrm{m}^2} + \mathrm{E}_0 \quad . \end{aligned} \tag{6.4}$$

The N_e ions will be located close to the bottom end of the hole where they were produced. In this region, the external electric field is too low for further electron amplification. In a first simplified case $\mathrm{E}_0 \ll \frac{10\,\mathrm{kV}}{\mathrm{cm}}$ is assumed to evaluate the number of ions N_e in the sphere with radius R_Q:

$$N_\mathrm{e} = 1\frac{\mathrm{V}}{\mu\mathrm{m}}\frac{4\pi\epsilon_0\cdot 1\cdot(20\,\mu\mathrm{m})^2}{e} \approx 0.3\times 10^6 \quad . \tag{6.5}$$

Here, ϵ_0 is the permittivity of the vacuum and we use $\epsilon_\mathrm{r} = 1$, which is a good enough approximation for this calculation [143]. The above gives the order of magnitude for N_e. The biggest uncertainty to this estimate comes from the radius R_Q, which is arbitrarily chosen. If its value is assumed to be 10 µm less or more, N_e turns out to be either 10^5 or 10^6. Both values are (slightly) lower than the *Raether limit* of $\sim 10^7$ charges [92]. In recent measurements and simulations, the *critical charge*, necessary to create a discharge in a GEM hole is determined to be $(5.0 \pm 0.3)\times 10^6$ charges in the case of Ar-CO_2 (90-10) [144]. This value is quite close to the estimate here. It however remains compatible by its order of magnitude.

The number of primary electrons entering the GEM hole, which amount in N_e charges after gas amplification, can be estimated from N_e and the gas gain. In the same paper where the critical charge is determined, discharges are observed with a single-GEM starting from a gain around 500 (in Ar-CO_2 (90-10) at $\Delta U_\mathrm{GEM} = 400\,\mathrm{V}$). A different group found a gain of about 1000 as threshold gain for discharges induced by alpha particles in an Argon based gas mixture [104]. Dividing N_e by these gains yields 400 to 1000 primary electrons, which all have to enter a single GEM hole in order to create $N_\mathrm{e} \sim 10^6$ electron-ion pairs.

Consideration of the external electric field

So far we neglect E_0, under the assumption that this field is much smaller than E_Q. To describe the GEM more realistically, the field without the space charge has to be taken into account. In this case E_0 from Equation (6.4) has to be added to Equation (6.5), as depicted in Figure 6.6. Depending on the local direction of E_0, the total field $\mathrm{E}_\mathrm{Q} + \mathrm{E}_0$ will be enhanced or weakened. In certain regions with increased field a smaller N_e may be sufficient to fulfil the streamer condition, while in the other direction more space charge would be needed.

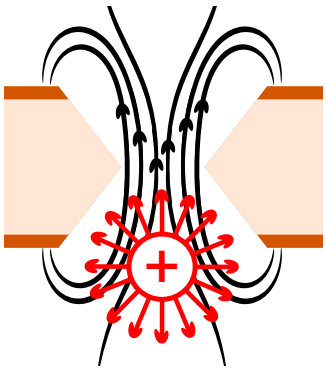

Figure 6.6: Space-charge field of the ions in a GEM hole. The black lines indicate the direction of the electric field in the displayed 2D. It corresponds to E_0 in the text. Below the hole a positive charge is located, with the direction of its electric field E_Q depicted as red arrows. On the hole side of the space charge the direction of E_0 and E_Q adds up to be bigger than E_0. In other regions this sum results in a smaller total field.

Another difference between the considerations above and a more realistic description of the charge in a GEM hole is the actual distribution of the ions. They are rather distributed in a disk and they drift towards the GEM hole where the field E_0 increases towards the region of the smallest hole diameter. The exact location of the smallest diameter differs for different GEM production techniques. Considering this, a smaller number of primary charges can already be sufficient to produce the conditions for streamer evolution. There is as well an opposing effect. If the E_0 experienced by certain ions is screened by other ions, the actual field experienced by the ions in the cloud is reduced. Such charge screening effects can increase the number of charges necessary for the streamer evolution.

Streamer growth in the GEM hole

As the streamer starts, it grows into a weakly conductive path between bottom and top side of the GEM foil. Because this process can not be observed, the most likely scenario can only be guessed based on the knowledge on streamer development as it is e.g. explained in [85]. During the streamer evolution it is likely that the streamer grows first towards the top side of the GEM foil – the cathode in this picture – because in this direction E_0 and E_Q add up and therefore the electric field at the cathode end of the streamer is the strongest. Like this it follows as well the path of the gas multiplication inside the GEM hole backwards. Additional electrons arriving into the GEM and the ones being released from excited atoms feed the streamer growth. As the streamer connects to the top side of the GEM foil, it is analogue to a conductor with a certain resistance and a tip close to the bottom electrode of the GEM – the anode in this model. The potential difference and the small distance between the end of the streamer and the anode will lead to a fast streamer growth to the GEMs bottom electrode and eventually the streamer connects top and bottom side of the GEM foil. It is also possible that the streamer connects first to the bottom side of the foil and then the increasing electric field between the other end of the streamer and the top side accelerates the streamer evolution. After the connection of both GEM sides, the conductivity of the weakly conducting plasma of the streamer increases and it turns eventually into a spark channel. Then the spark is expected to shorten the two sides of GEM foil and it ionises the gas in the GEM hole to an even larger extent. A great amount of photons is released, which can be noticed visually (Sec. 3.3.7).

6.3.2. GEM hole damage through discharges

The energy stored in the GEM foil is released during the discharge. If the GEM foil is sufficiently decoupled from a power supply, e.g. with protection resistors in the high voltage path to each GEM electrode, the discharge energy can be approximated by the formula for

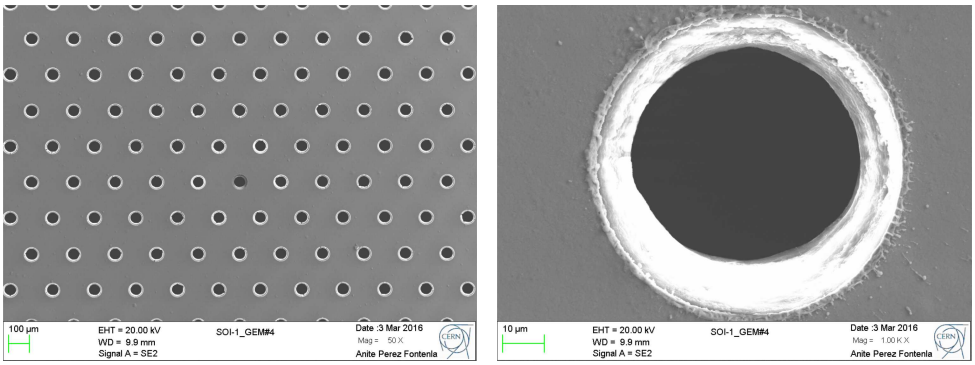

(a) (b)

Figure 6.7: Scanning electron microscope picture of a standard GEM foil. Figure (a) is centred around a damaged GEM hole (b) a close-up of this hole. The damage is most likely due to a discharge. Both pictures were done by Anité Perez Fontenla (CERN/EN/MME-MM) and provided to the author by C. Garabatos (GSI – Helmholtzzentrum für Schwerionenforschung GmbH, Germany), M. Jung (Johann-Wolfgang-Goethe Universität, Germany) and R. Negrão De Oliveira (Universidade de São Paulo, Brazil).

the energy stored in a capacitor

$$\varepsilon_{\mathrm{C}} = \frac{1}{2} \cdot C_{\mathrm{GEM}} \cdot (\Delta U_{\mathrm{GEM}})^2 \quad . \tag{6.6}$$

The capacity C_{GEM} of a $10 \times 10\,\mathrm{cm}^2$ is about 5 nF, which yields a stored energy of 400 µJ at $\Delta U_{\mathrm{GEM}} = 400\,\mathrm{V}$. During the discharge this energy is released in the GEM hole, which leads to a substantial heating of the gas. This affects first only the spark channel and eventually all of the gas in the GEM hole. To our knowledge there is no value for the temperature of such a discharge in a GEM hole in the literature. However, the fast heating and expansion of the gas in the spark region leads to a characteristic cracking noise, which can be heard as the discharge occurs.

This audible effect is not the only consequence of the heat created during the spark. The heating damages the copper layers as well as the polyimide. In Figure 6.7a a scanning electron microscope picture of a GEM with a damaged hole is shown. The hole in the centre of the picture appears darker, because its polyimide's shape, which is visible as bright ring in the other GEM holes, differs from the shape in the other GEM holes. Figure 6.7b shows a zoom of the hole appearing darker. There are splashes around the whole hole circumference, which are identified as melted material from the GEM. Such damaged holes are not only visible while looking at microscope pictures, but a dark spot can be seen by eye at their position. Matching such spots with sparks, allows to relate them to actual discharges.[b] The range of such damages differs from cases as presented in Figure 6.7, where the general shape of the hole seems to be still preserved, over strong deformations of a GEM hole up to the worst case scenario, where melted material forms a conductive path between two GEM sides.

How many discharges can a GEM hole stand

How many discharges in the same GEM hole result in a conductive path between top and bottom GEM electrode? This question is addressed in [145]. The authors use a special fabricated foil, where they can power single GEM holes. To simulate a full GEM, an additional capacitance is added. In order to create discharges, the voltage across the two sides of the

[b] One occasion to observe sparks as well as the following spots are high voltage tests, which are performed before a GEM is mounted inside a detector. During such a test, up to $\Delta U_{\mathrm{GEM}} = 600\,\mathrm{V}$ is applied to a GEM foil in air. If there is e.g. some instability of the foil or a piece of dust on the GEM, these will be burned away by a spark, which is visible during the test. A dark spot remains where the spark happens.

GEM hole is increased, until a discharge happens. The discharge mechanism differs thus from the one described in Section 6.3.1, because no radiation is involved. With this set-up the authors find that the number of discharges a GEM hole can stand until it fails decreases from about 10 to 3, with increasing energy of the discharge. For an ε_C (Eq. 6.6) of 400 µJ, corresponding to our example before, a hole is found to survive 3 discharges. More recent measurements using radiation induced discharges challenge these results [146]. They find – depending on the discharge energy – that a hole can stand a number of discharges which is higher by orders of magnitude. While studying the impact of the protection resistors in the HV path to the top electrode of the GEM foil, a lowest number of 10 discharges before the hole failure is reported for resistances up until $\sim 300\,\mathrm{k}\Omega$. For higher values of this decoupling resistor, the number of discharges per hole increases drastically [147].

Independent of the exact number of discharges needed to destroy a GEM hole, it is clear that there is indeed a maximal number of discharges a GEM hole can stand. With every discharge in the same hole, the probability to create a permanent short across the two sides of a GEM foil increases. Therefore it is not only crucial to minimise the overall discharge probability, but to avoid as well everything which can result in a certain number of discharges occurring in a small region of the GEM foil.

6.3.3. Rn as a source of alpha particles

As mentioned in Section 6.2.2, Rn is used as source of radiation to induce discharges. Before entering the detector, the counting gas passes through a container with traces of ^{230}Th. This Thorium isotope decays via ^{226}Ra to ^{222}Rn. While ^{230}Th and ^{226}Ra have a half-life time of 75 380 yr and 1602 yr, respectively, ^{222}Rn has a half-life time of 3.8235 d. Therefore, the most frequent decays are those of radon via emission of an alpha particle with a decay energy ($\varepsilon_{\alpha\mathrm{Rn}}$) of 6.4 MeV. Such decays are uniformly distributed over the whole gas volume and without any preferred direction. This has the advantage of exposing the whole detector volume to radiation, but has some limitation in discharge rate, as discussed below.

The W value (Sec. 3.2.3, Eq. 3.14) for alpha particles in Ar (CO_2) has been found to be 26-27 eV (34-35 eV) [148]. Combining W_{Ar} and $W_{\mathrm{CO_2}}$ according to their proportion in an Ar-CO_2 (90-10) mixture, the approximate number of ionisations produced is computed as

$$\begin{aligned} N_\alpha &= \frac{\varepsilon_{\alpha\mathrm{Rn}}}{W_{\text{Ar-CO}_2}} = \frac{6.4\,\mathrm{MeV}}{27.3\,\mathrm{eV}} \\ &= 235 \times 10^3 \quad . \end{aligned} \tag{6.7}$$

An α losing all its energy in the counting gas will produce N_α primary ionisations along its track. Their distribution is described by the *Bragg curve*, which models the energy loss of a particle in a medium as function of the distance it travelled in that medium. For alpha particles, the highest energy loss is expected as the particle is almost stopped. The corresponding peak of the Bragg curve is called *Bragg peak*.

In Figure 6.8 [24], GEANT [149] simulations of alpha particles in Ar-CO_2 (90-10) as well as Ne-CO_2-N_2 (90-10-5) are displayed. For alpha particles with an energy of 6.4 MeV a maximum range of about $d_{90\text{-}10}^{\text{Ar-CO}_2} = 5.6\,\mathrm{cm}$, is estimated from the end point of the Ar-CO_2 (90-10) curve.[c] Such alpha particles experience their largest energy loss after they travelled a distance of $\sim 4.6\,\mathrm{cm}$. The Bragg curve for this particular energy and gas mixture has a quite narrow peak, compared to the Bragg curves of the Neon based gas mixtures, displayed as well in Figure 6.8. The average ionisation density $N_\alpha / d_{90\text{-}10}^{\text{Ar-CO}_2}$ is only 4.2 electrons/µm for the full track of the alpha particle. Taking into account that most ionisations are produced at the position of the Bragg peak, a GEM hole still needs to collect electrons produced over several 10-100 µm along such a track. Only then there is the possibility to reach the 1000 primary electrons necessary for a GEM hole discharge as estimated in the previous section for a gain ranging from 500 to 1000. Therefore we expect only around the Bragg peak enough ionisation to trigger a discharge.

[c] This value and the respective values for Ne-CO_2-N_2 gas mixture are listed in Table 6.2.

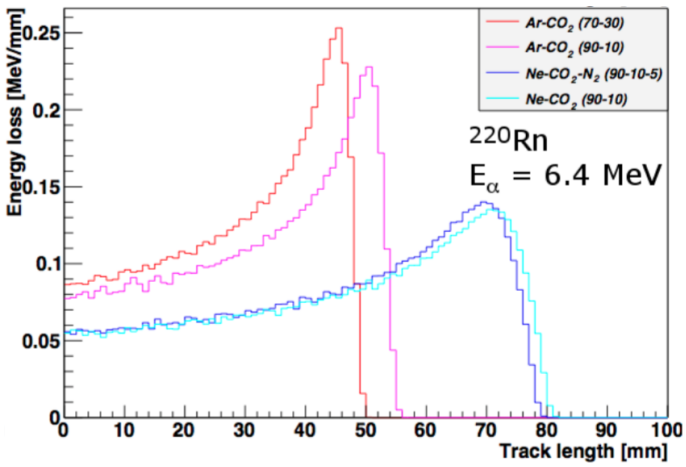

Figure 6.8: Bragg curves of alpha particles with an energy of $\varepsilon_{\alpha\mathrm{Rn}} = 6.4\,\mathrm{MeV}$. The Bragg peak is more pronounced for the Argon based gas mixtures than the Neon based ones. Adopted from [24].

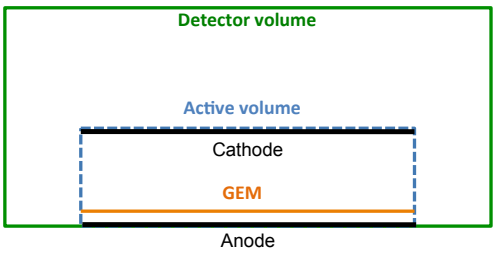

Figure 6.9: Not-to-scale sketch of the different volumes referred to in the description of the simulation of the track distribution (Sec. 6.3.3). The *detector volume* is the full gas volume enclosing the experimental set-up. The *active volume* is a part of this gas volume and extents vertically from anode to cathode and horizontally over the full active region of the GEM (Fig. 6.1).

Distribution of the track direction

A solid source emitting alpha particles in a given solid angle can be mounted at a distance to a GEM that corresponds to the Bragg peak of the α. If the solid angle of the source is small enough, the energy deposit of all the emitted particles happens at a comparable position and all particles have approximately the same probability to trigger a discharge. With a gaseous source, such as Rn, the tracks are emitted in all directions and from random locations in the whole detector volume. In the remaining part of this section, we estimate which fraction of the alpha particles emitted in the gas volume deposit most of their energy close to the GEM and what fraction of the emitted alpha particles can be expected to result in discharges in Ar-CO_2 (90-10) and Ne-CO_2-N_2 (90-10-5).

In a simulation we randomly distribute the starting points of 10^7 tracks with a random orientation in a volume corresponding to the size of the gas volume ($12 \times 12 \times 10\,\mathrm{cm}^3$) of the detector described in Section 6.2. The active volume, which is the actual detector, is embedded into the gas volume as illustrated in Figure 6.9. For simulations of the single-GEM set-up ($10 \times 10\,\mathrm{cm}^2$ GEM) a drift length of 3 cm and an induction gap of 2 mm is used, leading to an active volume of $10 \times 10 \times 3.2\,\mathrm{cm}^3$. Another GEM and a transfer gap of 2 mm is added for the simulation of the double-GEM configuration.[d] All these tracks have a length of $d_{90\text{-}10}^{\text{Ar-CO}_2}$, previously defined as the maximum range of alpha particles in Ar-CO_2 (90-10). The baseline gas mixture is simulated separately. Here, the maximum range of Rn

[d] To be exact: The width GEM (50 µm) has to be subtracted from the width of the gas gap above the respective GEM.

	Simulation parameters		Tracks in active area [%]	
	d	Width at 90 %	Single-GEM	Double-GEM
Ar-CO_2 (90-10)	5.6 cm	4 mm	54.01	55.04
Ne-CO_2-N_2 (90-10-5)	7.9 cm	9 mm	55.43	56.27

Table 6.2.: Maximal range (d) extracted from Bragg curves of 6.4 MeV alpha particles shown in Figure 6.8 [24]. The Bragg peak's width at 90 % of the maximal energy loss is given as well. These *simulation parameters* are used together with the detector geometry to calculate which fraction (denoted as *tracks in active area*) of the alpha particles created in the gas volume enters the active volume of the detector. For further explanations see Section 6.3.3. More results from the same simulation can be found in Table 6.3. The statistical uncertainty of the simulation is 0.01 to 0.03 % for all the given values.

alpha particles in Ne-CO_2-N_2 (90-10-5) ($d_{90\text{-}10\text{-}5}^{\text{Ne-CO}_2\text{-N}_2}$) is used as track length. The parameters entering the calculations are displayed in Table 6.2. For each track we check if it goes through the active region of the detector. A track not crossing the active volume, escapes detection in the actual experimental set-up. In the later steps, we therefore considered only tracks, which are at least partially in the active volume. The whole procedure is repeated 1000 times and each time the quantities of interest, e.g. the number of tracks in the active volume, are filled into separate histograms. The mean and standard deviation of each distribution in these histograms is reported in Table 6.2 and Table 6.3.

The results obtained for the single-GEM and double-GEM set-up are very similar. Differences can be attributed to the increased active region in case of the double-GEM set-up. Using $d_{90\text{-}10}^{\text{Ar-CO}_2}$, about one quarter of all tracks going through the active volume cross the GEM(s). For $d_{90\text{-}10\text{-}5}^{\text{Ne-CO}_2\text{-N}_2}$ this fraction increases to one third. We also checked whether the crossing of the GEM(s) coincides with the Bragg peak's position along the particles track. To this end, the peak is defined as the region at which the peak height is $\geq$ 90 % of the maximal energy loss. For example the Bragg curve of the Rn alpha in Ar-CO_2 (90-10) (Fig. 6.8) reaches at 48 mm 90 % of its maximal value. At 52 mm the energy loss per distance falls again below 90 %. Using this, the peak is defined as the region of 4 mm between a track length of 48 mm and 52 mm (Table 6.2). For the Ar-CO_2 (90-10) gas mixture $\sim$ 1.6 % of all tracks were found to have this region of maximal energy loss at the position of the GEM. This is the case for the single-GEM configuration as well as for each individual GEM in the double GEM set-up. Accordingly, 3.81 % of the tracks calculated with the baseline gas mixture's parameters cross the single GEM coinciding with the track's Bragg peak. The respective values for tracks intersecting either GEM1 or GEM2 in the double-GEM set-up is $\sim$ 3.5 %. For the configuration with two GEMs, it is possible to check as well how many tracks have a Bragg peak spanning over the position of both GEMs. In the case of the Argon based (respectively the baseline) mixture the fraction of tracks crossing at least one GEM or both GEMs at the same time is 2.81 % (respectively 4.85 %), and 0.37 % (respectively 2.00 %), respectively.

Effect of track distribution on discharge probability

The influence of the source position on the discharge probability is examined in [144]. In this paper a solid source emitting alpha particles in a small solid angle is used. By varying the distance between the source and the GEM different ionisation strengths, as given by the Bragg curve, can be realised at the postion of the GEM foil. In Ar-CO_2 (90-10), the discharge probability is found to increase moderately as the intersection point with the GEM moves along the curve towards the Bragg peak. At the Bragg peak, the discharge probability jumps by two orders of magnitude. If the source-GEM distance is further increased, resulting in tracks ending above the GEM, a strong drop in discharge probability can be observed. For this case, P. Gasik et. al. could only measure an upper limit on the discharge probability, being at least five orders of magnitude smaller than the probability measured at the Bragg peak. In Ne-CO_2-N_2 (90-10-5), similar results are found, with the difference that no strong increase in discharge probability in the region of the Bragg peak was noticed.

Single-GEM	All	At 90 %
Ar-CO_2 (90-10)	24.43	1.62
Ne-CO_2-N_2 (90-10-5)	32.42	3.58

	Double-GEM – All		Double-GEM – At 90 %			
	GEM1	GEM2	GEM1	GEM2	Both	Any
Ar-CO_2 (90-10)	26.54	25.10	1.58	1.58	0.37	2.81
Ne-CO_2-N_2 (90-10-5)	34.85	33.42	3.47	3.46	2.00	4.85

Table 6.3.: Results of the simulation described in Section 6.3.3. All the fractions here are given in %. These are calculated with respect to the percentage of tracks in the active area, which is given in Table 6.2. *All* corresponds to all tracks crossing a GEM, while *at* 90 % describes the tracks intersecting a GEM at a track length, corresponding to the Bragg peak. *Any* (*both*) includes all tracks which cross at least one (both) GEM(s) during their highest energy loss. (See as well Table 6.2.) The statistical error of the simulation is 0.01 to 0.03 % for all the given values.

The measurements in [144] show how the discharge probability changes as a track intersects a GEM at a different position along its Bragg peak. In the following, we use this dependence of the discharge probability on the intersection point to estimate which fraction of the Rn tracks are likely to result in a discharge. The measured discharge probability in the afore mentioned paper is only not negligible as alpha particle tracks cross the GEM. In our Ar-CO_2 (90-10) (respectively Ne-CO_2-N_2(90-10-5)) simulation about 1/4 (respectively 1/3) of the tracks in the active volume are found to cross the GEM (Table 6.3). Since the discharge probability for tracks not crossing the GEMs can be neglected, only 25 % (respectively 33 %) of the tracks in the active volume have at all the chance to produce a discharge in the Argon-based (respectively Neon-based) gas mixture.[e] From [144] we expect a two orders of magnitude higher discharge probability in Ar-CO_2 (90-10) for alpha particles intersecting a GEM at the position of their track's Bragg peak as compared to alpha particles just intersecting the GEM. The corresponding Rn tracks in our set-up represent 1.6 % of all tracks in the active volume. This is only ~ 6 % of all tracks crossing a GEM. Due to the significant higher discharge probability, these tracks should however dominate the overall discharge probability. In the Ne-CO_2-N_2 (90-10-5) gas mixture, these tracks are not expected to have such an effect, considering the previously discussed results from [144].

Caveats

The simulations do not include gas detector effects despite the Bragg curves. Furthermore we do not take the error on our definition of the Bragg peak's position along the Bragg curve and the error of the track length itself into account. This is why the results (Tables 6.2 and 6.3) and the above considerations should not be taken as exact. However, these results show that a comparison between different measurements is only possible if the source, its position, and the detector geometry are known. For example, consider our detector as described so far, but operated with a solid source of the same decay energy as the Rn source. If the source's distance to the GEM is tuned to have the maximal energy deposit close to the GEM, all the alpha particles have again approximately the same probability of inducing a discharge. While in case of Rn in Ar-CO_2 (90-10) (respectively Ne-CO_2-N_2 (90-10-5)) less than 2 % (respectively 4 %) of all alphas have this same probability for inducing a discharge. Discharge probability measurements with this two configurations, would result in a huge difference despite otherwise same settings.

In spite of the shortcomings of the simulation, the values discussed in this section should describe approximately our set-up. They thus allow to check the consistency of the measured

[e] In an extreme case, in which all particles crossing a GEM (the GEMs) result in a discharge, these percentages are also the highest fraction of discharges/decay rate measurable with our set-up.

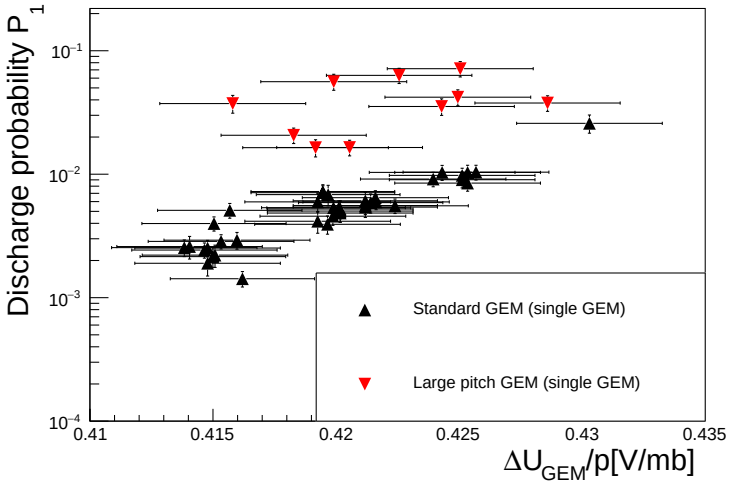

Figure 6.10: Probability as defined in Equation (6.8) for a discharge to occur in a standard or a large pitch GEM foil in a single-GEM set-up as function of ΔU_{GEM}. The increase in P_1 can be always explained with the increasing (average) charge density in a GEM hole: Either by increasing the gain (increasing potential of the discharging foil) or by forcing more charges to enter a GEM hole (large pitch foil). The measurements are done in Ar-CO_2 (90-10) using a Rn source. No decoupling resistor is used and $R_{\mathrm{L}} = 10\,\mathrm{M}\Omega$.

discharge probabilities. They can also serve as baseline for a qualitative comparison of measurements from other groups performed with similar settings, but different sources.

6.4. Measurements of the discharge probability

The probability that a radon decay induces a discharge can be measured using the decay rate (ν_{Rn}) and the counted discharges (N_{Dc}) during a measurement as

$$\text{Discharge Probability} = P_1 = \frac{N_{\mathrm{Dc}}/t_{\mathrm{Meas}}}{\nu_{\mathrm{Rn}}} \tag{6.8}$$

with the uncertainty

$$\delta(P_1) = P_1 \cdot \sqrt{\left(\frac{\delta(N_{\mathrm{Dc}})}{N_{\mathrm{Dc}}}\right)^2 + \left(\frac{\delta(\nu_{\mathrm{Rn}})}{\nu_{\mathrm{Rn}}}\right)^2} \quad . \tag{6.9}$$

The measurement time t_{Meas} is recorded by a scaler module with a precision better than 1 ms. The uncertainty on this time is neglected, since typical measurements last at least about 100 s. For $\delta(N_{\mathrm{Dc}})$ we take $\sqrt{N_{\mathrm{Dc}}}$. The decay rate is determined by counting signals of Rn decays for a given time. For this measurement, the attenuating elements at the anode plane, used for the discharge studies, are removed and replaced with a preamplifier. Decay rates between (8.6 ± 0.6) Hz and (15 ± 1) Hz have been measured for different radon sources. The discharge-rate is tuned by adjusting the voltages across the GEM(s) and is set to rates below 1 Hz.

Figure 6.10 and 6.11 show the result of several discharge probability measurements with the single- and double-GEM set-up, respectively. In all cases Rn is used as radiation source and discharges are measured in Ar-CO_2 (90-10) (Fig. 6.10 and Fig. 6.11a) as well as Ne-CO_2-N_2 (90-10-5) (Fig. 6.11b).

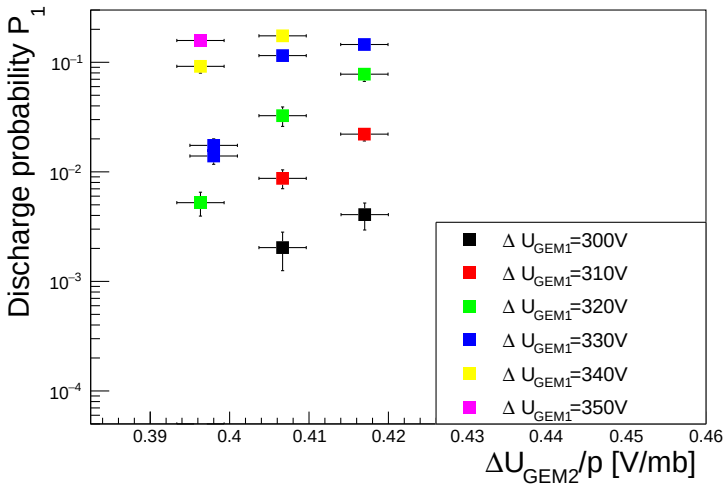

(a) Probability for a discharge to as function of ΔU_{GEM2} for different ΔU_{GEM1}. P_1 increases with the increasing (average) charge density in a GEM hole, which is done by increasing the gain either in the discharging foil or in GEM1. During these measurements the transfer field was set to a value near $E_T = 2000\,\mathrm{V\,cm^{-1}}$.

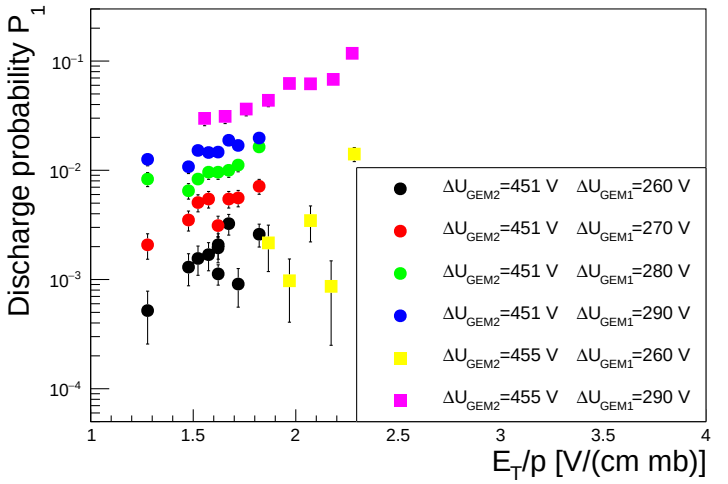

(b) Two effects influencing P_1 in a set-up with two GEMs: For a given potential difference in the discharging GEM, the discharge probability increases steeply for higher ΔU_{GEM1} and slightly with higher $\mathrm{E_T}$. Both trends are due to more charges, which arrive at GEM2 as the U_{GEM1} and $\mathrm{E_T}$ are increased.

Figure 6.11: Discharge probability as defined in Equation (6.8) measured with the double-GEM set-up in (a) Ar-CO_2 (90-10), and (b) in Ne-CO_2-N_2 (90-10-5). Discharges are induced in GEM2 using Rn decays and a high voltage in this GEM. No decoupling resistor is used and $R_{\mathrm{L}} = 10\,\mathrm{M\Omega}$.

6.4.1. Gain considerations

Using the geometry arguments from Section 6.3.3 we can compare the results of the measurements with the double-GEM set-up in Ar-CO_2 (90-10) (Fig. 6.11a) to measurements done at CERN[f] by another group [104]. They measure the discharge probability as function of the gas gain. By comparing our measured P_1 to their curve, we estimate the combined gain of the double-GEM stack to be around 6000 for the bulk of our measurements. During the highest measured P_1, however, a gain larger than 10^4 is achieved. In the baseline gas mixture, the gain has to be even higher since discharges in here are only observed at higher gains than in argon-carbon-dioxide mixtures. In light of our measured discharge rates, this gain estimate seems realistic.

6.4.2. Single-GEM configuration

The data-points in Figure 6.10 show an increase of the discharge probability with increasing potential across the GEM and, hence, higher gas amplification. There is a difference in P_1 between a Standard (S) and a Large Pitch[g] (LP) GEM foil. The different geometry of the two foil types leads to a different discharge behaviour at the same $\Delta U_{\mathrm{GEM}}/p$. Overlaying the S and LP hole pattern shows that there are four times more holes in the standard pitch foil. Analogue to the example made in Section 3.1.2 we can calculate the diffusion width from diffusion constants obtained with Magboltz [64]. Electrons can thus spread over up to four times more holes in the S GEM as compared to the LP GEM. This difference in the charge density per hole leads to a higher discharge probability for a large pitch GEM foil, at a given voltage difference across the foil sides. This behaviour is reflected in the figure. The data points recorded with the LP foil display a P_1 value two to three times higher than the corresponding points obtained when doing measurements with the standard GEM.

If we consider the difference of a LP foil and a S foil in a GEM stack, the diffusion of the electrons during their movement between GEMs has to be taken into account. With the gas conditions in our set-up and at an electric field of $4\,\mathrm{kV\,cm^{-1}}$ the transversal diffusion after 2 mm of drift is 157 µm in Ar-CO_2 (90-10) and 131 µm in Ne-CO_2-N_2 (90-10-5).[h] Therefore, electrons extracted from one GEM hole are only able to reach either one or two different holes of the next GEM, in case this GEM is a LP foil. In case the next GEM is a S GEM, between four and eight different holes can be reached. Therefore, in a GEM stack we expected a higher discharge probability for large-pitch foils as compared to standard foils.

6.4.3. Double-GEM configuration

Introducing another GEM into the set-up allows for a pre-amplification of the charge created during the Rn decays above the GEMs. The probability for discharges in GEM2 (the lower GEM) therefore depends on 1) ΔU_{GEM2}, 2) ΔU_{GEM1} and 3) the transfer field. The difference between the data series in Figure 6.11a shows how P_1 grows if one of the two ΔU_{GEM} is increased while the other one remains constant with a transfer field kept at $2\,\mathrm{kV\,cm^{-1}}$. Increasing the voltage difference between the two sides of either GEM1 or GEM2 by 10 V has a similar effect on the discharge probability.

Similar observations can be made from the discharge probabilities measured in Ne-CO_2-N_2 (90-10-5) (Fig. 6.11b). Each data series is measured with fixed voltages across both GEMs and a similar pressure of (966 ± 2) mbar. Comparing the different data series denoted by points (respectively squares) among each other shows the increase in discharge probability for increasing ΔU_{GEM1} at constant ΔU_{GEM2}. The value of P_1 increases by about half to one order of magnitude for a 10 V increase in ΔU_{GEM1} in a similar fashion as for the points in Figure 6.11a. It seems, however, that increasing ΔU_{GEM2} has a stronger effect on the

[f] The quoted measurements are done at the same physical location as the measurements presented here. The ambient and the gas pressure is therefore on average comparable between the two measurements and the gas gain is expected to be the same for the same ΔU_{GEM}. However the weather at the time of the different measurements adds a significant uncertainty to this comparison.

[g] A GEM foil with 280 µm hole pitch compared to 140 µm hole pitch of a standard GEM foil, while the diameter of the hole is the same.

[h] Applying a magnetic field, reduces this values.

discharge probability. The difference between the two data series with $\Delta U_{\mathrm{GEM1}} = 290\,\mathrm{V}$ illustrates the effect of increasing ΔU_{GEM2} for a constant voltage across GEM1. An increase of ΔU_{GEM2} by 4 V yields the same increase of discharge probability, which is observed for a 10 V change of ΔU_{GEM1}. The two series at $\Delta U_{\mathrm{GEM1}} = 260\,\mathrm{V}$ have a relative high spread, due to the low number of discharges recorded over time. A longer measurement time increases the statistics, but integrates as well fluctuations (e.g., in the gain) which introduce changes appearing significant on the logarithmic P_1 scale. No strong conclusion can be drawn from these two data series, with respect to the question if changing ΔU_{GEM2} has a larger effect on the discharge probability than changing ΔU_{GEM1}.

A higher discharge probability is related to a larger absolute number of charge in the holes of GEM2. Changing the gain in GEM1 and, hence, increasing or decreasing the number of electrons liberated there, does not lead to the same change of electrons arriving at a given GEM2 hole. Some fraction of the electrons never gets extracted from GEM1 because the extraction efficiency is less than 100 % [102]. In addition the electron density gets diluted by diffusion in the transfer gap. An increase of ΔU_{GEM2}, however, directly increases the number of charges in GEM2 and like this the value of P_1. Therefore, it would be reasonable if an increase of ΔU_{GEM2} leads to a higher discharge probability, than increasing ΔU_{GEM1} by the same amount. The exponential dependence of the gas amplification on the electric field (Sec. 3.3.1, Eq. (3.18)) justifies as well the expectation of a stronger dependence of P_1 on ΔU_{GEM2} than on ΔU_{GEM1}. Comparing a GEM with high and low gain, the same increase in absolute voltage should result in a stronger increase in gain of the GEM with higher gain. For the ΔU_{GEM1} and ΔU_{GEM2} applied to the GEM stack during the measurements in Figure 6.11b, increasing ΔU_{GEM2} should therefore have a larger effect on the overall gain and on the discharge probability.

An additional measurement scanning the parameter space of the different voltage differences between GEM sides for the two gas mixtures is needed to determine conclusively the role of each GEMs gain in the overall discharge probability.

Discharge probabilities dependence on the transfer field

Figure 6.11b illustrates the increase of discharge probability with increasing transfer field. In Ne-CO_2-N_2 (90-10-5), a growth of P_1 by a factor of two to five (depending on ΔU_{GEM1}) is measured when increasing $\mathrm{E_T}$ from $1.5\,\mathrm{V\,cm^{-1}\,mbar^{-1}}$ to $2\,\mathrm{V\,cm^{-1}\,mbar^{-1}}$. The efficiency to extract electrons from a GEM hole increases for increasing electric field below a GEM (at a constant ΔU_{GEM}) [102]. The efficiency to collect electrons into GEM holes as function of the field above the GEM is shown in the same paper to stay constant at almost 100 %, for the voltage setting which are used for measurements presented in this work. Applying these findings to our measurements, allows us to conclude that the transfer field dependence of P_1 can therefore be explained by the more efficient extraction of electrons from GEM1, while the electron collection at GEM2 remains constant.

P_1 as function of the induction field

No change of the discharge probability could be attributed to a variation of the induction field. To check this, measurements with similar GEM voltages and similar transfer field, but different induction fields are examined. In single-GEM measurements the same is observed. This result is sensible, because changes in the induction field affect mainly the electron extraction from the GEM closest to the anode. A change in electron extraction efficiency alters the effective gain, but it does not change the absolute gain inside the discharging GEM hole. As a consequence the discharge probability is not influenced.

6.4.4. A word on permanent short circuits across the two GEM sides

With the high number of discharges induced during our measurements some permanent short circuits across GEM foils have been observed, as expected from the discussion in Section 6.3.2. Experimenting with a small experimental set-up allows to easily access the GEM and recover it. In order to do so, the GEM is removed from the detector and in air a high voltage (500-600 V) is applied immediately and without resistor to one side of the foil, while the

other one is grounded. This harsh treatment leads to another discharge, burning the short circuit. This procedure may be applied as well in the counting gas, if the voltage is chosen accordingly and the voltage can be applied without loading (and decoupling) resistor(s). However, recovering a GEM in a GEM stack comes with the risk that the recovery discharge transfers GEM material from the GEM with the short onto the adjacent GEMs, as the short circuit is sparked away.

Usually between 6000 and 8000 discharges[i] are recorded before a foil fails (again). The total number including times where the recording is not enabled is most likely a factor two to five higher. However, with increasing number of discharges the frequency of failures increases until the afore mentioned recovery procedure is as well not successful any-more.

6.4.5. Conclusions

A high number of discharges has been obtained by operating a single- and a double-GEM set-up with high voltages across the discharging GEM and a Rn source. Since voltages across the GEMs have been optimised to produce many discharges, no quantitative statements about the discharge probability at commonly used voltages can be made. The measured probabilities are however consistent with expectations based on discharges being created by the streamer mechanism in a GEM hole (Sec. 6.3): The discharge probability of a GEM foil is driven by the charge created in its GEM holes as well as by charges entering the holes of the discharging GEM.

Comparison to other groups

Performing a sensible comparison of our results with published ones is not an easy task. To the best of our knowledge, most of the existing discharge and stability studies are neither performed in Ar-CO_2 (90-10), nor in Ne-CO_2-N_2 (90-10-5). The studies from [144], using the two gas mixtures are an exception. A few data points recorded with Ar-CO_2 (90-10) can also be found in [104]. There is however no overlap in $\Delta U_{\mathrm{GEM}}/p$ between their measurements and ours. The majority of these discharge probability measurements are in addition done using a directed α source and not a gaseous source as in the experiments presented here. In [24], the discharge probability for a single-GEM set-up with a Rn source in Ar-CO_2 (90-10), a similar detector geometry, and HV settings is reported as a function of the gain. The measured discharge probabilities are well compatible with our single-GEM measurements. No comparison between the discharge probability of different GEM types can however be found in the published material we are aware of.

ALICE TPC

In the future ALICE TPC, a GEM stack with four GEMs (S-LP-LP-S) will be used with voltage settings providing a gas gain of 2000. Example settings can be found in Table 6.4a. These settings are optimised to reach the desired Ion Back-Flow (IBF) and energy resolution. To achieve this goal, the highest voltage is foreseen for GEM4, which is the last in the cascade. From the stability point of view this setting is not beneficial, because the GEM with the largest gain is the one receiving the already multiplied electrons. Other parameters of the baseline settings for the ALICE TPC GEM stacks are more advantageous: Setting a standard GEM at the last position and not a large pitch foil is the better choice with respect to the discharge probability. The low transfer field between GEM3 and GEM4 helps furthermore lowering the probability for possible discharges.

Having the largest gain in GEM4 is common for settings optimised for low IBF. It thus can not be optimised much to reach a lower discharge probability. If, however, tuning of the HV settings is required in order to decrease the discharge probability, decreasing this voltage has to be considered. Lowering the transfer fields helps as well in reducing the discharge probability as shown previously. Lower transfer fields furthermore result in larger diffusion in the gaps between GEM foils and therefore in a smaller average charge arriving in the GEM holes of GEM2 to GEM4. A stability study by the ALICE TPC upgrade team

[i] About half the number of secondary discharges is observed at the same time.

ΔU_{GEM1}	ΔU_{GEM2}	ΔU_{GEM3}	ΔU_{GEM4}	E_{T1}	E_{T2}	E_{T3}	E_{Ind}
270 V	230 V	288 V	359 V	4.0 $\frac{\mathrm{kV}}{\mathrm{cm}}$	4.0 $\frac{\mathrm{kV}}{\mathrm{cm}}$	0.1 $\frac{\mathrm{kV}}{\mathrm{cm}}$	4.0 $\frac{\mathrm{kV}}{\mathrm{cm}}$

(a) *Settings A*

ΔU_{GEM1}	ΔU_{GEM2}	ΔU_{GEM3}	ΔU_{GEM4}	E_{T1}	E_{T2}	E_{T3}	E_{Ind}
270 V	230 V	320 V	320 V	3.5 $\frac{\mathrm{kV}}{\mathrm{cm}}$	3.5 $\frac{\mathrm{kV}}{\mathrm{cm}}$	0.1 $\frac{\mathrm{kV}}{\mathrm{cm}}$	3.5 $\frac{\mathrm{kV}}{\mathrm{cm}}$

(b) *Settings B*

Table 6.4.: *Settings A* are the baseline high voltage setting for the future ALICE TPC, which have been shown already in Table 4.1. *Settings B* are additional settings, optimised to have a lower discharge probability on the cost of having a higher ion back flow. However, the IBF is still low enough to fulfil the design requirements.

currently (2017) ongoing with IROCs and Outer ReadOut Chambers (OROCs) illustrates this. These chambers are mounted in the L3 magnet, about five meters away from the interaction point in ALICE. The location of the chambers at very forward rapidity is chosen such, that the rate of particles crossing the GEM stacks in the chambers is comparable to the expected rate during LHC Run 3 lead-lead runs. With the baseline HV settings (Table 6.4a) about 5 discharges have been observed in 10 hours per GEM stack. While with the settings optimised for low discharge probability (Table 6.4b) only 7 discharges in more than 500 hours. All discharges have been non-destructive. These studies are an important addition to the discharge probability measurement with hadron showers quoted in Section 4.3.3, because these allow to determine the uncertainty of the discharge probability measured with different chambers and GEM stacks.

The high number of discharges endured by our $10 \times 10\,\mathrm{cm}^2$ GEMs is on the one hand encouraging, because it illustrates that all the segments of the ALICE TPC GEMs will as well be able to stand some radiation induced discharges. On the other hand, there is no chance to recover a foil as the readout chambers are mounted inside the TPC. Burning a permanent short will be not possible, because the GEM design does not allow to power a foil without resistors. Therefore, the discharge probability has to be minimised in the first place by choosing appropriate settings.

6.5. Analysing the potentials of a discharging GEM

GEM potentials are measured during a discharge with one of the two high voltage probes described in Section 6.2.1. Figure 6.12 shows such a measurement of a discharge in a single-GEM. One probe is attached between the loading resistor and the top side of the GEM, while the probe at the bottom side is connected to the high voltage supply line close to the GEM. In plots of the GEM potentials as in Figure 6.12 higher potentials appear as more negative, because negative potentials are applied to all electrodes, while the anode plane is at ground potential.

6.5.1. The qualitative picture: ΔU_{GEM} after a discharge

At $t \sim 0$ the discharge occurs and the potential on the top side of the GEM foil (U_{Top}) approaches the value of the bottom potential (U_{Bot}). In the measurement in Figure 6.12 the top side of the GEM is powered through a loading resistor of 10 MΩ and the bottom side is directly connected to the power supply. Therefore the voltage drop occurs across the loading resistor and is measured as drop of U_{Top}, while U_{Bot} stays constant. If there is a decoupling resistor (Fig. 6.13) both potentials drop (respectively rise) and they meet at the same value, which is somewhere between the original U_{Top} and U_{Bot} potential, corresponding to the set values before the discharge. Both figures – the example with and without the decoupling resistor – show that the drop itself is abrupt. Additional measurements reveal that the voltage change at the top side of the GEM happens in less than 10 ns. A more precise statement can not be made due to the not known response time of the probes. However, the oscillations, which accompany the voltage drop, can already be seen for $t < 1$ ns. These

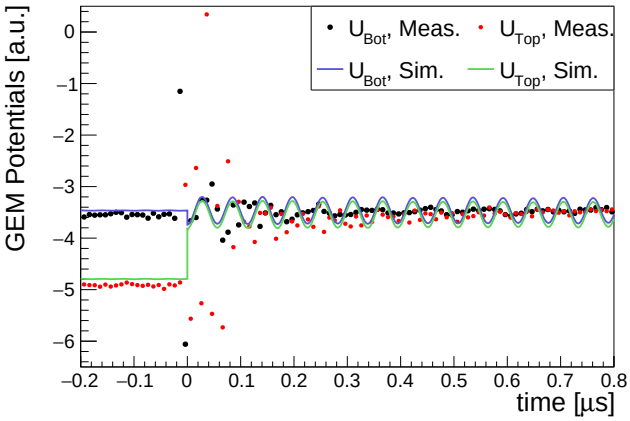

Figure 6.12: Simultaneous high voltage probe measurement of a GEM's top and bottom potential (U_{Top} and U_{Bot} *Meas.*) during a discharge at $t \sim 0$. Only the top potential changes, because there is a loading resistor (10 MΩ) at the top side of the GEM and the bottom side is directly connected to the power supply. In addition to the voltage drop both potentials oscillate. The plot is a zoom of the signals displayed in Figure 6.14a. Furthermore LTSpice [142] simulations of the signals are shown (U_{Top} and U_{Bot} *Sim.*).

oscillations are visible in the top and bottom potentials and start with the discharge as in the figures. Other electrodes as the sides of another GEM or the anode plane pick up AC signals, therefore oscillations are measured there as well. On the time scale of a micro second the oscillations die out, while the voltage drop of U_{Top} is restored in about 50-100 ms according to the RC constant of the GEM ($C_{\mathrm{GEM}} \sim 5\,\mathrm{nF}$) and the loading resistor.

The difference between U_{Top} and U_{Bot} yields the potential difference across the GEM. For times $t < 0$ this difference corresponds to the set ΔU_{GEM}. After the discharge, ΔU_{GEM} drops to zero, as in Figure 6.12. In case no decoupling resistor is used ΔU_{GEM} stays at zero for several µs. For the measurement with $R_{\mathrm{D}} = 10\,\mathrm{k\Omega}$ displayed in Figure 6.13, the case is more complicated, because U_{Top} and U_{Bot} are not recorded simultaneously.[j] However, examining all the U_{Bot} and U_{Top} signals in the respective measurement series shows that the absolute potential to which U_{Bot} and U_{Top} drop after the discharge ($t < 0.1\,\mu\mathrm{s}$) is always the same. Based on a comparison of these potentials, we can conclude that ΔU_{GEM} is as well zero after a discharge, if a decoupling resistor is used. However, we can not comment on the potential difference for $t > 0.1\,\mu\mathrm{s}$, because the time evolution differs among the recorded signals. This is why we can not give exemplary signals, showing the development of the ΔU_{GEM} during the first few 10 µs after the discharge. Only on longer time scales of several 10 µs all the signals look again the same. We will examine the magnitude of ΔU_{GEM} of the discharging GEM, after a discussion of the probe performance, based on simulations of the probes and the experimental set-up.

Simulating discharges with LTSpice

The probes' response to fast voltage drops is discussed in Section 6.2.1 as well as a calibration procedure, summarised in Equation (6.3), to correct for it. However, the probes' AC response to discharges has not been checked yet and it can differ from the previous parametrisation, since the used calibration circuit differs from the circuit of the experimental set-up.

We implement the set-up (Fig. 6.1) in LTSpice. To this end, all the non circuit elements, like the GEMs and the gaps between them, are approximated using circuit elements. For the GEMs 5 nF capacitors are used, while the transfer and induction gap are each resembled

[j] No oscilloscope with the function to write data to disk has been available during most of the measurements with the independent channel power supply and $R_{\mathrm{D}} \neq 0$. Therefore two non simultaneously recorded signals are shown, to give at all an example for the $R_{\mathrm{D}} = 10\,\mathrm{k\Omega}$ case.

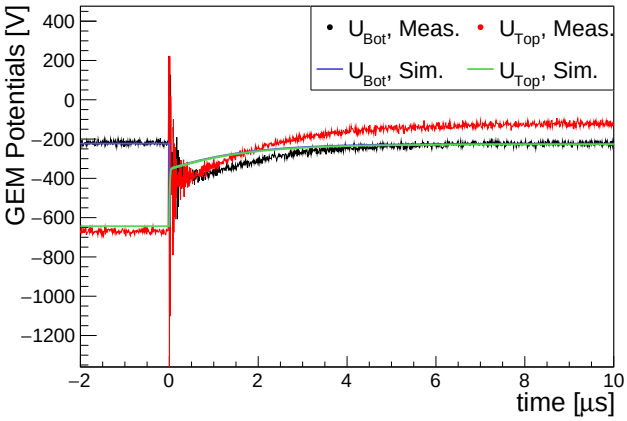

Figure 6.13: High voltage probe measurement of a GEM's top and bottom potential (U_{Top} and U_{Bot} *Meas.*) during a discharge at $t \sim 0$. The two measured signals are not recorded simultaneously, but during two different discharges. U_{Top} and U_{Bot} change both their potential, because of the loading resistor (10 MΩ) at the top side of the GEM and the decoupling resistor (10 kΩ) at the bottom side. In the displayed time-window U_{Bot} recovers already to the value present before the discharge. The signals are multiplied by the scaling factor of the probes. Simulations of the same signals with LTSpice [142] are shown (U_{Top} and U_{Bot} *Sim.*) as well. After the discharge U_{Top} *Sim.* lies on top of U_{Bot} *Sim.*

by a 44.3 pF capacitor. This value is chosen, because it approximates an argon[k] filled capacitor with $10 \times 10\,\mathrm{cm}^2$ plates at a distance of 2 mm. A capacitor with the according smaller capacitance is chosen for the drift gap of 3 cm width. The capacitor representing the induction gap is connected to ground via 10 kΩ, which corresponds to the anode plane's ground connection present during most measurements. We approximate the independent channel PS by five independent voltage sources, which connect with one terminal to ground and with the other one to the respective electrode (four GEM electrodes and the drift) in the experimental set-up. In the real set-up these connections are done with up to two meter long SHV cables. Therefore, a shunt capacitance (0.11 nF) and series inductance (0.4 µH) is included at each of the five connections.[l] Varying these values up to a factor 2 (respectively 1/2) does not have a significant influence on the outcome of the simulation.

Both probes and the scope input follow the circuit diagram in Figure 6.4, however we use as probe resistances the values found during the probe calibration (Table 6.1). The oscilloscope's input capacitance is set to 15 pF and we use different capacitances for the probes as explained later. To emulate a discharge we connect the top and bottom side of the GEM2 capacitor by enabling a switch. Different durations of this short between 1 ps and 10 ns are tested and show all the same result.

Simulation results versus measured data

Comparing the simulations to the measurement allows to judge if an AC response correction is necessary. A simulation of U_{Top} and U_{Bot} is included in Figure 6.12 in addition to the already discussed measurement. For this simulation the capacitance of the probes is tuned to allow perfect signal transmission to the oscilloscope, which requires to use a slightly lower capacitance in both probes as compared to the series connection of 22×1.5 pF. (Figure A.1 in the appendix (Sec. A.1) shows the same simulation, but with the 0.0682 pF probe capacitance. In this case an overshoot in the U_{Top} potential is seen, which we do not see in the data.) The rise time of the drop itself, which we estimate to be faster than < 1 ns

[k] We use a relative permittivity of $\epsilon_r = 1$, because the deviation from 1 expressed as $(1 - \epsilon_r) \times 10^{-6}$ is found to be 922 and 516 for argon and CO_2, respectively [143].

[l] For a coaxial cable with a wire diameter of 1.1 mm and a shield diameter of 7.8 mm, we calculate a shunt capacitance of $55\,\mathrm{pF\,m^{-1}}$ and a series inductance of $0.4\,\mu\mathrm{H\,m^{-1}}$ under the assumption of an insulating medium with $\epsilon_r = 2$ and $\mu_r = 1$.

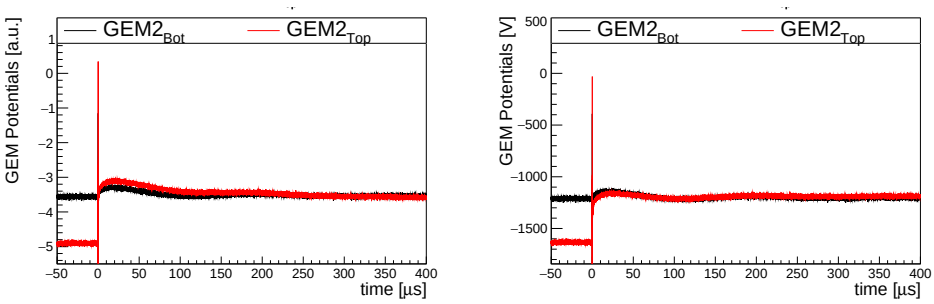

(a) (b)

Figure 6.14: The potentials at the top and bottom side of GEM2, recorded with high voltage probes. A discharge occurs at $t = 0$ and the potential applied to the top of the GEM foil drops towards the bottom potential. Plot (b) shows the same signals as (a), but with the correction of the probes' AC response (Eq. (6.3) and Table 6.1.) applied. The shown signals originate from a single-GEM measurements in Ar-CO_2 (90-10) using no decoupling resistance, the independent channel power supply (CAEN 470) and a loading resistor of 10 MΩ. A zoom into the discharge region can be found in Figure 6.12.

based on the measurements, is instantaneous in the simulation. Therefore, the actual rise time will be limited by the conductivity of the short between top and bottom side of the GEM foil, but not by the electronics as simulated.

In the first few micro seconds the simulation reproduce the data very well. Also, the oscillations of the measured top and bottom potential are reproduced. However, in the measured data they start at a higher amplitude and they are damped faster than in the simulation. Scanning different parameters reveals that these oscillations are due to the shunt capacitance and the series inductance of the cables. The simulation suggests that their amplitude and damping is also influenced by the resistance of the anode's connection to ground.

After a few µs a change in the top and bottom potentials towards more positive values is measured, but not present in the simulation. This increase is displayed in Figure 6.14a and discussed in more detail later on.

If a decoupling resistor is added to our simulation circuit, the data is again well reproduced. In Figure 6.13 we compare a measurement of U_{Bot} as well as one of U_{Top} ($R_{\mathrm{D}} = 10\,\mathrm{k\Omega}$) to the corresponding simulation. In the measured data the AC response is not corrected for and we use again the case of perfect impedance matching between probe and scope in LTSpice. All the features mentioned during the discussion of the potential evolution can be identified in the simulation: Both potentials change and they settle during the discharge at a value between the original top and bottom potential. However, for the case of $R_{\mathrm{D}} \neq 0$ the oscillations seen in the measurement are not present in the simulation. Statements on the evolution of the ΔU_{GEM} between measurement and simulation can not be made using Figure 6.13, because the two measured signals are not recorded simultaneously.

To use or not to use the correction for the AC response

Figure 6.14 shows the time development of the potentials in Figure 6.12 up to 400 µs. In Figure 6.14a the signals are displayed as measured, while in Figure 6.14b the same signals are corrected using the previous parametrisation (Table 6.1) of the probes' AC response. On this time scale it can be seen that U_{Top} as well as U_{Bot} move towards a less negative absolute potential and return eventually to the value of the set U_{Bot}. This effect has similarities to an overshoot and for U_{Top} this can be mitigated using the AC response correction with the parametrisation obtained during the calibration runs. However, this correction obviously affects U_{Top} over the whole period after the discharge and thus leads to a reduction of U_{Top} for small t. A very illustrative example is given by the probe signals from GEM1 before and

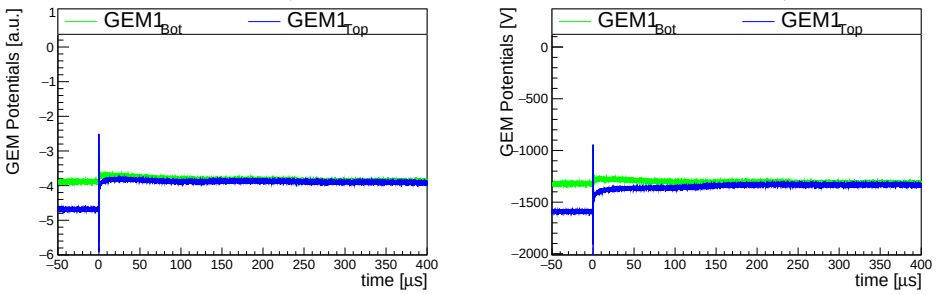

(a) (b)

Figure 6.15: High voltage probe recordings of the potentials at the top and bottom side of GEM1. As in similar figures, the discharge occurs at $t = 0$ and the potential applied to the top of the foils drops towards the bottom potential. Plot (b) shows the same signals as in (a), but with the correction of the probes' AC response (Eq. (6.3) and Table 6.1.) applied. The settings used for this measurement are the same as for the ones in Figure 6.14., except that here a double GEM set-up is used. The discharging GEM is GEM2, see the text for further explanations.

after calibration, which are given in Figures 6.15a and 6.15b, respectively.[m] In the case of the non corrected signals (Fig. 6.14a) the two potentials are similar at small t, while there is a significant difference as the correction is applied (Fig. 6.15b). A similar, but less drastic effect is visible in Figure 6.14, too. Applying this calibration leads hence to a $\Delta U_{\mathrm{GEM}} \neq 0$ directly after the discharge.

Despite the question if the parametrisation for an overshoot, which is obtained with the calibration signals (Sec. 6.2.1), is sensible for the discharge data, it has to be discussed if the excursion of the U_{Top} and U_{Bot} is at all related to bad impedance matching. After a GEM discharge at $t = 0$ the U_{Top} rises in a smooth way until it reaches its maximum value at a few 10 µs. Also, U_{Bot} shows the same behaviour, as U_{Top}. For an overshoot created by bad impedance matching the measured potential should be higher than its actual value as a fast voltage change is measured. This effect is expected to take place at the time of the voltage drop, similarly to what is seen with the calibration signals. Afterwards the measured value decays exponentially with a time constant given by the RC constant of the system. However, there is no voltage drop of U_{Bot} and therefore the evolution of this potential has to be driven by something different than a problem of the impedance matching between probe and oscilloscope or even between the respective electrode and the probe. The fact that both channels drop to a common potential and show the same time development of this common potential is a strong indication that the measurement of U_{Top} is as well not affected by a problem with the impedance matching. Otherwise, U_{Top} is expected to show a stronger excursion (as compared to U_{Bot}) towards more positive potentials and it should show this excursion already at time of the discharge. Furthermore the potential, to which U_{Top} and U_{Bot} settle, depends on the absolute voltage supplied to the GEM2 bottom electrode. At a set U_{Bot} of about $-200\,\mathrm{V}$ this common potential is more negative after the discharge, as compared to the potential at the bottom GEM electrode before the discharge. Around $-700\,\mathrm{V}$ this common potential is the same as the set U_{Bot} and at about $-1200\,\mathrm{V}$ a slight rise as in Figure 6.14 is observed. This suggests that the excursion in the top as well as the bottom potential is rather a result of the discharge itself and the PS response. It is probably not caused by an imperfect impedance matching between probe and oscilloscope.

The fact that the top and bottom potential have the same value directly after the discharge and the good agreement with the simulations, which assume a correct impedance matching, indicate as well that the probe measurements shows the potentials without significant distortions. Introducing a mismatch of the probes' and oscilloscope's impedance into

[m] It has to be noted that discharges are triggered in both cases in GEM2. The phenomenon creating a discharge in GEM1 as soon as GEM2 discharges (*discharge propagation*) is discussed in Section 6.5.3.

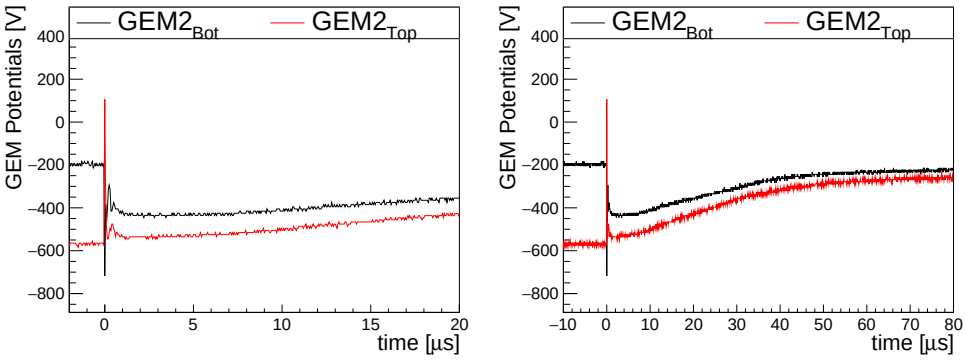

(a) (b)

Figure 6.16: Potentials during and after a discharge measured at GEM2 in a double-GEM set-up as the cascaded power supply is used to bias the GEMs. The measurements are done in Ar-CO_2 (90-10) with $R_L = 5\,M\Omega$ and $R_D = 50\,k\Omega$. There is no calibration applied to the probe signals, except for the scaling to V. Both figures show the same event on different time scales.

the simulation does not reproduce the signal shapes measured during discharges. Thus, the probes perform better than expected from the tests with the calibration signals. This is why we will use only the scaling parameters found during the calibration, which are denoted as $1/c_0$ in Table 6.1 and do not subtract an overshoot modelled by an exponential.

Difference between the top and bottom potential after a discharge

After this discussion of the quality of the probe measurement results, we now return to the question if the ΔU_{GEM} of the discharging GEM drops to zero after a discharge or if this is maybe is an artefact of the measurement procedure.

We found the AC response of the probes, due to a non proper impedance matching between probes and oscilloscope to be negligible. So we conclude that ΔU_{GEM} is compatible with zero directly after the discharge, as seen in our data and there is really a temporary short between the two sides of the GEM. This fits as well the expectation of the discharge mechanism as discussed in Section 6.3.

If no decoupling resistor is used three periods can be identified: Directly after the discharge ($t = 0$ to $\sim 2\,\mu s$) the potential difference is zero (e.g. Fig 6.12). Then follows a period during which ΔU_{GEM} is compatible with zero as well as with a value of a few 10 V ($t \sim 2\,\mu s$ to $\sim 25\,\mu s$), but eventually the potential difference decreases again to zero until the recharging of the top electrode of the GEM starts (Fig. 6.14a and Fig. 6.15a).

For the case where a decoupling and a loading resistor is used we can not base the discussion of the ΔU_{GEM}'s time evolution on Figure 6.13, because the potential measurements displayed in this figure are not done simultaneously. Instead, Figure 6.16 shows a simultaneous measurement of U_{Bot} and U_{Top}. During this measurement the set-up is powered with the cascaded power supply, which will be discussed in Section 6.6 together with its impact on the potential evolution. If a decoupling resistor is used, however, the qualitative features of the GEM potentials' time evolution are comparable if a cascaded or independent channel power supply is used. Analogue to the $R_D = 0$ case, we identify three periods: The period during which the potential difference between the two GEM sides is zero coincides with the potential oscillations and is shorter than 0.1 µs. Immediately afterwards a difference between the top and bottom potential of several 10 V builds up. During the same time U_{Bot} and U_{Top} drop towards more negative potentials ($t \sim 0.1\,\mu s$ to $\sim 2\,\mu s$, second period). The voltage at the bottom electrode drops across the decoupling resistor, because of the charges, that have been flowing from the top to the bottom side during the actual discharge. A drop of the bottom potential will lead to a drop of the top potential, because the two potentials are coupled by the GEM capacitance. This coupling is always present, except during the time of

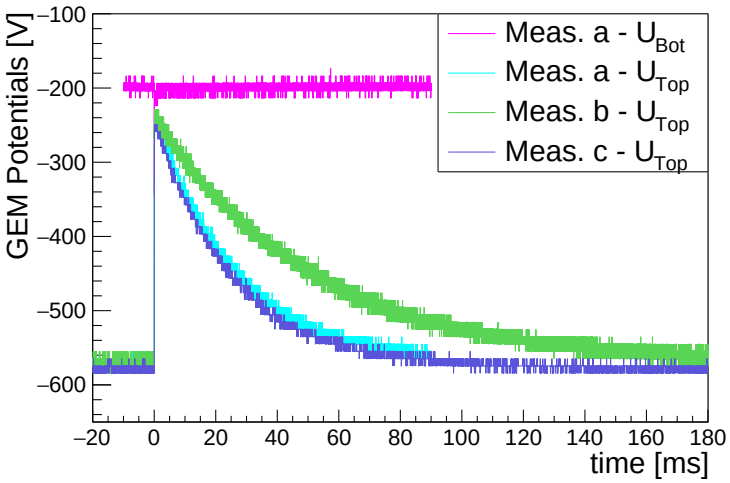

Figure 6.17: These measurements illustrate the recharging of a GEM after a discharge. Always GEM2 potentials are shown, while the GEM stack is powered with the cascaded power supply. The two measurements denoted as *Meas. a* have been recorded simultaneously as a loading resistor of 5 MΩ and a decoupling resistor of 50 kΩ is in place. For the other measurements no decoupling resistor is used, but a loading resistor of 10 MΩ (respectively 5 MΩ) is used in case of *Meas. b* (respectively *Meas. c*).

the discharge. After U_{Bot} and U_{Top} have reached their most negative value, both potentials move again towards more positive values ($t \sim 2\,\mu s$ to several 10 µs, third period). During this time ΔU_{GEM} decreases, but does not approach zero again. A small potential difference of (a few) 10 V is kept until the recharging of the top electrode starts. Previously, we have commented already that it takes ~ 200 ms until the top potential is restored ($R_{\mathrm{L}} = 10\,\mathrm{M}\Omega$). The corresponding measurement is shown in Figure 6.17. Again we use data which is recorded while the set-up is powered with the cascaded PS. In comparison to measurements with the independent channel PS, the potential evolution differs only for $t < 100\,\mu s$, which is not relevant on the time scale of the figure.

In LTSpice simulations of the set-up with decoupling resistor we see as well a difference between the top and bottom potential at small t. However, this difference is too small to resolve it with our measurement precision. Therefore, we think that the observation of $\Delta U_{\mathrm{GEM}} \neq 0$ in the measurements is on the one hand due to the power supplies' response to the discharge, which is not well modelled in the simulation. On the other hand the discharge between the two GEM sides may evolve differently if both electrodes are decoupled from the PS, which in turn affects the ΔU_{GEM} directly after the discharge. Such a phenomenon is as well not part of the LTSpice simulations.

6.5.2. Quantitative analysis of the GEM potentials

An analysis of all recorded signals with different high voltage settings allows to generalise the statement that the potential across the respective GEMs drops to zero during a discharge. This is illustrated in detail in the following.

Analysis procedure

In a single measurement series with a particular configuration of the experimental set-up and particular high voltage settings many waveforms are recorded, similar to the ones displayed in Figures 6.12 to 6.15. For each of these waveforms we calculate the potential before (U_{Bef}) and after the discharge (U_{Aft}). U_{Bef} is the average of all data points of a waveform for which $t < -0.2\,\mu s$, while U_{Aft} is the average of all points with $t \in [300\,\mu s, 320\,\mu s]$.[n] In this time

[n] Furthermore it was checked that no *secondary discharge* (Ch. 7) is present in the waveforms before or during the time interval used to calculate the potential after the voltage drop.

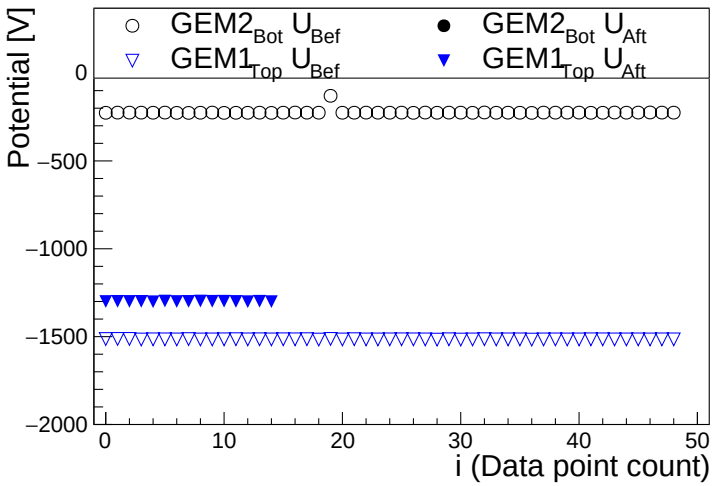

Figure 6.18: Result of an analysis of the high voltage probe signals. For the measurements one probe is connected to the bottom electrode of GEM2 and the other one to the top electrode of GEM1. The other hardware settings are the same as e.g. in the data displayed in Figure 6.15. For all waveforms recorded with this particular setting an U_{Bef} value is extracted, which is shown in the plot. U_{Aft} values are only shown if they are not similar (including their error bars) to the U_{Bef} value and if no secondary discharge is recorded in the waveforms. The exact procedure is described in Section 6.5.2.

range the top and bottom potential appear to be rather constant. The standard deviation σ_{Bef} and σ_{Aft} of these averages are calculated as well. A set of different $(U_{\mathrm{Bef}}, \sigma_{\mathrm{Bef}})_i$ and $(U_{\mathrm{Aft}}, \sigma_{\mathrm{Aft}})_i$ is obtained for each measurement series. The index i is used here to indicate the ith measurement in the series. An example is shown in Figure 6.18. For 49 discharges two high voltage probe signals have been recorded and 49 U_{Bef} values are calculated for each probe. In order to exclude signals with no voltage drop, U_{Aft} values are only taken into account if the potential range $U_{\mathrm{Aft}i} \pm 2 \cdot \sigma_{\mathrm{Aft}i}$ has no overlap with $U_{\mathrm{Bef}i} \pm 2 \cdot \sigma_{\mathrm{Bef}i}$. Because of this, there can be less values for U_{Aft} than U_{Bef}. This is illustrated as well in Figure 6.18: For this particular measurement series no voltage drop is found in all the waveforms of the GEM2 bottom potential (no U_{Aft} values), while the voltage at the top side of GEM1 drops in one third of the cases (15 U_{Aft} values).

For the full measurement series the weighted means are calculated

$$\langle U_k \rangle = \frac{\sum_i^{N_k} U_{ki}/\sigma_{ki}^2}{\sum_i^{N_k} 1/\sigma_{ki}^2}, \quad k = \mathrm{Bef}, \mathrm{Aft}$$

based on the previously found $(U_k, \sigma_k)_i$ and using the weight $w = 1/\sigma_{ki}^2$. The corresponding errors are calculated as follows:

$$\delta\langle U_k \rangle = \frac{1}{\sqrt{\sum_i^{N_k} 1/\sigma_{ki}^2}}, \quad k = \mathrm{Bef}, \mathrm{Aft} \quad .$$

Measurement of the mean voltage drop after a discharge

By subtracting $\langle U_{\mathrm{Bef}} \rangle$ from $\langle U_{\mathrm{Aft}} \rangle$ we obtain the mean voltage drop $\langle U_{\mathrm{Drop}} \rangle$. In Figure 6.19 the voltage drop at a GEM electrode is displayed as function of the applied potential U_{Bef}. In order to relate the voltage drops to the potentials across the respective GEM we plot $\langle U_{\mathrm{Drop}} \rangle / \Delta U_{\mathrm{GEM}}$ instead of the absolute value $\langle U_{\mathrm{Drop}} \rangle$. The analysis procedure yields only

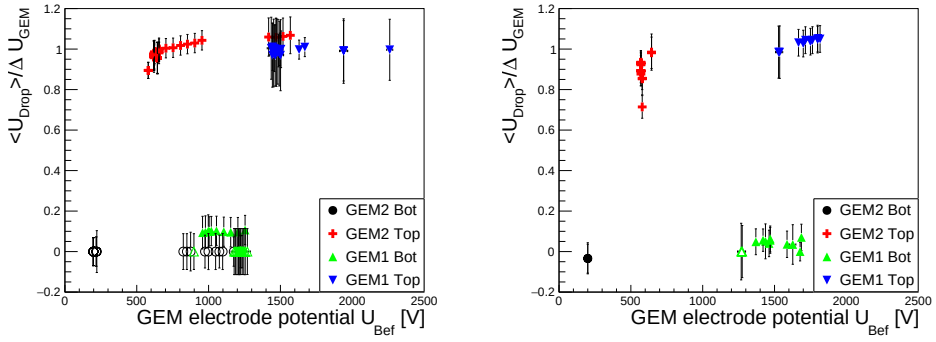

(a) (b)

Figure 6.19: The mean voltage drop $\langle U_{\mathrm{Drop}} \rangle$ at a given GEM electrode over the voltage across the corresponding GEM as function of the potential present at this GEM electrode. (a) Measurements with the independent channel PS, but no decoupling resistor are shown, while (b) shows measurements with the cascaded PS (respectively independent channel PS) with and without (respectively with) decoupling resistor. (See the text for more details.) The analysis procedure (Sec. 6.5.2) does not yield an entry in this plot if the potentials before and after the discharge are compatible. These cases are added nevertheless as open points.

a result if at least one $U_{\mathrm{Aft}i}$ is found different from the corresponding $U_{\mathrm{Bef}i}$. In case no such $U_{\mathrm{Aft}i}$ is present in a measurement series, a $\langle U_{\mathrm{Drop}} \rangle / \Delta U_{\mathrm{GEM}} = 0$ is added as open point to the respective plot. We distinguish measurements without decoupling resistor, where ΔU_{GEM} is found to be compatible with zero at the time used to extract the different $\langle U_{\mathrm{Bef}} \rangle$ and $\langle U_{\mathrm{Aft}} \rangle$ (Fig. 6.19a) and such measurements, where this is not the case (Fig. 6.19b).

Therefore, all the points in Figure 6.19a correspond to sets of measurements which have in common that: 1) the value of the loading resistor is 10 MΩ, 2) the independent channel power supply (CAEN 470) is used, 3) discharges are always induced in GEM2. Data points for Ar-CO_2 (90-10) and Ne-CO_2-N_2 (90-10-5) are included in the plot. Only one difference between the two gas mixtures is found, which will be discussed later on.

In Figure 6.19b measurements with $R_{\mathrm{D}} \neq 0$ and either $R_{\mathrm{L}} = 10\,\mathrm{M\Omega}$ or $R_{\mathrm{L}} = 5\,\mathrm{M\Omega}$ are displayed, while the GEMs are either powered with the independent channel PS or the cascaded PS (CAEN A1515). We include as well measurements with the cascaded PS, but without decoupling resistor, because for these measurements the potentials after a discharge behave similarly to the case where the independent channel PS with a decoupling resistor is used. This is shown in Section 6.6.1. Again, discharges are always induced in GEM2 and in this case Ar-CO_2 (90-10) is used as counting gas.

For all measurements different induction and transfer fields are applied, while the drift field is kept at $400\,\mathrm{V\,cm^{-1}}$. With the independent channel PS the GEM voltages are varied in the range between 410 V to 460 V and from 220 V to 320 V for ΔU_{GEM2} and ΔU_{GEM1}, respectively. While with the cascaded PS GEM voltages between 370 V and 387 V (respectively 330 V and 361 V) are set for ΔU_{GEM2} (respectively ΔU_{GEM1}).

Results: Independent channel PS with $R_{\mathrm{D}} = 0$

The quantitative analysis shows that the top potential of GEM1 and GEM2 drops the full ΔU_{GEM} after a discharge, while the bottom potential does not drop (Fig. 6.19a). This quantifies our previous observation, that ΔU_{GEM} returns to zero after a short period during which a small potential difference builds up and eventually decays again. The drop of the GEM2 top potential shows an increasing trend with increasing U_{Bef}, which is applied to the top electrode. Most likely this is an effect of the power supply's response to the discharge. In Figure 6.14a an example for this response can be seen, illustrating the changing U_{Top} as well as U_{Bot} on a time scale of more than 100 µs after the discharge. A slight overestimation of the probes' scaling factor, which we use to transform the measured signal amplitude to volts,

may result in a similar increase of the voltage drop for increasing set voltage. However, in this case the GEM1 top electrode potential should show an even worse behaviour, because of the higher U_{Bef}. The question why the top potential of GEM1 drops at all during a discharge in GEM2 is addressed in Section 6.5.3.

We observe for some measurements of the GEM1 bottom potential a systematically higher voltage drop than $\langle U_{\mathrm{Drop}} \rangle \sim 0$, however, the drop for these measurements is still compatible with zero. All these points have in common that they are measured in Ne-CO_2-N_2 (90-10-5), but no change in the nature of the voltage drop is expected while changing the gas mixture. No other differences in the detector configuration are found, as compared to the other data points. There are no data points for the GEM2 bottom potential for this gas-mixture, which would allow a comparison between the two GEMs for the exact same detector settings. A drop of the GEM2 top potential can lead to a drop of the GEM1 potentials, because GEM1 and GEM2 are capacitively coupled by the transfer gap. This effect is e.g. visible in Figure 6.15a. However, while checking recorded waveforms against each other it seems as if the corresponding drop recovers fast enough to not influence the U_{Aft} measurement, if the bottom GEM electrode is connected directly to the power supply.

Results: Configurations with $R_{\mathbf{D}} \neq 0$

Using a decoupling resistor obviously decouples the bottom GEM electrodes better from the respective PS. The cascaded PS has built-in resistors in its voltage outputs. Therefore, operating the cascaded PS without decoupling resistors results still in a better decoupling of the GEM bottom electrodes from the PS, as compared to the independent channel PS without a decoupling resistor.

For systems with better decoupling (Fig. 6.19b) the voltage drop observed at the GEM2 top electrode is in most cases significantly smaller than ΔU_{GEM2}. Previously (Fig. 6.16), we have already observed that a GEM bottom electrode, which is decoupled from the PS, leads to a ΔU_{GEM} being not compatible with zero from $\sim 1\,\mu\mathrm{s}$ after the discharge. This remaining potential difference manifests itself in the observation that $\langle U_{\mathrm{Drop}} \rangle / U_{\mathrm{GEM2}} < 1$ for the potential drop at the GEM2 top electrode.

For the GEM2 bottom potential, only one point is measured, hence no quantitative statement can be made. However, for GEM1 U_{Bot} more measurement series have been analysed. This potential drops about $(5 \pm 5)\,\%$ of the set ΔU_{GEM1} (Fig. 6.19b). As compared to similar measurement series, which contribute to the points in Figure 6.19a, we observe a higher number of measurements for which $U_{\mathrm{Bef}i}$ and $U_{\mathrm{Aft}i}$ differ significantly. These drops of GEM1 U_{Bot} are caused by the capacitive coupling to the GEM2 top electrode. Because the GEM1 bottom electrode is better decoupled from the PS, the GEM2 U_{Top} drop results now in a larger drop of GEM1 U_{Bot}, as compared to the measurements without any from of decoupling resistor.
Also the drop of the potential at the top electrode of GEM1 is affected by the stronger drop of GEM1 bottom. Although the drop is still compatible with a drop by ΔU_{GEM1}, it seems to be systematically larger than this value. The potential at the bottom and top electrode are coupled by the GEM capacitance. As long as a PS does not recharge the GEM or the GEM does not discharge further, this capacitance will keep the ΔU_{GEM} at its value. Therefore the drop of U_{Bot} GEM1, together with the small ΔU_{GEM1} due to a GEM1 discharge, is expected to results in a drop of the GEM1 top potential, which is – as compared to its set value before the discharge – higher than ΔU_{GEM1}. The fact that there is still a remaining ΔU_{GEM1} left, if there is a decoupling resistor present, counteracts this effect.

6.5.3. Propagation of discharges

In the measurement series in Figure 6.18 we see a drop of the GEM1 top potential by the full ΔU_{GEM1} in about 1/3 of the corresponding waveforms, while in the other 2/3 of the waveforms no difference between $U_{\mathrm{Bef}i}$ and $U_{\mathrm{Aft}i}$, hence no voltage drop, is found. These voltage drops of the GEM1 top potential indicate that GEM1 discharges ($\Delta U_{\mathrm{GEM1}} = 0$), because the GEM1 bottom potential stays constant. In this section we will discuss the origin of the discharges in GEM1, although the HV settings are optimised to induce discharges in

GEM2.

Simultaneous discharges in both GEMs of the double GEM set-up

If GEM1 discharges it turns out that the discharge happens at the same time as the discharge of GEM2, as simultaneous measurements of the GEM2 top and GEM1 top potential show. The time resolution of these measurements is about 10 ns. However, the probability for an initial discharge in GEM1 corresponds to the probabilities discussed for a single-GEM, while the probability for a discharge in GEM2 is orders of magnitude higher, due to the charge amplification in GEM1 (Sec. 6.4, Fig. 6.11a). It is therefore unlikely that GEM1 is discharging in the first place.[o] This is confirmed by measurements with reduced ΔU_{GEM2} but the other voltages (especially ΔU_{GEM1}) at their original value. No discharges are observed with such reduced voltage settings. Increasing again ΔU_{GEM2} leads to a measurable discharge probability. In order to explain this number of events with simultaneous discharges in both GEMs, there has to be a mechanism *propagating* the original discharge from one GEM to the other, in this case from GEM2 to GEM1. To quantify discharge propagation we look at all the measurement series, during which the GEM1 top potential is recorded, while discharges are induced in GEM2. The propagation probability is then defined by the number of events in which a drop of the GEM1 top potential ($N_{\mathrm{GEM1\ drops}}$) is found, divided by all events in the measurement series ($N_{\mathrm{all\ signals}}$)

$$P_{\mathrm{Prop}} = \frac{N_{\mathrm{GEM1\ drops}}}{N_{\mathrm{all\ signals}}} \tag{6.10}$$

with the error

$$\delta(P_{\mathrm{Prop}}) = P_{\mathrm{Prop}} \cdot \sqrt{\left(\frac{\delta(N_{\mathrm{GEM1\ drops}})}{N_{\mathrm{GEM1\ drops}}}\right)^2 + \left(\frac{\delta(N_{\mathrm{all\ signals}})}{N_{\mathrm{all\ signals}}}\right)^2} \quad . \tag{6.11}$$

We use again $\sqrt{N}$ as uncertainty $\delta(N)$ for the respective number of signals.

Dependence on the potential difference across GEM1

Figure 6.20 shows P_{Prop} as function of the voltage difference present across the two sides of GEM1. All measurements done with Ar-CO_2 (90-10) are plotted, which includes measurements with different loading and decoupling resistors and with the independent channel (CAEN 470) as well as the cascaded power supply (CAEN A1515). (The choice of the biasing schema and HV PS only affects the way a potential drops during a discharge, but not the occurrence of discharges (Fig. 6.19b).)

Three different regions of ΔU_{GEM1} can be examined using these measurements. For the lowest examined $\Delta U_{\mathrm{GEM1}}/p$ of about $0.22\,\mathrm{V\,mbar^{-1}}$ a propagation probability in the range $P_{\mathrm{Prop}} \in [0.1, 0.5]$ is found. Around the second measured $\Delta U_{\mathrm{GEM1}}/p \sim 0.27\,\mathrm{V\,mbar^{-1}}$ a P_{Prop} compatible with 1 is already observed for most of the analysed measurement series. However, values as low as 1/4 are found, too. For the highest probed voltage difference across GEM1 (about $0.34\,\mathrm{V\,mbar^{-1}}$) we measure $P_{\mathrm{Prop}} = 1$ in all cases. Other dependencies ($\mathrm{E_T}$, ΔU_{GEM2}) have been examined as well. However, no correlation with P_{Prop} and the respective other parameter is found.

Cause of the discharge propagation

Electrons moving through the transfer gap can not propagate a discharge from GEM2 to GEM1, because the propagation occurs against the drift direction of electrons. In Ar-CO_2 (90-10) we find the reduced ion mobility to be $1.8\,\mathrm{cm^2\,V^{-1}\,s^{-1}}$ (Sec. 5.5.2, Table 5.1).

[o] In addition, we have simulated with Magboltz [64] the electron drift velocity in Ar-CO_2 (90-10) at ambient pressure and temperature. For electric fields in the range between $1\,\mathrm{kV\,cm^{-1}}$ and $5\,\mathrm{kV\,cm^{-1}}$, this drift velocity varies between about $4.7\,\mathrm{cm\,\mu s^{-1}}$ and $5.1\,\mathrm{cm\,\mu s^{-1}}$. Therefore electrons need about 40 ns to move from GEM1 to GEM2 in the transfer fields we apply to the detector. If the discharges in GEM1 are actually the initial discharges and the discharge is then propagated by electrons to GEM2, we should have seen a delay between the discharges in the two GEMs.

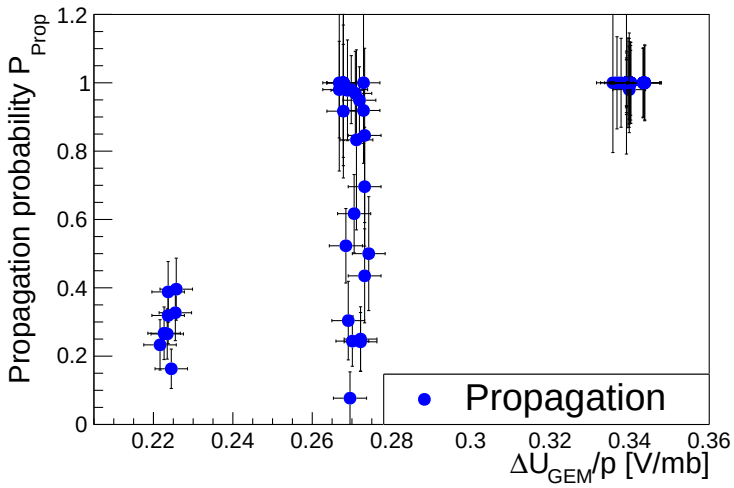

Figure 6.20: In the double-GEM set-up a discharge in GEM2 can be followed by a discharge in GEM1, as explained in the text. The probability for *discharge propagation* from one GEM to the other is shown (P_{Prop}) as function of $\Delta U_{\mathrm{GEM}}/p$ of the GEM the discharge is propagated to. All the points in the plot result from measurements, where the discharges propagate against the drift direction of the electrons in the transfer field. The applied transfer fields are in the range given by $\mathrm{E_T} = 1.5 - 5\,\mathrm{V\,cm^{-1}\,mbar^{-1}}$. All measurements are done in Ar-CO_2 (90-10).

Assuming an electric field of $5\,\mathrm{kV\,cm^{-1}}$ ions need about 22 µs to cross the transfer gap. However, the discharge propagates in less than 10 ns as mentioned before, therefore ions can not be responsible. Only photons remain to explain the propagation of discharges.

Interpretation of the measurement

We find the propagation probability to rise with increasing potential difference across the GEM to which the discharge is propagated. The spread among the P_{Prop} values for the two regions of lower $\Delta U_{\mathrm{GEM1}}/p$, may be caused by other parameters the discharge propagation depends on.

The dependence of the discharge propagation probability on ΔU_{GEM1} suggests that a certain gas gain is necessary in order to reach the critical charge in a hole of GEM1, which will in turn lead to the propagated discharge. Electrons can be provided by the photons emitted during the spark between the top and bottom electrode of GEM2. These photons can ionise the gas directly in the GEM1 holes or they eject electrons from the (GEM1) electrodes or the polyimide. The lowest ionisation energy of Copper is 7.73 eV [150], which is in the right order of magnitude that photons with energies in the near Ultra Violet (UV) and UV regime can liberate electrons from the GEM electrodes. For the case of electron emission from a metal cathode, the yield of electrons per photon is estimated in [85] to be about 10^{-3} to 10^{-1} for near UV and far UV photons, respectively. However, the quencher in the gas will reduce this yield significantly. Still, due to the large amount of photons produced during the discharge in GEM2, it seems possible that electrons are ejected from GEM1 surfaces.

These electrons, as well as electrons liberated in the gas, would then be amplified in GEM1. Ions, being still present in the GEM1 holes from the amplification of the electrons, which led to the discharge of GEM2 in the first place, may reduce the amount of additional charges needed to reach the critical charge for a discharge in GEM1. If the discharge propagation depends on the gas gain in the GEM, the discharge is propagated to, the P_{Prop} versus $\Delta U_{\mathrm{GEM}}/p$ should be differently distributed as in Figure 6.20 if the experiment is done in e.g. Ne-CO_2-N_2 (90-10-5). Another possibility to confirm or dismiss this theory is a dedicated measurement with a different Ar-CO_2 mixture, but more or less quencher.

The Sauli group observed a similar phenomenon in [104]. They report as well that the propagation probability depends on the voltage difference across the GEM to which the discharge is propagated. In their case they also see a dependence on the direction of the transfer field. However, similar to our conclusions, their conclusions are not final and the topic is left for further investigations.

6.5.4. Consequences for the operation of GEM stacks

The potential difference between the two sides of the GEM drops (close) to zero during a discharge. Afterwards the GEM recharges (Fig. 6.17) and during this period the gain of the GEM will increase from zero to its set value and in consequence there will not be (reliable) signals during this time. Therefore a discharge will result in a dead-time on the order of 200 ms for a $10 \times 10\,\mathrm{cm}^2$ standard GEM with a loading resistor of about 10 MΩ. The time constant of the recharging curve changes according to the RC constant for different biasing settings. Another consequence is the increase of the transfer field above a discharging GEM by $\Delta U_{\mathrm{GEM}}/d_{\mathrm{Gap}}$, where d_{Gap} is the width of the transfer gap. For typical ΔU_{GEM} between 200 V and 300 V, this increase will amount to an increase of $\mathrm{E_T}$ in the range between $1\,\mathrm{kV\,cm^{-1}}$ and $1.5\,\mathrm{kV\,cm^{-1}}$, for a transfer gap of 2 mm. While choosing the voltage settings for a GEM stack, $\mathrm{E_T} + \Delta U_{\mathrm{GEM}}/d_{\mathrm{Gap}}$ has to be smaller than the onset of gas amplification. Otherwise gas amplification in the transfer gap starts, which can result in additional instabilities of the GEM stack.

Furthermore all the ΔU_{GEM} in a stack should be, if possible, tuned to minimise the discharge propagation probability. Propagated discharges have the same effect on the GEM stack operation as the original discharge. They will not introduce additional dead time, if all GEMs are powered in the same way, since they happen basically at the same time as the original ones. However the goal is to minimise the number of discharges, in order to minimise the associated risks such as producing a permanent short between the GEM sides. As a consequence, discharge propagation should be mitigated.

6.6. The ALICE TPC settings: Segmented GEMs and a cascaded power supply

The ALICE TPC GEMs are segmented on the top side, while the bottom side is not. The number of segments varies from 18 (IROC GEMs) up to 24 (OROC3 GEMs), depending on the GEM type. Each segment has a surface of roughly $100\,\mathrm{cm}^2$ and is powered through a loading resistor of 5 MΩ. Therefore the dead time arguments made in Section 6.5.4 apply as well to a discharging segment of the ALICE TPC GEMs. After a discharge the pads below the affected segments will not provide useful data, until the segment has recharged.

However the bottom side of each foil is not segmented and powered through a decoupling resistor. It is planned to power the bottom side through one resistor with a resistance of about 50 kΩ. Since the full bottom side is connected via this resistor to the power supply, the change in U_{Bot} (e.g. previously shown in Figure 6.13) will affect all segments of this foil. The goal of this section's study is to look at the potential changes in different segments as one segment discharges. This is studied with a mock-up of a double-GEM stack with two segmented GEMs as described in Section 6.6.2. To power the GEMs in the mock-up a CAEN A1515 cascaded 16 channel PS [138] is used. This power supply is also considered to be used in the final upgraded TPC system. Before discussing the studies with the mock-up, we introduce the concept of a cascaded power supply and point out the differences to an independent channel power supply.

6.6.1. Cascaded power supplies

Working principle

In order to explain the working principle of a cascaded power supply, we briefly mention *independent channel power supplies*. Such power supplies have a certain number of channels, each driven by a voltage source. There are different approaches concerning the ground each

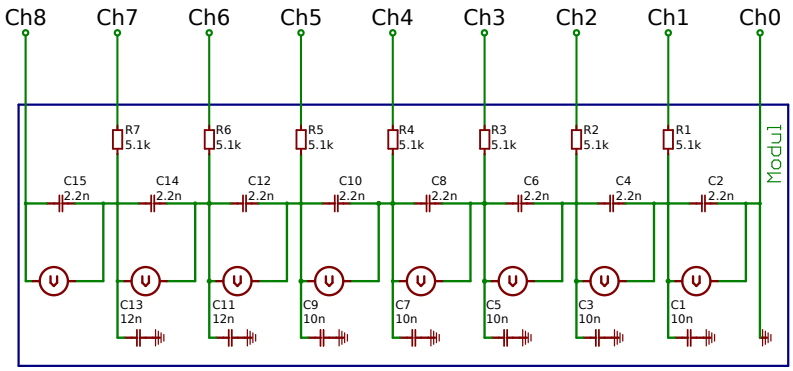

Figure 6.21: The output circuit of a CAEN A1515 [138] power supply prototype. This particular PS has two times eight channels, where eight channels each are provided by one module as sketched here. The ground of each voltage source (*Ch1* to *Ch8*) is the set-voltage of the previous one. *Ch0* is used to provide the ground potential of *Ch1*. The original figure has been provided to the author by R. Renfordt (Johann-Wolfgang-Goethe Universität, Germany) and has been slightly altered to be displayed here.

voltage source is connected to. For example the CAEN 470 [123] power supply has four independent channels, where the output voltage of each channel is referred to the same ground potential (coinciding with earth ground). There are as well models with a (common) floating ground.

Cascaded power supplies, on the other hand, are multi channel power supplies applying a different grounding schema for each voltage source. The voltage sources are connected in series, therefore the ground potential of the $(i + 1)$ voltage source corresponds to the output voltage of the i voltage source. Figure 6.21 shows a layout of the output circuit of a CAEN A1515 cascaded power supply. The eight voltage sources in series (with a capacitor in parallel) are well visible. In case of this cascaded PS the ground of the first voltage source in the cascade has to be provided externally. It can either be (earth) ground or some different potential. Having such a cascade of voltage sources also implies that all the potentials upstream in the cascade have to change as the output potential at one channel is changed. If the voltage difference between two channels is changed, the set voltage difference between all other adjacent channels in the cascade is maintained, but the absolute voltages change.

Operating a cascaded power supply

A cascaded power supply is very well suited for powering gas amplification stages with GEMs.[P]

It has to be avoided that a too high voltage difference is applied between the two sides of a GEM, while ramping up the voltages of a GEM stack. With a cascaded power supply it is ensured that the voltage difference between two channels defining the ΔU_{GEM} is at most the set voltage of the channel. If a channel trips, its absolute potential drops only to the potential of the previous channel in the cascade. These are important safety features during the ramping process or as a channel trips. If ΔU_{GEM} is set by two channels of an independent channel power supply, problems can arise if e.g. one channel ramps faster than the other or if one channel suddenly trips and switches off.

Changes in the HV supply circuit

Compared to the circuit used for the previous measurements of GEM potentials, the biasing circuit changes as we use the CAEN A1515 cascaded power supply. There is a 2.2 nF

[P] Already the fact that we usually refer to potential differences, such as ΔU_{GEM}, while discussing voltage settings of a GEM stack, illustrates this very well.

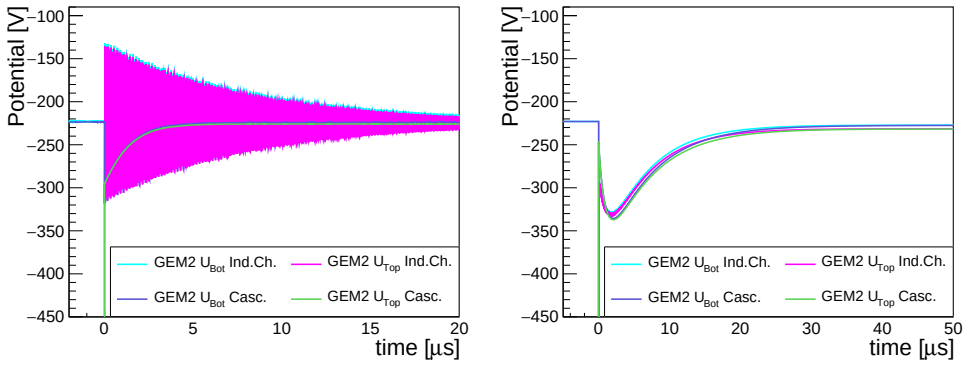

(a) No decoupling resistor

(b) Decoupling resistor $R_{\mathrm{D}} = 50\,\mathrm{k\Omega}$

Figure 6.22: LTSpice [142] simulations of the GEM2 potentials during and after a discharge. The GEM's ΔU_{GEM2} was set to 400 V before the discharge. In the plots simulations for the independent channel power supply (*Ind.Ch.*) and the cascaded PS (*Casc.*) is shown. The latter is implemented in LTSpice according to the circuit in Figure 6.21. The other parts of the set-up, as well as the independent channel PS, are simulated similar to the definition in Section 6.5.1.

capacitor in parallel to each voltage source and a 5.1 kΩ resistor in the output of each channel as visible in Figure 6.21. These resistors decouple the voltage sources and the capacitors in the power supply module from the cable, through which the HV is supplied to the detector. In Section 6.5 (e.g. Figures 6.16 and 6.19b) we already mentioned the different behaviour of the cascaded PS and the independent channel PS, when a discharge occurs across the two sides of a GEM. This will be discussed in more detail in the following.

In addition to the change of the PS, the protection resistors (5 MΩ, respectively 10 MΩ) to ground at each channel supplying a GEM electrode (Fig. 6.1) are removed. During our studies with the independent channel PS, we used these resistors to sink excess current in case of a discharge. However, in order to make our set-up as similar as possible to the circuit layout of the future ALICE TPC readout chambers, we do not use such resistors while running with the cascaded PS.

Simulations of potential changes during and after a discharge

With LTSpice [142] the potentials during and after a discharge are simulated in order to test the effect of these circuit changes. The layout of these simulations corresponds to the previously used layout of a double-GEM stack (Sec. 6.5.1), but with a loading resistor of 5 MΩ. We use again the previously introduced implementation of the independent channel PS and realise the cascaded PS following the circuit diagram in Figure 6.21. Different simulations are done with and without a 50 kΩ decoupling resistor. Always U_{Top} and U_{Bot} of GEM2 are examined. The resulting four sets of potentials are displayed in Figure 6.22. We group the results by decoupling resistance and show potentials for both power supplies in the same plot.

In case of the simulation with $R_{\mathrm{D}} = 0$ (Fig. 6.22a) the potential curves obtained for the independent channel PS are similar to the simulations presented before (Fig. 6.12). However, the different time scale in Figure 6.22a does not allow to identify the oscillations' frequency. The most obvious difference between the cascaded PS and the independent channel PS is the non-occurrence of these oscillations, while using the cascaded PS. Furthermore, there is a drop of the bottom potential, which is not observed with the independent channel PS. For $t > 10\,\mu\mathrm{s}$, however, the potentials simulated with the cascaded PS circuit approach the ones – except for the oscillations – simulated for the independent channel PS after the first 10 µs.

Figure 6.22b illustrates that the evolution of the potentials is very similar for both PSs when a decoupling resistor is present. At the time of the discharge U_{Top} and U_{Bot} move towards each other. At a very small t both potentials meet at an absolute value close to,

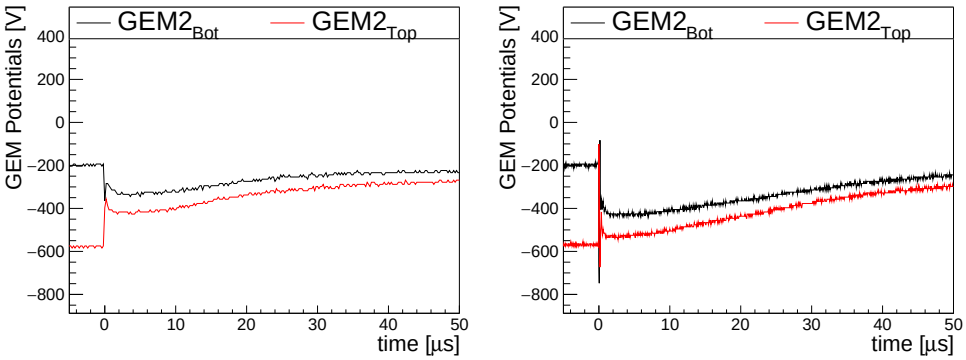

(a) No decoupling resistor

(b) Decoupling resistor $R_D = 50\,k\Omega$

Figure 6.23: Potentials during and after a discharge measured at GEM2 in a double-GEM set-up as the cascaded power supply is used to bias the GEMs. The measurements are done in Ar-CO_2 (90-10) and in both cases a loading resistor of $5\,M\Omega$ is present. There is no calibration applied to the probe signals, except for the scaling to V. A comparison of this two measurements to the simulations in Figure 6.22 is done in the text. The different appearance of the signals between Figure (a) and (b) is due to the different time resolution set at the oscilloscope, while recording the data sets.

but lower as, the original value of the bottom potential. Then both potentials move towards smaller absolute values. During this process the top and bottom potentials start to slightly deviate from each other, which is barely visible in the figure. Eventually U_{Top} and U_{Bot} reach their lowest value ($t \sim 2\,\mu s$, Fig. 6.22b) and afterwards both potentials start to rise again until U_{Bot} is restored ($\sim 30\,\mu s$) to its original value. In Figure 6.22 the curves are only shown for $t \leq 50\,\mu s$, however, the long term evolution of the potentials follows closely similar curves seen in measurements (Fig. 6.17).

Simulations for different values of R_D reveal a change in time and amplitude of the local extreme-value observed at $t \sim 2\,\mu s$ (Fig. 6.22b), when U_{Top} and U_{Bot} move towards more negative potentials. Increasing the value of R_D shifts this extrema to larger t and smaller absolute value of the potentials. However, this development saturates around $R_D \sim 100\,k\Omega$. Judging from this dependence on R_D, the difference between independent channel power supply and cascaded power supply in the simulation can be explained by the $5.1\,k\Omega$ resistor in the output of the cascaded power supply's channels. Adding a decoupling resistor increases this $5.1\,k\Omega$ by R_D and thus changes the coordinates of the extreme-value to higher t and lower amplitude. Comparing the potential curves for cascaded PS in Figure 6.22a and 6.22b illustrates this.

Comparison of simulations to measurements

Figure 6.23 shows two measurements with the cascaded PS, corresponding to the HV and resistor settings of the simulations. A similar qualitative behaviour of the potentials is observed, as compared to the simulations (Fig. 6.22). We see that the potentials on the two GEM electrodes meet at an intermediate value between the original U_{Top} and U_{Bot} during the time of the discharge. However, the measurement without (Fig. 6.23a) as well as with decoupling resistor (Fig. 6.23b), show a greater resemblance with the qualitative features of the simulation of the cascaded PS with decoupling resistor (Fig. 6.22b). Checking the measurements with cascaded PS for $R_D = 0$ (Fig. 6.23a) against the measurements with the independent channel PS, there are more similarities to the potential evolution for the case of $R_D = 10\,k\Omega$ (Fig. 6.13) as to the $R_D = 0$ (Fig. 6.14a) case. This is most likely due to the $5\,k\Omega$ series resistance in the output of each channel of the cascaded PS.

After the two potentials have met, both potentials move to more negative values, before this trend is reversed and eventually U_{Bot} is restored (Fig 6.23). The absolute value of

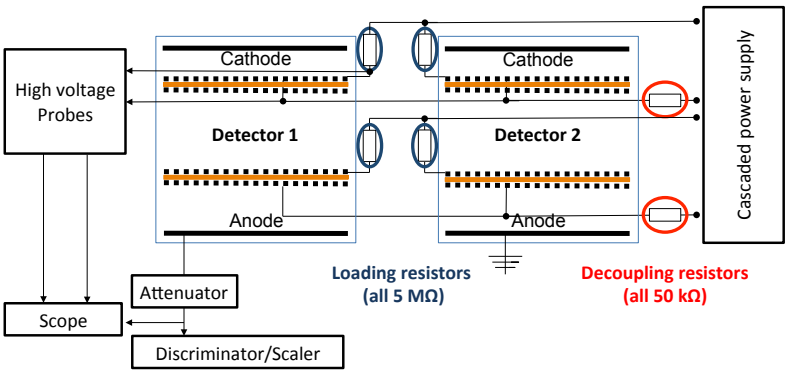

Figure 6.24: In order to simulate segmented GEMs, the set-up displayed in Figure 6.1. is extended by another, similar, detector. The bottom sides of the GEM2 (respectively GEM1) in *Detector 1* and *Detector 2* are connected directly together by a short cable. Then the combined GEM2 (respectively GEM1) bottom channel is connected through a decoupling resistor of 50 kΩ to a channel of the cascaded power supply. The top electrode of each of the four GEMs is connected to a loading resistor of 5 MΩ. On the HV supply side of these loading resistors of the two GEM2 (respectively GEM1) top sides, the two GEMs are connected together and the resulting channel is supplied from the cascaded power supply as well. All the resistors are mounted as close as possible to the detectors. The two high voltage probes – in this sketch connected to the GEM1 top segment in detector 1 and to GEM1 bottom – are used on different GEM electrodes to probe different potentials during discharges. The cathodes are powered from independent power supplies.

both potentials at their extrema ($t \sim 5\,\mu s$) is more negative when a decoupling resistor is introduced, as a comparison of Figure 6.23b ($R_D = 50\,k\Omega$) and Figure 6.23a ($R_D = 0$) shows. This is seen for the simulated data as well, although this local extrema in the LTSpcie simulation has an amplitude value, which is closer to U_{Bot} before the discharge.

After the time of the discharge a certain ΔU_{GEM} is kept at all times. However, this ΔU_{GEM} is barely visible in the simulations, but we measure it to be on the order of 50 V to 100 V. As discussed during the qualitative analysis of the potentials of a discharging GEM (e.g. using Fig. 6.16), this potential difference decreases again as U_{Bot} is restored. The fact that we do not see such a behaviour in the simulations, points again to the possibility that we do not include all parasitic and shunt capacitances as well as series resistances and shunt conductances. Furthermore, the processes happening during the actual discharge differ from its implementation in the LTSpice simulations, therefore we do not expect to reproduce the first $\sim 10\,\mu s$ (or more) after the discharge quantitatively. This is why it is crucial to perform the actual measurements, to gain insights in the exact behaviour of the potentials.

6.6.2. Mock-up of segmented GEMs

In the following the measurement of the potential changes at different GEM segments, following a discharge, is discussed. The set-up is constructed similarly to the layout of the future ALICE TPC's biasing schema. Therefore the cascaded PS, loading resistors of 5 MΩ and decoupling resistors of 50 kΩ are used. Because of a lack of segmented GEM foils available, a mock-up approximates two GEMs with two segments. Each two-segment GEM in this set-up is composed out of two $10 \times 10\,cm^2$ GEMs, as explained in Figure 6.24. Two gas volumes are utilised. In *Detector 1 segment 1* of GEM1 and GEM2 is located, while *segment 2* of both GEMs is mounted in *Detector 2*. Cables as short as possible connect the corresponding bottom GEM sides together. The gas mixture is Ar-CO_2 (90-10). For the potential studies shown later on, only detector 1 was flushed with the counting gas, while the other one is filled with air. The HV settings favour discharges in GEM2. These voltages are

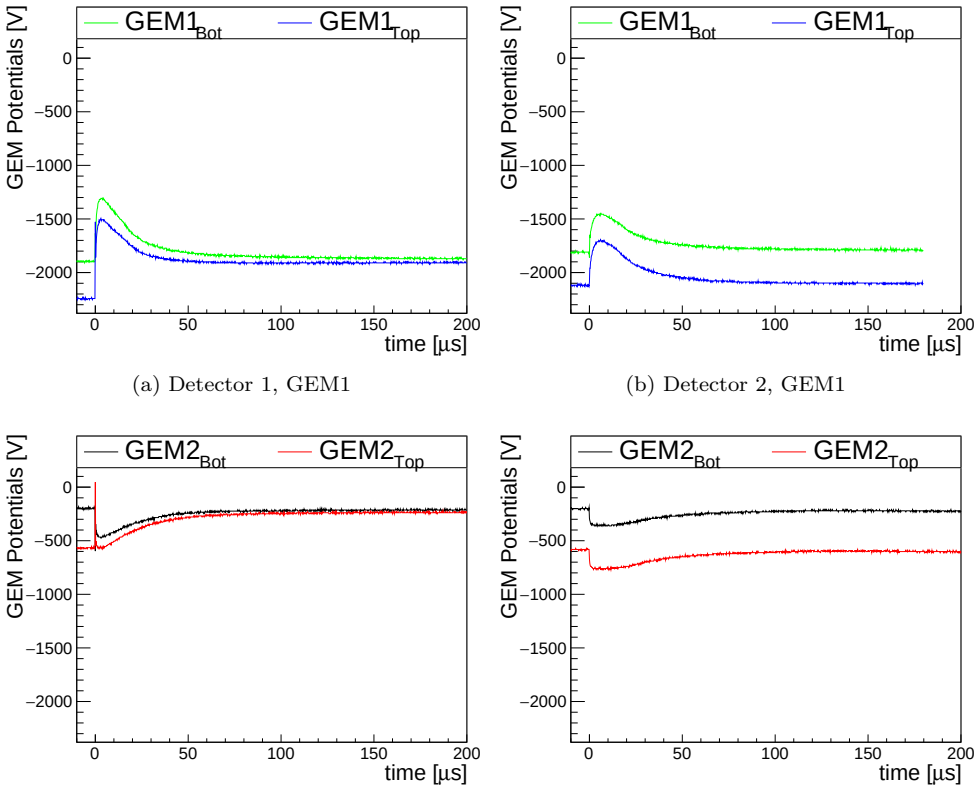

(a) Detector 1, GEM1

(b) Detector 2, GEM1

(c) Detector 1, GEM2

(d) Detector 2, GEM2

Figure 6.25: (a), (c), (c): High voltage probe signals at different electrodes of the set-up depicted in Figure 6.24. Figure (d) was recorded as well with the same set-up, however during this recording $R_{\mathrm{L}} = 10\,\mathrm{M\Omega}$ and the independent channel PS has been used. Each plot shows a simultaneous recording of two signals, while GEM2 in detector 1 is discharging. All the signals are scaled according to V, but the AC response of the probes is not corrected for.

too low to produce discharges in air and hence it is ensured that there are only discharges in segment 1 of GEM2. As a discharge happens, the potentials at all GEM segments react accordingly and are observed by the HV probes in different measurement series.

Potential changes at different GEM segments

Figure 6.25 shows measurements of U_{Top} and U_{Bot} at different segments as segment 1 of GEM2 is discharging.

The potentials in the discharging segment (Fig. 6.25c) show a similar change with time as observed in the previously discussed measurement (Fig. 6.23b). After the top and bottom electrode are at the same potentials during the discharge, the potentials at both electrodes move all the way to the absolute value of top potential before the discharge. Afterwards the bottom side of GEM2 is first recharged, while the recharging of the top side is not visible on the time scale of the plot.

As pointed out before, both segments of a GEM have a common bottom side, therefore the change of the bottom potential is the same in Segment 1 as well in Segment 2 (of GEM2), which is shown in Figure 6.25d. Comparing U_{Bot} here to the measurement at the discharging segment (Fig. 6.25c) shows a significant difference, which is due to a different biasing circuit used during this measurement. Unfortunately no data with the ALICE TPC configuration has been saved for Segment 2, GEM2. Instead, we show a measurement during which the mock-up is biased with the independent channel PS, a loading resistor of $10\,\mathrm{M\Omega}$ and a decoupling resistor of $50\,\mathrm{k\Omega}$. These differences affect the behaviour of the

potentials as Segment 1 of GEM2 discharges and therefore U_{Bot} measured in Segment 2. The interconnection between different GEMs of the mock-up, and the capacitive coupling between GEMs and between the two sides of each GEM foil are not changed. The circuit changes only affect the connection to and the power supply. Comparing U_{Bot} in Figure 6.25c and Figure 6.25d, shows that the drop of U_{Bot} to a more negative potential is not as strong as with the cascaded PS and $R_{\mathrm{D}} = 5\,\mathrm{M}\Omega$. After this drop, we observe the recharging curve of U_{Bot}, as expected after a discharge. Because there is no discharge in this segment and due to the capacitive coupling between GEM2 top and GEM2 bottom, U_{Top} evolves in a similar way as U_{Bot}. About 100 µs after the discharge, the bottom potential is restored again to its value before the discharge. The top potential shows the same behaviour, so that ΔU_{GEM2} (Segment 2) seems to be constant at its set value, while ΔU_{GEM2} (Segment 1) moves to zero and evolves then as discussed in Section 6.5 or Section 6.6.1, Figure 6.23b. However, the evolution of U_{Top} in Segment 1 (GEM2) has no influence on the top potential in the other segment, because the loading resistors decouple different segments on a GEM's top side.

The GEM1 potentials are again recorded with the configuration of the mock-up, being close to the desired configuration of the future ALICE TPC. In Figure 6.25b the top and bottom potential of Segment 2, GEM1 are shown. This is the segment facing the non-discharging part of GEM2 in the detector full of air. No discharge is propagated to this segment, therefore the potential changes visible are on the one hand due to the capacitive coupling between the GEM1 top and bottom side. On the other hand the common bottom electrode of Segment 1 and Segment 2 (GEM1), reacts to the discharge in GEM2, Segment 1. This is why U_{Bot} and U_{Top} (Segment 2) move to less negative potentials, while $\Delta U_{\mathrm{GEM1,\ Seg2}}$ stays all the time roughly constant. Both GEM1 potentials (Segment 2) are restored after $\sim 100\,\mu\mathrm{s}$.

The picture is different for Segment 1, GEM1 (Fig. 6.25a). There is a voltage change in both GEM1 potentials towards less negative values, because of the capacitive coupling to the top side of GEM2 (Segment 1) and the change of the potential there. On top of this drop, a propagated discharge is visible. It is interesting to note, that U_{Bot} does not move towards U_{Top}, as e.g. the potentials of the originally discharging segment do. Instead, the bottom potential evolves as expected from the capacitive coupling of GEM1 to the discharging GEM2 segment. This has the effect that the voltage drop due to the propagated discharge affects only U_{Top} and the magnitude of this drop is higher than the set ΔU_{GEM1}. However, there is a significant voltage difference between the top and bottom electrode of GEM1 (Segment 1) in the first few 10 µs after the discharge. The evolution of U_{Top} and U_{Bot} with time seems to be dominated by the capacitive coupling to the originally discharging segment, while ΔU_{GEM1} (Segment 1) shows a similar time evolution as for the other discharging segment. Furthermore, the propagated discharge in Segment 1 of GEM1 has no effect on the potentials in Segment 2 of GEM1, because this discharge does not induce additional changes of the GEM1 bottom potential.

General comments

Potential changes up to 500 V are measured at the GEM1 bottom side. The potential changes at both GEM1 top segments is of a similar magnitude. We find a spread of almost 100 V between the minimal and maximal absolute value of the potentials after the discharge as we analyse all the GEM1 U_{Bot} (respectively U_{Top}) waveforms during one measurement series. However, the voltage difference between the top and bottom side of the non-discharging GEM segments seems to stay constant all the time.

In the originally discharging segment the potentials behave very similarly for all waveforms recorded with the same settings. No spread between single measurements is observed in this case. Also, no big spread is observed between single measurements of the potentials at the segment, which shares the bottom potential with the discharging segment.

In case of a real segmented GEM, the segments are obviously located next to each other. Our set-up does not allow us to study effects, which may occur if a segment discharges and a neighbouring segment in its proximity reacts to it. From our studies presented in Figure 6.25 we think, however, that after a discharge, the potential difference between two neighbouring segments of the same GEM will be at most slightly higher than the set ΔU_{GEM}. The segment

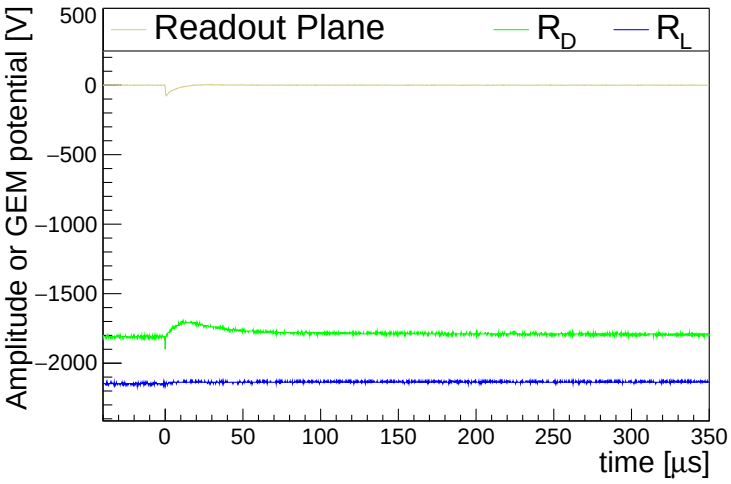

Figure 6.26: Measurement with the high voltage probes connected to the HV supply path to the GEM1 bottom and top electrode. In contrast to similar plots in this section, the probes are connected at the PS side of the loading (R_{L}) and decoupling resistor (R_{D}). Figure 6.25b shows the corresponding measurement with the HV probes connected close to the GEM electrodes. See the description of the detector settings in that figure.

boundaries have usually a width on the order of (several) 100 µm, therefore, the electric field will be lower as e.g. the field in the holes and no discharges between the top electrode of a discharged segment and a neighbouring segment at full voltage is expected.

6.6.3. Discussion

Comparing the measurements with the double-GEM set-up powered with the CAEN A1515 cascaded PS to the corresponding simulations, we find a similar shape of the evolution of the potentials. However, the absolute values differ significantly. Measurements, as those presented here with the with the mock-up, are necessary to see the actual potential changes. Based on these measurements the simulations could be further tuned to incorporate series and shunt capacitances as well as resistances and conductances to the end of achieving an accurate description of the set-up.

The voltage drop across the decoupling or loading resistor

We argued that we do not expect a discharge between a discharged segment and its neighbouring segment at full ΔU_{GEM}. However, the potential difference between all electrodes which change potential after a discharge and such elements which stay at constant potential, can drastically increase. Here we see the danger of additional discharges. An example for such an HV element with constant potential is the HV path, which brings the HV to a GEM segment but is decoupled by the loading or decoupling resistor from that segment. If the potentials at the GEM electrodes drop in response to a discharge charge, the decoupled supply circuit reacts delayed to potential changes of the GEM. This is why discharges can create substantial voltage differences between circuit elements and the GEM sides. Therefore the maximal possible potential difference and the physical distance between GEM electrodes and other, decoupled elements at HV have to be taken into account. The distance between such elements has to be high enough to avoid discharges at the highest potential differences, or insulating material has to be added where possible. In case of the mock-up U_{Top} of both GEM1 segments drops significantly after a discharge (Fig. 6.25a and Fig. 6.25b). However the high voltage path supplying all the segments of the top side of this GEM stays for some time at the set GEM1 top electrode potential. The comparison of Figure 6.26 and Figure 6.25b illustrates this. The potentials displayed in Figure 6.26 are measured on the PS side of the decoupling and loading resistor. There, the potential at the loading resistor remains

constant and the potential at the decoupling resistor features a drop. However, the latter drop is smaller than the actual drop of the GEM bottom electrode (Fig. 6.25b). Considering the potential difference across the loading resistor, we notice that this difference becomes larger than the set ΔU_{GEM1}. Therefore a too narrow separation between non isolated parts of HV supply path and the actual segments can lead to additional discharges.

During tests with a full size prototype of an outer readout chamber discharges between the HV path side of the loading resistor and the GEM top side have been observed. These are now mitigated by adding glue as insulation at the resistor itself.

Induced voltages on the anode plane

Fast potential oscillations with high amplitude are observed in the first micro seconds after a discharge. They are induced onto the anode plane and they will be induced onto the pads of the ALICE TPC ReadOut Chambers (ROCs), too.As compared to the coupling between anode plane and GEMs in our set-up, the smaller pad size will lead to a smaller capacitive coupling between the pads and the bottom side of an ALICE TPC GEM foil. This will result as well in a smaller amplitude of induced signals in each pad and therefore potential oscillations or fast voltage drops do not pose a threat to the front end electronics. Discharge measurements with a quadruple GEM stack and prototype electronics for the future TPC show this [151].

Effect of the decoupling resistors

On top of this decoupling resistors – as well as resistors in the output of the PS channels – dampen oscillations of the potentials after a discharge. We will see in Section 7.5 that such resistors also reduce the probability of observing secondary discharges.

In case $R_{\mathrm{D}} \neq 0$, the bottom potential of a GEM foil moves towards the value of the top potential after a discharge, while it stays constant otherwise. For GEMs, that are only segmented on the top side – as they are foreseen for the ALICE TPC upgrade – this change of U_{Bot} is present in all segments and induces a change of the potential at all the corresponding U_{Top}. It takes about 100 µs for the potential at the bottom side of the GEM to restore. Therefore, the same time is needed for the top potential of all the non-discharging segments to reach again their set value. Because of the capacitive coupling between different GEMs, such potential changes are not only observed at one GEM in the stack. Form the results with the mock-up we can say that ΔU_{GEM} of each non discharging GEM segment stays roughly constant after the discharge, but the absolute potential present at each electrode changes. The voltage differences across the gaps between GEMs are altered and thus the electric fields between GEMs change. These will influence the performance (e.g. gain) of the whole stack until all the potentials in the non-discharged segments are restored.

Possible influence on the ALICE TPC's data taking

In the future ALICE TPC ROCs the capacitive coupling of GEMs to each other will be different than in the mock-up, because the segments are not mounted in separate gas volumes. The potential changes of all segments in the discharging GEM will have a combined effect on the adjacent GEMs, which will be most likely less drastic as what we have seen with the mock-up. For example, a discharge in a GEM i will make the top potentials of all not discharging segments move to higher negative potentials as seen in Figure 6.25d. The potential at the bottom side of the GEM $i-1$, which is mounted on top of GEM i, will therefore rather move to more negative potentials and not feature a drop, like we have measured with the mock-up configuration (Fig. 6.25b and 6.25a). The exact effects have to be examined with actual segmented GEMs.

However, it is reasonable to assume that it takes at least ~ 100 µs until the bottom potential of a ALICE TPC GEM is restored after a discharge if this GEM is biased like the GEMs in the mock-up. For the same arguments as made before, the whole stack will be affected during this time. In the ALICE TPC operated with Ne-CO_2-N_2 (90-10-5) it takes an electron slightly about 90 µs to drift the full drift length, which is coincidently about the time needed to restore the potentials in all but the discharged segment. At 50 kHz lead-lead

data taking five events will be not properly recorded by a full GEM stack, which is recovering from a discharge.

In the very beginning of this chapter we argued based on the discharge probability measured in [24], that there will be on average 2 to 8 discharges per GEM stack per one month of lead-lead data taking. Therefore a possible loss of events, because of recharging GEMs seems to be no problem. The discharging segments need three orders of magnitude longer until they are fully recharged, however the active area of a segment contributes only a insignificant fraction to the full TPC readout area.

7. Secondary discharges

The phenomenon of secondary discharges was first observed in discharge studies similar to the ones described in Section 6.4, Chapter 6. After examining the induced signal of discharges on the anode plane, V. Peskov *et al.* were the first to report on this phenomenon and named it *delayed breakdown* [93]. Also, the authors of [104] observed *fully propagated discharges*, which seem to correspond to what we here refer to as secondary discharges. However, it is only mentioned in the single-GEM studies described in [27] that the probability of observing a secondary discharge is a function of the induction field (E_{Ind}), which is the electric field between GEM and anode plane. P. Gasik *et al.* found among other things, that 1) Secondary discharges occur after an initial discharge in a GEM, 2) Secondary discharges are only observed if E_{Ind} is larger than a certain threshold electric field, 3) When the set E_{Ind} has the same value like this threshold field, the probability of occurrence of secondary discharges rises fast from zero to one as E_{Ind} is further increased, and 4) The time between initial and secondary discharge decreases for increasing E_{Ind}. In the following we discuss this points extensively and present our measurements on the quest for a deeper understanding of the phenomenon of secondary discharges.

7.1. Chapter outline

The commissioning of the set-up described in Section 6.2 has been done to study *secondary discharges*. In this chapter we present these studies and their results.

In Section 7.2, the phenomenon of secondary discharges is introduced from measurements of such discharges in the induction gap of the single-GEM and double-GEM set-up with Ar-CO_2 (90-10) as counting gas. Our GEM(s) are equipped with 10 MΩ loading resistors and no decoupling resistor is used. Furthermore the set-up is biased with the independent channel power supply (CAEN 470 [123]). We reproduce previous measurements of the probability of occurrence of secondary discharges (Sec. 7.2.2) as a function of the induction field. We also measure the average time between initial and secondary discharge (Sec. 7.2.3). These previously known results of our collaborators are extended by dedicated studies of the anode plane signals and of the GEM potentials during secondary discharges (Sec. 7.2.1 and Sec. 7.2.4), which allow drawing further conclusions on the nature of the phenomenon. We then preform the same studies for secondary discharges in the transfer gap of the double-GEM set-up (Sec. 7.3). Secondary discharges are as well measured in Ne-CO_2-N_2 (90-10-5) and presented in Section 7.4. These results are compared to previous studies of secondary discharges in the induction gap relying on the two gas mixtures.

In Section 7.5 we discuss the measurements in [152]. These measurements show a way to mitigating secondary discharges using decoupling resistors. After, we present our measurements of secondary discharges while biasing the set-up with a cascaded power supply (CAEN A1515 [138]) and a voltage divider chain (Sec. 7.6). Studying these two ways of supplying the high voltage (HV) to the GEMs is particular interesting, because these are the two options for the HV supply system of the ALICE TPC GEM stacks.

In Section 7.7 we discuss, which consequences secondary discharges have for the operation of a GEM stack. Especially, we evaluate these consequences for ALICE TPC GEM stacks. Therefore we extrapolate from our findings with the double-GEM system and propose as well additional measurements.

Afterwards (Sec.7.8) we propose a mechanism responsible for secondary discharges, based on the results found during our studies of secondary discharges. A final summary is given at the end (Sec. 7.9).

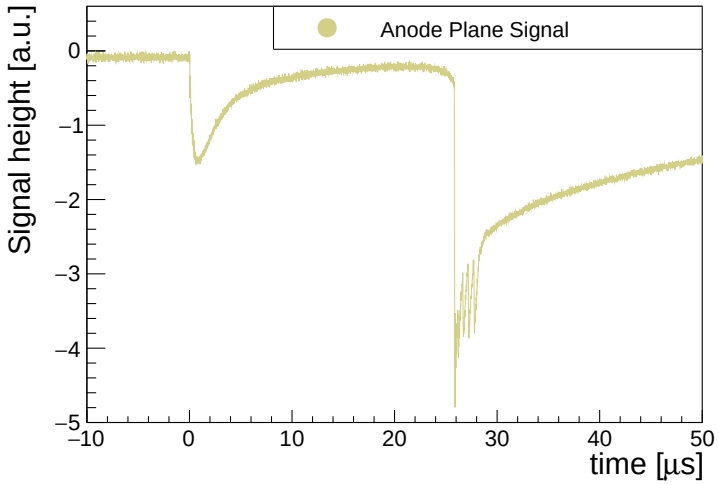

Figure 7.1: A discharge at $t \sim 0$ and a subsequent secondary discharge approximately 26 µs later. The initial discharge occurs in GEM2 in the double GEM set-up powered by the independent channel power supply. This signal is measured with an induction field and transfer field of 6.25 kV cm^{-1} and 2 kV cm^{-1}, respectively. A slight increase in the anode plane signal observed about 2 µs before the secondary discharge can be identified as a precursor of the secondary discharge. For this measurement we use a 10 kΩ resistor followed by a 12 dB T-type attenuator and we observe the signal then with an oscilloscope. A longer view of the same signal along with simultaneously recorded HV probe signals are shown in Figure 7.4b. Ar-CO_2 (90-10) is used as counting gas and we use no decoupling resistor, but a loading resistor of 10 MΩ ($R_D = 0, R_L = 10$ MΩ).

7.2. Secondary discharges in the induction gap

The experimental set-up introduced in Section 6.2, Figure 6.1 is used for the measurements presented in this section. We use it in the single-GEM as well in the double-GEM configuration. As counting gas always Ar-CO_2 (90-10) is used. Discharges are induced with the Rn source (Sec. 6.3.3) and high voltage settings resulting in a high gain as described in Section 6.2.2. We supply HV to the GEM electrodes using no decoupling resistor and a loading resistor of 10 MΩ. Furthermore the independent channel Power Supply (PS) is used [123].

In the anode plane signal, secondary discharges appear with an amplitude higher than that of the original discharge signal, as shown in Figure 7.1.[a] The first part of the signal, starting at $t = 0$, is the signal of an initial discharge in the GEM close to the anode plane and looks similar to all the discharges observed with an equivalent attenuation (e.g. Fig. 6.3). The secondary discharge at $t \sim 26$ µs has a different shape and a much higher amplitude. This shape and amplitude depend on the attenuation, the decoupling resistor, and the location of the secondary discharge, as will be discussed later on.

7.2.1. A precursor in the anode plane signal

After the signal of the initial discharge has decayed (Fig. 7.1) we observe a slight increase in the anode plane signal, which is visible at $t \sim 24$ µs in the figure. Then, at $t \sim 26$ µs the strong rise of the secondary discharge is observed. A similar rise can not be found in signals where no secondary discharge are observed. This rise is therefore likely to be a precursor of the secondary discharge. To the best of our knowledge, this has not yet been reported in published works on that topic.

[a] In this case the signal is attenuated with a 10 kΩ resistor and a 12 dB T-type attenuator. Different forms of attenuation obviously affect the amplitudes of the signals. Secondary discharges in the transfer gap result in different signal shapes.

7.2.2. Probability of occurrence

In order to quantify the occurrence of secondary discharges, the counting logic described in Section 6.2 is extended by another discriminator, gate and scaler. The significant difference in signal amplitude between the normal discharges in a GEM and secondary discharges is used to discriminate the two. We split the signal from the anode plane after the attenuating elements and feed it in two discriminators with different thresholds. A discharge signal higher than the respective set threshold enables a gate and is counted as either an initial or a secondary discharge. Each counter does not accept new signals as long as the gate is enabled and the gate length is chosen more than 100 µs longer than the longest time difference between an initial and secondary discharge.[b] No precondition, such as the occurrence of a previous discharge, is imposed on the counting of the secondary discharges. However, if a secondary discharge occurs before an initial discharge, it would increase both counters at the same time, due to its signal amplitude which is higher than the threshold of both discriminators.

A careful analysis of the counts and recorded waveforms shows that secondary discharges are only observed after an initial discharge. Secondary discharges are therefore never counted as the initial one, because the gate connected to the counter for initial discharges is already enabled from the previous normal discharge.

Measuring the secondary discharge probability

In Figure 7.2, different sets of measurement series are displayed. They are conducted with varying hardware configuration of single- as well as double-GEM set-up. For each configuration, the induction field ($\mathrm{E_{Ind}}$) is increased stepwise while the potential differences between all the other electrodes are kept constant. For each high voltage setting a measurement series is recorded, in which discharges are counted and different waveforms are stored.[c] The secondary discharge probability is calculated as

$$P_2 = \frac{N_{\mathrm{Dc}}^{\mathrm{Sec}}}{N_{\mathrm{Dc}}} \quad , \tag{7.1}$$

where N_{Dc} is the number of discharges during a measurement series and $N_{\mathrm{Dc}}^{\mathrm{Sec}}$ is the corresponding number of secondary discharges. Using $\delta(N_{\mathrm{Dc}}) = \sqrt{N_{\mathrm{Dc}}}$ and $\delta(N_{\mathrm{Dc}}^{\mathrm{Sec}}) = \sqrt{N_{\mathrm{Dc}}^{\mathrm{Sec}}}$, we estimate the error as

$$\begin{aligned} \delta(P_2) &= P_2 \cdot \sqrt{\left(\frac{\delta(N_{\mathrm{Dc}})}{N_{\mathrm{Dc}}}\right)^2 + \left(\frac{\delta(N_{\mathrm{Dc}}^{\mathrm{Sec}})}{N_{\mathrm{Dc}}^{\mathrm{Sec}}}\right)^2} \\ &= P_2 \cdot \sqrt{\frac{1}{N_{\mathrm{Dc}}} + \frac{1}{N_{\mathrm{Dc}}^{\mathrm{Sec}}}} \quad . \end{aligned} \tag{7.2}$$

When no secondary discharge is observed, we use $N_{\mathrm{Dc}}^{\mathrm{Sec}} = 1$ in the error calculation. Each point in Figure 7.2 is the result of one measurement series with a given HV setting. P_2 equals zero up until a given value of the induction field (Fig. 7.2). Then, data points show a steep rise in the secondary discharge probability up until $P_2 = 1$. From there, every discharge is followed by a secondary one. This rather typical onset curve for Ar-CO_2 (90-10) is as well observed as well in the single-GEM measurements presented in [27].

Onset of secondary discharges

To quantify at which electric field the discharge probability rises from zero to one, we define the *onset field* ($\mathrm{E_{Ind}^{On}}/p$) as the electric field at which P_2 reaches 0.5. Thus, the measurements

[b] After an initial discharge the GEM needs to recharge for more than 100 ms (Sec. 6.5.1, Fig. 6.17). The gate length is therefore not significant compared to the maximal discharge rate, which is limited by this recharging time. However, multiple secondary discharges are counted as one secondary discharge with this counting logic.

[c] Similar measurement series are done as well for changing transfer field ($\mathrm{E_T}$) (Sec. 7.3) and keeping the other fields and $\Delta U_{\mathrm{GEM}i}$ $i \in 1, 2$ constant.

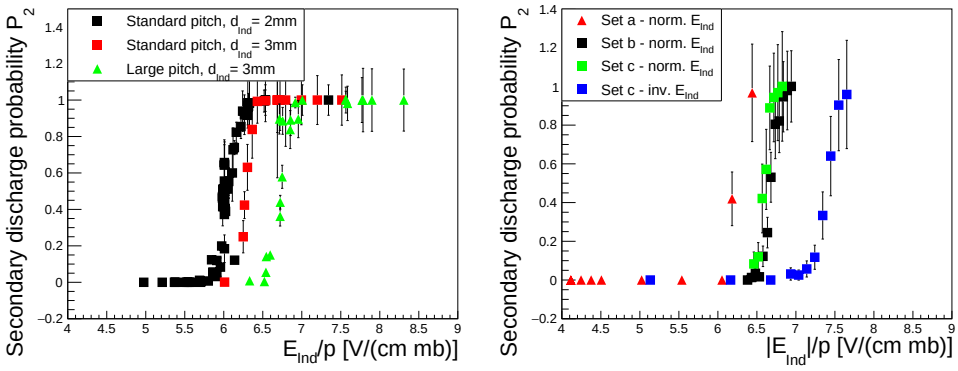

(a) Single-GEM configuration

(b) Double-GEM configuration

Figure 7.2: Secondary discharge probability as defined by (7.1) plotted against the induction field. Each point results from a series of measurements with the same HV settings. (a) A large pitch or a standard GEM and two different widths of the induction gap (d_{Ind}) are considered (single-GEM set-up) as well as (b) different standard GEMs (double-GEM st-up). In *Set a* and *Set. b* (respectively *Set b* and *Set c*) the same GEM1 (respectively GEM2) is used, while a different one is used for *Set c* (respectively *Set a*). The two series of *Set c* data points differ by the direction of the induction field, which is inverted for *Set c – inv.* E_{Ind}. For the double-GEM measurements, $d_{\mathrm{Ind}} = d_{\mathrm{T}} = 2\,\mathrm{mm}$ holds. For all the measurements in (a) and (b), the set-up is flushed with Ar-CO_2 (90-10) and a loading resistor of $10\,\mathrm{M\Omega}$, but no decoupling resistor, is used. The set-up is powered with the independent channel power supply [123]. The drift field is in all cases $400\,\mathrm{V\,cm^{-1}}$ and a transfer field of $500\,\mathrm{V\,cm^{-1}}$ (*Set a*, *Set c*) or $2\,\mathrm{kV\,cm^{-1}}$ (*Set b*) is applied. For all measurements with the double-GEM set-up, initial discharges are always induced in GEM2.

in Figure 7.2a yield onset fields of $(6.1 \pm 0.1)\,\mathrm{V\,cm^{-1}\,mbar^{-1}}$ and $(6.3 \pm 0.1)\,\mathrm{V\,cm^{-1}\,mbar^{-1}}$ in settings with the same standard GEM but a 2 mm and 3 mm wide induction gap, respectively. While using a Large Pitch (LP) foil and an induction gap width of 3 mm, an onset field of $(6.7 \pm 0.1)\,\mathrm{V\,cm^{-1}\,mbar^{-1}}$ is obtained. The difference between the measured $\mathrm{E}^{\mathrm{On}}_{\mathrm{Ind}}/p$ using the standard GEM is not significant, but the $\mathrm{E}^{\mathrm{On}}_{\mathrm{Ind}}/p$ we observe for the LP foil differs.

For the double GEM set-up (Fig. 7.2b), the measurements with the configurations denoted as *Set b* and *Set c* yield similar onset fields of $(6.6 \pm 0.1)\,\mathrm{V\,cm^{-1}\,mbar^{-1}}$ and $(6.7 \pm 0.1)\,\mathrm{V\,cm^{-1}\,mbar^{-1}}$, respectively. These two values are obtained with the same GEM in the position of GEM2. Only few data points are taken when repeating the experiment using another GEM as GEM2 (*Set a*). The onset field $\mathrm{E}^{\mathrm{On}}_{\mathrm{Ind}}/p = (6.2 \pm 0.2)\,\mathrm{V\,cm^{-1}\,mbar^{-1}}$, however, seems to have a lower value compared to the other settings.

Possible explanations for the observed range of onset field values

In experiments with the single- and double-GEM set-up the distributions of data points for different GEM configurations looks alike, except for different values of $\mathrm{E}^{\mathrm{On}}_{\mathrm{Ind}}/p$. All measured onset fields are in the range $\mathrm{E}^{\mathrm{On}}_{\mathrm{Ind}}/p \in [6.1, 6.7]\,\mathrm{V\,cm^{-1}\,mbar^{-1}}$, and therefore differ at most by 10 %.

We propose two possible explanations for this difference. First, the onset field depends on a parameter of the discharging GEM (e.g., the exact cross-section of the holes). In this case, it is hard to tell if a spread of 10 % between the $\mathrm{E}^{\mathrm{On}}_{\mathrm{Ind}}/p$ values of the different GEMs is reasonable. Second, the difference is due to a difference in d_{Ind}. The width of the induction gap is defined by the width of the GEM frame as well as of the spacers between the GEMs. The widths of the frames and that of the spacers are supposed to be 0.5 mm. However, the exact widths have not been measured. In measurements with a standard GEM in the single GEM set-up (Fig. 7.2a), very similar $\mathrm{E}^{\mathrm{On}}_{\mathrm{Ind}}/p$ are found for the two different values of the induction gap's width. Therefore a deviation of the spacers' widths of several percent as compared to their specified value seems unlikely. A statement about the precision of the GEM frame's width can not be made from the comparison of the $d_{\mathrm{Ind}} = 2\,\mathrm{mm}$ and 3 mm results. Bending of the GEM frames, when mounted into the detector, changes the effective d_{Ind} at different positions of the GEM. The way each GEM bends differs and is therefore a GEM dependent parameter, which influences the effective induction field. To explain the spread of the $\mathrm{E}^{\mathrm{On}}_{\mathrm{Ind}}/p$ values, a variation of less than 200 µm in the induction gap width is sufficient. This would result in a 10 % error on $\mathrm{E}_{\mathrm{Ind}}$ and hence $\mathrm{E}^{\mathrm{On}}_{\mathrm{Ind}}/p$. The uncertainty is a fully correlated systematic error for all measurement series, conducted with a particular GEM. It provides a likely explanation for the different onset fields. Effect of other GEM dependent parameters also can not be fully excluded.

Secondary discharges with inverse induction field direction

Secondary discharges are also observed when the direction of the induction field is inverted. From *Set c – inv.* E_{Ind}, we find an onset field of $-(7.45 \pm 0.10)\,\mathrm{V\,cm^{-1}\,mbar^{-1}}$, which differs from the onset field observed with the same GEM while using the normal field direction. In this case any effect due to a difference in the induction gap can be excluded, since the hardware is not changed. In conclusion, the absolute value of the onset field seems to depend on the field direction.

P_2 (non)dependency on other parameters

Using the single GEM set-up, different drift field values are tested between $180\,\mathrm{V\,cm^{-1}}$ and $560\,\mathrm{V\,cm^{-1}}$. Using the double GEM set-up, the transfer field is chosen to be between $700\,\mathrm{V\,cm^{-1}}$ and $1\,\mathrm{kV\,cm^{-1}}$. In these field ranges, no dependency of P_2 on the field above the discharging GEM is observed.

The voltage difference across the discharging GEM is varied between 400 V and 440 V, however, the observed $\mathrm{E}^{\mathrm{On}}_{\mathrm{Ind}}/p$ is not affected by this variation.

For some measurement series, a positive potential is applied to the anode plane and the GEM(2) bottom electrode is referred to ground. While doing so, no difference is identified as compared to the onset curves measured with the normal HV configuration. This indicates

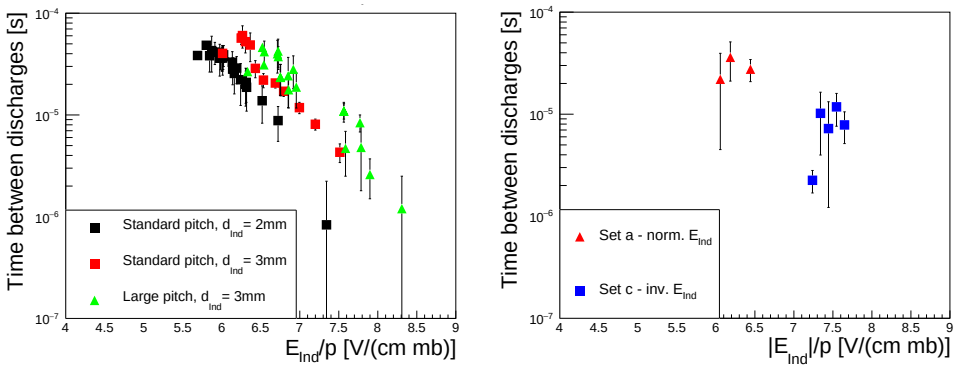

(a) Single-GEM configuration

(b) Double-GEM configuration

Figure 7.3: Average time $\langle t_{\mathrm{Sec}} \rangle$ between initial and secondary discharges for the measurements introduced in Figure 7.2. The same configurations of the experimental set-up apply.

that the occurrence of the secondary discharges does not depend on the absolute voltage at the GEM electrode.

All measurements, during which a parameter is varied but this variation is found not to affect $\mathrm{E}^{\mathrm{On}}_{\mathrm{Ind}}/p$, are included in Figure 7.2 (and Figure 7.3). The settings of the points shown in these figures, therefore, do not only differ by the parameters indicated in the figure. They partially differ as well in parameters, which have been found to not affect the occurrence of secondary discharges.

7.2.3. Time between initial and secondary discharge

Measurements of the average time between initial and secondary discharge $\langle t_{\mathrm{Sec}} \rangle$ are shown in Figure 7.3. We extract t_{Sec}, the time between initial and secondary discharge, from each waveform recorded during one measurement series. These times are then binned in a histogram. This procedure is applied to each measurement series. The different plotted $\langle t_{\mathrm{Sec}} \rangle$ correspond to the mean values of the t_{Sec}-distributions in these histograms. The corresponding RMS is chosen as error.

The time measurements obtained with the different single-GEM configurations in Figure 7.3a have their corresponding point in Figure 7.2a. All three sets of measurements displayed show the same functional behaviour, namely that $\langle t_{\mathrm{Sec}} \rangle$ decrease exponentially as the induction field increases. However, a shift between the three different curves can be seen, as it it observed for the three corresponding P_2 curves in Figure 7.2a. At the onset field value we measure a $\langle t_{\mathrm{Sec}} \rangle \in [20, 70]\,\mu\mathrm{s}$.

Few measurement series allowing for a t_{Sec} analysis are recorded with the double-GEM configuration. We therefore can not draw strong conclusions from Figure 7.3b. As compared to the corresponding onset field in Figure 7.2b, the $\langle t_{\mathrm{Sec}} \rangle$ values of *Set a* points fall in the same time range observed in the single GEM measurements (Fig. 7.3a). Comparatively, the time differences recorded with the inverted induction filed direction (*Set c – inv.* E_{Ind}) are smaller than 20 µs around the onset of secondary discharges. and therefore smaller than the $\langle t_{\mathrm{Sec}} \rangle$ observed with the normal induction field direction around the corresponding $\mathrm{E}^{\mathrm{On}}_{\mathrm{Ind}}/p$.

Comparing $\langle t_{\mathrm{Sec}} \rangle$ to drift times of charge carriers

Ions need about 16 µs to cross a 2 mm gap with an electric field of $6.7\,\mathrm{V\,cm^{-1}\,mbar^{-1}}$ in Ar-CO_2 (90-10), what can be calculated from our ion mobility measurements presented in Section 5.5.2 (Table 5.1). The corresponding drift time of electrons is smaller than 50 ns (Fig. 3.1). Therefore, the values measured for $\langle t_{\mathrm{Sec}} \rangle$ are only on the same order of magnitude as the expected ion drift time, considering an electric field of about $\mathrm{E}^{\mathrm{On}}_{\mathrm{Ind}}/p$. However, the low $\langle t_{\mathrm{Sec}} \rangle$ measured at $\mathrm{E_{Ind}}/p \sim 8\,\mathrm{V\,cm^{-1}\,mbar^{-1}}$ are significantly shorter than the corresponding ion drift time. Furthermore, most ions are produced in or in the vicinity of the GEM holes and

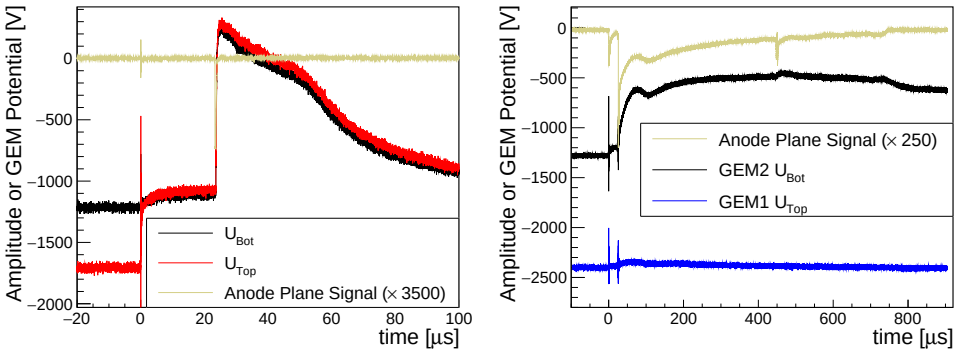

(a) Single-GEM configuration

(b) Double-GEM configuration

Figure 7.4: Secondary discharges in the induction gap with two different resistances from the anode plane to ground. In (a), a resistance of several Ω to ground is applied, as provided by the 12 dB t-type attenuator. A zoomed-out version of these signals is shown in Figure A.3. In (b), the resistance to ground is 10 kΩ. Here, the anode plane signal from Figure 7.1 is displayed on a longer time scale. Its amplitude is scaled up by 250, and two HV probe signals are also presented. These three signals are simultaneously recorded, while in (a), simultaneous HV probe measurements are overlaid with a different anode plane signal. Ar-CO_2 (90-10) is always used as counting gas and discharges are induced in GEM2. In both chases, no decoupling resistor and a loading resistor of 10 MΩ are used and the set-up is powered by the independent channel power supply.

therefore do not drift through the induction gap. Therefore, the ion drift back into GEM holes and thus the electric field in the vicinity of the GEM holes has to be considered, if ions are involved in the mechanism producing the secondary discharge. During the discussion of a possible mechanism creating for secondary discharge we will comment again on this thought (Sec. 7.8).

7.2.4. Potential changes during a secondary discharge

We study the GEM potentials during secondary discharges with high voltage probes. The probes themselves are described in Section 6.2.1. In Chapter 6, they are used to analyse potential changes caused by discharges at different electrodes in a GEM stack. During these studies of initial discharges (Sections 6.5 and 6.6) the performance of the probes is discussed as well.

The two plots of Figure 7.4 show an anode plane signals and HV probe measurements of GEM potentials as a secondary discharge occurs. In Figure 7.4a, the discharge at $t \sim 0$ results in $\Delta U_{\mathrm{GEM}} \sim 0$ and is followed by a secondary discharge at $t \sim 26\,\mu\mathrm{s}$. After the discharge, both GEM potentials move by 100-200 V towards more positive potentials, thus decreasing the induction field.

The recording of the GEM2 U_{Bot} potential in Figure 7.4b shows as well the previously described drop to more positive potentials after the initial discharge. The signal from the GEM1 top electrode picks up the potential oscillations happening during initial and secondary discharge, but is otherwise hardly affected. This shows that the secondary discharge in the induction gap does not have an effect on the second GEM, for a low value of the transfer field.

As we compare the evolution of the GEM potentials before the secondary discharge to measurements where no secondary discharge is present (e.g. Fig. 6.14a), we do not observe a difference. The precursor discussed in Section 7.2.1 (Fig. 7.1) does not have an equivalent in the GEM potentials. It happens in addition before the secondary discharge becomes visible in terms of a potential change. This can be an indication that the precursor and the subsequent secondary discharge are caused by an effect in the counting gas, which affects

potentials only as the secondary discharge occurs.

Different resistance in the ground path of the anode plane

Before discussing the exact evolution of the potentials during a secondary discharge, we have to point out the difference in the circuit used to obtain the measurements shown in Figure 7.4. The fact that in one case the single- and in the other the double-GEM configuration is used, is not relevant for the observed potential changes during a secondary discharge in the induction gap.[d] In both cases a 12 dB t-type attenuator splits the signal from the anode plane in two. One part of the signal is sunk to ground and the other part continues in the signal line. The exact splitting of the signal is defined by different resistors at the input, to ground and at the output of the attenuator. Together with the other resistances in the line, these resistors define the attenuation factor. The resistances of the attenuators considered in this work are at most a few 10 Ω. For the measurements depicted in Figure 7.4a, the signal is first fed into the attenuator and a 10 kΩ resistor is added at the output. Therefore, the anode plane has a resistance to ground of a few Ω. For the signals in Figure 7.4b the 10 kΩ resistor is placed ahead of the attenuator, hence the ground connection of the anode plane has a resistance of $\gtrsim 10\,\mathrm{k\Omega}$. In this case the effective attenuation of the signal is lower, as compared to the configuration where the resistor is connected after the attenuator as seen from the anode plane.

Low resistance ground path

When using the low resistance path to ground, only oscillations during the initial discharge are visible in the anode plane signal (Fig. 7.4a). In this configuration, secondary discharges result in a peak with a width smaller than 1 µs and a rise time of less than 20 ns. The peak amplitude in the figure is cut due to settings of the oscilloscope used for this recording.

The potential at the top side of the GEM drops to the bottom potential during the discharge, as discussed in Section 6.5. Therefore, the potential difference between U_{Top} and U_{Bot} gets close to zero and remains like this during the secondary discharge. Both potentials move in less than 1 µs towards the ground potential as the secondary discharge occurs. In the figure, they even seem to reach a positive value. We, however, think that the voltage can not move higher than the ground potential, and we observe here an overshoot as discussed during the introduction of the high-voltage probes (Sec. 6.2.1).

If U_{Top} and U_{Bot} drop to ground, this drop amounts to 1200 V, which is more than a factor two to three more than the voltage drops associated with a discharge in a GEM. Although in Section 6.5 we do not observe a AC response of the probes during our measurements of GEM discharges, it is not unlikely to see such a response for such large voltage changes.[e]

High resistance ground path

In case the anode plane's ground connection has a resistance of 10 kΩ, the evolution of the potentials differs (Fig. 7.4b). Due to the low attenuation and higher RC constant when compared to the previous setting, more than the AC part of the discharge signal is visible at the anode plane. The secondary discharge displays again a fast rise, but it lasts for several 100 µs. The potential on the bottom side of GEM2 does not exhibit a drop similar to that observed with a low resistance from the anode plane to ground (Fig 7.4a): It drops about half its original value in the measurement in Figure 7.4b. During the first $\sim 100\,\mu\mathrm{s}$ the shape of the anode plane signal and the measured GEM2 bottom potential can be observed to fit together as if they were two puzzle pieces.

Only two potentials are examined at the same time with the HV probes. The behaviour of the two potentials, which are not measured in Figure 7.4b (GEM1 U_{Bot} and GEM2 U_{Top}),

[d] If the same biasing and grounding schema is used for the set-up in either the single- or the double-GEM configuration, no difference in the shape of the anode plane signal can be observed during a secondary discharge. The same applies to HV probe signals. However, the time t at which the secondary discharge occurs differs of course among individual measurements.

[e] Figure A.3 features the same HV probe signals as in Figure 7.4a, this time with an AC response correction using the parametrisation from Table 6.1. The outcome is sensible, but there is no strong justification hinting that the parametrisation found for the calibration signals should apply to secondary discharges.

is known from similar measurements with the same configuration. Such measurements show that the potential at the GEM2 top electrode drops during the initial discharge towards the corresponding bottom electrode's potential. During the secondary discharge GEM2 U_{Top} has the same evolution as U_{Bot}, which is displayed in the figure. The behaviour of GEM1 U_{Bot} is the same as of the displayed GEM1 U_{Top} potential. However, its set value is 260 V less negative than the set value of GEM1 U_{Top}.

Transfer field after a secondary discharge in the induction gap

The voltage difference between the GEM1 bottom and the GEM2 top electrode in the detector increases during the initial discharge, due to the drop of GEM2 U_{Top}. Eventually, this voltage difference is even further increased, because GEM2 U_{Top} and U_{Bot} move towards less negative potentials during the secondary discharge. The problems associated with this increase are discussed in Section 7.7.

Interpretation of the measurements

The matching shapes of the anode plane signal and GEM2 bottom potential (Fig. 7.4b) as well as the large potential drop of U_{Bot} (Fig. 7.4a) presumably to ground, together suggest that there is a short circuit through the induction gap during a secondary discharge. The anode plane potential and the GEM potentials reach the same absolute value at this time. We therefore conclude that the secondary discharge is a full discharge of the induction gap. Different resistances to ground alter the exact voltage where the potentials meet. They also alter the development after the short circuit and therefore give rise to different signal shapes. This behaviour shows similarities to the way the GEM electrode potentials behave after an initial discharges when different decoupling resistors are used (Sec. 6.5.1).

Comparison to LTSpice simulations

Using LTSpice [142] we attempt to understand how different resistances to ground affect the evolution of the potentials at the anode plane and at the GEM2 top and bottom electrodes, when the induction gap is shortened 20 µs after an initial discharge. The secondary discharge is thus approximated in a similar way as the discharge in a GEM (Sec. 6.5.1): The two sides of the capacitor defining the induction gap are connected temporally, by enabling a switch. Except for this additional switch, the double-GEM set-up powered by the independent channel PS ($R_{\mathrm{D}} = 0$, $R_{\mathrm{L}} = 10\,\mathrm{M\Omega}$) is approximated in the same way in LTSpice as for the simulations in Section 6.5.1.

As the short circuit through the induction gap is established, the anode plane potential rises fast from ground towards the GEM bottom potential. The fall time after this rise depends on the resistance to ground and increases from a few ns (1 Ω) to a few µs (10 kΩ). After this rise of the anode plane potential, the bottom and top GEM potential drop together towards the ground potential. The magnitude of this drop decreases with an increase of the resistance from the anode plane to ground. The shape of the GEM bottom potential follows the shape of the anode plane potential, as it is observed as well for the measurements in Figure 7.4a and 7.4b.

However, the exact potential curves measured (Fig. 7.4) could not be reproduced by LTSpice simulations, but the qualitative behaviour fits the measurements. Furthermore, this qualitative behaviour matches only the one seen in measurements, if our LTSpice simulations feature a temporarily short circuit through the induction gap. Therefore, the hypothesis stating that the secondary discharge is a full discharge of the induction gap is supported by the simulation results.

The slight rise in the anode plane potential mentioned as a precursor of the secondary discharge (Fig. 7.1) is not observed in LTSpice simulation results. Furthermore, secondary discharges need to be created in our LTSpice simulations. The corresponding potential changes are e.g. not observed in the long term development of a discharge simulation. This is as well a slight hint that secondary discharges are an effect triggered in the counting gas after the initial discharge. (See the later Section 7.8). It is worth keeping in mind that LTSpice merely helps understanding the effects driven by the circuit elements and is not

expected to exactly reproduce the consequences of a short circuit through the 2 mm induction gap. Furthermore, the reaction of the power supply to (secondary) discharges differs between reality and simulation introducing deviations between measurement and simulation. This limitation is already mentioned in the previous Section 6.5.1, while discussing the simulation of a discharge in a GEM.

Closing remark

The signals considered in this analysis were good examples of potential and anode plane signals after a secondary discharge in the induction gap. Our findings thus apply to measurements of secondary discharges in general.

7.2.5. Wrap up: Secondary discharges in the induction gap

We observed secondary discharges after an initial discharge, if the induction field is higher than a certain threshold value. The occurrence probability for secondary discharge (P_2, Eq. 7.1) was observed to rise fast from 0 to 1 as the induction field is increased further than this threshold value (Fig. 7.2). We quantified this threshold field by the onset field ($\mathrm{E}^{\mathrm{On}}_{\mathrm{Ind}}/p$), which corresponds to the electric field where $P_2 = 0.5$ is reached. Different values of the onset field in the range $6.1\,\mathrm{V\,cm^{-1}\,mbar^{-1}} < \mathrm{E}^{\mathrm{On}}_{\mathrm{Ind}}/p < 6.7\,\mathrm{V\,cm^{-1}\,mbar^{-1}}$, were observed with different GEMs. For one GEM, the induction field was applied with the inverted field direction and a different (absolute) value of $\mathrm{E}^{\mathrm{On}}_{\mathrm{Ind}}/p = -(7.45 \pm 0.10)\,\mathrm{V\,cm^{-1}\,mbar^{-1}}$ was found. For the measurements with the normal induction field direction, the spread of the onset field values may be caused by variations of the induction gap's width, which is introduced by a slight bending of the GEM frames (Sec. 7.2.2).

The average time between initial discharge and secondary discharge ($\langle t_{\mathrm{Sec}} \rangle$) was found to decreases exponentially with increasing induction field (Fig. 7.3a). Around $\mathrm{E}^{\mathrm{On}}_{\mathrm{Ind}}/p$, average times in the range of $20\,\mu\mathrm{s} < \langle t_{\mathrm{Sec}} \rangle < 70\,\mu\mathrm{s}$ were observed (Sec. 7.2.3). In an electric field of $\mathrm{E}^{\mathrm{On}}_{\mathrm{Ind}}/p$, ions drifting through the induction gap have a drift time at the order of $\langle t_{\mathrm{Sec}} \rangle$. Electrons are three orders of magnitude faster.

We observed an precursor roughly $\sim 2\,\mu\mathrm{s}$ before the occurrence of a secondary discharge (Fig. 7.1, Sec. 7.2.1), which was not observed if no secondary discharge is measured.

An analysis of HV probe signals (Sec. 7.2.4) revealed that secondary discharges in the induction gap correspond to a full discharge of the gap. We were able to reproduce qualitative features of the evolution of different potentials during a secondary discharge with LTSpice simulations, only if we implemented a temporarily short circuit through the induction gap in the simulations. No precursor was seen in the potential measurements, in fact, the potentials at the GEM top and bottom electrode before a secondary discharge showed no difference to signals without a subsequent secondary discharge.

The observed $\mathrm{E}^{\mathrm{On}}_{\mathrm{Ind}}/p$ are significantly lower than the field strength necessary for gas amplification in the counting gas, namely Ar-CO_2 (90-10) (Sec. 3.3.2, Fig. 3.5). Furthermore, we did not observe an increase of the induction field prior to the secondary discharge. Because of the initial discharge, the voltage difference between the two GEM electrodes is compatible with zero at the time the secondary discharge occurs (see also Sec. 6.5.1, Fig. 6.14a). The observed precursor points to a process in the counting gas as responsible for the secondary discharge, although the fields in the detector are too low for classical breakdown mechanisms. Also, the time between initial and secondary discharge is too long, as compared to the time-scale of breakdown phenomena as the streamer mechanism (Sec. 3.3.6).

Our results confirm the findings by P. Gasik *et al.* [27] and extend the current knowledge on secondary discharges by the observation of the precursor and the proof that a secondary discharge in the induction gap corresponds to a temporarily, full breakdown of this gap. We refer to the very beginning of this Section 7.2 for exact experimental settings, because the occurrence of secondary discharges varies for different detector settings as is shown later in this chapter.

7.3. Secondary discharges in the transfer gap

We examine secondary discharges in the transfer gap using our set-up in the double-GEM configuration. This study complements our understanding of the effect of secondary discharges on the operation of a GEM stack. The hardware settings are the same as for the measurements presented in the previous Section 7.2: 1) $R_{\mathrm{L}} = 10\,\mathrm{M}\Omega$ and no decoupling resistor is used, 2) the set-up is powered with the independent channel power supply 3) Ar-CO_2 (90-10) is used as counting gas.

7.3.1. Probing the potentials at four GEM electrodes

Since only two potentials can be measured simultaneously, measurements such as those appearing in Figure 7.5 are repeated with the HV probes in different positions.[f] In addition, we can infer the potential at the bottom electrode of a GEM from the measured potential at the top electrode. We observed in Section 6.5, that the potential at a GEM's top electrode drops during a discharge to the value of the potential at the bottom electrode and afterwards both potentials evolve in a similar manner for some time. After the recharging of a GEM's top electrode has started, inferring the bottom potential from the top potential is no longer possible. However, the time until the recharging becomes visible in a potential measurement is longer than the time between initial and secondary discharge.

During most measurements with the double-GEM system we have focused on processes in the transfer gap. Simultaneous measurements of U_{Top} (GEM2) and U_{Bot} (GEM1) as in Figure 7.5 reveal the time evolution of the transfer field ($\mathrm{E_T}$), because $\mathrm{E_T}$ is defined as the difference between the potential at the GEM2 top and GEM1 bottom electrode over the width of the transfer gap. We realised only later the importance of measuring the potential at the GEM1 top electrode, because the information on discharges in GEM1 is needed for example for discharge propagation studies (Sec. 6.5.3).

7.3.2. Potential changes during a secondary discharge in the transfer gap

Figure 7.5 shows a measurement of the anode plane signal and of the potentials at the GEM2 top and GEM1 bottom electrode. At $t = 0$ GEM2 discharges, accordingly the top potential of GEM2 drops and a discharge signal is visible at the anode plane. The GEM1 bottom potential drops slightly due to the capacitive coupling of the GEM1 bottom electrode to the GEM2 top electrode. However, this drop is less severe than that observed with a decoupling resistor (Sec. 6.6.2). We can not tell from this measurement if the discharge in GEM2 is propagated to GEM1.

A secondary discharge is observed at $t = 25\,\mu\mathrm{s}$ and the GEM2 top potential and the GEM1 bottom potential approach each other. This behaviour is similar to that observed in Section 7.2.4 (Fig. 7.4) for secondary discharges in the induction gap, where the anode plane potential and the GEM2 bottom potential meet. For secondary discharges in the transfer gap (Fig. 7.5) the time interval of equal potentials seems to happen during the oscillations observed in the first µs of the secondary discharge. The frequency of these oscillations is around 25 MHz which is a similar value to that of the potential oscillations observed directly after an initial discharge (e.g. Fig. 6.12). Leaving these oscillations aside, the voltage drop (respectively increase) during the secondary discharge is similar to the voltage changes measured as a GEM discharges. We have shown (Sec. 6.5), that the probe measurement is not distorted (e.g. by bad impedance matching) for such voltage changes. Therefore, measurements as in Figure 7.5 allow to conclude that the GEM2 U_{Top} and GEM1 U_{Bot} potential approach each other in less than 100 V. A more precise statement can not be made, because the oscillations overlay the region of closest approach. Nevertheless, we propose that the secondary discharge in the transfer gap is a full discharge of that gap. This is based on the similarities of the potential evolution during a secondary discharge in the transfer gap to the same evolution during discharges in GEMs and during secondary

[f] The measurement in Figure 7.16 is done with the HV probes at the two GEM electrodes that are not probed for those measurements in Figure 7.5.

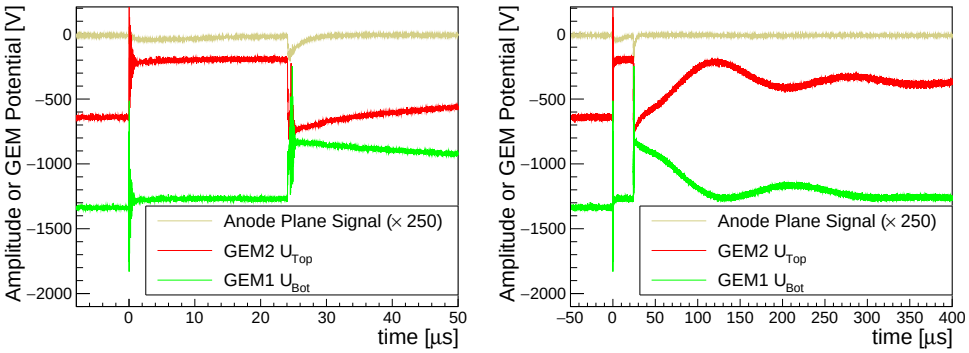

(a) (b)

Figure 7.5: Secondary discharge at $t \sim 25\,\mu s$ after a discharge in GEM2 ($t \sim 0$). The anode plane and high voltage probe signals of GEM2 top and GEM1 bottom potential are recorded simultaneously. (a) Zoom into the signals displayed in (b). The measurement is done with the double-GEM stack biased with the independent channel power supply ($R_L = 10\,M\Omega$, $R_D = 0$). The detector is flushed with Ar-CO_2 (90-10). As attenuation at the anode plane, a $10\,k\Omega$ in series with a 12 dB attenuator is used.

discharges in the induction gap.

Furthermore, we simulate the secondary discharge in the transfer gap with LTSpice [142], as temporary short circuit across the capacitor representing this gap, as is done for secondary discharges in the induction gap (Sec. 7.2.4). Such simulations suggest that the resistance across the gap can at most be of a few Ω in order to reach a so similar potential value at the GEM2 top and GEM1 bottom electrode, as is measured. The quantitative evolution of the potentials at both electrodes after they reached the same value is not well reproducible with LTSpice, as in Section 7.2.4. The arguments made before about the limitations of our LTSpice simulations apply here as well.

The anode plane signal of a secondary discharges in the transfer gap differs from that of a secondary discharge in the induction gap. This is due to the fact that in the first case the signal is caused by capacitive coupling of the anode plane to the GEM2 bottom electrode, while in the second case there is a short circuit across the induction gap. The system to count initial and secondary discharges is therefore adjusted to account for the lower amplitude of the secondary discharges. As described in beginning of Section 7.2.2, the counting logic discriminates between the two types of discharges based on their amplitude, without imposing a precondition on the secondary discharge. With the new counting logic, a discharge is counted as secondary discharge if it occurs not later than a few 100 µs after a previous initial discharge. The system is save against counting two initial discharges as initial and secondary discharge, because the minimal time between two discharges is $\gtrsim 100\,ms$. An isolated secondary discharge could be counted as primary discharge, however, no such isolated secondary discharge has been observed in the transfer gap. This is in line with the same observation for secondary discharges in the induction gap.

7.3.3. Necessity of a propagated discharge

As discussed before, we can infer the evolution of the GEM2 bottom potential, which is not measured in Figure 7.5, from measurements with similar settings and our experience with the potential evolution of discharges in GEMs. For a case as shown in Figure 7.5, GEM2 U_{Bot} follows GEM2 U_{Top} after the initial discharge and continues to do so during the secondary discharge in the transfer gap. Which in turn means that the induction field is increased during such a secondary discharge. The capacitive coupling between the top and bottom side of a GEM foil, may be responsible for this. GEM1 U_{Top} can not be accessed from the corresponding bottom electrode potential as mentioned before.

Like secondary discharges in the induction gap, secondary discharges in the transfer gap appear only after a discharge in a GEM. Since the induction gap is enclosed by a single GEM, secondary discharges in this gap must be triggered by discharges in the GEM that is closest to the anode plane.Considering only measurements, which are done with HV settings leading to an initial discharge in GEM2. Then, secondary discharges in the transfer gap either result from an effect related to the discharge in GEM2 or GEM1 plays a role as well.

Judging from all measurement series, where we observed the GEM1 top potential, we conclude that secondary discharge in the transfer gap are only observed when a (propagated) discharge happens in GEM1. This is best illustrated by measurement series with initial discharges in GEM2 and with HV settings, resulting on one hand in $P_{\mathrm{Prop}} \neq 1$ (Sec. 6.5.3, Eq. (6.11)) but having on the other hand a high set $\mathrm{E_T}$. All events without a propagated discharge from GEM2 to GEM1 do not feature a secondary discharge in the transfer gap, while all events with a propagated discharge do. During another measurement series, we apply HV settings with a high ΔU_{GEM1}, a low $\mathrm{E_T}$, a low $\Delta U_{\mathrm{GEM2}} < \Delta U_{\mathrm{GEM1}}$ and a high $\mathrm{E_{Ind}}$ to perform an additional test of the necessity of a propagated discharge. The setting results in initial discharges in GEM1 and a discharge propagation probability from GEM1 to GEM2 that is lower than 1. Furthermore, $\mathrm{E_T}$ is too low to have secondary discharges in the transfer gap, while $\mathrm{E_{Ind}}/p$ is higher than $\mathrm{E_{Ind}^{On}}/p$ for this GEM configuration. With these high voltage settings, secondary discharges in the induction gap are only observed if a discharge is propagated to GEM2. This shows that propagated discharges can induce secondary discharges.

Unfortunately, the role of the discharge propagation for secondary discharges in the transfer gap has been only discovered while writing this work. Therefore, the proof for the claim that *secondary discharges happen always in the gap below an initially discharging GEM* needs still to be delivered in measurements.

7.3.4. Accounting for the increase of $\mathrm{E_T}$ after a discharge

In analogy to the procedure from Section 7.2.2, we examine the occurrence of secondary discharges for changing transfer field for the different GEM configurations of the double-GEM set-up. During these measurements (Fig. 7.6.) the induction field is kept constant at a moderate value between $1\,\mathrm{kV\,cm^{-1}}$ and $1.125\,\mathrm{kV\,cm^{-1}}$. Before discussing these measurements, we motivate the unit used on the horizontal axis in the plots of figure 7.6.

$\mathrm{E_T}$ increase after a discharge in GEM2

$\mathrm{E_T}$ increases after the initial discharge in GEM2, due to the U_{Top} drop in GEM2 (e.g. Fig. 7.5). For a GEM powered with the independent channel PS and $R_{\mathrm{D}} = 0$ this drop has been quantified to be as big as ΔU_{GEM2} (Fig. 6.19). After GEM2 has discharged the transfer field is close to $\mathrm{E_T} + \Delta U_{\mathrm{GEM2}}/d_{\mathrm{T}}$, where in this case $\mathrm{E_T}$ corresponds to the transfer field supplied to the detector and $d_{\mathrm{T}} = 2\,\mathrm{mm}$ is the width of the transfer gap. After a discharge in GEM2 the GEM1 bottom potential moves as well towards more positive values, because of the capacitive coupling to GEM2. This effect slightly counteracts the increase of $\mathrm{E_T}$ after the discharge.

In order to reflect the fact that the transfer field after the discharge is higher than the set $\mathrm{E_T}$, we plot P_2 and $\langle t_{\mathrm{Sec}} \rangle$ against $(\Delta U_{\mathrm{GEM2}} \cdot d_{\mathrm{T}}^{-1} + \mathrm{E_T})/p$, where ΔU_{GEM2} (respectively $\mathrm{E_T}$) refers to the applied voltage difference across GEM2 (respectively the set transfer field). This quantity allows correlating the occurrence of secondary discharges to the applied HV. Furthermore, when the independent channel PS is used $(\Delta U_{\mathrm{GEM2}} \cdot d_{\mathrm{T}}^{-1} + \mathrm{E_T})/p$ is closer to that of the actual transfer field after a discharge than $\mathrm{E_T}/p$. Nevertheless, this definition overestimates the field in the transfer gap by the potential drop at the bottom GEM1 electrode, which has to be kept in mind when interpreting the electric field values in the transfer gap after the initial discharge.

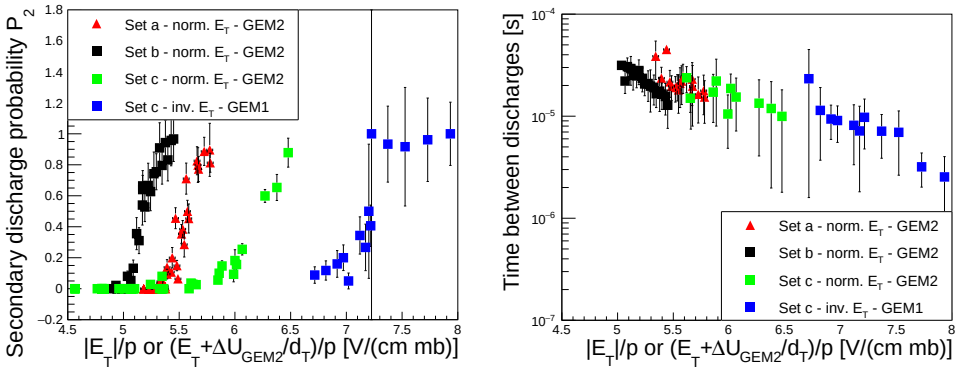

(a) (b)

Figure 7.6: (a) P_2 (Eq. (7.1)) and (b) $\langle t_{\mathrm{Sec}} \rangle$ (Sec. 7.2.3) for secondary discharges in the transfer gap plotted against the absolute value $|\mathrm{E_T}| \cdot p^{-1}$ (*Set c.– inv E_T*) and $\left(\mathrm{E_T} + \Delta U_{\mathrm{GEM2}} \cdot d_{\mathrm{T}}^{-1}\right) \cdot p^{-1}$ (all other settings), where d_{T} is the width of the transfer gap. The different settings *Set a* to *Set c* correspond to the use of different GEMs (same settings as in Figure 7.2b). *GEM2* or *GEM1* indicates whether discharges are triggered in GEM2 or GEM1. The hardware settings are $R_{\mathrm{L}} = 10\,\mathrm{M\Omega}$ and $R_{\mathrm{D}} = 0$, Ar-CO_2 (90-10) as counting gas, and the detector is powered with an independent channel power supply. Figure A.4 illustrates the same data as a function of $|\mathrm{E_T}| \cdot p^{-1}$.

7.3.5. Onset of secondary discharges

The distribution of P_2 points in Figure 7.6a shows the same steep onset as observed in the occurrence of secondary discharges in the induction gap.[g] From the onset curves we extract the onset field, as the value at which $P_2 = 0.5$. Doing so, the onset field for secondary discharges in the transfer gap ($\mathrm{E_T^{On}}/p$) is defined with respect to

$$\mathrm{E_T^{On}} p^{-1} = \frac{\Delta U_{\mathrm{GEM2}}}{d_{\mathrm{T}}} + \mathrm{E_T} p^{-1} \quad , \tag{7.3}$$

and not only with respect to the applied transfer field $\mathrm{E_T}$. In Table 7.1, $\mathrm{E_T^{On}}/p$ is listed for different GEM configurations together with the corresponding $\mathrm{E_{Ind}^{On}}/p$.

$\mathbf{E_T^{On}}/p$ for different GEM configurations

The potential at the GEM1 bottom electrode moves towards less negative potential, after an initial discharge in GEM2 occurs. This voltage drop is of up to 100 V. The transfer field in the detector is therefore up to $\sim 0.5\,\mathrm{V\,cm^{-1}\,mbar^{-1}}$ lower as compared to the value used to calculate $\mathrm{E_T^{On}}/p$ in Table 7.1. A similar drop in GEM2 U_{Bot} is also not taken into account for the calculation of $\mathrm{E_{Ind}^{On}}/p$, which is based on the set $\mathrm{E_{Ind}}$. The difference between $\mathrm{E_T^{On}}/p$ and $\mathrm{E_{Ind}^{On}}/p$ roughly corresponds to the difference between the actual electric field in the respective gap as a secondary discharge occurs because the onset fields in both gaps are similarly overestimated. From the different $\mathrm{E^{On}}/p$ in Table 7.1 it can be concluded that secondary discharges in the transfer gap occur at an electric field that is smaller to the one needed for secondary discharges in the induction gap.

The measured $\mathrm{E_T^{On}}/p$ support the previous claim that GEM1 is responsible for the secondary discharges in the transfer gap (Sec. 7.3.3). The values of $\mathrm{E_T^{On}}/p$ for the *Set a* ($\mathrm{E_T^{On}}/p = (5.5 \pm 0.1)\,\mathrm{V\,cm^{-1}\,mbar^{-1}}$) and *Set b* ($\mathrm{E_T^{On}}/p = (5.2 \pm 0.1)\,\mathrm{V\,cm^{-1}\,mbar^{-1}}$) GEM configuration (Table 7.1) are similar. During these two measurement campaigns the same GEM1, but a different GEM2 is used. The difference between $\mathrm{E_T^{On}}/p$ in *Set a* and *Set b* may be due to a slight change in d_{T} associated with the exchange of GEM2 and the reassembly

[g] For completeness, Figure 7.6 can be found in the Appendix (Fig. A.4), this time as a function of the applied transfer field.

Configuration		E_{Ind}^{On}/p $\left[\mathrm{V\,cm^{-1}\,mbar^{-1}}\right]$	E_{T}^{On}/p $\left[\mathrm{V\,cm^{-1}\,mbar^{-1}}\right]$
S, $d_{Ind} = 2\,mm$	single-GEM	6.1 ± 0.1	n/a
S, $d_{Ind} = 3\,mm$	single-GEM	6.3 ± 0.1	n/a
LP, $d_{Ind} = 3\,mm$	single-GEM	6.7 ± 0.1	n/a
Set a	GEM2	6.2 ± 0.2	5.5 ± 0.1
Set b	GEM2	6.6 ± 0.1	5.2 ± 0.1
Set c	GEM2	6.7 ± 0.1	6.2 ± 0.2
Set c – inv. E_{Ind}	GEM2	-7.45 ± 0.10	n/a
Set c – inv. E_T	GEM1		-7.2 ± 0.2

Table 7.1.: Onset field values for secondary discharges in the induction (Fig. 7.2) and transfer (Fig 7.6a) gap. The measurements listed in this table are extracted from sets of measurements using the detector configuration quoted in each corresponding figures. Discharges are induced in the GEM indicated in the second column. E_{T}^{On}/p is calculated following Equation (7.3). The value given in the last line is an exception. There E_{T}^{On}/p corresponds to the set transfer field divided by the pressure.

of the GEM stack.

In the GEM configuration denoted as *Set c* the same GEM2 as for *Set b* but a different GEM1 is used. The measured E_{T}^{On}/p with this different GEM1 (*Set c*) significantly differs from the observed E_{T}^{On}/p for the other two settings (*Set a*, *Set b*). This discrepancy seems too high, to be properly explained a random variation of the gap width, introduced when exchanging GEMs. Therefore, the high E_{T}^{On}/p for *Set c* seems more likely to be attributed to a parameter of this particular GEM1. One possibility is again that the way the GEM frame bends in the GEM stack is different compared to the other GEM1. However, a variation of almost 20 % between E_{T}^{On}/p for the GEM1 used in *Set a* and *Set b* when compared to E_{T}^{On}/p for the GEM1 used in *Set b* seems too high to be only explained by a different banding of the respective GEM frame.

E_{T}^{On}/p and E_{Ind}^{On}/p measured with the same GEM as GEM1 and GEM2

We observe that $E_{T}^{On}/p < E_{Ind}^{On}/p$ holds for all our measurements (Table 7.1). This is as well the case for onset fields (E_{T}^{On}/p and E_{Ind}^{On}/p) which are measured with the same GEM either in the GEM1 or in the GEM2 position.

The exact GEM, which is used as GEM1 in *Set a* and *Set b*, is used in measurements with the single-GEM set-up (*S*, $d_{Ind} = 2\,mm$ and *S*, $d_{Ind} = 3\,mm$ in Table 7.1), which have been discussed while examining discharges in the induction gap (Sec. 7.2.2, Fig. 7.2a). The measured E_{Ind}^{On}/p are as well significantly higher than the corresponding onset fields for discharges in the transfer gap.

It seems unlikely that this discrepancy is caused by a systematic overestimation (respectively underestimation) of the transfer (respectively induction) gap's width by 10-20 %. Variations up to 10 % seem likely if the bending of the GEM's frame is included, as discussed in the Section 7.2.2. However, we are comparing measurements with the same GEM, but in a different position in the GEM stack and the bending of a GEM frame is independent of the GEM's position in the stack. This speaks against an explanation, where the difference between the respective E_{Ind}^{On}/p and E_{T}^{On}/p value is due to uncertainties of the gap widths.

Considering the E_{Ind}^{On}/p and E_{T}^{On}/p discussed here for the same GEM as GEM2 and GEM1 and all results in Table 7.1, it is even harder to believe that a random variation of the gap width would always lead to $E_{T}^{On}/p < E_{Ind}^{On}/p$, as observed in practice for all GEM configurations.

Measurements with inverted transfer field

During the measurement with inverted transfer field direction and discharges in GEM1 (*Set c - inv.* E_T) a low GEM2 voltage is set, leading to no discharge propagation from GEM1 to GEM2. Since there is no change in the GEM2 top potential, we decided not to use

Equation (7.3) in this case, but calculate E_T^{On}/p from the applied E_T instead. The onset field value we observe in the transfer gap is compatible with the E_{Ind}^{On}/p, which is measured with the inverted induction field direction (*Set c – inv. E_{Ind}*, Table 7.1). This similarity is most likely due to the fact, that the two experiments with inverted field direction are very similar. In both cases, secondary discharges are happening in the gap below the initially discharging GEM and the field direction in this gap is inverted. Furthermore ΔU_{GEM} across the discharging GEM is in both cases similar and the absolute voltage on the low potential side of the respective gap stays roughly constant, due to the absence of a discharges in GEM2.

The resemblance of measurements with inverted induction and transfer field, respectively, questions once more why secondary discharges in the transfer gap occur at significantly lower electric field than the ones in the induction gap. We do not know the exact mechanism of the discharges in the gaps, i.e. the secondary discharges. It is therefore hard to judge how measurement with an inverted field direction can be compared to measurements with a normal field direction. If the same mechanism is responsible for the gap discharge in either field direction, all measurements should be affected in a similar way by e.g. differences in the with of the gaps or by a GEM dependent parameter. In this case $|E_T^{On}/p| < |E_{Ind}^{On}/p|$ would be expected.

Influence of the voltage difference across the GEM1 electrodes

The ΔU_{GEM} of the initially discharging GEM is quite similar for the experiments with inverted electric field in the two gaps. This illustrates a parameter that differs in the E_{Ind}^{On}/p and E_T^{On}/p measurements with the normal field directions. The original discharge in GEM2 happens when $\Delta U_{GEM2} \in [400, 420]$ V, while ΔU_{GEM1} is usually around 260 V.

In [152] secondary discharges are studied with our exact set-up. They measure E_T^{On}/p for secondary discharges in the transfer gap with initial discharges in GEM2 as well as initial discharges in GEM1. In both cases the initially discharging GEM is set to $\Delta U_{GEM} > 400$ V, while the other GEM is set to a ΔU_{GEM}, which is close to the onset of discharge propagation. No strong statement can be made on which fraction of discharges is propagated to the respective other GEM, however they observed discharge propagation. If we assume $(\Delta U_{GEM2} \cdot d_T^{-1} + E_T)/p$ is a good measure for the onset field in their measurements, they find a similar onset field around $E_T^{On}/p \sim 5.35\,\mathrm{V\,cm^{-1}\,mbar^{-1}}$ for both the cases, i.e. initial discharges in GEM1 and GEM2. This result is in line with our E_T^{On}/p for *Set a* and *Set b* (Table 7.1), which are measured with the very same GEM1. If the secondary discharge in the transfer gap is always induced by a (propagated) discharge in GEM1, their measurements show that the different ΔU_{GEM} does not influence the onset field. A different theory is therefore needed to explain that $E_{Ind}^{On}/p > E_T^{On}/p$. However, the fact that in [152] a very similar value of E_T^{On}/p is found for initially discharging GEM1 and GEM2 hints that the mechanism for secondary discharges is in both cases the same. However, discharge propagation is observed from GEM1 to GEM2 and vice versa, therefore no answer to the question which GEM is the main responsible for secondary discharges in the transfer gap can be taken from the result of [152] discussed here.

7.3.6. Average time between initial and secondary discharge

Data points in Figure 7.6b are obtained while studying $\langle t_{Sec} \rangle$ for secondary discharges in the transfer gap, in analogy to the study of such discharges in the induction gap (Sec. 7.2.3). We observe an exponential decrease of $\langle t_{Sec} \rangle$ for increasing transfer field, together with a shift of this exponential depending on E_T^{On}/p. This similar to the measured $\langle t_{Sec} \rangle$ for secondary discharges in the induction gap (Fig. 7.3). The distribution of the data points in Figure 7.6b is however not as well ordered as for the study of secondary discharges in the induction gap. A possible reason could be the method used to estimate the electric field in the transfer gap. The quantity on the horizontal axis in Figure 7.6b differs from the actual field present at the time of the secondary discharge.

For *Set b*, $\langle t_{Sec} \rangle \in [20, 40]$ µs is found at the corresponding E_T^{On}/p. The $\langle t_{Sec} \rangle \in [20, 40]$ µs for the other configurations at E_T^{On}/p are between about 25 µs and 10 µs. All these times are

smaller than those observed for secondary discharges in the induction gap. They however still coincides within their error bars.

Inverted field direction

The measurements with inverted transfer field can not be well compared to these with the inverted induction field, since, for the latter, not many data points are available (Fig. 7.3b). Nevertheless, for experiments with the inverted field direction, $\langle t_{\mathrm{Sec}} \rangle$ seems to be smaller at the value of the onset field, as compared to experiments with the normal field direction. This holds for secondary discharges in both gaps.

7.3.7. Wrap up: Secondary discharges in the transfer gap

We extended measurements on secondary discharges in the induction gap with measurements of such discharges in the transfer gap. Secondary discharges were observed in the transfer gap for transfer fields higher than a certain threshold value (Sec. 7.3.5). It was measured that there is a temporarily short circuit between the GEM1 bottom and the GEM2 top electrode as a secondary discharge happens in the transfer gap (Sec. 7.3.2). Therefore, secondary discharges in the transfer gap are full discharges of that gap.

Secondary discharges in the transfer gap have been found to exhibit the same qualitative behaviour than secondary discharges in the induction gap. We observed a steep increase of their occurrence probability (Fig. 7.6a) around the onset field $\mathrm{E}_{\mathrm{T}}^{\mathrm{On}}/p$. Furthermore the average time between an initial discharge and a secondary discharge decreases exponentially with increasing transfer field (Fig 7.6b). The $\mathrm{E}_{\mathrm{T}}^{\mathrm{On}}/p$ were always found to be systematically lower than the measured $\mathrm{E}_{\mathrm{Ind}}^{\mathrm{On}}/p$ (Table 7.1) and the actual electric field in the respective gaps is found to resemble this trend. An explanation for this observation was not found. The spread found between the $\mathrm{E}_{\mathrm{T}}^{\mathrm{On}}/p$ values, measured with different GEMs, is larger than the spread observed among the $\mathrm{E}_{\mathrm{Ind}}^{\mathrm{On}}/p$ values. In case the direction of the transfer field is inverted, a similar value of for $\mathrm{E}_{\mathrm{T}}^{\mathrm{On}}/p$ was observed as was found for $\mathrm{E}_{\mathrm{Ind}}^{\mathrm{On}}/p$ measured for inverted induction field.

In most of our experiments initial discharges were always happening in GEM2. It was realised with measurements of the GEM1 top electrode potential that secondary discharges only occur in the transfer gap, if there is a propagated discharge to GEM1. We therefore propose that secondary discharges happen always in the gap below a GEM, after that GEM discharged. Measurements of $\mathrm{E}_{\mathrm{T}}^{\mathrm{On}}/p$ for different GEMs in the GEM1 position support this proposal. However, additional measurements examining the role of discharge propagation in secondary discharges are needed to confirm this theory.

7.4. Secondary discharges in the baseline gas mixture

In order to complement the tests in Ar-CO_2 (90-10) presented in Sections 7.2 and 7.3, measurement series with Ne-CO_2-N_2 (90-10-5) are done as well. Measurements in this gas mixture are furthermore important for the ALICE TPC upgrade [23] and allow to estimate possible the occurrence of secondary discharges in the upgraded TPC. We use the same hardware configuration as we use in the studies described in the previous sections (Sections 7.2 and 7.3).

Figure 7.7 shows the result of these measurements. For comparison the Ar-CO_2 (90-10) results obtained with the same GEM configuration are indicated in the figure as well. The results from Figure 7.7a are already reported in [153].

We use the quantity in Equation (7.3) on the horizontal axis of the plots in Figure 7.7, to account for the voltage drop at the GEM2 top electrode during the initial discharge (see Sec. 7.3.4). Doing so, we find the onset field in the baseline gas mixture to be $\mathrm{E}_{\mathrm{T}}^{\mathrm{On}}/p = (4.50 \pm 0.15)\,\mathrm{V\,cm^{-1}\,mbar^{-1}}$ (Fig. 7.7a). This is notably lower than the corresponding measurement in Ar-CO_2 (90-10), namely $\mathrm{E}_{\mathrm{T}}^{\mathrm{On}}/p = (5.5 \pm 0.1)\,\mathrm{V\,cm^{-1}\,mbar^{-1}}$.

A similar trend is observed by P. Gasik *et al.* during measurements of secondary discharges in the induction gap, where the change from Ar-CO_2 (90-10) to Ne-CO_2-N_2 (90-10-5) also results in a lower value of the onset field [154, 155]. The relative difference between $\mathrm{E}_{\mathrm{T}}^{\mathrm{On}}/p$

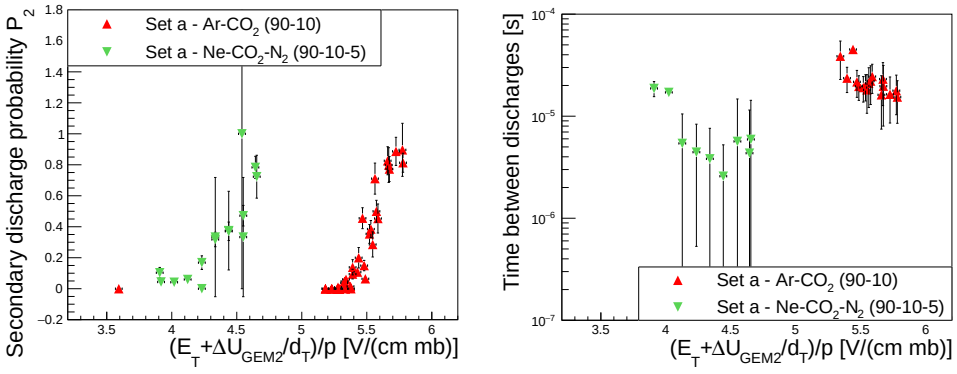

(a) (b)

Figure 7.7: Secondary discharges in the transfer gap measured with a Ne-CO_2-N_2 (90-10-5) gas mixture. (a) P_2 (Eq. (7.1)) and (b) $\langle t_{\mathrm{Sec}} \rangle$ (Sec. 7.2.3) are shown for different measurement series with varying high voltage settings. Data are displayed as a function of $\left(\mathrm{E_T} + \Delta U_{\mathrm{GEM2}} \cdot d_{\mathrm{T}}^{-1}\right) \cdot p^{-1}$. A thorough explanation can be found in Section 7.3.4. The same plot as a function of $\mathrm{E_T} \cdot p^{-1}$ can be found in Figure A.5. The hardware configuration used to inside and outside of the detector is similar as the one to obtain the data displayed in Figure 7.6. For comparison we show Ar-CO_2 (90-10) points obtained with the exact hardware settings, except for the counting gas.

as found here for the baseline and the argon-based gas mixture is of the order of 20 %. A similar relative difference is observed in the $\mathrm{E_T^{On}}/p$ obtained for *Set b* and *Set c* in Ar-CO_2 (90-10) (Table 7.1). The effect of changing the GEM configuration therefore seems to be comparable to that of changing the counting gas between the two discussed mixtures.

Figure 7.7b immediately shows that the average time between initial and secondary discharge is significantly smaller than the one found for measurements in Ar-CO_2 (90-10) (Fig. 7.6b). At an electric field in the transfer gap corresponding to the value of $\mathrm{E_T^{On}}/p$, $\langle t_{\mathrm{Sec}} \rangle < 10\,\mu\mathrm{s}$ is measured. For comparison: $\langle t_{\mathrm{Sec}} \rangle \gtrsim 20\,\mu\mathrm{s}$ is found with the same settings in Ar-CO_2 (90-10).

7.4.1. Connecting $\mathbf{E_T^{On}}/p$ and $\langle t_{\mathbf{Sec}} \rangle$ with gas properties

The potential measurements in Section 7.2.4 and 7.3.2 reveal that the secondary discharge is a full discharge of the transfer or induction gap. In Section 7.2.5 we already consider that the phenomenon of secondary discharges can not easily be correlated with a known description of breakdown of a gas filled gap. However, the precursor to the secondary discharge, which is observed in the anode plane signal (Fig. 7.1, Sec. 7.2.1) but has no equivalent in the measured potentials (Sec. 7.2.4), points to drifting charge carriers being involved in the creation of the secondary discharges.

While changing from Ar-CO_2 (90-10) to Ne-CO_2-N_2 (90-10-5) we observe an about a factor two shorter $\langle t_{\mathrm{Sec}} \rangle$, while $\mathrm{E_T^{On}}/p$ decreases by 20 %. The decrease of $\langle t_{\mathrm{Sec}} \rangle$ could be a result of the higher ion mobility in Ne-CO_2-N_2 (90-10-5), which is about a factor 1.6 larger as compared to Ar-CO_2 (90-10) (Table 5.1, Sec. 5.5.2). According to Magboltz [64], electrons in an electric field range between about $5\,\mathrm{kV\,cm^{-1}}$ to about $10\,\mathrm{kV\,cm^{-1}}$ are in Ne-CO_2-N_2 (90-10-5) about a factor two faster than in Ar-CO_2 (90-10). For higher electric field the electron velocity continues to grow more strongly in Ne-CO_2-N_2 (90-10-5) than in Ar-CO_2 (90-10). Observing short $\langle t_{\mathrm{Sec}} \rangle$ in Ne-CO_2-N_2 (90-10-5) as compared to Ar-CO_2 (90-10) is thus another hint that drifting charge carriers play a role for the creation of secondary discharges.

The first Townsend coefficient (e.g. Fig. 3.5) of the argon-based mixture is lower than the one of Ne-CO_2-N_2 (90-10-5) for electric fields smaller than $50\,\mathrm{kV\,cm^{-1}}$. The highest electric field at the moment of the secondary discharge will be most likely lower smaller

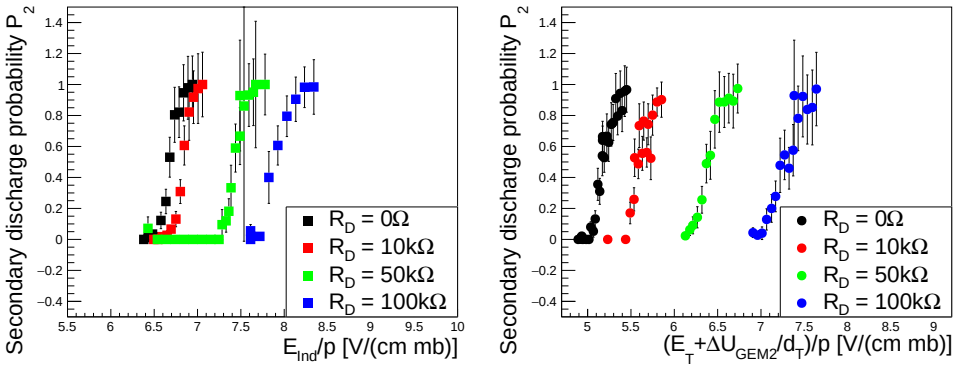

Figure 7.8: Secondary discharge probability P_2 as a function of (a) the induction field and (b) the transfer field is for different decoupling resistors. These results [152, 156] are obtained with a double-GEM set-up, powered with the independent channel power supply, a loading resistor of 10 MΩ, in Ar-CO_2 (90-10). The GEM configuration corresponds to *Set b* in figures 7.2b and 7.6.

than this number, because the GEM triggering the secondary discharge has discharged and its ΔU_{GEM} will be at most several 10 V. Therefore the decrease of $\mathrm{E_T^{On}}/p$, which is observed after changing from the argon-based mixture to Ne-CO_2-N_2 (90-10-5) could hint to an increase in the gas amplification factor while changing the gas mixture. We discuss the consequences for the ALICE TPC GEM stacks in Section 7.7.

7.5. Mitigation of secondary discharges with decoupling resistors

7.5.1. Shift of the onset and $\langle t_{\mathrm{Sec}} \rangle$ curves with different R_{D}

Previous work [152] examines the effect of the decoupling resistance on the onset field of secondary discharges in the induction and transfer gap. There, the measurements are performed with our double-GEM set-up, which has been used for most of the studies presented so far in this section. During the measurements in [152], the set-up is biased with the independent channel PS, and Ar-CO_2 (90-10) is used as counting gas. The $R_{\mathrm{D}} \neq 0$ points in Figures 7.8a, 7.8b and 7.9a are all obtained during the measurements for [152]. We discuss them in the following.

Figure 7.8 illustrates how the onset of the secondary discharges is affected by R_{D} when these discharges are studied in the induction (Fig. 7.8a) and transfer (Fig. 7.8b) gap, respectively. Instead of the set transfer field $\mathrm{E_T}/p$, we plot its approximation as defined in Equation (7.3).

The higher the resistance, the higher the electric field at which secondary discharges are observed. In Figure 7.9a, the onset field for each of the curves from Figure 7.8 is displayed. For secondary discharges in the induction and in the transfer gap, the onset field follows a linear trend as a function of the decoupling resistance. In [157], secondary discharges in the induction gap were studied for varying R_{D} and linear trend has been found, which was then confirmed by [152]. The dependency of $\mathrm{E_T^{On}}/p$ in R_{D} yields a steeper slope than that in $\mathrm{E_{Ind}^{On}}/p$. A systematic difference of the onset field in the transfer and induction gap is already observed without decoupling resistor (Sec. 7.3.5, Table 7.1).

Using a different GEM configuration

The GEM configuration for the measurement series shown in Figure 7.8 corresponds to *Set b* from Figure 7.2b and Table 7.1. Previous P_2 measurements with the *Set c* configuration for $R_{\mathrm{D}} = 0$ (Fig. 7.2b, Table 7.1) are shown again in Figure 7.9b, together with a few

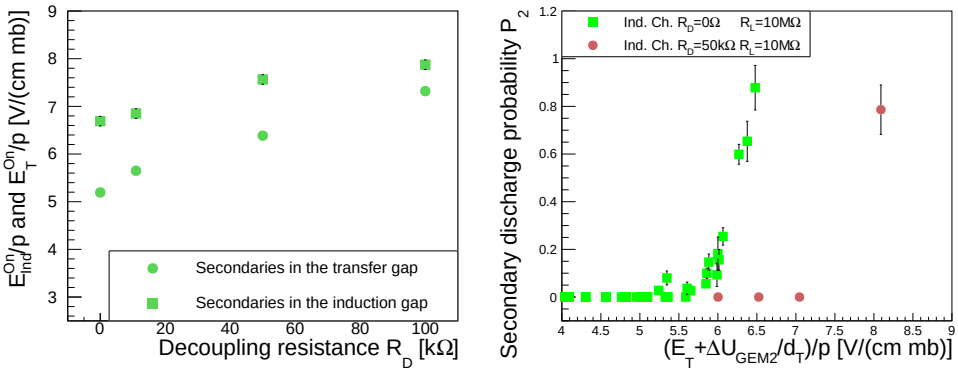

(a) (b)

Figure 7.9: (a) E^{On}_{Ind}/p and E^{On}_{T}/p) extracted form Figures 7.8a and 7.8b plotted as a function of R_D [152, 156]. Each point corresponds to the E^{On}/p of one set of data points in the corresponding figures. (b) P_2 (Eq. (7.1)) of secondary discharges in the transfer gap as a function of $\left(E_T + \Delta U_{GEM2} \cdot d_T^{-1}\right) \cdot p^{-1}$. For these measurements, the double-GEM set-up is biased with the independent channel power supply and another GEM1 is used as in Figure 7.8. Ar-CO_2 (90-10) is used as counting gas and E_{Ind} is always set to $1\,kV\,cm^{-1}$. In Figure A.6, the same data points are shown as a function of $E_T \cdot p^{-1}$.

points measured with the same GEMs but $R_D = 50\,k\Omega$. These points allow to roughly constrain the onset field: Adding the $50\,k\Omega$ resistor shifts the onset field from $E^{On}_T/p = (6.1 \pm 0.3)\,V\,cm^{-1}\,mbar^{-1}$ ($R_D = 0$) to a value comprised between $7.1\,V\,cm^{-1}\,mbar^{-1}$ and $8.1\,V\,cm^{-1}\,mbar^{-1}$. Judging from the data, E^{On}_T/p is most likely closer to the upper boundary of this range than to the lower one, as the only $P_2 \neq 0$ point is smaller than one and the rise of P_2 from zero to one happens usually over a small field range. The shift in E^{On}_T/p observed when changing the decoupling resistor from 0 to $50\,k\Omega$ is larger than the shift obtained in the *Set b* configuration (Figure 7.9a). Also, the E^{On}_T/p obtained without decoupling resistor is already larger for *Set c* (Fig. 7.9b) as compared to *Set b* (Fig. 7.8b).

We argue that the difference in E^{On}/p between different GEM configurations for $R_D = 0$ could be attributed to an uncertainty in the actual width of the gap (Sections 7.2.2 and 7.3.5). This change is introduced, because the frame of each GEM bends differently and therefore the gap width changes slightly. In case the actual gap width differs from the assumed width, a linear bias is introduced in the calculated electric field. This bias increases with the applied voltage difference. As a result, the stronger shift of E^{On}_T/p with R_D observed in *Set c* as compared to *Set b* may be attributed to this effect as well.

Time between secondary and initial discharge

The average time between initial and secondary discharge, $\langle t_{Sec} \rangle$, is analysed for all measurements in which waveforms are recorded. The procedure is similar to that presented in Section 7.2.3. In Figure 7.10a two $\langle t_{Sec} \rangle$ data sets are shown for different R_D with their corresponding P_2 data in Figure 7.8b. The average time between discharges when $R_D = 10\,k\Omega$ decays exponentially with increasing electric field in the transfer gap. As compared to the $R_D = 0$ data in the same figure, the curve is shifted on the horizontal axis. The shift matches the qualitative difference in E^{On}_T/p between the $R_D = 0$ and $R_D = 10\,k\Omega$ points. A similar shift has been observed for other $\langle t_{Sec} \rangle$ curves, with varying onset field (Figures 7.3, 7.6b and 7.7b). The curve corresponding to measurements with $R_D = 10\,k\Omega$ seems to decay faster as that with $R_D = 0$. However, the slope of both data sets are equivalent in the range of the uncertainties of the respective data points.

The $\langle t_{Sec} \rangle$ data for the measurements with the *Set c* GEM configuration is shown in Figure 7.10b. In Figure 7.9b the corresponding P_2 data are displayed. A single point exists for the $R_D = 50\,k\Omega$ measurement. No statement can thus be made about the evolution of

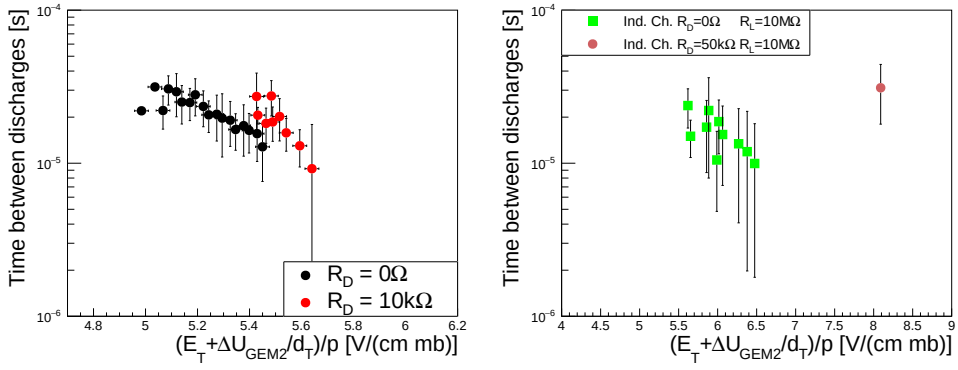

(a) (b)

Figure 7.10: Average time $\langle t_{\mathrm{Sec}} \rangle$ between discharges for (a) the two indicated data sets from Figure 7.8b and (b) the data sets from Figure 7.9b. The corresponding detector configuration is described in the caption of these figures.

$\langle t_{\mathrm{Sec}} \rangle$. However, the $R_{\mathrm{D}} = 50\,\mathrm{k\Omega}$ point seems shifted from the $R_{\mathrm{D}} = 0$ data, according to the difference in $\mathrm{E}_{\mathrm{T}}^{\mathrm{On}}/p$ among the tow data sets (Fig. 7.9b).

7.5.2. Potential evolution with and without a decoupling resistor

We consider the different evolution of the potentials at a GEM electrode after a discharge, before discussing a possible explanation for the $\mathrm{E}^{\mathrm{On}}/p$ shift for different R_{D} (Sec. 7.5.5). As a decoupling resistor is added to the set-up powered by the independent channel PS, the evolution of the potentials after a discharge is affected. In Section 6.5.1 different phases after a discharge have been identified:

$t \lesssim 0.1\,\mu\mathrm{s}$: During the discharge the potential at the GEM top and bottom electrode meet when a short circuit is established for a short time. In the absence of a decoupling resistor, U_{Top} drops by ΔU_{GEM} towards the potential at the GEM bottom electrode (Fig. 6.12).
However, when a decoupling resistor is used the drop of U_{Top} towards more positive potentials is less drastic. At the same time U_{Bot} moves to more negative potentials (Fig. 6.13).

$0.1\,\mu\mathrm{s} \lesssim t \lesssim 2\,\mu\mathrm{s}$: In case there is no decoupling resistor, the potentials stay rather constant and ΔU_{GEM} remains zero.
When $R_{\mathrm{D}} \neq 0$, U_{Top} and U_{Bot} move towards more negative potentials for a short period. During this time a certain potential difference of several 10 V builds up between the GEM bottom and top electrode.

$2\,\mu\mathrm{s} \lesssim t \lesssim 25\,\mu\mathrm{s}$: During this phase there is a potential difference between top and bottom electrode, which is found to range between zero and several 10 V ($R_{\mathrm{D}} = 0$). Both potentials, U_{Bot} and U_{Top}, move slightly to more positive values during this period. At approximately $t \sim 25\,\mu\mathrm{s}$ this potential difference has decayed again to zero or is compatible with zero.
For a set-up with decoupling resistor the absolute value of U_{Bot} and U_{Top} moves to more positive values again. However, ΔU_{GEM} decreases, but becomes not compatible with zero. Eventually the bottom potential reaches its set value again. This can happen as well a bit latter than $t \sim 25\,\mu\mathrm{s}$.

$t > 25\,\mu\mathrm{s}$: For $t > 25\,\mu\mathrm{s}$, the GEM maintains the current ΔU_{GEM} until the recharging of the top GEM electrode starts. In case no (respectively a) decoupling resistor is used, this potential difference is zero (respectively as big as a few 10 V).

This recap of our findings in Section 6.5.1 illustrates that there are two developments, which may influence the shift of $\mathrm{E}^{\mathrm{On}}/p$ with changing R_{D}. Both are due to the evolution of the

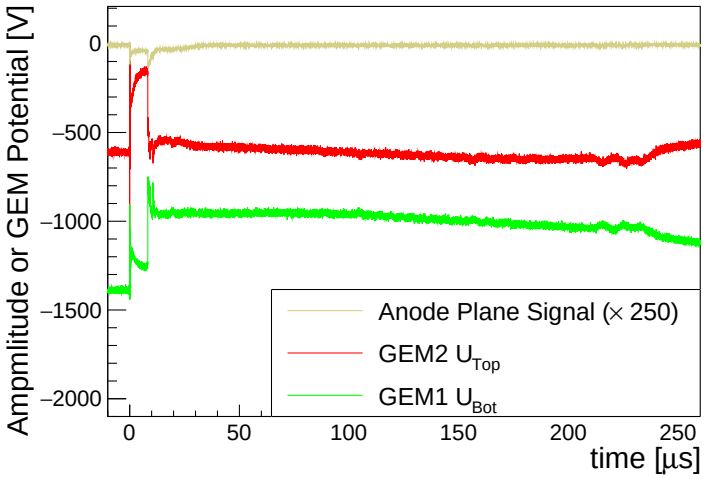

Figure 7.11: A secondary discharge at $t \sim 8\,\mu s$ in the transfer gap. The double GEM set-up is biased with $R_D = 10\,k\Omega$, $R_L = 10\,M\Omega$ and the independent channel power supply. The evolution of the potential after the discharge ($t = 0$) features the elements discussed in Section 6.5 and summarised in Section 7.5.2. In contrast to a situation where $R_D = 0$, GEM2 U_{Top} does not drop immediately to its least negative value and GEM1 U_{Bot} moves towards a more positive potential. During the secondary discharge, some differences also appear when compared to the set-up without decoupling resistor (Fig. 7.5). The GEM2 top and GEM1 bottom potential do not display oscillations and they do not meet. Furthermore the potential excursions induced by the secondary discharge last longer than compared to the $R_D = 0$ measurement.

GEM potentials after a discharge, which varies for different values of R_D. First, the time evolution of electric fields and, second, the time evolution of the ΔU_{GEM} depend thus on the value of R_D. In addition to the way the potentials evolve after a discharge, the RC constants in set-up change and so does the effect visible due to the capacitive coupling of the GEM1 bottom electrode to the GEM2 top electrode. The effect of the capacitive coupling is e.g. discussed using Figure 6.25.

7.5.3. GEM potentials between discharge and secondary discharge

Figure 7.11 illustrates some of the these features, we present here. A measurement of GEM2 U_{Top}, GEM1 U_{Bot} and the anode plane signal is displayed. In the measurement, the set-up is powered with the independent channel PS, $R_D = 10\,k\Omega$ and $R_L = 10\,M\Omega$. After the discharge in GEM2, we observe the GEM2 top potential to first drop rapidly and then smoothly towards more positive potentials. In a similar measurement with $R_D = 0$ (Fig. 7.5) the drop of the GEM2 top potential is instantaneous. In that measurement without decoupling resistor, the potential on the bottom side of GEM1 is not affected strongly, because the electrode is connected directly to the PS. However, in Figure 7.11 we notice the GEM1 bottom potential to have a more pronounced drop, which decays with a time constant of a few 10 µs. In the situation with decoupling resistor, the GEM1 bottom electrode is better decoupled from the PS and therefore more prone to the drop of the GEM2 top potential. The decay of the drop corresponds to the recharging time through R_D.

An enhancement of the induction field and a reduction of the transfer field is observed, checking the potentials for $R_D = 0$ (Fig. 7.5) against $R_D = 10\,k\Omega$ (Fig. 7.11). The reduction of the transfer field is most prominent for $t \lesssim 30\,\mu s$, while the enhancement of the induction field is only seen for a short period of time ($\sim 10\,\mu s$).

7.5.4. Effect of the decoupling resistor on the potential evolution during a secondary discharge

Comparing the experiments with $R_D = 0$ (Fig. 7.5) and $R_D = 10\,k\Omega$ (Fig. 7.11), we observe the development of the potentials during and after a secondary discharge in the transfer gap also differ. First, the oscillations seen in the first µs of the secondary discharge are absent when a decoupling resistors is in place. Second, the higher the decoupling resistor, the higher the potential difference between the GEM2 U_{Top} and GEM1 U_{Bot} (ΔU_{Gap}) after the secondary discharge. These two observations relate to the potential measurements of a discharging GEM. Introducing a decoupling resistor dampens the fast oscillations during and directly after the discharge and results in a larger ΔU_{GEM} (or ΔU_{Gap}). This analogy is as well evidence for the secondary discharges, being real discharges of the respective gaps. However, in case of the GEM discharge some oscillations always remained and the ΔU_{GEM} is found to be zero for a short time during the discharge. Furthermore, the absolute values of the potentials after secondary discharge stay roughly constant for a time of several 100 µs (Fig. 7.11) while, without decoupling resistors the restoration of the potentials after the secondary discharge starts earlier (Fig. 7.5b).

7.5.5. Possible contributions to the onset field change

The actual fields in the gaps

We measure E_{Ind}^{On}/p and E_T^{On}/p with respect to a quantity based on the set voltages. The actual electric field in the detector is different, because of the way the potentials evolve after an initial discharge. The difference between the actual electric field and the set voltages is larger in the situation where a decoupling resistor is used as compared to such situations without. We consider these differences for times up to several 10 µs after the initial discharge, which is the relevant time scale for the occurrence of secondary discharges.

The measure for the induction field is the set E_{Ind} in plots like Figure 7.8a. However, the actual E_{Ind} increases after an initial discharge when $R_D \neq 0$, while it stays constant or decreases when no decoupling resistor is present. In Figure 7.8b we quantify the transfer field by $\Delta U_{GEM2}/d_T + E_T$ (Eq. (7.3)), where the ΔU_{GEM2} and E_T are the set voltage difference across the sides of GEM2 and the transfer field, respectively. When no decoupling resistor is used, this quantity is close to the actual value of the transfer field after a discharge in GEM2 (Sec. 7.3.4). In a situation where the detector is biased with the independent channel PS and a decoupling resistor is used, the evolution of ΔU_{Gap} in the transfer gap changes as compared to the $R_D = 0$ case. Comparing e.g. Figures 7.11 and 7.5b reveals that ΔU_{Gap} and thus the actual transfer field is reduced in the time range relevant, after changing from $R_D = 0$ to $R_D = 10\,k\Omega$.

A shift to higher E_T^{On}/p and E_{Ind}^{On}/p for secondary discharges in both gaps is observed in [152] (Fig. 7.9a). However, introducing a decoupling resistor effectively increases the actual induction field and decreases the actual transfer field. In order to explain the common trend in E_T^{On}/p and E_{Ind}^{On}/p both fields should change in the same direction. Therefore, we think that the effect of the decoupling resistor on the evolution of ΔU_{Gap} of the respective gap is not the main reason why a shift to higher onset fields is observed for higher decoupling resistance. It is worth to mention, that using the actual fields in the detector for the plot in Figure 7.9a would increase the difference between the E_T^{On}/p and E_{Ind}^{On}/p points and not lead to a more similar slope.

Potential difference across the sides of the GEMs

The time evolution of the respective U_{Gap} is not the only one to be affected by a change of decoupling resistance. The ΔU_{GEM} also behaves differently after a discharge in presence or absence of a certain decoupling resistors (Sections 6.5.1 and 7.5.2). Unfortunately, we have not quantified the exact time evolution of ΔU_{GEM} for different decoupling resistors. From the studies summarised in Section 7.5.2 we however know that there are substantial differences in ΔU_{GEM} comparing the same set-up but once biased with and without decoupling resistor.

It seems reasonable that the development of a secondary discharge starts close to a discharging GEM, because the initial discharge is a necessary condition for a secondary discharge. In the vicinity of the GEM holes the actual electric field is a combination of the field in the GEM hole and the field in the gap (E_{Gap}) (Fig. 3.13b). As compared to the $R_D = 0$ case, ΔU_{GEM} in the time range of interest for secondary discharges is higher when a decoupling resistor is used. Although this ΔU_{GEM} is small when compared to the set potential difference across the GEM, its influence on the electric field in the vicinity of the GEM holes can be high. When the onset of secondary discharges is not only driven by E_{Gap} but also by a combination of E_{Gap} and that of the remaining ΔU_{GEM}, a higher E_{Gap} may be needed to compensate for $\Delta U_{GEM} \neq 0$.

In case the behaviour of E^{On}/p as a function of R_D is an indicator that the electric field in the GEM holes (E_{Hole}) plays a role in the creation of secondary discharges, this role may help explaining several other observations. The different E^{On}/p observed for individual GEMs could be related to a different hole geometry among the individual foils. Together with the ΔU_{GEM} after a discharge, the hole geometry defines the exact E_{Hole}. Previously, we proposed that a variation in the width of the gap, due to the bending of the individual GEM frames, may lead to a bias of the calculated electric field and therefore to the spread in E^{On}/p for secondary discharges in that gap (Sec. 7.2.2). However, the spread among the measured E_T^{On}/p is found to be rather high for this explanation to apply (Sec. 7.3.5). A difference in the GEM hole geometry among individual foils may be able to improve the explanation for the measured spread in E^{On}/p for different GEMs.

Furthermore, in our experiments with initial discharges in GEM2 we observe a systematic difference in the onset fields for secondary discharges in the transfer gap and in the induction gap (Sec. 7.3.5, Table 7.1 and Fig. 7.9a in the current section). Assuming our hypothesis is correct, that secondary discharges in the transfer gap are produced by discharges propagated from GEM2 to GEM1, this systematic difference may indicate that ΔU_{GEM1} is different as compared to ΔU_{GEM2} after an initial discharge. We think that there can be indeed a systematic difference between ΔU_{GEM1} and ΔU_{GEM2}, because the GEM1 potentials are affected at the same time by the propagated discharge and by the discharge in GEM2, due to the capacitive coupling to the GEM2 top electrode. The potentials at the top and bottom electrode of GEM2, on the other hand, are only affected by the discharge in GEM2.

However, dedicated measurements of these phenomena are necessary, exploring as well the effect of different R_D on ΔU_{GEM}. These measurements may help to gain more insight in the underlying mechanism, which is responsible for secondary discharges.

7.5.6. Wrap up: Decoupling resistors as way to mitigate secondary discharges

Adding decoupling resistors in the HV path to the bottom electrode of each GEM results in a higher onset field for secondary discharges with increasing resistance (Fig. 7.9a) as has been found in [152]. A linear fit to the E_T^{On}/p (respectively E_{Ind}^{On}/p) measured with different R_D yields a slope of $(20 \pm 2)\,\mathrm{V\,cm^{-1}\,mbar^{-1}\,\Omega^{-1}}$ (respectively $(12 \pm 1)\,\mathrm{V\,cm^{-1}\,mbar^{-1}\,\Omega^{-1}}$). The crossing with the E^{On}/p axis is in both cases compatible with the $R_D = 0$ measurement. We have shown furthermore, that the exact value of the slope depends as well on the GEM configuration used (Fig. 7.9b) in the measurement.

Based on the observed shift in E^{On}/p for different R_D, we propose to consider the remaining potential difference in a GEM after an initial discharge as parameter of the process responsible for secondary discharges (Sec. 7.5.5). More measurements are needed in order to explain why decoupling resistors shift the onset of secondary discharges to higher electric field values in the gaps.

Decoupling resistors are a suitable solution to make the occurrence of secondary discharges in an experiment less likely. For example the HV settings of the ALICE TPC GEM stacks (Table 4.1) have a $\Delta U_{GEM} \cdot d_T^{-1} + E_T$ as high as $5440\,\mathrm{V\,cm^{-1}}$. Considering an ambient pressure of 980 mbar, which is not unlikely for the CERN area, yields $(\Delta U_{GEM} \cdot d_T^{-1} + E_T)/p \gtrsim 5.5\,\mathrm{V\,cm^{-1}\,mbar^{-1}}$, which is higher than most of the E_T^{On}/p measured in Ar-CO_2 (90-10). Furthermore, we found that E_T^{On}/p decreases if the counting gas is changed from Ar-CO_2 (90-10) to Ne-CO_2-N_2 (90-10-5) for otherwise the same settings

i	Ind	GEM2	T	GEM1	D
R_i [MΩ]	0.48	0.881	3.126	0.8	2.8
ΔU_i [V]	202	370	1319	342	1197

Table 7.2.: Example setting of the voltage divider biasing the double-GEM set-up. For this particular setting, the input voltage is 3430 V and the current 428 µA. During our measurements, one HV probe is connected to the GEM1 bottom electrode and one to the GEM2 top electrode, therefore, the path to ground from these electrodes through the respective probe has to be considered. The ΔU_i are thus calculated with the given R_i and the resistance from the GEM1 bottom electrode (respectively GEM2 top electrode) to ground, which is $R_{\text{Probe 1}} + R_{\text{O}} = (345.5 + 1)\,\text{M}\Omega$ (respectively $R_{\text{Probe 2}} + R_{\text{L}} + R_{\text{O}} = (343.7 + 5 + 1)\,\text{M}\Omega$). R_{O} is the internal resistance of the oscilloscope. When $R_{\text{D}} \neq 0$, it is included in the calculation. To reach different E_{T}, different R_{T} ranging from 1.211 MΩ to 3.607 MΩ are used.

(Section 7.4). For the ALICE TPC ReadOut Chambers (ROCs) it is therefore mandatory to use decoupling resistors, to lower the risk of having secondary discharges. However, the size of the decoupling resistor has to be carefully optimised. When the chambers are operated at the ALICE TPC, the charges arriving at each GEM bottom electrode will be evacuated through the decoupling resistor. This current is expected to be as high as $5\,\text{nA}\,\text{cm}^{-2}$ [23] and therefore the decoupling resistors have to be chosen such, that the voltage drop across this resistor for such a current remains tolerable. In addition the ALICE TPC GEM stacks will not be powered by independent channel PS. Therefore the value of the decoupling resistor has to be optimised using a powering schema close to the future powering schema of the upgraded ALICE TPC.

7.6. Effect of different power supplies on the occurrence of secondary discharges

The future readout chambers of the ALICE TPC will be either supplied with cascaded power supplies or with voltage dividers, which are then powered by a power supply. In this section we examine the effect of different power supplies on the onset of secondary discharges. Secondary discharges in the transfer gap are thus examined when either the CAEN A1515 cascaded power supply [138] or a voltage divider (Sec. 3.5.5) biases the set-up. For these tests we always use the same GEM configuration, to ensure that the results are not due to effects related to the exchange of GEMs. Furthermore we compare our results with results shown in the previous sections. At the time of our measurements, a decoupling resistor of $R_{\text{D}} = 50\,\text{k}\Omega$ has been discussed for the future TPC. Therefore, we use such an according resistor in situations where $R_{\text{D}} \neq 0$. A loading resistor of 5 MΩ is used, because it is foreseen for the GEM stacks of the new ALICE TPC ROCs. The measurements are done in Ar-CO_2 (90-10).

The cascaded PS has already been introduced in Section 6.6. However, voltage dividers as possible way to power a GEM stack have only been mentioned briefly in Section 3.5.5 (Fig. 3.14). Therefore we discuss the particular voltage divider we use in our measurements in Section 7.6.1. The response of the GEM stack to discharges when powered with the divider is as well covered. In Section 7.6.2 and 7.6.3 we report then on the onset field and on the average time between discharges, respectively, measured for different power supplies and decoupling resistors.

7.6.1. Discharges while powering the set-up with a voltage divider

Voltage divider set-up

Our voltage divider is used to power all GEM electrodes and the drift cathode in the double GEM set-up. The voltage difference across the gaps between GEMs and across the GEM

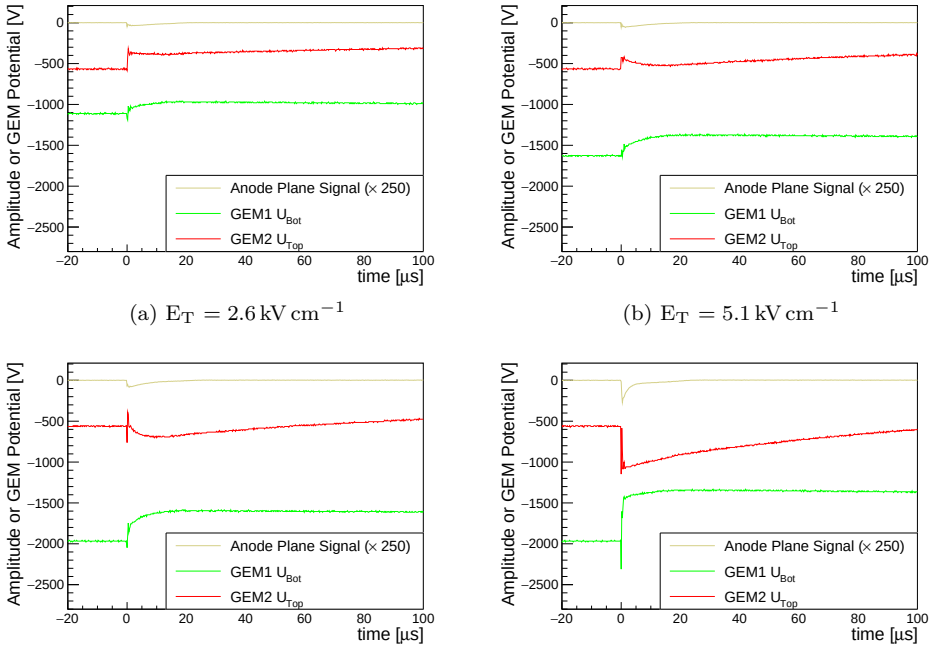

(a) $E_T = 2.6\,kV\,cm^{-1}$ (b) $E_T = 5.1\,kV\,cm^{-1}$

(c) $E_T = 6.7\,kV\,cm^{-1}$ (d) $E_T = 6.7\,kV\,cm^{-1}$

Figure 7.12: Each measurement corresponds to a simultaneous recording of the GEM1 bottom and GEM2 top potential as well as of the anode plane signal. During the measurements the set-up is powered by the voltage divider, while a loading resistor of 5 MΩ but no decoupling resistor is used. Discharges are always induced in GEM2. In (a) to (c) an initial discharge at $t \sim 0$ is observed. In (d) the discharge at $t \sim 0$ is followed by a secondary discharge in the transfer gap shortly after.

electrodes is defined by the voltage drop across each of these resistors. Therefore, the divider contains five resistors. Table 7.2 gives an example of the resistance values in the divider and of the resulting voltages. The voltage divider chain is itself powered by the independent channel power supply.

For the study of secondary discharges in the transfer gap, it is necessary to change E_T for different measurement series. To this end the resistor defining the voltage difference between the GEM1 bottom and GEM2 top electrode is changed. At the same time, the input voltage of the divider is adjusted to keep the remaining voltage differences at a value that is similar to the one before the change. The high voltage probes introduce a resistance to ground (Fig. 6.4) in parallel to the resistance in the voltage divider. All the resistors in the divider are chosen to provide the desired voltage drops across them, when one probe is connected to the GEM1 bottom electrode and one probe is connected to the GEM2 top electrode.

Response of the voltage divider to discharges

Figure 7.12 shows four different measurements of the GEM1 bottom and the GEM2 top potential for three different values of E_T as the set-up is powered with the voltage divider. The potentials at the GEMs react differently as a discharge happens than when the detector is powered by the cascaded or independent channel PS.[h] We observe that all the measurements with only a discharge (respectively with an initial and a secondary discharge) have the same time evolution, if the same HV settings are used.

[h] See the potential measurements in Sections 6.5 and 6.6.

Potential changes after the discharge of GEM2 and GEM1

The reaction of both measured potentials to the discharge in GEM2 ($t \sim 0$) is observed to change with E_T (Figures 7.12a, 7.12b and 7.12c). The drop of GEM2 U_{Top} towards less negative potentials decreases with increasing value of the transfer field. From a given set E_T, GEM2 U_{Top} even moves towards more negative potentials (Fig. 7.12c). In addition, an increasing transfer field results in a stronger drop of the GEM1 bottom potential towards less negative values. This dependence of the GEM2 top and GEM1 bottom potential changes on the set E_T or on the resistance of the voltage divider results either in the presence of approximately the same transfer field before and after the discharge (Fig. 7.12a) or in a decrease of E_T (Figures 7.12b and 7.12c) after the discharge.

To plot P_2 and $\langle t_{Sec} \rangle$ versus the field (Figures 7.13 and 7.14, respectively) we again use the definition of the effective transfer field (Eq. (7.3)), where $\Delta U_{GEM2} \cdot d_T^{-1} \cdot p^{-1}$ is added to $E_T \cdot p^{-1}$ before the discharge (Sec. 7.3.4). As a result all data obtained with the different power supplies are plotted against the same quantity, constructed from the applied HV settings. To discuss the origin of the secondary discharges it has to be kept in mind that the transfer field after a discharge is significantly lower than $(\Delta U_{GEM2} \cdot d_T^{-1} + E_T) \cdot p^{-1}$ when the set-up is biased with the voltage divider. In fact, it can even be lower than the set E_T.

No dedicated study of the GEM2 bottom and GEM1 top potentials has been done. Considering our results on discharge propagation (Sec. 6.5.3) and that $\Delta U_{GEM1} \sim 340\,V$ for all these measurements, we expect that a discharge is always propagated to GEM1 and hence that this GEM discharges as well. Furthermore we do not know how ΔU_{GEM} evolves as the GEMs are powered with the voltage divider. However, we think that this measurement can provide useful insights, especially considering the possible role of ΔU_{GEM} for the secondary discharge evolution.

Long term development of the potentials

We use the HV setting with $E_T = 6.7\,kV\,cm^{-1}$ as an example of the potentials' long term development. Starting from the situation displayed in Figure 7.12d the GEM2 top potential continues to move towards more positive values. After 100-200 µs it is smaller than its set value and after 400-500 µs the lowest value is reached, which is close to the set value of the GEM2 bottom potential. From there the recharging starts eventually. The GEM1 bottom potential needs more than a ms to reach again the value it had before-discharge .

We simulate our set-up with LTSpice [142] using the parameters described in Sections 6.5.1 and , but powered by a voltage divider as described in Table 7.2. Comparing the potential measurements in Figure 7.12 to the LTSpice simulations, we find the short-term time evolution of the potentials not to agree with the measurements. However, the values the GEM2 top and GEM1 bottom potential settles at for larger t are in agreement in the simulations and measurements. In simulations, these values are in fact already reached shortly after the discharge.

Secondary discharges

The potentials in Figure 7.12c and 7.12d are recorded with the same HV settings. In the latter plot, the discharge in GEM2 (and, supposedly, the propagated discharge in GEM1) at $t = 0$ is however shortly after followed by a secondary discharge in the latter plot. During the secondary discharge the potentials at the GEM1 bottom and at the GEM2 top electrode approach each other up to a few 100 V. A similar potential difference in the gap has been observed with decoupling resistors and the independent channel PS (Fig. 7.11). After the secondary discharge the GEM2 top potential recovers within ~ 200 µs the value it had in the absence of a secondary discharge. The GEM1 bottom potential takes several ms for this recovery.

7.6.2. Measurements of the onset field values

Figure 7.13 shows P_2 as a function of the set transfer field and ΔU_{GEM2} using the definition in Equation (7.3). The occurrence probability of secondary discharges P_2 is plotted for

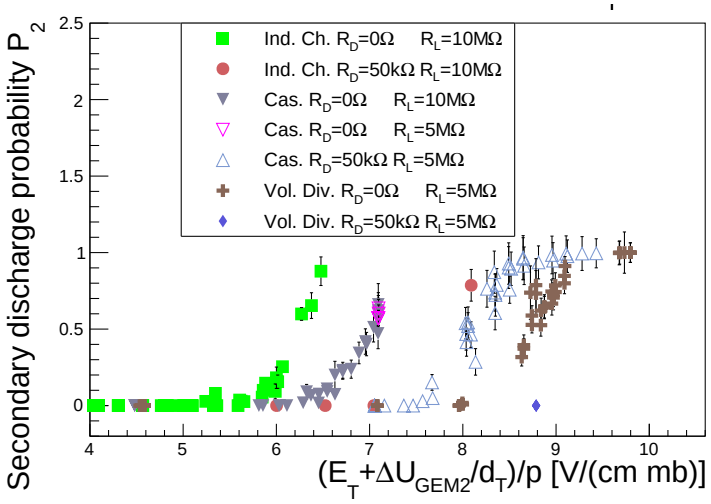

Figure 7.13: Occurrence probability P_2 (Eq. (7.1)) for secondary discharges in the transfer gap as a function of the transfer field and ΔU_{GEM2} as defined in Equation (7.3). (See Section 7.3.4 for a full explanation and Figure A.6 for the same plot as a function of $\mathrm{E_T} \cdot p^{-1}$.) The points result from measurement series in Ar-CO_2 (90-10) with the double-GEM set-up either biased by the independent channel power supply (PS) (*Ind. Ch.*), the cascaded PS (*Cas.*) or a voltage divider (*Vol. Div.*). The *Set c* GEM configuration (Fig. 7.6) is always used. Points from previously discussed measurements (Fig. 7.9b) are shown here as *Ind. Ch.* $R_D = 0$ $R_L = 10\,\mathrm{M\Omega}$ and *Ind. Ch.* $R_D = 50\,\mathrm{k\Omega}$ $R_L = 10\,\mathrm{M\Omega}$. For all measurements, $\mathrm{E_{Ind}}$ is set to $1\,\mathrm{kV\,cm^{-1}}$ and discharges are always induced in GEM2. The $\langle t_{\mathrm{Sec}} \rangle$ corresponding to the P_2 data displayed here are reported in Figure 7.14.

	$R_\mathrm{D} = 0$	$R_\mathrm{D} = 50\,\mathrm{k\Omega}$
Ind. Ch.	6.1 ± 0.3	$7.1 < \mathrm{E_T^{On}}/p < 8.1$
Cas.	7.1 ± 0.2	8.1 ± 0.2
Vol. Div.	8.8 ± 0.1	$\mathrm{E_T^{On}}/p > 8.8$

Table 7.3.: Onset field extracted from the sets of measurements in Figure 7.13. All values are in $\mathrm{V\,cm^{-1}\,mbar^{-1}}$. Since no difference in $\mathrm{E_T^{On}}/p$ is observed for $R_\mathrm{L} = 5\,\mathrm{M\Omega}$ and $R_\mathrm{L} = 10\,\mathrm{M\Omega}$, they are not separated here.

measurements where either the cascaded PS, or the voltage divider or the independent channel PS is used.[i] All measurements are done with the same GEM two GEMs as GEM1 and GEM2. The shape of the different onset curves shows the same fast rise from zero to one at a given $\mathrm{E_T^{On}}/p$ as observed in similar measurements in Sections 7.3.5, 7.4 and 7.5.1. In Table 7.3, the onset field values extracted from these data are listed.

Differences with the cascaded and independent channel PS

Changing the value of the loading resistor from $5\,\mathrm{M\Omega}$ to $10\,\mathrm{M\Omega}$ ($R_\mathrm{D} = 0$) does not affect the onset field measured with the cascaded PS (Fig. 7.13). However, introducing a decoupling resistor of $50\,\mathrm{k\Omega}$ increases the onset field by $1\,\mathrm{V\,cm^{-1}\,mbar^{-1}}$.[j] A similar increase with R_D has been observed in Section 7.5.1 with a different GEM configuration and the independent channel PS (Fig. 7.9a).

For the GEM configuration considered here, the $R_\mathrm{D} = 0$ and $R_\mathrm{D} = 50\,\mathrm{k\Omega}$ data series

[i] The data series recorded with the independent channel PS have been discused previously in this chapter and are displayed in Figures 7.10b and 7.9b.

[j] At a pressure of 970 mbar relevant for our measurements, $1\,\mathrm{V\,cm^{-1}\,mbar^{-1}}$ corresponds to an increase of $\mathrm{E_T^{On}}/p$ by $970\,\mathrm{V\,cm^{-1}}$.

measured with the independent channel PS indicate an even stronger increase of the onset field with decoupling resistance (Fig. 7.13). For $R_D = 0$, the onset field using the cascaded PS is $1\,V\,cm^{-1}\,mbar^{-1}$ higher, than the one measured using the independent channel PS. When $R_D = 50\,k\Omega$ is used, E_T^{On}/p seems to be similar regardless whether the cascaded PS or the independent channel PS is biasing the set-up. With a decoupling resistor the GEMs are better decoupled from the respective PS and for increasing R_D the evolution of the GEM potentials is less affected by the reaction of the power supply to a discharge. Therefore, it seems to be sensible that the E_T^{On}/p of the two power supplies approach each other for higher R_D, as observed for the E_T^{On}/p measured with the independent channel and the cascaded PS ($R_D = 50\,k\Omega$). Following this argumentation, a measurements of E_T^{On}/p at even higher R_D with the two power supplies should agree even better and a similar effect should be observed for E_{Ind}^{On}/p when using the two power supplies and different R_D.

We think that the difference in E_T^{On}/p measured for the independent channel and the cascaded PS is due to the different evolution of ΔU_{GEM} after a discharge, which is observed while using either of the two PSs. The cascaded PS behaves with $R_D = 0$ similar to the independent channel PS with $R_D \neq 0$ (Sections 6.5.1 and 6.6.1). Based on the shift of the onset field while introducing a decoupling resistor, the cascaded PS is thus expected to have a higher E^{On}/p for secondary discharges than the independent channel PS for otherwise similar settings.

E_T^{On}/p measured with the voltage divider

When the set-up is powered with the voltage divider ($R_D = 0$), an even higher onset field of $E_T^{On}/p = (8.8 \pm 0.1)\,V\,cm^{-1}\,mbar^{-1}$ is observed as compared to the same set-up powered with the cascaded PS ($E_T^{On}/p = (7.1 \pm 0.2)\,V\,cm^{-1}\,mbar^{-1}$) or the independent channel PS ($E_T^{On}/p = (6.1 \pm 0.3)\,V\,cm^{-1}\,mbar^{-1}$) (Table 7.3).[k] The reason for the high E_T^{On}/p observed with the voltage divider may be related to the fact that the transfer field is effectively reduced after a discharge if the voltage divider is used (Sec. 7.6.1). With the cascaded or independent channel PS a voltage drop of the potential at the GEM2 top electrode is observed after a discharge, while when the voltage divider is used, the GEM2 top potential increases (towards more negative potentials) for high values of set E_T (Fig. 7.12).

We can not comment on a possible influence of the ΔU_{GEM} on the observed E_T^{On}/p with the voltage divider, because we have not measured it.

For increasing R_D an increase of E_T^{On}/p is observed with the voltage divider (Fig 7.13, Table 7.3). However, the value of the onset field has not been quantified. For a decoupling resistor of $50\,k\Omega$ it is only confirmed that $P_2 = 0$ at the electric field corresponding to E_T^{On}/p for the set-up without decoupling resistor.

P. Gasik *et al.* have shown that the onset field for secondary discharges in the induction gap is as well higher when a voltage divider is used, as compared to measurements with an independent channel PS [27]. A study of the GEM potentials for high induction field can show whether there is as well an effect reducing the induction field after an initial discharge or if the high E_{Ind}^{On}/p observed by P. Gasik *et al.* is caused by a different effect, e.g. a peculiarity of the ΔU_{GEM} evolution after a discharge, which is present for GEMs powered with a voltage divider.

7.6.3. Measurement of the average time between initial and secondary discharge

In Figure 7.14, the $\langle t_{Sec} \rangle$ corresponding to the P_2 from Figure 7.13 are reported. All $\langle t_{Sec} \rangle$ curves for the different power supplies are shifted with respect to their onset field. Only the *Ind. Ch.* points however exhibit an exponential decay for increasing electric field. The other time distributions are compatible with a constant $\langle t_{Sec} \rangle$. For each curve in Figure 7.14, we find the $\langle t_{Sec} \rangle$ value at the electric field value corresponding to E_T^{On}/p to be in the range of $\sim 10\,\mu s$ to $40\,\mu s$, except for the measurements with the voltage divider. When the set-up is

[k] The relative difference between the E_T^{On}/p obtained with the different power supplies does not change if the set E_T is used on the horizontal axis of Figure 7.13, because ΔU_{GEM2} is similar in all measurements. The corresponding plot can be found in the Appendix, Figure A.6.

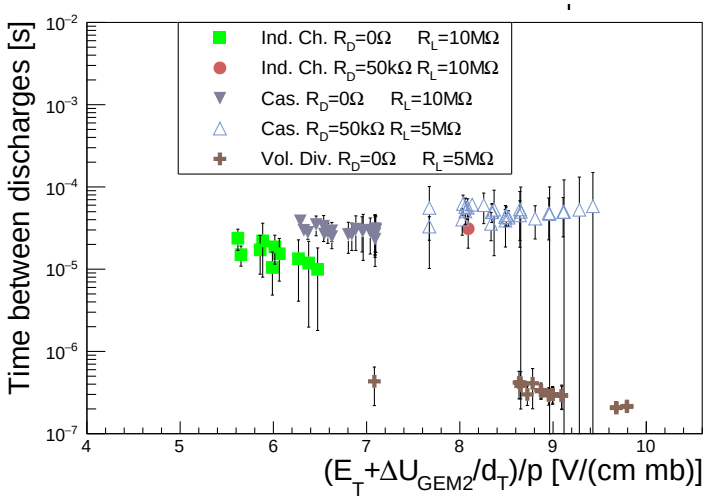

Figure 7.14: $\langle t_{\mathrm{Sec}} \rangle$ (Sec. 7.2.3) of secondary discharges in the transfer gap as a function of the transfer field and ΔU_{GEM2} (Eq. (7.3)). (A motivation is provided in Section 7.3.4.) The same plots as a function of $\mathrm{E_T} \cdot p^{-1}$ can be found in Figure A.6. The data result from the same measurements as the P_2 data from Figure 7.13. The detector settings are listed in the caption of that figure.

powered with the voltage divider chain, $\langle t_{\mathrm{Sec}} \rangle$ is always less than 1 µs.

When the observed $\langle t_{\mathrm{Sec}} \rangle$ are due to the movement of charger carries, the measurements with different power supplies show that this motion is not proportional to the field in the transfer gap. The times measured while the voltage divider is powering the set-up would otherwise be closer to or even larger than the times measured with the other power supplies. Therefore the distribution of the different $\langle t_{\mathrm{Sec}} \rangle$ may be due to the motion of charge carriers in an electric field higher than $\mathrm{E_T}$, namely the electric field in the vicinity of the GEM holes. To discuss $\langle t_{\mathrm{Sec}} \rangle$ as a function of ΔU_{GEM} after the discharge, more measurements with both probes connected to the electrodes of the discharging GEM would be needed. In particular understanding the differences between the set-up powered by the voltage divider to the same set-up powered with a PS, seems like a good route to learn more about the origin of secondary discharges.

7.6.4. Wrap up: Secondary discharges with different power supplies

Based on the curves from Figure 7.13, we conclude that powering the double-GEM set-up with the voltage divider provides the best stability against secondary discharges in the transfer gap. Using the cascaded power supply results in a higher $\mathrm{E_T^{On}}/p$ than using the independent channel PS. However, the observed onset field is lower as compared to the one observed with the voltage divider.

Introducing a decoupling resistor pushes the onset fields to higher values for all three ways of biasing the GEM stack (independent channel PS, cascaded PS and voltage divider). Studies of secondary discharges in the induction gap have not been performed. It has however been observed in [27] that a single-GEM set-up powered with a voltage divider has a higher $\mathrm{E_{Ind}^{On}}/p$ than a single-GEM set-up powered with an independent channel PS.

Considering that the ROCs of the upgraded ALICE TPC will be either powered with a voltage divider or a cascaded PS, the onset fields observed with these two supplies for $R_{\mathrm{D}} = 50\,\mathrm{k\Omega}$ are encouraging. As discussed in Section 7.5.6, the highest $(\Delta U_{\mathrm{GEM}} \cdot d_{\mathrm{T}}^{-1} + \mathrm{E_T})/p$ of the ALICE TPC HV settings (Table 4.1) (considering an ambient pressure of 980 mbar) is about $5.5\,\mathrm{V\,cm^{-1}\,mbar^{-1}}$. This value is more than 30 % lower than the onset field with the cascaded PS and a decoupling resistor of 50 kΩ. We obtained our results presented in this section in Ar-CO_2 (90-10). In Section 7.4 we found $\mathrm{E_T^{On}}/p$ to be about 20 % lower in Ne-CO_2-N_2 (90-10-5) than in Ar-CO_2 (90-10) for otherwise the same settings. Therefore we expect the onset fields listed in Table 7.3 to be as well lower in Ne-CO_2-N_2 (90-10-5).

However, the configuration with the cascaded PS and a $R_{\mathrm{D}} = 50\,\mathrm{k}\Omega$ seems to be not far of from operational settings, which allow secondary discharge free operation. Measurements in Ne-CO_2-N_2 (90-10-5) with different GEM stacks are needed to find the real $\mathrm{E}_{\mathrm{T}}^{\mathrm{On}}/p$ and $\mathrm{E}_{\mathrm{Ind}}^{\mathrm{On}}/p$ in this gas mixture and to study systematic differences for different GEM configurations. A configuration without secondary discharges seems even simpler to achieve, if voltage dividers will be used to power the ALICE TPC ROCs.

Analysing the time between initial and secondary discharges, we find that the $\langle t_{\mathrm{Sec}} \rangle$ distributions are shifted with respect to their onset field, as observed in similar measurements (Figures 7.3, 7.6b, 7.7b and 7.10). The time difference between initial and secondary discharge seems to remain constant between about 10 µs and 40 µs (respectively below 1 µs) for measurements where the cascaded PS (respectively the voltage divider) is used to bias the set-up. Previous analysis (Figures 7.3, 7.6b, 7.7b and 7.10) of measurements with the independent channel PS showed an exponential decay of $\langle t_{\mathrm{Sec}} \rangle$ for increasing field.

7.7. Consequences for the operation of GEM stacks

During secondary discharge studies in the induction (Sections 7.2 and 7.5) and transfer gap (Sections. 7.3, 7.4, 7.5 and 7.6) the field in the respective other gap is always set to a small value in order to avoid secondary discharges in both gaps. In this section, we discuss the recovery from secondary discharges and give an example of a field setting allowing secondary discharges both in the transfer and induction gaps. First, however, we discuss a change in the GEM configuration of the future ALICE TPC GEM stacks.

7.7.1. Design changes of the ALICE TPC GEM stacks

Figure 7.15a shows the GEM configuration as foreseen for the ALICE TPC GEM stacks in [23]. At that time it was planned to orient each GEM1 such, that it faces the drift volume with its unsegmented side. When a discharge happens in a segment of GEM1, the voltage drops across the loading resistor at the bottom side of the GEM, will the unsegmented top side stays at its set potential. If the top side stays at a constant potential, this configuration would allow for minimal distortions of the drift field inside the TPC.

In case of a propagated discharge, which is propagated form a segment of GEM1 to an opposite segment of GEM2 or vice versa, the transfer field increases to $(\Delta U_{\mathrm{GEM1}} + \Delta U_{\mathrm{GEM2}})/d_{\mathrm{T}} + \mathrm{E}_{\mathrm{T1}}$. Considering that a value of $4\,\mathrm{kV\,cm^{-1}}$ is foreseen for E_{T1}, the resulting electric field is by far higher than the onset field of secondary discharges. This problem was addressed in the very first studies of secondary discharges in the induction gap, where the loading resistor was either mounted on the top or bottom electrode of the GEM foil [27]. To improve the stability against secondary discharges, the layout of the GEM stacks has been changed as to orient all GEMs with their segmented side towards the drift volume of the TPC. Figure 7.15b shows this new layout.

7.7.2. Recovery time after a secondary discharge

If the detector is powered by an independent channel PS and without a decoupling resistor, it takes several ms until the potentials, affected by a secondary discharge, recover to the values they take when only a normal discharge has happened. Secondary discharges thus do not significantly prolong the down time of the discharging GEM, because the GEM's recharging time is on the order of 100 ms (Fig. 6.17). This statement can be extended from our $10 \times 10\,\mathrm{cm^2}$ GEMs to a discharging segment in a segmented GEM foil, as foreseen for the upgrade of ALICE TPC. The time until a GEM has recovered from a secondary discharge takes longer in a configuration with a decoupling resistor. However, even the longest recovery times seen, are still small compared to the recharging time of GEM segment after a discharge.

ALICE TPC GEM stacks

The future ALICE TPC GEMs are only segmented on the top side and all segments therefore share a common bottom electrode [23]. Secondary discharges affects the bottom side and

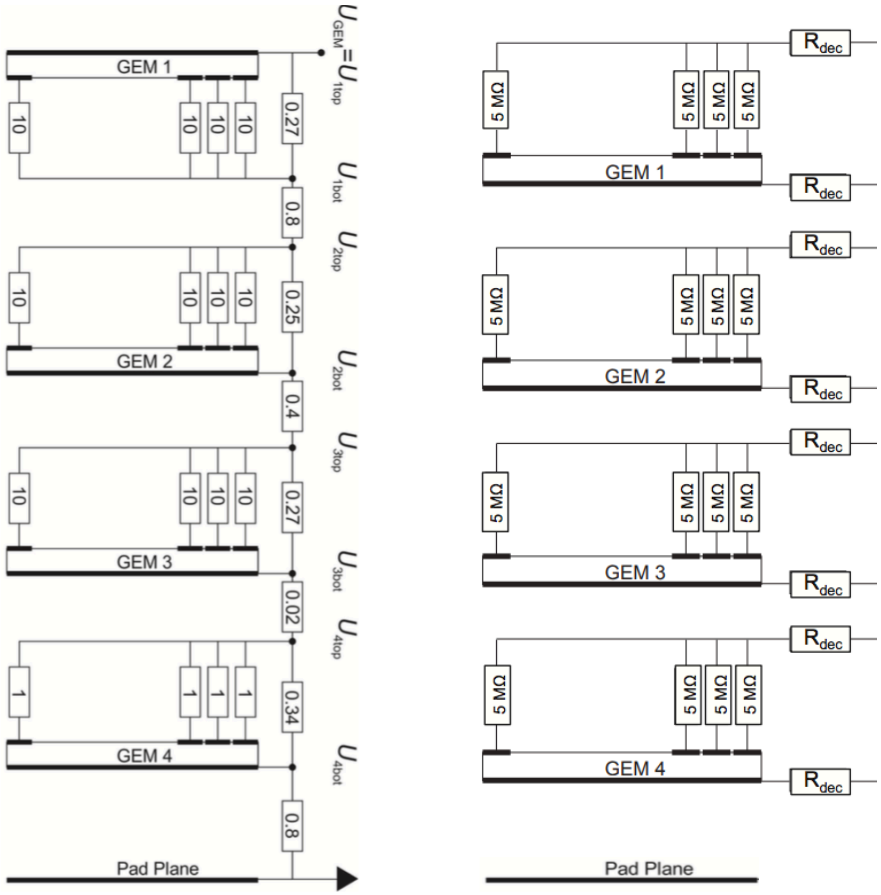

Figure 7.15: Two different stages of the biasing circuit and GEM configuration of the ALICE TPC readout chambers. The resistor values in the figures are given in MΩ. (a) Layout given in [23]. The unsegmented side of GEM1 top faces the drift volume. (b) After the results of the secondary discharge studies, the configuration of the GEMs has been changed. Figure adopted from [158].

therefore change U_{Bot} for all segments. When a secondary discharge takes place in one segment, the ΔU_{GEM} of the segments that are not affected by the secondary discharge do not change. This we know from measurements with our mock-up set-up, where we measured the ΔU_{GEM} of different GEM segments with one HV probe connected to the top and one probe connected to the bottom electrode of the same GEM segment.[1] Also, discharged segments maintain $\Delta U_{\mathrm{GEM}} = 0$ during the potential evolution induced by the secondary discharge. Even though ΔU_{GEM} is maintained, the absolute potentials at the top and bottom electrodes in all these segments change quite drastically. This is similar to what has been observed with discharges in the mock-up set-up (Fig. 6.25), although the potential changes considered in Section 6.6.2 are smaller, i.e. they resulted only from initial discharges.

Due to these potential changes at least two transfer fields (one transfer and the induction field, respectively) deviate significantly from the set fields. For this reason, a full GEM stack does not produce useful data before the potentials have recovered from the secondary discharge. When a secondary discharge occurs in an ALICE TPC GEM stack, the fact that all GEMs have an unsegmented bottom electrode means thus that the full area of the stack can not take part in the data taking until the potentials have recovered from a secondary discharge.

As discussed in Section 6.6.3, less then 10 discharge are expected per GEM stack during one month of lead-lead data taking at 50 kHz at the Large Hadron Collider (LHC) [24]. If we assume that all 144 GEM stacks have 10 initial and secondary discharges and we take a rather conservative recovery time of 100 ms, the recovery time over the running time is still less than 0.006 % and thus negligible.

The gain in a GEM stack defines the number of ions, which drift back into the drift volume. When a GEM stack is recovering from a secondary discharge the gain is expected to differ from its nominal value and therefore the ion back drift differs. The upgraded ALICE TPC will rely on dynamic space charge maps, which are created during the data taking [23]. If these algorithms would not be able to cope with the non nominal gain in a stack recovering from a secondary discharge, it would be necessary to wait for one full ion drift time through the TPC, until the ion density has recovered. The ion drift time over the full drift length of the TPC (2.5 m) is slightly less than 214 ms at a drift field of $400\,\mathrm{V\,cm^{-1}}$ in Ne-CO_2-N_2 (90-10-5) (Sec. 5.6). If this drift time is included into the recovery time, the new recovery time over the data taking time of one month is 0.02 %, which is still negligible.

These considerations are based on the assumption that the PS, supplying the GEM stack, does not trip when the initial and secondary discharge occurs. The expected performance loss of the GEM stack or the TPC in case of a PS trip depends on the time needed to bring the GEM stack back to the desired voltages. Considering sensible ramping speeds for a cascaded PS, we assume that in the best case rather minutes are needed to recover the GEM stack, after a power supply has tripped. Therefore a loss of data taking time of a few % can be expected, for the region of the pad plane below the affected GEM stack. The whole TPC is affected, in case the space charge correction procedure does not work with one stack off.

7.7.3. Multiple secondary discharges

A change of potential at a GEM electrode can create an electric field high enough for the onset of secondary discharges. It is therefore not surprising that changes of the electric fields between GEMs (respectively between a GEM and the anode plane) can lead to additional (secondary) discharges in gap(s) between GEMs (respectively between a GEM and the anode plane).

Figure 7.16 shows an event where the double-GEM set-up is operated at an induction field of $4\,\mathrm{kV\,cm^{-1}}$ and transfer field of $2.8\,\mathrm{kV\,cm^{-1}}$. These two are values in the range of commonly used fields for GEM stacks in Ar-CO_2 (90-10). A discharge first occurs in GEM2 at $t = 0$, and is propagated to GEM1. In the measurement GEM2 U_{Top} and GEM1 U_{Bot} are not recorded. After the (propagated) discharge, however, $\Delta U_{\mathrm{GEM2}} \sim \Delta U_{\mathrm{GEM1}} \sim 0$ and GEM2 U_{Bot} (respectively GEM1 U_{Top}) gets indistinguishable from GEM2 U_{Top} (respectively

[1] The mock-up set-up for simulating a double-GEM set-up with two GEMs containing two segments each is introduced in Section 6.6.2, Figure 6.24.

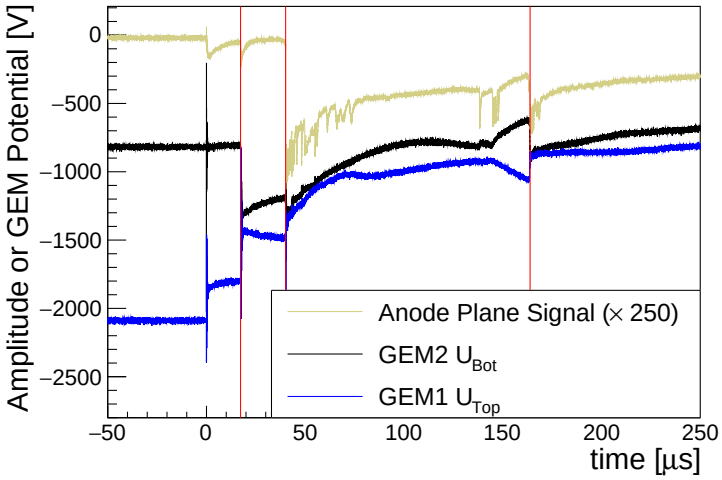

Figure 7.16: The discharge in GEM2 at $t \sim 0$ with a propagated discharge in GEM1 is first followed by a secondary discharge in the transfer gap at $\sim 17\,\mu s$. At $40\,\mu s$ a secondary in the induction gap occurs until eventually at $164\,\mu s$ another secondary is present. Each secondary discharge is indicated by a vertical red line. During these measurement Ar-CO_2 (90-10) has been used as counting gas and the detector is biased with the independent channel PS ($R_L = 10\,M\Omega$, $R_D = 0$).

GEM1 U_{Bot}). Therefore the two displayed potentials give an impression of the GEM2 U_{Top} and GEM1 U_{Bot} potential as well. The discharge in GEM2 increases the effective transfer field by $\Delta U_{GEM2}/d_T = 420\,V/2\,mm = 2.1\,kV\,cm^{-1}$. Knowing the ambient pressure of 970 mbar the resulting transfer field after the discharge is close to the E_T^{On}/p value for this configuration (*Set a* in Table 7.1 or Fig. 7.6a). At $t \sim 17\,\mu s$ (first red line in Fig. 7.16), a secondary discharge in the transfer gap can be seen, as discussed in Figure 7.5. This secondary discharge leads to an increase of the induction field to $\sim 1.3\,kV/2\,mm$, which can be read from GEM2 U_{Bot} (Figure 7.16). Since this field is higher than E_{Ind}^{On}/p in this configuration (*Set a*, Table 7.1), another secondary discharge in the induction gap is observed at $t \sim 40\,\mu s$ (second red line). The anode plane potential moves to a negative value and its consequent decay towards zero fits the observations made for secondary discharges in the induction gap using a high resistance path from the anode plane to ground (Fig. 7.4b). The potential difference between the anode plane and GEM2 U_{Bot} is decreased by this potential change and further secondary discharges are quenched. U_{Top} and U_{Bot} from both GEMs have very similar values after the two secondary discharges, resulting in a low E_T at this time. There, nevertheless, seems to be a third event at $t \sim 164\,\mu s$ that exhibits features of a secondary discharge in the transfer gap. The transfer field at this time is far lower than E_T^{On}/p.

With a third and or fourth GEM in the GEM stack, even more secondary discharges among the different gaps could be expected since the corresponding fields increase as well. The transfer fields should be therefore chosen such, that the sum of E_T and the corresponding $\Delta U_{GEM}/d_T$ remain below onset field values for secondary discharges in the relevant gas mixture so as to avoid the first occurrence of secondary discharges. This is in fact why our set-up is either operated at high E_T or at high E_{Ind}. Choosing too high values for both fields prevents operating the set-up in a stable way, even by this works' standards in which we are interested in many discharges.

We have already mentioned frequently that the ALICE TPC HV settings (Table 4.1) feature too high $(\Delta U_{GEM} \cdot d_T^{-1} + E_T)/p$ as compared to the E_T^{On}/p measured in this work (Sections 7.5.6 and 7.6.4). However, we have not tested the exact configuration of the ALICE ROCs. The E^{On}/p obtained with decoupling resistors and the cascaded PS as well as the voltage divider are promising milestones on the quest for a secondary discharge free operation of the future ROCs. Measurements with the real configuration in Ne-CO_2-N_2

(90-10-5) are needed to gain confidence in the final configuration.

7.7.4. Possible role of discharge propagation

As far as we can tell, secondary discharges only occur in the transfer gap of our set-up when a discharge in GEM2 is propagated to GEM1. In other words, secondary discharge always take place in the gap below a GEM (Sec. 7.3.3). In case a counter example for this hypothesis is found, we still know that secondary discharges can be created by propagated discharges. In order to minimise the amount of secondary discharges or discharges in general, the discharge propagation probability (Sec. 6.5.3) should be as low as possible. To our knowledge, however, a dedicated discharge propagation study in Ne-CO_2-N_2 (90-10-5) does not exist. The according measurements could give some hints to a further minimisation of the occurrence of discharges.

7.7.5. Damage created by secondary discharges

We have not observed permanent short circuits between the two sides of a GEM foil, which could be exclusively attributed to a secondary discharges. Therefore it is hard to judge how harmful a secondary discharge can be to a GEM foil. For our measurements with $10 \times 10\,\mathrm{cm}^2$ GEM foils, the energy stored by the capacitance of the gaps is significantly lower than the energy stored in a GEM foil. As the energy in the discharging capacitor is released during the discharge, the secondary discharge can be considered as less harmful.

However, the cascades of discharges as in the example from Figure 7.16 are harmful if they go on and accumulate more secondary discharges.

Readout electronics of the ALICE TPC

The large changes of the anode plane potential as for example observed in Figure 7.16, will affect the readout electronics of the future TPC. In a recent study for the ALICE TPC Upgrade prototype readout electronics has been tested with a small quadruple GEM prototype, with $10 \times 10\,\mathrm{cm}^2$ GEMs [151]. They induce as well discharges by using a highly ionising source and increasing the gain in their GEM stack. Although their study did not focus on secondary discharges, some of their signals look similar to what we have presented in this chapter and the readout electronics survived. However, a dedicated test enforcing secondary discharges with a close to final system will show if something has been overlooked with the small prototype studies.

7.8. The origin of secondary discharges

We know from the GEM potentials and the anode plane signal that the induction or transfer gap discharges during a secondary discharge. The question so as to how it is possible remains to be answered. The measured onset fields ($\mathrm{E}^{\mathrm{On}}_{\mathrm{Ind}}/p$ and $\mathrm{E}^{\mathrm{On}}_{\mathrm{T}}/p$, Table 7.1) are significantly lower than the onset of gas amplification (Sec. 3.3, Fig. 3.5). A mechanism which triggers breakdown at lower electric fields as than expected form the first Townsend coefficient is thus needed. Two possible causes, which may be responsible individually or together for the secondary discharge can be identified. First, effects in the counting gas triggered after the initial discharge, and, second, responses of the power supply and the biasing circuit to the discharges.

7.8.1. Ion-driven secondary discharges

The different onset fields we measure show that the electric field plays a role for the creation of the secondary discharge. Furthermore we have indications from the measurements with decoupling resistors and the different power supplies, that the remaining ΔU_{GEM} after the discharge may play a role as well (Sections 7.5.5 and 7.6). The average time between initial and secondary discharge points to the involvement of ions, because it is too long considering electrons or even photons (e.g. Sections 7.2.3 and 7.4.1).

As a discharge occurs in the GEM foil, a short circuit between the two foil sides develops, U_{Top} and U_{Bot} take the same value for a short time, as shown in the previous chapter. The spark is quenched by this potential drop of either one or both GEM potentials. During the discharge the gas is ionised along along the spark channel. A fraction of the produced electrons and ions recombines after the spark, while the electric field removes some of remaining electrons towards the anode plane. Compared to the situation before the discharge, there is at most a low electric field in the GEM hole. It is provided by the remaining potential difference $\Delta U_{\mathrm{GEM}} \sim 0$ and by the field above and below the GEM leaking into the GEM holes.

Secondary discharges are only observed at a given onset field. It might be related to the field value from which, the field below the GEM is strong enough to push more ions back into the GEM holes than those being evacuated in the same time. From this point on, ions are concentrated into the confined space of the hole. This might create a space charge with an electric field that is large enough to start a streamer. This process is analogue to what has been discussed for a discharge of a GEM hole in Section 6.3.1. Anode directed streamers have a negatively charged streamer head [85]. The precursor seen in the anode plane signal (Sec. 7.2.1, Fig. 7.1) might be related to the movement of the streamer towards the anode. The delay between the initial and secondary discharge would, according to this explanation, be due to the time needed to focus the ions back into the GEM hole. The higher the field below the GEM, the faster the ions velocity. The fact that a shorter $\langle t_{\mathrm{Sec}} \rangle$ is observed in Ne-CO_2-N_2 (90-10-5) as compared to Ar-CO_2 (90-10) (Sec. 7.4) would then be due to the larger ion mobility. Different onset field values observed with and without decoupling resistor (Table 7.1, and Sec. 7.5, Fig. 7.9a) and various power supplies (Table 7.3) can arise by a different value of ΔU_{GEM} after the initial discharge, which evolves in a different manner for different supplies .

For secondary discharges in the inverted field direction, the electric field below a GEM and the remaining field in the GEM hole cancel themselves out to a certain extend. Furthermore ions are in this scenario extracted into the gap above and below the GEM foil. With increasing field strength, the electric field below the GEM starts to collect and extract all the ions through the GEM hole into the gap below the GEM. A higher absolute value of the electric field, as compared to the normal field direction, is thus needed for the accumulation of ions in the hole. In this way such a streamer-based mechanism provides an explanation for the high absolute value of $\mathrm{E}^{\mathrm{On}}/p$ when the field direction is inverted. This value must in fact be higher than the absolute value of the onset field for a normal field direction.

It is worth noting that the field setting during the first $\sim 10\,\mu\mathrm{s}$ imposes whether there is a secondary discharge or not. To test this, we use high voltage settings larger than $\mathrm{E}^{\mathrm{On}}_{\mathrm{Ind}}/p$ and make sure secondary discharges are observed in the induction gap. This is done using the independent channel PS and no decoupling resistor. The resistance from the anode plane to ground is then changed. We use $100\,\mathrm{k}\Omega$, which is significantly larger than the resistances used in Figure 7.4. Due to the higher RC constant charge from the anode plane arriving there during the initial discharge takes longer to evacuate. In turn, the anode plane remains charged at a negative potential for a longer time, effectively decreasing $\mathrm{E}_{\mathrm{Ind}}$. The induction field is restored in more than the typical $\langle t_{\mathrm{Sec}} \rangle$ of $20\,\mu\mathrm{s}$. For comparison, the time needed to evacuate charges with the classical resistance of $10\,\mathrm{k}\Omega$ from the anode plane is $\sim 5\,\mu\mathrm{s}$ (Fig. 7.1). A temporarily change of the field below a GEM during a few $10\,\mu\mathrm{s}$ therefore helps counteracting the conditions needed to have a secondary discharge.

7.8.2. Possible contributions of the biasing circuit

In addition to the hypothetical streamer creating the secondary discharge, the biasing circuit contributes as well to the behaviour of the discharging set-up. The addition of resistors or other circuit elements affects the potential evolution during the initial discharge and thus influences as well secondary discharges. An effect can be attributed to the storage of additional charges in the cables due to their capacity. The additional charge in the cable affects the GEM during the discharge when no decoupling resistor is used, because on the one hand the energy of the discharge is increased and on the other hand the recharging process of the GEM is affected. Decoupling resistors decouple the cables and their capacitance from

the GEM. The RC constants governing the recharging of all GEM electrodes are influenced by the set-up itself and by the circuit elements, which includes the power supply. Different studies are right now in preparation e.g. at CERN and at the Technische Universität München, Germany, examining these effects in more detail [159].

The phenomenon of secondary discharges has to the best of our knowledge not been so far observed without a previous discharge of a GEM foil. This includes simulations of a GEM stack, where all the hardware of a real set-up is used, but the GEMs are replaced by gas discharge tubes. The cause of secondary discharges must thus be related to a phenomenon in the counting gas. Since the occurrence of secondary discharges is governed by the electric fields and not by absolute potentials, it is more likely for their source to be an effect from the gas than an effect from the supply circuit.

7.9. Summary

After a discharge in a GEM foil secondary discharge are occasionally observed. High voltage probe measurements of the potentials at different electrodes in our set-up showed that secondary discharges are (full) discharges of a respective gap (transfer or induction) below the discharging GEM. Future measurements need to show if a secondary discharge can occur as well in the gab above a discharging GEM.[m] Their occurrence probability was found to depend on the electric field in the gap, where the secondary discharge occurs. We observed a steep increase of this probability from zero to one around a certain electric field value, i.e. the onset field (E^{On}/p). In Ar-CO_2 (90-10) this field was found to be about $6\,V\,cm^{-1}\,mbar^{-1}$ (respectively $5.5\,V\,cm^{-1}\,mbar^{-1}$) for secondary discharges in the induction (respectively transfer) gap.[n] Using different GEMs in our set-up yielded different onset fields. These differences may be compatible with slight changes of the gap widths, introduced by the bending of the GEM frames when mounted in a stack. We found no satisfying explanation why the onset field in the transfer gap is systematically lower than in the induction gap. When the electric field direction in a gap was inverted, a similar onset field around -7.3 $V\,cm^{-1}\,mbar^{-1}$ was found in both gaps. Discharges propagated from one GEM to another can also result in a secondary discharge, if the field below the GEM is high enough.

Using Ne-CO_2-N_2 (90-10-5) the onset field for secondary discharges in the transfer field is found to be 20 % lower than the one obtained for Ar-CO_2 (90-10) using the exact same hardware.

The time between initial and secondary discharges decreases from several 10 µs down to less than 1 µs with increasing electric field. This decrease is exponential and similar results were obtained for the different settings tested, which feature different onset fields. The data point distribution, however, was found to be shifted according to the shift of the onset fields. These results were obtained with a GEM stack biased with the independent channel PS.

Introducing a decoupling resistor at the high voltage path of the bottom side of the GEM foil resulted in an increase of E^{On}_{Ind}/p and E^{On}_{T}/p [152]. For increasing resistance R_D, the onset fields for secondary discharges in the induction and transfer gap increase. Since the transfer fields of the ALICE TPC high voltage settings will be higher than the observed onset of secondary discharges in the transfer gap, introducing such resistors seems promising to reduce the likelihood of the occurrence of secondary discharges.

When the GEM stack is powered with a cascaded PS or a voltage divider, significantly higher onset fields are observed as compared to the same set-up when the independent channel PS is used. The combination of a cascaded PS and a decoupling resistor of $\gtrsim 50\,k\Omega$ showed in Ar-CO_2 (90-10) a higher E^{On}_{T}/p, than the largest transfer field in the ALICE TPC HV settings. With the voltage divider an even higher E^{On}_{T}/p was observed. These results

[m] In measurements where discharges were filmed with a camera (Sec. 8.2), only one discharge location per video frame was observed. The frame rate of the videos was larger than the inverse time between primary and secondary discharge. If secondary discharges produce light, like an initial discharge does, the fact that only one discharge location per frame was observed implies that initial and secondary discharge occur at the same position. However, it is well possible that secondary discharges do not emit as many visible photons as are emitted during the spark between two GEM electrodes. Performing the same measurement as in Section 8.2 with a high-speed camera could clarify this.

[n] These onset fields were measured when an independent channel PS is used to bias the set-up and when no decoupling resistor in the HV path to the bottom electrode of the GEMs is used.

are a promising starting point to test the actual ALICE TPC HV system in Ne-CO_2-N_2 (90-10-5). Furthermore, we observed with the cascaded PS and the voltage divider a constant time between initial and secondary discharge, independent of the electric field. When the voltage divider was used, this time was found to be $\lesssim 1\,\mu s$.

Independent of the presence or absence of a decoupling resistor, the potentials on both sides of the GEM closest to the anode plane will change in the event of a secondary discharge in the induction gap. For a secondary discharge in the gap between two GEMs, all these GEMs' potentials will be affected. Such potential changes can result in an increase of the fields between GEMs in a GEM stack, leading to series of multiple (secondary) discharges. The magnitude of the GEMs' potential changes during a secondary discharge were found smaller, when the GEMs were equipped with decoupling resistors. Since the recovery from a secondary discharges happened relatively fast (several ms) as compared to recharging times of GEM foils (several 100 ms), secondary discharges are expected not to introduce additional dead-time. However for segmented GEMs with one non-segmented side, secondary discharges are expected to affect the whole GEM stack and not a single segment. Based on the discharge probability measured for ALICE TPC GEM stacks, we estimate the time needed for the GEM stacks' recovery from secondary discharges as negligible compared to the total time of data taking with the upgraded TPC. Because of the dangers associated with series of secondary discharges, the HV settings of the future ALICE TPC's GEM stacks should be optimised as to observe no secondary discharges.

Only few other measurements examining this phenomenon are available for comparison. Our measurements of the probability of occurrence of secondary discharges in the induction gap agree with the observations from [27]. The same group also investigated secondary discharges with Ne-CO_2-N_2 (90-10-5) and Ar-CO_2 (90-10) in the induction gap. In [154], a relative change of E_{Ind}^{On}/p is observed between the two gas mixtures, similar to the relative change we observed for E_T^{On}/p. In [157] an increase of E_{Ind}^{On}/p with R_D is reported. It is compatible with the results in [152] we discussed here.

The mechanism triggering secondary discharges is not yet fully understood. We believe these discharges to be created by a streamer. This streamer is generated by ions created during an initial discharge, located in the vicinity of the GEM. The several 10 µs delay between the intial and secondary discharge can than be explained by the time needed to focus ions in a confined region and create a sufficient space charge density to start a streamer.

8. Sagging studies with large GEMs and an analysis of discharges' locations using videos

The gas gain, energy resolution, discharge probability and Ion Back Flow (IBF) (Sec. 3.5.3, Eq. (3.22)) of a GEM stack depend not only on the voltages across the GEM foils, but also on the transfer fields and the induction field. In this work we have shown that the discharge probability depends on the transfer field (Sec. 6.4.3, Fig 6.11b). In studies for the ALICE TPC upgrade the impact of the transfer fields on the energy resolution and IBF has been extensively studied [23, 24]. This role of the transfer fields can be explained with the different electron collection and extraction from the GEM holes if the field above and below the GEM, respectively, is varied [102].

Uniform transfer fields and a uniform induction field are desired to have a homogeneous performance of the GEM stack. To this end the distance between two GEMs (respectively a GEM and the anode plane) has to be constant everywhere in the corresponding transfer gaps (respectively induction gap). In order to ensure such a uniform distance, the raw GEM foils are stretched and attached to a frame. This frame preserves ideally the full stretching force of about $10\,\mathrm{N\,cm^{-1}}$ and provides the support needed to mount a foil into a detector [23, 160]. In order to keep a constant distance between the parallel surfaces in the GEM stack, the stretching force has to be high enough to withstand the electrostatic forces and keep the foil from sagging. In case a foil sags the width of the respective gap decreases and the electric field in the gap increases. The possible results of such a change of electric field range from a change in IBF performance up to (secondary) discharges across the gap.

In this chapter, we present tests of GEM foil sagging in Section 8.1, using the largest GEM foils needed for the future ALICE TPC readout chambers. These are the foils used in the stacks at the outer end of the Outer ReadOut Chambers (OROCs). They are referred to as OROC3 GEMs. In addition, we examine whether having pieces of the frame in contact with the active area of the GEM foil can result in additional discharges (Sec. 8.2). This chapter concludes with a summary in Section 8.3.

8.1. Foil sagging due to electrostatic forces

8.1.1. A word on GEM framing

A raw GEM foil is typically larger than the size of the active area of the final GEM. In Figure 8.1a a raw foil of an ALICE TPC GEM is shown as example. The trapezoidal shape visible in the middle shows the actual dimension of the final foil. The additional foil material around the actual GEM makes it easier to handle the raw foil, and it is as well used for the stretching process. If only the excess material is manipulated during the GEM production process, physical contact with the future active area of the GEM foil can be entirely avoided. In this way the risk to contaminate the active area with glue or dust is minimised, and therefore the risk of inducing discharges. In fact, the discharge probability of contaminated region increases and as discussed in Section 6.3.2, there is a finite number of discharges a GEM hole can stand. Therefore, it is crucial that the framing process does not create a region with an enhanced discharge probability.

All ALICE TPC GEM foils are glued to a frame. After the raw GEM foil is stretched, the frame is glued to the foil onto the region where no copper is present. This region corresponds to the trapezoidal shape in Figure 8.1a. The initial frame design includes a *spacer grid* as shown in Figure 8.1b. The bars of the spacer grid are designed to be aligned with the boundaries of the GEM segments. However, the grid is not glued to the GEM and it is only

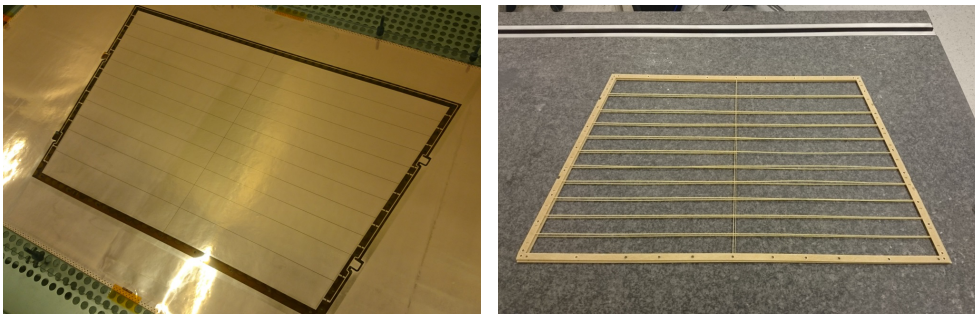

(a) (b)

Figure 8.1: (a) An ALICE TPC GEM foil for an OROC1 GEM stack as it is after production. The larger copper area around the trapezoidal foil is removed after the stretching and GEM framing. The outline of the active region of the foil is not covered with copper. The GEM frame will be glued on this region. (b) Two such frames lying on top of each other. The four thicker sides defining the trapezoidal shape are the actual GEM frame, while the grid in the middle is referred to as spacer grid.

connected to the GEM frame. By design, the spacer grid touches the unsegmented bottom side of the GEM foil it belongs to, it thus is in contact with the active area. The height of the spacer grid is 2 mm, as is the inter GEM distance (respectively the distance between GEM and pad plane). Therefore the spacer grid of three of the four GEMs in a stack is in contact with the top side of the corresponding neighbouring foil. Precautions have to be taken in order to make sure that the spacer grid does not contaminate the active area of the GEM foil.

8.1.2. Sagging studies with OROC3 GEM foils

It is expensive to produce frames with a refined spacer grid, as it was foreseen in the initial frame design (Fig. 8.1b). To test if the spacer grid is necessary to keep the width of the gaps between GEMs constant, several OROC3 GEMs have been framed without such a grid. These are the largest GEMs[a] produced for the ALICE TPC, and they therefore allow to test the strongest effect of the electrostatic forces on an ALICE GEM foil. A full OROC3 GEM stack has been commissioned with these GEMs as part of the first OROC prototype. See [161] for informations on the construction of that chamber. As High Voltage (HV) is supplied to this GEM stack we observe a high rate of discharges starting from certain voltages. The other stacks, which have been framed with the spacer grid, hold the supplied voltages.

Sagging tests with a single OROC3 foil

In a clean room, the chamber is opened again to examine the OROC3 GEM stack. The stack is taken apart and a single foil is placed directly on the pad plane of the chamber. All pads are grounded and the same potential is supplied to both electrodes of the GEM. As HV is applied to the GEM, the foil moves immediately towards the pad plane. For a sufficient potential difference between the foil and the pad plane, the foil touches eventually the pads and the capacitor formed by the GEM foil and the pad plane discharges. Afterwards the foil moves back to its initial position and starts sagging and the process is repeated. The voltage necessary to make the foil sag 2 mm is found to be between -650 V and -750 V. This voltage range arises if the screws, which fix the GEM foil to the readout chamber, are relaxed and fixed again. This illustrates the importance of fixing the GEM stack thoroughly to the pad plane.

[a] OROC3 GEM foils have a trapezoidal shape as all ALICE TPC GEM foils. The length of the two parallel sides a and b is 85 cm and 71 cm, respectively. The hight h has a length of 38 cm.

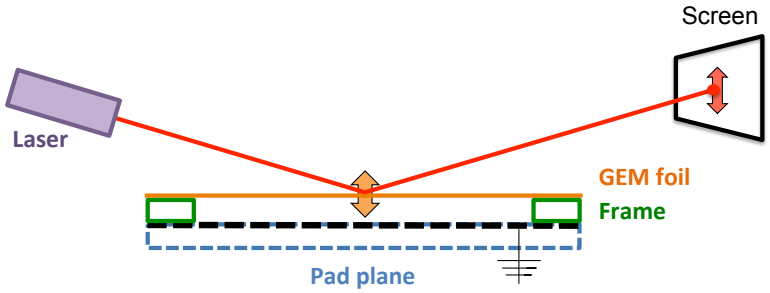

Figure 8.2: Set-up to test foil sagging with a single OROC3 GEM foil. The framed foil is placed on the pad plane, which is grounded. A laser is shot onto the foil, reflected there and observed on a screen. If HV is applied to the GEM foil, the foil sags towards the pad plane and the position of the laser dot changes on the screen.

(a) (b)

Figure 8.3: Bottom side of a framed OROC3 GEM foil. In (a), one bar is added to the frame while, in (b), two bars form a cross. In the latter configuration no foil sagging is visible any-more.

To be able to observe sagging of small amplitude, a laser pointer is mounted on a support structure and shines onto the GEM foil, as sketched in Figure 8.2. The reflection is observed on a sheet of paper serving as screen. A small sheet of aluminised Mylar is placed on the GEM to increase reflectivity and to avoid observing diffraction patterns due to the GEM holes. As HV is applied to the GEM, the sheet charges up and flattens, attaching itself to the GEM. With this set-up, quantitative measurements of the foil sagging can be obtained.

Adding a moderate spacer grid

In order to determine what kind of spacer grid can prevent the foil from sagging, first a bar parallel to the two long sides of the GEM frame is added (Fig. 8.3a). The bar has a width of 1 mm and a height of 2 mm, corresponding to the desired gap width. It is carefully sanded to remove small splints and rough edges. The bar is then cleaned and attached to the GEM frame at two locations. With this configuration, we observe foil sagging starting at a difference of about -900 V between the pad plane and the GEM, which is already higher than the largest foreseen voltage difference (-800 V) across any gap of the ALICE TPC GEM stacks (Table 4.1.). The maximal sagging amplitude is reduced as compared to the case without any spacer grid. As a result the foil and the pad plane do not touch any-more. Adding another similar bar to the spacer grid (Fig. 8.3b) perpendicular to the first one results in no measurable sagging. Based on these results the ALICE TPC upgrade decided to move from spacer grids as shown in Figure 8.1b to grids, which consist only of one cross as discussed here.

Exact sagging amplitudes for the different voltages are not determined because the exact position of the deepest point on the GEM foil can not be determined, if the foil does not touch the pad plane. In the case where pad plane and GEM touch, the location of the

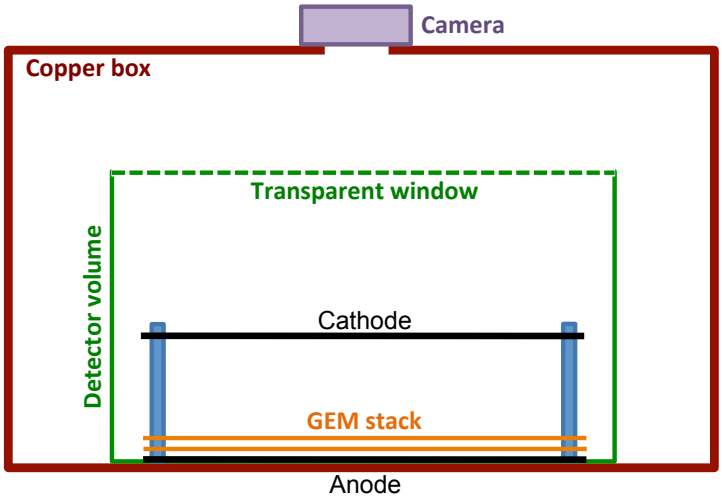

Figure 8.4: Sketch of the set-up used for recording discharges with a camera (not to scale). A copper box acting as a Faraday cage, encloses the detector in a light-tight manner. A camera is placed in a hole on this box and records the discharging detector. Even discharges in the lower GEM can be filmed as both the mesh, serving as drift cathode, and the GEMs have a high optical transparency.

discharge marks the location of the maximal sagging amplitude. Without the position of the minimum, the calculation of the sagging depth from the measured shift of the laser spot on the screen is not possible.

8.2. Spatial distribution of discharges

The design of the GEM frames for the ALICE TPC GEMs has been changed to incorporate the observation that a cross is a sufficient spacer grid. Also with the new design, the bars forming the spacer grid are in contact with the active area of the GEM foil. Using $10\times10\,\mathrm{cm}^2$ GEM foils we study if the discharge probability is enhanced in regions where the spacer grid touches the GEM foil.

8.2.1. Video analysis of discharges

We add a cross between the two GEMs in the experimental set-up (Sec. 6.2) we used for the discharge studies presented in Chapters 6 and 7. The two bars forming the cross are thoroughly sanded and cleaned as is done for the longer bars used for the previous tests with the OROC3 foil. As illustrated in Figure 8.4, the set-up is enclosed in a light-tight box and a camera is placed in a hole in the centre of the lid of the box. The space needed to fix the HV supplies, gas supplies and HV probes into the box, however, prevents the detector from being centred under this hole. For this reason the camera can not capture the full GEM. Discharges are induced in the lower GEM by a combination of a highly ionising Rn source in the gas and high voltage settings, allowing for a high rate of discharges. The high voltage settings are tuned to yield a high probability for discharge propagation (see Sec. 6.5.3) from the lower to the upper GEM. Therefore, discharges are expected in the GEM both below and above the cross. The camera is a simple mobile phone camera recording at a rate of 30 frames/s. In the recordings of the discharging set-up, discharges appear as bright white-blue spots, while everything else remains dark. Most of the recorded frames are empty and when a frame includes a discharge, only a single one is usually observed. We record discharges during times when a cross is mounted in the detector as well as when no cross is there.

The videos are analysed with *MATLAB® R2016b* [162]. Doing so, sparks are identified by their intensity. Furthermore, a background model is computed from the entire video

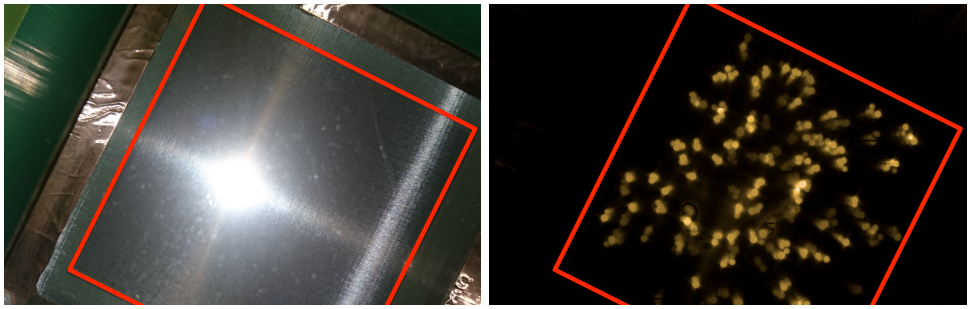

(a) (b)

Figure 8.5: A video of discharges in the detector is recorded with the set-up sketched in Figure 8.4. (a) A photo is also taken to match the identified discharges to their position in the detector. Integrating all discharges from the video results in (b). The red line marks the active are of the upper GEM, which can be easily identified. However, the discharges are induced in the lower GEM.

and subtracted from each frame. When a spark is detected the corresponding frame is filtered to better define the spatial extent of the spark and identify its location. In the end, all identified sparks are normalised to the same intensity range and integrated in a single picture. This normalisation allows identifying brighter regions where a higher density of sparks is recorded. In addition to the videos a static photo of the set-up is taken. This photo is then compared to the integrated discharge picture in order to determine the physical location of the discharges.

Such a photo is displayed in Figure 8.5a and the visible active area of the upper GEM is highlighted. The visible area of the discharging lower GEM is slightly smaller, but can not be seen here. Figure 8.5b illustrates the analysis result from a 7 min discharge video. The active area of the upper GEM, obtained from Figure 8.5a is highlighted. Figure 8.5 is the analysis result of a recording made when a cross is placed between the two GEMs.

8.2.2. Results

Due to the spherical aberration and the cameras resolution, the exact locations of the sparks can not be obtained. Nevertheless, comparing the picture integrating all discharges to the one of the set-up allows to conclude that the sparks are distributed randomly over the area of the GEM. Although some regions seem to exhibit more or fewer discharges relative to other areas on the foil, these regions change for different recordings of the same set-up. At the time of this study, the GEMs had already suffered from several thousand discharges. Therefore the observed regions are most likely related to the deterioration of the GEM foils. The discharge locations also do not seem to follow the outline of the spacer grid cross, and no difference is observed when analysing videos of discharges taken with and without the cross. The spacer grid touching the active area of the GEM foil does therefore not seem to influence the discharge probability.

The global P_1 (primary discharge probability, as defined in Equation (6.9), Section 6.4) with the spacer grid is similar to the P_1 without, when measurements with similar HV settings are compared. Secondary discharges have not been studied in detail. Since HV settings resulting in secondary discharges with a high P_2 (secondary discharge probability, as defined in Equation (7.2), Section 7.2.2) are applied, at most only a single discharge spot is observed per video frame. Primary and secondary discharges are captured with a high probability in the same frame, since one frame integrates over 33 ms. The fact that only single bright spots are observed hence indicates that initial and secondary discharge occur

in the same spot. It is well possible that the secondary discharge is less bright, because the energy stored by the capacitance of the transfer (respectively induction) gap is smaller than the discharge energy of the GEM. A definite answer could be obtained by repeating such measurements with a high speed camera and making a similar analysis as shown here.

The same argument can be applied to the initial and the propagated discharge. These two discharges seem to occur as well very close to each other, because only single bright spots are observed. A dedicated study of the recorded discharges' intensities for HV settings with either a low or high discharge propagation probability can provide more information on this topic.

8.3. Summary and conclusion

The sagging of a trapezoidal OROC3 GEM foil ($a = 85\,\text{cm}$, $b = 71\,\text{cm}$ and $h = 38\,\text{cm}$) of the future ALICE TPC was investigated for various voltage differences between the bottom side of the GEM foil and the pad plane. Without any spacer grid, the GEM sagged by 2 mm, which corresponds to the full distance between the foil and pad plane. The amplitude of the sagging depends on the applied voltage. Furthermore, it was found that the amplitude depends as well on the strength used to tighten the screws, which hold the GEM frame to the readout chamber. No sagging was observed when using a spacer grid formed by a cross of two perpendicular pieces with a width of 1 mm and a height of 2 mm, which corresponds to the desired gap width. We conclude that a spacer grid as described here also prevents GEM foils smaller than OROC3 foils from sagging. Therefore, no sophisticated spacer grid (Fig. 8.1b) is needed to maintain the planarity of the ALICE TPC GEM foils [119]. The new and final design of the ALICE TPC GEM frames and spacer grids was based on these results.

The bars of the spacer grids are in contact with the active area of the foil. To test whether the proximity of the spacer grid to the active area results in an increased discharge probability, a $10 \times 10\,\text{cm}^2$ GEM was equipped with a spacer grid. The upper GEM of a double-GEM set-up was used for this study, thus the grid was placed in-between two GEMs. Discharges were voluntarily triggered and the set-up was filmed. Based on the video analysis of discharges in the set-up with and without spacer grid we conclude that the grid touching the active area did not increase the discharge probability.

Several chambers relying on the new design of the spacer grid have already been built and were successfully commissioned and tested, confirming our findings in this work. See [163] for a description of the commissioning steps and tests, which are done in order to build and qualify OROCs for the future ALICE TPC.

9. Conclusion

In this work we have commissioned a set-up to measure ion mobility and used it for different gas mixtures (Chapter 5), we measured initial and secondary discharges in a small prototype set-up (Chapters6, and 7) and did a research and development study for larger area GEM foils (Chapter 8). In the following, we stress some important points of the more detailed summaries in each of these chapters.

We measured the mobility of ions drifting through a gap between a GEM stack and a wire grid. The induced signal of the ions on the wire grid was recorded for the full ion drift time. In order to determine the time of arrival at the grid, we rely on the inflection point in these signals. This method was tested thoroughly with computer simulations of drifting charges and by comparing our measured mobilities to previous results. Because our system relies on rather common hardware for gaseous detector laboratories, it is feasible to adopt our ansatz elsewhere and to determine the ion mobility of a desired gas mixture. For the ALICE TPC gas mixture, which is Ne-CO_2-N_2 (90-10-5), we found a mobility of $(2.92 \pm 0.04)\,\mathrm{cm^2\,V^{-1}\,s^{-1}}$. The mixture had a water content of $(130 \pm 1)\,\mathrm{ppm}$, similar to the water content in the TPC. Compared to the previously assumed value, this mobility is by 30 % lower. Thus, ions in the TPC will accumulate longer in the drift volume, than expected. The goal of an ion back drift better than 1 %, which was based on the too high mobility estimate, included a safety margin. Therefore the measured lower mobility should not constitute a problem for the performance of the future TPC. However, the margin to adjust other parameters resulting in a larger amount of ions in the drift volume is reduced.

In a study with large GEM foils dedicated for the future readout chambers we showed that a cross shaped spacer grid is enough to ensure a good planarity of the GEM foil.

During our discharge studies, we induced discharge voluntarily in a GEM using alpha particles and high voltage settings with high gain. We obtained a large number of discharges and we were therefore able to perform quantitative measurements of discharge properties, such as the potential evolution on the GEM electrodes during a discharge. High voltage probes which can measure these potentials are an excellent tool for these studies. We were able to quantify the potential drops at different GEM electrodes during a discharge and we studied the evolution of the potential difference across discharging GEM foils qualitatively. We measured discharge propagation with them and find that the probability to propagate a discharge from one GEM to another depends on the voltage difference at the GEM to which the discharge is propagated to.

With high voltage probe measurements we were able to show that secondary discharges are discharges of the gap below a GEM. We observe secondary discharges to have harsh consequences for a GEM stack, considering the potential changes occurring when one gap in the stack discharges. Secondary discharges occur only when the electric field in a gap is higher than a given threshold field value. This threshold field was found to be significantly lower than the electric field for which breakdown would be expected. For example, in Ar-CO_2 (90-10) we observed secondary discharges already at a $\mathrm{E_T} + \Delta U_{\mathrm{GEM}}/d_{\mathrm{T}}$ lower than $5\,\mathrm{kV\,cm^{-1}}$. Here, $\mathrm{E_T}$ is the field in a $d_{\mathrm{T}} = 2\,\mathrm{mm}$ wide transfer gap and ΔU_{GEM} is the voltage difference across the GEM foil at the lower end of this gap. This value has been obtained with an independent channel PS and a loading resistor of $10\,\mathrm{M\Omega}$ on the top electrode of the GEM. The threshold value depends on the way the GEMs are supplied with high voltage. Especially using decoupling resistors in combination with a voltage divider chain or a cascaded power supply showed high onset fields. Therefore it seems feasible to operate the future ALICE TPC readout chambers in a regime where few or no secondary discharges are expected. However, it appears critical to test this phenomenon with real chambers and not only with small prototypes, to make sure the change while going from a small to the real system does not introduce an effect, which may have been overlooked with the prototypes.

It will not be possible to avoid discharges in a GEM based detector, but our studies helped to gain better knowledge on the consequences. Knowing these consequences, adjustments to the HV settings can be made in order to make the future readout chambers safer in case of a (secondary) discharge.

10. Acknowledgements

I thank Prof. Masciocchi for giving me the opportunity to do research for three year at CERN. Furthermore I thank you, Silvia, for the supervision and the support – especially during the final phase of the thesis writing. The hospitality and the general atmosphere I have experienced in the ALICE GSI group, are always great. This of course due to the many nice people working there, but to some extend also your responsibility.

Next I thank Dr. Garabatos for supervising my research at CERN. I learned a lot through our common work in the lab and during our many discussions on gaseous detectors and everything else. Interacting with the broad community of researches working with gaseous detectors was particular easy at CERN: Partially, this may be due to the location itself, but the fact that you, Chilo, know everybody contributed for sure. Three years are a long time and they impacted me in the way I do research and in the way I interact in the scientific world. There you had a great influence, I believe. All in all I am grateful for the experiences at CERN. Thank you Chilo!

Furthermore I want to thank the remaining ALICE TPC group at CERN. Especially C. Lippmann, R. Münzer, R. Negrão De Oliveira. It was a pleasure working with you on the (upgrade of the) largest TPC in the world as well as in the laboratory with smaller detectors. D. Vranic, who is no longer at CERN, needs to be mentioned here as well. Your passion for sexy, professional hardware had an impact on us all. The way of interacting in the TPC group at CERN is something I already miss. Weitermachen!

When being involved in the ALICE TPC upgrade, it is hard not to get into contact with P. Gasik and M. Ball. I enjoyed a lot our discussions at beam-times, upgrade meetings, DPGs, beers or various combinations of these things.

I thank my parents for their continuous support and my dearest girlfriend for her presence and support. In addition I thank the the Bundesbrüder of the Bonner Wingolf as well as les sœurs et frères de couleurs of the Valdesia Lausanne, because without them all the studying would have been too focused on studying.

A. Supplementary plots and information

A.1. Simulation of the double-GEM set-up with LTSpice

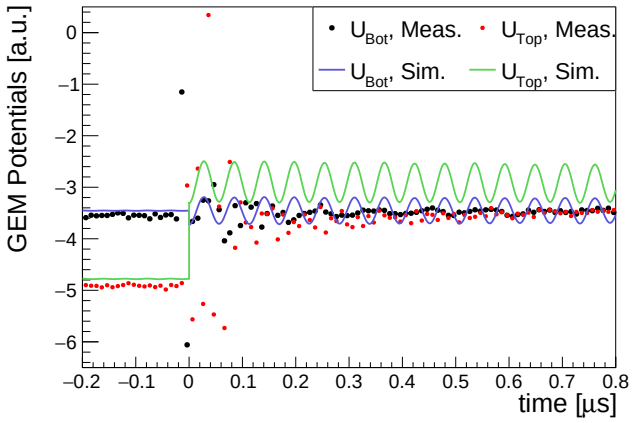

Figure A.1: Simultaneous high voltage probe measurement of a GEM's top and bottom potential (U_{Top} and U_{Bot} *Meas.*) during a discharge at $t \sim 0$. Only the top potential changes, because there is a loading resistor (10 MΩ) at the top side of the GEM and the bottom side is directly connected to the power supply. In addition to the voltage drop, both potentials oscillate. The plot is a zoom of the signals displayed in Figure 6.14a. Furthermore LTSpice [142] simulations of the signals are shown (U_{Top} and U_{Bot} *Sim.*). In contrast to the figure in the text (Fig. 6.12), the internal capacitance of the probes is chosen to be 0.0682 pF.

Figure A.1 shows the same data as displayed in Figure 6.12, but the curves simulated with LTSpice differ. The figure here shows the simulation for a probe capacitance of 0.0682 pF, while a perfect impedance matching between probes and oscilloscope is used for the simulations in Figure 6.12. Otherwise all parameters are the same. The difference of U_{Top} potential between the two different simulations, reveals the AC response of the probe as the impedance matching is not perfect.

A.2. Discharge studies with the cascaded power supply

Figure A.2 shows the same signals as displayed in Figure 6.25. See Figure 6.24 for an explanations of the measurement. The high-voltage probes' AC response is corrected for in the measurements shown here. A too strong correction for small t ($t < 50\,\mu\text{s}$) is expected.

A.3. Secondary discharges

A.3.1. Secondary discharges in the induction gap

Figure A.3. shows the same signals as visible in Figure 7.4a. They are displayed here to illustrate two facts: First, after the secondary discharge it takes more than 500 µs until the U_{Top} and U_{Bot} reach again the value of the bottom potential before the discharge. From there, the top potential is eventually restored. Second, the correction procedure to remove the probes' AC response yields a reasonable value for the potentials after the secondary discharge, even if the parametrisation in Table 6.1 is used. Using this parametrisation for

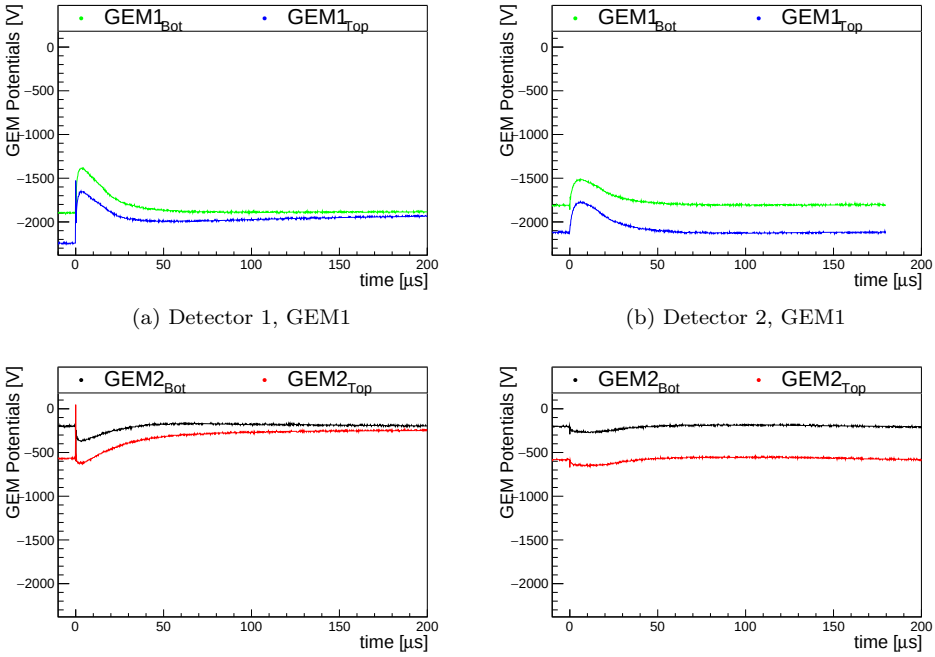

(a) Detector 1, GEM1

(b) Detector 2, GEM1

(c) Detector 1, GEM2

(d) Detector 2, GEM2

Figure A.2: (a), (c), (c): High voltage probe signals at different electrodes of the set-up depicted in Figure 6.24. Figure (d) was recorded as well with the same set-up, however during this recording $R_{\mathrm{L}} = 10\,\mathrm{M\Omega}$ and the independent channel PS has been used. Each plot shows a simultaneous recording of two signals, while GEM2 in detector 1 is discharging. All the signals are scaled according to V, and the AC response of the probes is corrected for. Figure 6.25 shows the same plot but with only the scaling applied.

secondary discharges is not well motivated, because there are differences in the calibration circuit and the experimental set-up.

A.3.2. Secondary discharges in the transfer gap

The P_2 and $\langle t_{\mathrm{Sec}} \rangle$ curves for secondary discharges in the transfer gap are plotted in the text as a function of $\mathrm{E_T} + \Delta U_{\mathrm{GEM2}}/d_{\mathrm{T}}$ (Figures 7.6 and 7.7). In this section we plot them as well as function of the set transfer field $\mathrm{E_T}$ (Figures A.4 and A.5)

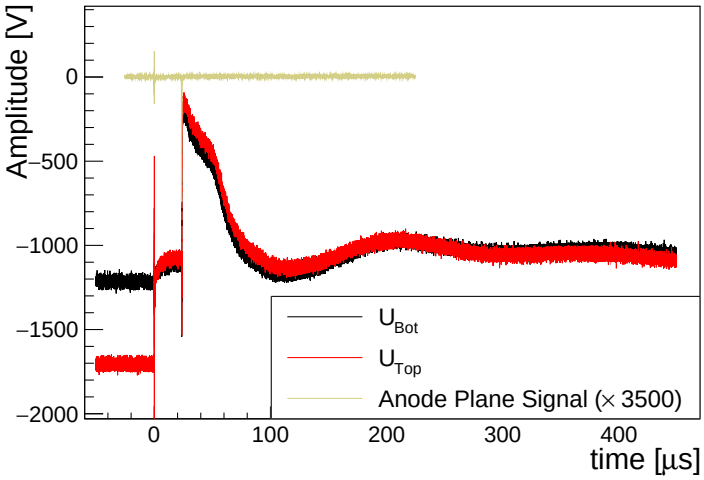

Figure A.3: A longer view of the anode plane and HV probe signals displayed in Figure 7.4a. The correction for the HV probes' AC response (parametrisation in Tab. 6.1.) and the scaling to V is applied, while in the original figure non corrected signals are shown.

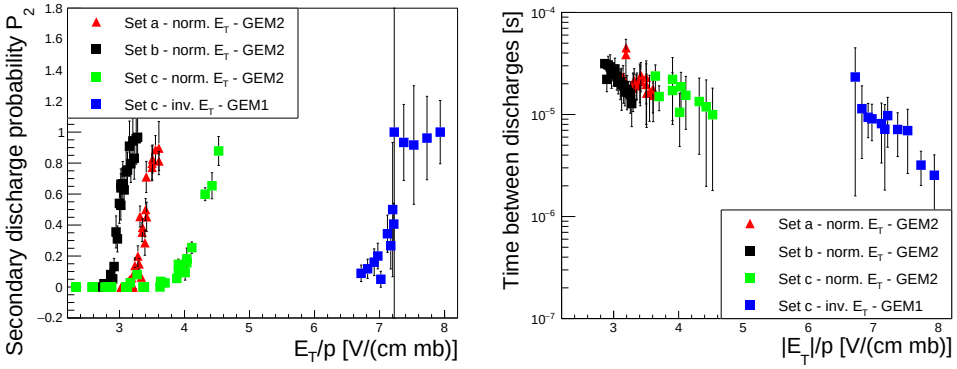

(a) (b)

Figure A.4: (a) P_2 (Eq. (7.1)) and (b) $\langle t_{\mathrm{Sec}} \rangle$ (Sec. 7.2.3) for secondary discharges in the transfer gap as function of the absolute value $|\mathrm{E_T}|/p$. The different settings *Set a* to *Set c* indicate different GEMs in use and correspond to the same settings as in Figure 7.3b. *GEM2* or *GEM1* tells if discharges are triggered in GEM2 or GEM1. The hardware settings: $R_{\mathrm{L}} = 10\,\mathrm{M\Omega}$ and $R_{\mathrm{D}} = 0$, Ar-CO_2 (90-10) as counting gas and the detector is powered with the independent channel power supply. Figure 7.6. shows the same plots as function of $\left|\left(\mathrm{E_T} + \Delta U_{\mathrm{GEM2}} \cdot d_{\mathrm{T}}^{-1}\right) \cdot p^{-1}\right|$.

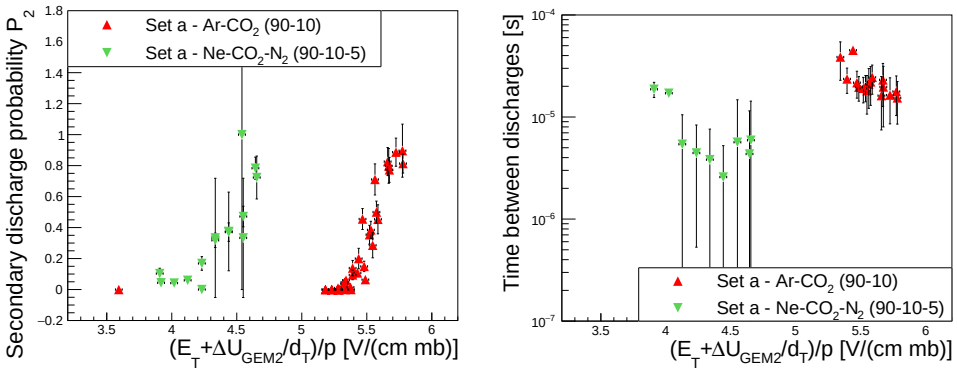

(a) (b)

Figure A.5: Secondary discharges in the transfer gap measured with the Ne-CO_2-N_2 (90-10-5) gas mixture. (a) P_2 (Eq. (7.1)) and (b) $\langle t_{\mathrm{Sec}} \rangle$ (Sec. 7.2.3) is shown for different measurement series with varying high voltage settings and the data is displayed as function of $\mathrm{E_T} \cdot p^{-1}$. See Figure 7.7 for the same plots as function of $\left(\mathrm{E_T} + \Delta U_{\mathrm{GEM2}} \cdot d_{\mathrm{T}}^{-1}\right) \cdot p^{-1}$ and more explanations. The same hardware configuration is present in the detector as for the data displayed in Figure 7.6. Furthermore, the Ar-CO_2 (90-10) points here are the same as in this figure.

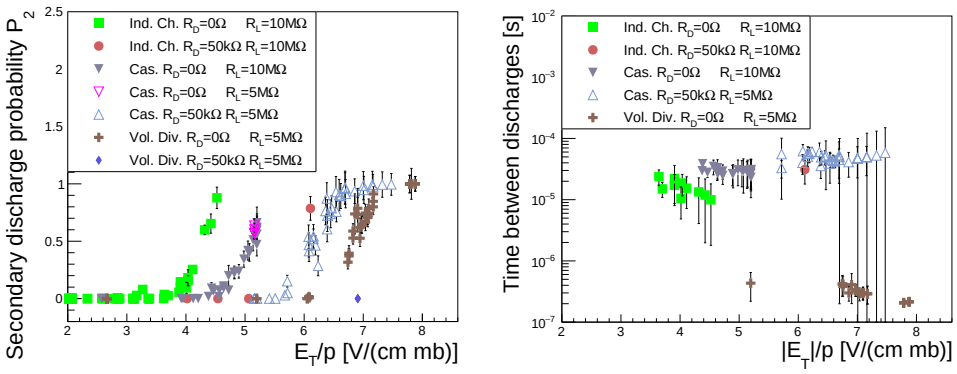

(a) (b)

Figure A.6: (a) P_2 (Eq. (7.1)) and (b) $\langle t_{\mathrm{Sec}} \rangle$ (e.g. Sec. 7.2.3) of secondary discharges in the transfer gap as function of $\mathrm{E_T} \cdot p^{-1}$. (See Figures 7.13 and 7.14 for the same plots as function of $\left(\mathrm{E_T} + \Delta U_{\mathrm{GEM2}} \cdot d_{\mathrm{T}}^{-1}\right) \cdot p^{-1}$ and for further explanations.)

B. Published work

The following peer-reviewed papers contain ideas and results presented throughout this work. Thus, they are listed in the Bibliography as well and cited accordingly in the text.

A. Deisting for the ALICE Collaboration. 'Status of the R&D activities for the upgrade of the ALICE TPC'. Proceedings of 4th Conference on Micro-Pattern Gaseous Detectors, accepted for publication in EPJ Web of Conferences. Jan. 2016. arXiv: 1601.02183 [physics.ins-det]

A. Deisting, C. Garabatos, A. Szabo and Danilo Vranic. 'Measurements of ion mobility in argon and neon based gas mixtures'. *Nuclear Instruments and Methods in Physics Research Section A: Accelerators, Spectrometers, Detectors and Associated Equipment* 845 (2017). Proceedings of the Vienna Conference on Instrumentation 2016, pp. 215-217. DOI: http://doi.org/10.1016/j.nima.2016.06.093

A. Deisting and C. Garabatos. 'Discharge and stability studies for the new readout chambers of the upgraded ALICE TPC'. *Journal of Instrumentation* 12.05 (2017), p. C05017

C. Bibliography

[1] D. R. Nygren. *Proposal to investigate the feasibility of a novel concept in particle detection*. 1974 (cit. on pp. 11, 33, 55).

[2] D. Fancher et al. 'Performance of a Time Projection Chamber'. In: *Nucl. Instrum. Meth.* 161 (1979), p. 383. DOI: 10.1016/0029-554X(79)90411-7 (cit. on p. 11).

[3] J. N. Marx and D. R. Nygren. 'The Time Projection Chamber'. In: *Phys. Today* 31N10 (1978), pp. 46–53. DOI: 10.1063/1.2994775 (cit. on p. 11).

[4] The ALEPH Collaboration. 'ALEPH: A detector for electron-positron annihilations at LEP'. In: *Nuclear Instruments and Methods in Physics Research Section A: Accelerators, Spectrometers, Detectors and Associated Equipment* 294.1 (1990), pp. 121–178. ISSN: 0168-9002. DOI: https://doi.org/10.1016/0168-9002(90)91831-U (cit. on pp. 11, 47).

[5] S. Wenig. 'Performance of the large-scale TPC system in the CERN heavy ion experiment NA49'. In: *Nuclear Instruments and Methods in Physics Research Section A: Accelerators, Spectrometers, Detectors and Associated Equipment* 409.1 (1998), pp. 100–104. ISSN: 0168-9002. DOI: https://doi.org/10.1016/S0168-9002(97)01245-X (cit. on pp. 11, 58, 59).

[6] D. Adamova et al. 'The CERES/NA45 radial drift Time Projection Chamber'. In: *Nuclear Instruments and Methods in Physics Research Section A: Accelerators, Spectrometers, Detectors and Associated Equipment* 593.3 (2008), pp. 203–231. ISSN: 0168-9002. DOI: https://doi.org/10.1016/j.nima.2008.04.056 (cit. on pp. 11, 58).

[7] M. Anderson et al. 'The STAR time projection chamber: a unique tool for studying high multiplicity events at RHIC'. In: *Nuclear Instruments and Methods in Physics Research Section A: Accelerators, Spectrometers, Detectors and Associated Equipment* 499.2 (2003). The Relativistic Heavy Ion Collider Project: RHIC and its Detectors, pp. 659–678. ISSN: 0168-9002. DOI: https://doi.org/10.1016/S0168-9002(02)01964-2 (cit. on p. 11).

[8] C. Garabatos. *Overview on Gas Detector*. 52. International Winter Meeting on Nuclear Physics, Bormio (Italy). URL: http://indico.uni-giessen.de/indico/materialDisplay.py?contribId=49&sessionId=2&materialId=slides&confId=138 (cit. on pp. 11, 58).

[9] The ALICE Collaboration. *ALICE time projection chamber: Technical Design Report*. Tech. rep. Geneva, 2000 (cit. on pp. 11, 47, 48, 59).

[10] The ALICE Collaboration. 'The ALICE experiment at the CERN LHC'. In: *Journal of Instrumentation* 3.08 (2008), S08002 (cit. on pp. 11, 12, 17, 24).

[11] C. Garabatos. 'The ALICE TPC'. In: *Nuclear Instruments and Methods in Physics Research Section A: Accelerators, Spectrometers, Detectors and Associated Equipment* 535.1 (2004). Proceedings of the 10th International Vienna Conference on Instrumentation, pp. 197–200. ISSN: 0168-9002. DOI: https://doi.org/10.1016/j.nima.2004.07.127 (cit. on pp. 11, 84).

[12] J. Alme et al. 'The ALICE TPC, a large 3-dimensional tracking device with fast readout for ultra-high multiplicity events'. In: *Nuclear Instruments and Methods in Physics Research Section A: Accelerators, Spectrometers, Detectors and Associated Equipment* 622.1 (2010), pp. 316–367 (cit. on pp. 11, 38, 47, 49, 55, 57, 59, 60).

[13] L. Evans. 'The Large Hadron Collider'. In: *New Journal of Physics* 9.9 (2007), p. 335 (cit. on p. 11).

[14] G. Charpak et al. 'The use of multiwire proportional counters to select and localize charged particles'. In: *Nuclear Instruments and Methods* 62.3 (1968), pp. 262–268. ISSN: 0029-554X. DOI: https://doi.org/10.1016/0029-554X(68)90371-6 (cit. on pp. 11, 46).

[15] G. Charpak et al. *New Approaches To High Rate Particle Detectors*. 1978 (cit. on pp. 12, 47).

[16] A. Breskin et al. 'The multistep avalanche chamber: A new family of fast, high-rate particle detectors'. In: *Nuclear Instruments and Methods* 161.1 (1979), pp. 19–34. ISSN: 0029-554X. DOI: https://doi.org/10.1016/0029-554X(79)90358-6 (cit. on pp. 12, 47).

[17] P. Braun-Munzinger and J. Stachel. 'The quest for the quark–gluon plasma'. In: *Nature* 448.7151 (2007), pp. 302–309 (cit. on pp. 12, 23).

[18] The ATLAS Collaboration. 'The ATLAS Experiment at the CERN Large Hadron Collider'. In: *Journal of Instrumentation* 3.08 (2008), S08003 (cit. on p. 12).

[19] The CMS Collaboration. 'The CMS experiment at the CERN LHC'. In: *Journal of Instrumentation* 3.08 (2008), S08004 (cit. on p. 12).

[20] The LHCb Collaboration. 'The LHCb Detector at the LHC'. In: *Journal of Instrumentation* 3.08 (2008), S08005 (cit. on p. 12).

[21] H. Appelsäuser et al. *Space-charge distortion measurements and their calibration in the ALICE TPC*. ALICE note in preparation for publication. 2017 (cit. on pp. 12, 26, 60, 67).

[22] The ALICE Collaboration. 'Upgrade of the ALICE Experiment: Letter Of Intent'. In: *Journal of Physics G: Nuclear and Particle Physics* 41.8 (2014), p. 087001 (cit. on pp. 12, 28, 61).

[23] *Upgrade of the ALICE Time Projection Chamber*. Tech. rep. CERN-LHCC-2013-020. ALICE-TDR-016. Geneva: CERN, Oct. 2013 (cit. on pp. 12, 13, 28, 36, 52, 57, 60–62, 65, 67, 84, 88, 147, 155, 161–163, 169).

[24] *Addendum to the Technical Design Report for the Upgrade of the ALICE Time Projection Chamber*. Tech. rep. CERN-LHCC-2015-002. ALICE-TDR-016-ADD-1. Geneva: CERN, Feb. 2015 (cit. on pp. 12, 28, 61, 63, 89, 100–102, 108, 130, 163, 169).

[25] F. Sauli. 'GEM: A new concept for electron amplification in gas detectors'. In: *Nuclear Instruments and Methods in Physics Research Section A: Accelerators, Spectrometers, Detectors and Associated Equipment* 386.2 (1997), pp. 531–534 (cit. on pp. 12, 49, 61).

[26] H. Abramowicz et al. *The International Linear Collider Technical Design Report – Volume 4: Detectors*. Tech. rep. 2013. arXiv: 1306.6329 [physics.ins-det] (cit. on pp. 12, 58).

[27] Piotr Gasik. *Discharge Studies with single- and multi-GEM Structures in a scope of the ALICE TPC Upgrade*. Talk at the RD51 Collaboration Meeting, March 2016. URL: https://indico.cern.ch/event/496113/contributions/2008281/attachments/1242032/1827187/gasik_11032016_sparks_RD51.pdf (cit. on pp. 14, 131, 133, 140, 159–161, 168).

[28] The ATLAS collaboration. 'Observation of a new particle in the search for the Standard Model Higgs boson with the ATLAS detector at the LHC'. In: *Physics Letters B* 716.1 (2012), pp. 1–29. ISSN: 0370-2693. DOI: https://doi.org/10.1016/j.physletb.2012.08.020 (cit. on p. 17).

[29] The CMC collaboration. 'Observation of a new boson at a mass of 125 GeV with the CMS experiment at the LHC'. In: *Physics Letters B* 716.1 (2012), pp. 30–61. ISSN: 0370-2693. DOI: https://doi.org/10.1016/j.physletb.2012.08.021 (cit. on p. 17).

[30] C. Patrignani et al. 'Review of Particle Physics'. In: *Chin. Phys.* C40.10 (2016), p. 100001. DOI: 10.1088/1674-1137/40/10/100001 (cit. on pp. 18, 36).

[31] H. Satz. 'The Quark-Gluon Plasma: A Short Introduction'. In: *Nucl. Phys.* A862-863 (2011), pp. 4–12. DOI: 10.1016/j.nuclphysa.2011.05.014. arXiv: 1101.3937 [hep-ph] (cit. on pp. 18, 19).

[32] P. Braun-Munzinger and J. Wambach. 'Colloquium: Phase diagram of strongly interacting matter'. In: *Rev. Mod. Phys.* 81 (3 July 2009), pp. 1031–1050. DOI: 10.1103/RevModPhys.81.1031 (cit. on pp. 18, 19).

[33] K. G. Wilson. 'Confinement of quarks'. In: *Phys. Rev. D* 10 (8 Oct. 1974), pp. 2445–2459. DOI: 10.1103/PhysRevD.10.2445 (cit. on p. 19).

[34] A. Bazavov et al. 'Equation of state in $(2+1)$-flavor QCD'. In: *Phys. Rev. D* 90 (9 Nov. 2014), p. 094503. DOI: 10.1103/PhysRevD.90.094503 (cit. on p. 20).

[35] S. Ejiri et al. 'Study of QCD Thermodynamics at Finite Density by Taylor Expansion'. In: *Progress of Theoretical Physics Supplement* 153 (2004), pp. 118–126. DOI: 10.1143/PTPS.153.118. eprint: /oup/backfile/content_public/journal/ptps/153/10.1143/ptps.153.118/2/153-118.pdf (cit. on p. 20).

[36] G. F. Chapline et al. 'Highly Excited Nuclear Matter'. In: *Phys. Rev. D* 8 (12 Dec. 1973), pp. 4302–4308. DOI: 10.1103/PhysRevD.8.4302 (cit. on p. 20).

[37] A. Andronic. 'An overview of the experimental study of quark–gluon matter in high-energy nucleus–nucleus collisions'. In: *International Journal of Modern Physics A* 29.22 (2014), p. 1430047. DOI: 10.1142/S0217751X14300476. eprint: http://www.worldscientific.com/doi/pdf/10.1142/S0217751X14300476 (cit. on pp. 20, 21).

[38] U. W. Heinz and M. Jacob. *Evidence for a new state of matter: An Assessment of the results from the CERN lead beam program.* 2000. arXiv: nucl-th/0002042 [nucl-th] (cit. on p. 20).

[39] The BRAHMS collaboration. 'Quark–gluon plasma and color glass condensate at RHIC? The perspective from the BRAHMS experiment'. In: *Nuclear Physics A* 757.1 (2005). First Three Years of Operation of RHIC, pp. 1–27. ISSN: 0375-9474. DOI: https://doi.org/10.1016/j.nuclphysa.2005.02.130 (cit. on p. 20).

[40] The PHOBOS Collaboration. 'The PHOBOS perspective on discoveries at RHIC'. In: *Nuclear Physics A* 757.1 (2005). First Three Years of Operation of RHIC, pp. 28–101. ISSN: 0375-9474. DOI: https://doi.org/10.1016/j.nuclphysa.2005.03.084 (cit. on p. 20).

[41] The PHENIX Collaboration. 'Formation of dense partonic matter in relativistic nucleus–nucleus collisions at RHIC: Experimental evaluation by the PHENIX Collaboration'. In: *Nuclear Physics A* 757.1 (2005). First Three Years of Operation of RHIC, pp. 184–283. ISSN: 0375-9474. DOI: https://doi.org/10.1016/j.nuclphysa.2005.03.086 (cit. on p. 20).

[42] The Star Collaborations. 'Experimental and theoretical challenges in the search for the quark–gluon plasma: The STAR Collaboration's critical assessment of the evidence from RHIC collisions'. In: *Nuclear Physics A* 757.1 (2005). First Three Years of Operation of RHIC, pp. 102–183. ISSN: 0375-9474. DOI: https://doi.org/10.1016/j.nuclphysa.2005.03.085 (cit. on p. 20).

[43] V. Friese. 'The CBM experiment at GSI/FAIR'. In: *Nuclear Physics A* 774.Supplement C (2006). QUARK MATTER 2005, pp. 377–386. ISSN: 0375-9474. DOI: https://doi.org/10.1016/j.nuclphysa.2006.06.018 (cit. on p. 20).

[44] P. Spiller and G. Franchetti. 'The FAIR accelerator project at GSI'. In: *Nuclear Instruments and Methods in Physics Research Section A: Accelerators, Spectrometers, Detectors and Associated Equipment* 561.2 (2006). Proceedings of the Workshop on High Intensity Beam Dynamics, pp. 305–309. ISSN: 0168-9002. DOI: https://doi.org/10.1016/j.nima.2006.01.043 (cit. on p. 20).

[45] A. Andronic, P. Braun-Munzinger and J. Stachel. 'Thermal hadron production in relativistic nuclear collisions: The hadron mass spectrum, the horn, and the QCD phase transition'. In: *Physics Letters B* 673.2 (2009), pp. 142–145. ISSN: 0370-2693. DOI: https://doi.org/10.1016/j.physletb.2009.02.014 (cit. on p. 22).

[46] P. Braun-Munzinger, K. Redlich and J. Stachel. *Particle production in heavy ion collisions*. 2003. arXiv: nucl-th/0304013 [nucl-th] (cit. on p. 22).

[47] M. Floris. 'Hadron yields and the phase diagram of strongly interacting matter'. In: *Nuclear Physics A* 931.Supplement C (2014). QUARK MATTER 2014, pp. 103–112. ISSN: 0375-9474. DOI: https://doi.org/10.1016/j.nuclphysa.2014.09.002 (cit. on p. 22).

[48] The ALICE Collaboration. 'Direct photon production in Pb–Pb collisions at'. In: *Physics Letters B* 754 (2016), pp. 235–248. ISSN: 0370-2693. DOI: https://doi.org/10.1016/j.physletb.2016.01.020 (cit. on p. 23).

[49] T. Matsui and H. Satz. 'J/ψ suppression by quark-gluon plasma formation'. In: *Physics Letters B* 178.4 (1986), pp. 416–422. ISSN: 0370-2693. DOI: https://doi.org/10.1016/0370-2693(86)91404-8 (cit. on p. 23).

[50] A. Adare et al. 'J/ψ Production vs Centrality, Transverse Momentum, and Rapidity in Au+Au Collisions at $\sqrt{s_{NN}} = 200$ GeV'. In: *Phys. Rev. Lett.* 98 (2007), p. 232301. DOI: 10.1103/PhysRevLett.98.232301. arXiv: nucl-ex/0611020 [nucl-ex] (cit. on p. 23).

[51] P. Braun-Munzinger and J. Stachel. '(Non)thermal aspects of charmonium production and a new look at J / ψ suppression'. In: *Phys. Lett.* B490 (2000), pp. 196–202. DOI: 10.1016/S0370-2693(00)00991-6. arXiv: nucl-th/0007059 [nucl-th] (cit. on p. 23).

[52] B. B. Abelev et al. 'Centrality, rapidity and transverse momentum dependence of J/ψ suppression in Pb-Pb collisions at $\sqrt{s_{\mathrm{NN}}}$=2.76 TeV'. In: *Phys. Lett.* B734 (2014), pp. 314–327. DOI: 10.1016/j.physletb.2014.05.064. arXiv: 1311.0214 [nucl-ex] (cit. on p. 23).

[53] H. Kolanoski and N. Wermes. *Teilchendetektoren Grundlagen und Anwendungen*. Vol. 1. Springer Spektrum, Berlin, Heidelberg, 2016. DOI: https://doi.org/10.1007/978-3-662-45350-6 (cit. on pp. 23, 49).

[54] J. Schukraft. 'Heavy-ion physics with the ALICE experiment at the CERN Large Hadron Collider'. In: *Philosophical Transactions of the Royal Society of London A: Mathematical, Physical and Engineering Sciences* 370.1961 (2012), pp. 917–932. ISSN: 1364-503X. DOI: 10.1098/rsta.2011.0469 (cit. on p. 24).

[55] The L3 Collaboration. 'The construction of the L3 experiment'. In: *Nuclear Instruments and Methods in Physics Research Section A: Accelerators, Spectrometers, Detectors and Associated Equipment* 289.1 (1990), pp. 35–102. ISSN: 0168-9002. DOI: https://doi.org/10.1016/0168-9002(90)90250-A (cit. on p. 25).

[56] E. C. Zeballos et al. 'A new type of resistive plate chamber: The multigap RPC'. In: *Nuclear Instruments and Methods in Physics Research Section A: Accelerators, Spectrometers, Detectors and Associated Equipment* 374.1 (1996), pp. 132–135. ISSN: 0168-9002. DOI: https://doi.org/10.1016/0168-9002(96)00158-1 (cit. on p. 26).

[57] P. Buncic, M. Krzewicki and P. Vande Vyvre. *Technical Design Report for the Upgrade of the Online-Offline Computing System*. Tech. rep. CERN-LHCC-2015-006. ALICE-TDR-019. Apr. 2015 (cit. on p. 28).

[58] *Technical Design Report for the Muon Forward Tracker*. Tech. rep. CERN-LHCC-2015-001. ALICE-TDR-018. Jan. 2015 (cit. on p. 28).

[59] The ALICE Collaboration. *Technical Design Report for the Upgrade of the ALICE Inner Tracking System*. Tech. rep. CERN-LHCC-2013-024. ALICE-TDR-017. Nov. 2013 (cit. on p. 28).

[60] P. Antonioli, A. Kluge and W. Riegler. *Upgrade of the ALICE Readout & Trigger System*. Tech. rep. CERN-LHCC-2013-019. ALICE-TDR-015. Presently we require a LHCC-TDR reference number. At a later stage we will fill the required information. Sept. 2013 (cit. on p. 28).

[61] P. Langevin. 'Sur la théorie du mouvement brownien'. In: *CR Acad. Sci. Paris* 146.530-533 (1908), p. 530 (cit. on p. 29).

[62] D. S. Lemons and A. Gythiel. 'Paul Langevin's 1908 paper "on the theory of Brownian motion"["Sur la théorie du mouvement brownien," CR Acad. Sci.(Paris) 146, 530–533 (1908)]'. In: *American Journal of Physics* 65.11 (1997), pp. 1079–1081 (cit. on p. 29).

[63] W. Blum, W. Riegler and L. Rolandi. *Particle detection with drift chambers*. Springer Science & Business Media, 2008 (cit. on pp. 30, 32, 33, 36, 43, 46, 49).

[64] S. Biagi. 'Magboltz 2'. In: *CERN computer newsletter No.2000-001 in section 'Scientific Applications and Software Engineering'* (Apr. 2000) (cit. on pp. 30, 31, 34, 39–41, 71, 106, 119, 148).

[65] L. Koch. 'Measurements and simulations of drift gas properties'. In: (Sept. 2013). Masterarbeit in Physik vorgelegt der Fakultät für Mathematik, Informatik und Naturwissenschaften der RWTH Aachen (cit. on p. 31).

[66] C. Ramsauer. 'Über den Wirkungsquerschnitt der Gasmoleküle gegenüber langsamen Elektronen. I. Fortsetzung'. In: *Annalen der Physik* 371.24 (1922), pp. 546–558 (cit. on p. 31).

[67] J. A. Hornbeck. 'The Drift Velocities of Molecular and Atomic Ions in Helium, Neon, and Argon'. In: *Phys. Rev.* 84 (4 Nov. 1951), pp. 615–620. DOI: 10.1103/PhysRev.84.615 (cit. on p. 31).

[68] E. W. McDaniel and E. A. Mason. *The mobility and diffusion of ions in gases*. 1973 (cit. on pp. 32, 33, 80).

[69] M. A. Blanc. 'Mobilité des Ions'. In: *J. Phys. Theor. Appl.* 7 (1908), pp. 825–839 (cit. on pp. 32, 82, 84).

[70] H. W. Ellis et al. 'Transport properties of gaseous ions over a wide energy range'. In: *Atomic data abd nuclear data tables* 17.3 (1976), pp. 177–210. ISSN: 0092-640X. DOI: https://doi.org/10.1016/0092-640X(76)90001-2 (cit. on pp. 32, 67, 80).

[71] H. W. Ellis et al. 'Transport properties of gaseous ions over a wide energy range. Part II'. In: *Atomic Data and Nuclear Data Tables* 22 (1978), pp. 179–217 (cit. on pp. 32, 67).

[72] H. Ellis et al. 'Transport properties of gaseous ions over a wide energy range. Part III'. In: *Atomic Data and Nuclear Data Tables* 31.1 (1984), pp. 113–151. ISSN: 0092-640X. DOI: https://doi.org/10.1016/0092-640X(84)90018-4 (cit. on pp. 32, 67).

[73] L. Viehland and E. Mason. 'Transport Properties of Gaseous Ions over a Wide Energy Range, IV'. In: *Atomic Data and Nuclear Data Tables* 60.1 (1995), pp. 37–95. ISSN: 0092-640X. DOI: https://doi.org/10.1006/adnd.1995.1004 (cit. on pp. 32, 67).

[74] L. Meitner. 'Über die Entstehung der β-Strahl-Spektren radioaktiver Substanzen'. In: *Zeitschrift für Physik* 9.1 (Dec. 1922), pp. 131–144. ISSN: 0044-3328. DOI: 10.1007/BF01326962 (cit. on p. 35).

[75] P. Auger. 'Sur les rayons β secondaires produits dans un gaz par des rayons X'. In: *C.R.A.S.* 177 (1923) (cit. on p. 35).

[76] F. M. Penning. 'Über Ionisation durch metastabile Atome'. In: *Naturwissenschaften* 15.40 (Oct. 1927), pp. 818–818. ISSN: 1432-1904. DOI: 10.1007/BF01505431 (cit. on p. 35).

[77] Y. Kalkan et al. 'Cluster ions in gas-based detectors'. In: *Journal of Instrumentation* 10.07 (2015), P07004 (cit. on pp. 35, 80, 82–85, 88).

[78] Y. Ikezoe et al. 'Ions in carbon dioxide at an atmospheric pressure'. In: *Radiation Physics and Chemistry (1977)* 20.4 (1982), pp. 253–257. ISSN: 0146-5724. DOI: https://doi.org/10.1016/0146-5724(82)90034-6 (cit. on pp. 35, 80).

[79] H. Bethe and J. Ashkin. 'Passage of radiation through matter'. In: *Experimental Nuclear Physics* (1953) (cit. on p. 36).

[80] F. Bloch. 'Zur Bremsung Rasch Bewegter Teilchen beim Durchgang durch Materie'. In: *Annalen Phys.* 408 (1933), pp. 285–320. DOI: 10.1002/andp.19334080303 (cit. on p. 36).

[81] Particle Data Group and e. a. J. Beringer. 'Review of Particle Physics'. In: *J. Phys. G* (2012) (cit. on p. 37).

[82] E. Fermi. 'The Ionization Loss of Energy in Gases and in Condensed Materials'. In: *Phys. Rev.* 57 (6 Mar. 1940), pp. 485–493. DOI: 10.1103/PhysRev.57.485 (cit. on p. 37).

[83] C. Lippmann. 'Time-projection chambers'. In: *Review of Particle Physics Chin. Phys.* C40.10 (2015). Ed. by C. Patrignani et al. Particle Data Group (cit. on p. 38).

[84] The ALICE collaboration. ALICE-PUBLIC-2015-004. 2015 (cit. on p. 38).

[85] Y. P. Raizer and J. E. Allen. *Gas discharge physics*. Vol. 2. Springer Berlin, 1997 (cit. on pp. 38, 42–44, 46, 97, 98, 120, 166).

[86] *Cross sections used by Magboltz 7.1*. [Online; accessed 11-November-2017]. URL: http://rjd.web.cern.ch/rjd/cgi-bin/cross?update (cit. on p. 41).

[87] H. Geiger and W. Müller. 'Elektronenzählrohr zur Messung schwächster Aktivitäten'. In: *Naturwissenschaften* 16.31 (Aug. 1928), pp. 617–618. ISSN: 1432-1904. DOI: 10.1007/BF01494093 (cit. on pp. 40, 44).

[88] *Free Art License 1.1*. Online; accessed 11-November-2017]. URL: http://artlibre.org/licence/lal/de/ (cit. on p. 43).

[89] F. Paschen. 'Ueber die zum Funkenübergang in Luft, Wasserstoff und Kohlensäure bei verschiedenen Drucken erforderliche Potentialdifferenz'. In: *Annalen der Physik* 273.5 (1889), pp. 69–96. ISSN: 1521-3889. DOI: 10.1002/andp.18892730505 (cit. on p. 43).

[90] J. Townsend. *The theory of ionization of gases by collision*. Constable, Limited, 1910 (cit. on p. 43).

[91] B. Dolgoshein, B. Rodionov and B. Luchkov. 'Streamer chamber'. In: *Nuclear Instruments and Methods* 29.2 (1964), pp. 270–276. ISSN: 0029-554X. DOI: https://doi.org/10.1016/0029-554X(64)90379-9 (cit. on p. 44).

[92] H. Raether. *Electron avalanches and breakdown in gases*. Butterworths advanced physics series. London: Butterworths, 1964 (cit. on pp. 44, 97).

[93] V. Peskov and P. Fonte. *Research on discharges in micropattern and small gap gaseous detectors*. 2009. arXiv: 0911.0463 [physics.ins-det] (cit. on pp. 46, 131).

[94] Veenhof, Rob. 'Garfield-simulation of gaseous detectors'. In: *Cern Program Library W* 5050 (1984), p. 2001 (cit. on pp. 47, 48, 51, 67, 71, 72, 78).

[95] The ALEPH collaboration. 'The ALEPH Handbook'. In: *ALEPH* (1989). Ed. by W. Blum (cit. on pp. 47, 58).

[96] D. R. Nygren. 'Future Prospects of the TPC Idea'. In: *Physica Scripta* 23.4A (1981), p. 584 (cit. on p. 47).

[97] F. Sauli. *Gaseous radiation detectors: fundamentals and applications*. 36. Cambridge University Press, 2014 (cit. on p. 49).

[98] M. Villa et al. 'Progress on large area GEMs'. In: *Nuclear Instruments and Methods in Physics Research Section A: Accelerators, Spectrometers, Detectors and Associated Equipment* 628.1 (2011), pp. 182–186 (cit. on pp. 49, 50).

[99] F. Sauli. 'The gas electron multiplier (GEM): Operating principles and applications'. In: *Nuclear Instruments and Methods in Physics Research Section A: Accelerators, Spectrometers, Detectors and Associated Equipment* 805 (2016), pp. 2–24 (cit. on pp. 50, 52).

[100] ANSYS® Academic Research Release 16.2 (cit. on pp. 50, 51).

[101] F. Böhmer et al. 'Simulation of space-charge effects in an ungated GEM-based TPC'. In: *Nuclear Instruments and Methods in Physics Research Section A: Accelerators, Spectrometers, Detectors and Associated Equipment* 719 (2013), pp. 101–108. ISSN: 0168-9002. DOI: http://dx.doi.org/10.1016/j.nima.2013.04.020. arXiv: 1209.0482 [physics.ins-det] (cit. on pp. 51, 60, 67).

[102] M. Killenberg et al. 'Modelling and measurement of charge transfer in multiple GEM structures'. In: *Nuclear Instruments and Methods in Physics Research Section A: Accelerators, Spectrometers, Detectors and Associated Equipment* 498.1 (2003), pp. 369–383 (cit. on pp. 50, 107, 169).

[103] V. Ratza et al. 'A model for charge transfer processes in GEM foils'. In: *Paper in preperation* (2017) (cit. on p. 50).

[104] S. Bachmann et al. 'Discharge studies and prevention in the gas electron multiplier (GEM)'. In: *Nuclear Instruments and Methods in Physics Research Section A: Accelerators, Spectrometers, Detectors and Associated Equipment* 479.2 (2002), pp. 294–308 (cit. on pp. 52, 97, 106, 108, 121, 131).

[105] R. E. Bosch et al. 'The ALTRO chip: a 16-channel A/D converter and digital processor for gas detectors'. In: *2002 IEEE Nuclear Science Symposium Conference Record*. Vol. 1. Nov. 2002, 566–570 vol.1. DOI: 10.1109/NSSMIC.2002.1239377 (cit. on p. 55).

[106] C. Rubbia. *The liquid-argon time projection chamber: a new concept for neutrino detectors*. Tech. rep. CERN-EP-INT-77-8. Geneva: CERN, 1977 (cit. on p. 57).

[107] S. Amerio et al. 'Design, construction and tests of the ICARUS T600 detector'. In: *Nuclear Instruments and Methods in Physics Research Section A: Accelerators, Spectrometers, Detectors and Associated Equipment* 527.3 (2004), pp. 329–410. ISSN: 0168-9002. DOI: https://doi.org/10.1016/j.nima.2004.02.044 (cit. on p. 57).

[108] A. Badertscher et al. 'First operation and performance of a 200 lt double phase LAr LEM-TPC with a 40×76 cm^2 readout'. In: *Journal of Instrumentation* 8.04 (2013), P04012 (cit. on p. 57).

[109] A. Lebedev. 'A laser calibration system for the STAR TPC'. In: *Nuclear Instruments and Methods in Physics Research Section A: Accelerators, Spectrometers, Detectors and Associated Equipment* 478.1 (2002). Proceedings of the ninth Int.Conf. on Instrumentation, pp. 163–165. ISSN: 0168-9002. DOI: https://doi.org/10.1016/S0168-9002(01)01747-8 (cit. on p. 58).

[110] T. Krautscheid. 'Simulation of a pixelized TPC at the ILD'. In: *Design Studies for the Pixelized Readout of a TPC for the ILD* (2015) (cit. on pp. 60, 67).

[111] The ALICE Collaboration. 'Performance of the ALICE experiment at the CERN LHC'. In: *International Journal of Modern Physics A* 29.24 (2014), p. 1430044. DOI: 10.1142/S0217751X14300440 (cit. on p. 60).

[112] L. Fabbietti et al. 'The PANDA GEM-based TPC prototype'. In: *Nuclear Instruments and Methods in Physics Research Section A: Accelerators, Spectrometers, Detectors and Associated Equipment* 628.1 (2011). VCI 2010, pp. 204–208. ISSN: 0168-9002. DOI: https://doi.org/10.1016/j.nima.2010.06.317 (cit. on p. 61).

[113] F. Böhmer et al. 'First measurement of dE/dx with a GEM-based TPC'. In: *Nuclear Instruments and Methods in Physics Research Section A: Accelerators, Spectrometers, Detectors and Associated Equipment* 737.Supplement C (2014), pp. 214–221. ISSN: 0168-9002. DOI: https://doi.org/10.1016/j.nima.2013.10.094 (cit. on p. 61).

[114] B. Ketzer. 'A time projection chamber for high-rate experiments: Towards an upgrade of the ALICE TPC'. In: *Nuclear Instruments and Methods in Physics Research Section A: Accelerators, Spectrometers, Detectors and Associated Equipment* 732.Supplement C (2013). Vienna Conference on Instrumentation 2013, pp. 237–240. ISSN: 0168-9002. DOI: https://doi.org/10.1016/j.nima.2013.08.027 (cit. on p. 61).

[115] M. Berger et al. 'A large ungated TPC with GEM amplification'. In: *Nuclear Instruments and Methods in Physics Research Section A: Accelerators, Spectrometers, Detectors and Associated Equipment* 869 (2017), pp. 180–204. ISSN: 0168-9002. DOI: http://dx.doi.org/10.1016/j.nima.2017.05.027 (cit. on p. 61).

[116] H. Junde. In: *Nuclear Data Sheets* 109 (2008), p. 787 (cit. on p. 61).

[117] The ALICE Collaboration. *Readout chamber production, Part I, Final Readout Chambers characterization*. 2017. [Online; accessed 21-June-2017]. URL: https://indico.cern.ch/event/617818/contributions/2493327/attachments/1422943/2186698/gasik_PRR_PART_I.pdf (cit. on p. 63).

[118] A. Mathis. *Study of the dE/dx resolution of a GEM Readout Chamber prototype for the upgrade of the ALICE TPC*. 2017. arXiv: 1707.05779 [physics.ins-det]. URL: https://inspirehep.net/record/1610652/files/arXiv:1707.05779.pdf (cit. on p. 63).

[119] A. Deisting. 'Status of the R&D activities for the upgrade of the ALICE TPC'. In: Proceedings of 4th Conference on Micro-Pattern Gaseous Detectors. Jan. 2016. arXiv: 1601.02183 [physics.ins-det] (cit. on pp. 63, 174).

[120] R. Veenhof. *Choosing a gas mixture for the ALICE TPC*. 2003 (cit. on pp. 65, 67, 88).

[121] A. ORTEC. *Model 142IH Preamplifier Operating and Service Manual*. 2013. [Online; accessed 06-October-2017]. URL: http://www.ortec-online.com/-/media/ametekortec/manuals/142ih-mnl.pdf (cit. on p. 69).

[122] CAEN. *MOD. N471 2 FOLD H.V. POWER SUPPLY*. 21st April 1999. [Online; accessed 06-October-2017]. URL: http://www.caen.it/servlet/checkCaenManualFile?Id=5301 (cit. on p. 69).

[123] CAEN. *MOD. N 470 4 CHANNEL PROGRAMMABLE H.V. POWER SUPPLY*. 2002. [Online; accessed 07-June-2017]. URL: www.caen.it/servlet/checkCaenManualFile?Id=5240 (cit. on pp. 69, 90, 122, 131, 132, 134).

[124] S. Ramo. 'Currents induced by electron motion'. In: *Proc. Ire* 27.9 (1939), pp. 584–585 (cit. on pp. 70, 73).

[125] I. Smirnov. *HEED version 1.01: Detailed Simulation of the Initial Ionization in Gases*. CERN-CNL-ARTICLE-1997-041. Mar. 1997. URL: http://cds.cern.ch/record/1018083 (cit. on p. 71).

[126] J. G. Proakis and D. G. Manolakis. *Digital signal processing: principles, algorithms, and applications*. Pearson Prentice Hall, 2007 (cit. on p. 75).

[127] Rene Brun and Fons Rademakers. 'ROOT - An Object Oriented Data Analysis Framework'. In: *Nuclear Instruments and Methods in Physics Research Section A: Accelerators, Spectrometers, Detectors and Associated Equipment* 389 (1997). Proceedings AIHENP'96 Workshop, Lausanne, Sep. 1996, pp. 81–86 (cit. on p. 75).

[128] M. Frigo and S. Johnson. 'The Design and Implementation of FFTW3'. In: *Proceedings of the IEEE* 93.2 (2005). Special issue on "Program Generation, Optimization, and Platform Adaptation", pp. 216–231 (cit. on p. 75).

[129] In: *Wutz Handbuch Vakuumtechnik* 7 (). Ed. by K. Jousten, p. 668 (cit. on p. 80).

[130] G. Schultz, G. Charpak and F. Sauli. 'Mobilities of positive ions in some gas mixtures used in proportional and drift chambers'. In: *Revue de Physique Appliquée* 12.1 (1977), pp. 67–70 (cit. on pp. 83, 84, 88).

[131] P. Encarnação et al. 'Experimental ion mobility measurements in Ar-CO2 mixtures'. In: *Journal of Instrumentation* 10.01 (2015), P01010 (cit. on pp. 83, 84, 88).

[132] D. Varga. *Ion mobility: preliminary results*. Talk at the RD51 mini week, June 2014. URL: https://indico.cern.ch/event/323839/contributions/751953/attachments/627122/862953/mobility_ArNe.pdf (cit. on pp. 83, 84, 88).

[133] A. Deisting et al. 'Measurements of ion mobility in argon and neon based gas mixtures'. In: *Nuclear Instruments and Methods in Physics Research Section A: Accelerators, Spectrometers, Detectors and Associated Equipment* 845 (2017). Proceedings of the Vienna Conference on Instrumentation 2016, pp. 215–217. ISSN: 0168-9002. DOI: http://doi.org/10.1016/j.nima.2016.06.093 (cit. on p. 83).

[134] R. Veenhof. Personal communication (cit. on p. 84).

[135] S. Lias. 'Ionization Energy Evaluation'. In: *NIST Chemistry WebBook, NIST Standard Reference Database* 69 (2017). Ed. by P. Linstrom and W. Mallard. retrieved October 29, 2017 (cit. on p. 85).

[136] A. Cortez et al. 'Experimental ion mobility measurements in Ne-N2'. In: *Journal of Instrumentation* 11.11 (2016), P11019 (cit. on pp. 85, 86).

[137] M. J. Renato Negrão and C. Garabots. 'Ageing studies with GEMs at relatively high gains'. In: *MPGD Applications Beyond Fundamental Science Workshop and the 18th RD51 Collaboration Meeting*. Aveiro, Portugal. 2016 (cit. on p. 89).

[138] CAEN. *A1515 1-1.3kV/1-3mA HV Reversible Ch. Boards Rev.5-22May2017*. 2017. [Online; accessed 17-July-2017]. URL: http://www.caen.it/servlet/checkCaenManualFile?Id=12498 (cit. on pp. 90, 121, 122, 131, 155).

[139] Keysight Technologies. *Infiniium 9000 Series Oscilloscopes – Data Sheet*. 2017. [Online; accessed 06-June-2017]. URL: http://literature.cdn.keysight.com/litweb/pdf/5990-3746EN.pdf?id=1705234 (cit. on p. 92).

[140] Rode & Schwarz. *R&S RTE – Digitales Oszilloskop – Scope of the art*. 2014. [Online; accessed 06-June-2017]. URL: http://cdn1.shop.rohde-schwarz.com/media/catalog/product/R/T/RTE_bro_de_3606-9033-11_v0800_72dpi.pdf (cit. on p. 92).

[141] tyco electronics. *FT2/FU2 realy*. 2004. [Online; accessed 06-June-2017]. URL: http://www.tycorelay.com/pdf/ft2_fu2.pdf (cit. on p. 92).

[142] Engelhardt, Mike. *LTspice IV for OS X*. ©2012-2015 Linear Technology Corporation. All rights reserved. URL: http://www.linear.com/designtools/software/%5C-%7B%5C#%7DLTspice (cit. on pp. 95, 110, 111, 123, 139, 142, 157, 179).

[143] K. Bergström and S. Sunner. 'The Relative Permittivity of Argon, Carbon Dioxide, and Hydrogen, Determined at 10 kHz Using a Transformer Bridge Method'. In: *Physica Scripta* 13.1 (1976), p. 51 (cit. on pp. 97, 111).

[144] P. Gasik et al. 'Charge density as a driving factor of discharge formation in GEM-based detectors'. In: *Nuclear Instruments and Methods in Physics Research Section A: Accelerators, Spectrometers, Detectors and Associated Equipment* 870 (2017), pp. 116–122. ISSN: 0168-9002. DOI: http://dx.doi.org/10.1016/j.nima.2017.07.042 (cit. on pp. 97, 102, 103, 108).

[145] Alessandro Cardini. 'A systematic study on discharge-induced GEM-failure phenomena'. In: *Nuclear Science Symposium Conference Record, 2005 IEEE*. Vol. 2. IEEE. 2005, 1127–1131 (cit. on p. 99).

[146] *Work in Progress: Discharge studies – GEM single-hole discharges*. J. Merlin, A. Petusseau, A. H. Shah (all CMS) and P. Thuiner (CERN EP-DT-DD). (2017) (cit. on p. 100).

[147] Merlin, J. A. and Thuiner, P. and Shah A. H. *Effect of discharges on GEM detectors – preliminary test and plan*. Talk at the RD51 Collaboration Meeting, Sept. 2017. URL: https://indico.cern.ch/event/667256/contributions/2731750/ (cit. on p. 100).

[148] T. Bortner and G. Hurst. 'Ionization of pure gases and mixtures of gases by 5-MeV alpha particles'. In: *Physical Review* 93.6 (1954), p. 1236 (cit. on p. 100).

[149] S. Agostinelli et al. 'Geant4—a simulation toolkit'. In: *Nuclear Instruments and Methods in Physics Research Section A: Accelerators, Spectrometers, Detectors and Associated Equipment* 506.3 (2003), pp. 250–303. ISSN: 0168-9002. DOI: http://dx.doi.org/10.1016/S0168-9002(03)01368-8 (cit. on p. 100).

[150] K. B. MacAdam et al. 'Laser-Microwave Spectroscopy of Cu I Atoms in S, P, D, F and G Rydberg States'. In: *Journal of Physics B: Atomic, Molecular and Optical Physics* 42.16 (2009), p. 165009. DOI: DOI:10.1088/0953-4075/42/16/165009 (cit. on p. 120).

[151] Tambave, Ganesh Jagannath. *GEM discharge survival test of SAMPA*. Talk at the ALICE TPC Upgrade meeting, March 2017. URL: https://indico.cern.ch/event/623127/contributions/2524363/attachments/1431141/2198538/TPCU_Meeting_ESD_tests_21March2017.pdf (cit. on pp. 129, 165).

[152] Alexandra Datz. 'Studies on Secondary Discharges and their Mitigation with a two GEM Detector'. In: (March 2017). Bachelor Thesis submitted to the University of Heidelberg (cit. on pp. 131, 146, 149, 150, 153, 154, 167, 168).

[153] A. Deisting, and C. Garabatos, and S. Masciocchi. 'Study of secondary discharges in Ar-CO_2 (90-10) and Ne-CO_2-N_2 (90-10-5)'. In: *GSI scientific report 2016* (2016), p. 144. DOI: {10.15120/GR-2017-1} (cit. on p. 147).

[154] P. Gasik. *Discharge propagation studies with a single GEM in various Ar- and Ne-based gas mixtures*. Talk at the ALICE TPC Upgrade meeting, March 2016. URL: https://indico.cern.ch/event/496488/contributions/2016582/attachments/1247147/1837245/gasik_22032016.pdf (cit. on pp. 147, 168).

[155] P. Gasik and A. Deisting. *Discharge studies with single GEMs*. Talk at the RD51 Mini-Week, June 2016. URL: https://indico.cern.ch/event/532518/contributions/2187809/attachments/1286129/1913118/RD51-meeting-7-6-16.pdf (cit. on p. 147).

[156] A. Deisting and C. Garabatos. 'Discharge and stability studies for the new readout chambers of the upgraded ALICE TPC'. In: *Journal of Instrumentation* 12.05 (2017), p. C05017 (cit. on pp. 149, 150).

[157] Piotr Gasik. *Resistor studies*. Talk at the ALICE TPC project review (14^{th} Sept. 2016). URL: https://indico.cern.ch/event/563976/ (cit. on pp. 149, 168).

[158] The ALICE Collaboration. *ALICE TPC upgrade HV engineering design report*. 2017. [Online; accessed 26-November-2017]. URL: https://indico.cern.ch/event/677082/ (cit. on p. 162).

[159] P. Gasik, and the ALICE TPC collaboration. 'Quadruple GEM PCB simulator'. In: *GSI scientific report 2016* (2016), p. 145. DOI: {10.15120/GR-2017-1} (cit. on p. 167).

[160] The ALICE Collaboration. *Chamber construction and assembly*. 2015. [Online; accessed 31-October-2017]. URL: https://indico.cern.ch/event/448484/contributions/1955854/ (cit. on p. 169).

[161] P. Gasik and the ALICE Collaboration and others. 'Building a large-area GEM-based readout chamber for the upgrade of the ALICE TPC'. In: *Nuclear Instruments and Methods in Physics Research Section A: Accelerators, Spectrometers, Detectors and Associated Equipment* 845 (2017), 222–225 (cit. on p. 170).

[162] MATLAB®. *version 9.1.0 (R2016b)*. Natick, Massachusetts, USA: The MathWorks Inc., 2016 (cit. on p. 172).

[163] T. T. Rudzki. 'Commissioning and testing of large-area GEM-based readout chambers for the high-rate ALICE TPC'. In: (Oct. 2017). Master Thesis submitted to the University of Heidelberg (cit. on p. 174).

D. Erklärung zu dieser Arbeit

Erklärung:

Hiermit verischere ich, Alexander Deisting, dass ich diese Arbeit selbstständig verfasst habe und keine anderen als die angegebenen Quellen und Hilfsmittel benutzt habe.

Darmstadt, den 27.11.2017 .....